

Aus dem Institut für Molekular- und Zellbiologie
der Hochschule Mannheim
(Direktor: Prof. Dr. rer. nat. Mathias Hafner)

Targeted 2D- and 3D-cell cultures reveal mechanistic effects of
extracellular matrix and stromal cells on the metastatic niche formation
and metabolism of cancer cells.

Inauguraldissertation
zur Erlangung des Doctor scientiarum humanarum (Dr. sc. hum.)
der
Medizinischen Fakultät Mannheim
der Ruprecht-Karls-Universität
zu
Heidelberg

vorgelegt von
Florian Keller

aus
Karlsruhe
2021

Dekan: Prof. Dr. med. Sergij Goerd
Referent: Prof. Dr. rer. nat. Mathias Hafner

To those who believed in me ...

... and those who did not at all.

TABLE OF CONTENTS

	Page
ABBREVIATIONS	1
1 INTRODUCTION	3
1.1 Properties of the extracellular matrix and its cues	3
1.2 Cell Lines chosen to study intercellular signaling that is mediated by the ECM	10
1.3 Primary ECM as a cell culture material.....	12
1.4 Cell culture modeling	14
1.4.1 2D-derived cell culture modeling as method of choice for basic screening.....	14
1.4.2 3D-cell cultures with additional finetuning for specific physiological analysis	16
1.5 Aims and research questions	19
2 ARTICLE 1: BONE SIALOPROTEIN SHOWS ENHANCED EXPRESSION IN EARLY, HIGH-PROLIFERATION STAGES OF THREE-DIMENSIONAL SPHEROID CELL CULTURES OF BREAST CANCER CELL LINE MDA-MB-231	21
3 ARTICLE 2: TOWARDS OPTIMIZED BREAST CANCER 3D-SPHEROID MONO- AND CO-CULTURE MODELS FOR PHARMACOLOGICAL RESEARCH AND SCREENING	42
4 ARTICLE 3: ROUTINE OPTICAL CLEARING OF 3D-CELL CULTURES: SIMPLICITY FORWARD	55
5 ARTICLE 4: EXTRACELLULAR MATRIX COMPONENTS REGULATE BONE SIALOPROTEIN EXPRESSION IN MDA-MB-231 BREAST CANCER CELLS	79

6	ARTICLE 5: A SCAFFOLD-FREE 3-D CO-CULTURE MIMICS THE MAJOR FEATURES OF THE REVERSE WARBURG EFFECT IN VITRO	95
7	CONCLUSIVE DISCUSSION	117
7.1	Cancer cell homing and metastatic niche formation are induced by the secretion of ECM-modulating factors	117
7.2	Metabolic interactions with ECM-providing stromal cells support cancer progression.....	118
7.3	Technological advances improve cell culture and data acquisition quality to obtain comprehensive information on classified populations.....	121
7.4	Broader considerations of relevant literature as future perspective	122
7.5	Summarizing outlook.....	124
8	SUMMARY	126
9	ZUSAMMENFASSUNG.....	128
10	REFERENCES.....	130
11	SUPPLEMENTARY MATERIAL	166
12	PUBLICATIONS	191
13	CURRICULUM VITAE	192
14	DANKSAGUNG.....	193

ABBREVIATIONS

ACL	Adenosine Triphosphate Citrate Lyase
AF	Alexa Fluor
AF165	human anti-human BSP antibody
ANOVA	Analysis of Variance
ATP	Adenosine Triphosphate
AU	Arbitrary Units
BME	Basal Membrane Extract
BMP-7	Bone Morphogenic Protein 7
BSA	Bovine Serum Albumin
BSP	Bone Sialoprotein
CAF	Cancer Associated Fibroblast
Cav1	Caveolin 1
CCD	CCD-1137Sk
CEA	Carcino Embryonic Antigen
Coll1/4	Type-I/IV collagen
CTg/r/dr	CellTracker green/red/deep red
DAPI	4',6-Diamidino-2-Phenylindole
DiV	Days in Vitro
DMP1	Dentin Matrix Protein I
DMSO	Dimethyl Sulfoxide
DRAQ5	Deep Red Anthraquinone 5
ECM	Extracellular Matrix
EGF	Epithelial Growth Factor
EGFR	Epithelial Growth Factor Receptor
EMT	Epithelial Mesenchymal Transition
ER	Oestrogen Receptor
ERK	Extracellular-signal Regulated Kinases
FACITs	Fibril-Associated Collagens with Interrupted Triple-helices
FBS	Fetal Bovine Serum
FP21	Mouse anti-human BSP antibody
GAPDH	Glyceraldehyde 3-phosphate dehydrogenase
GelMA	Gelatin-Methacryloyl
HD	Hanging Drop Technique
HEPES	N-2-Hydroxyethylpiperazine-N'-2-Ethanesulfonic Acid
HER2	Epidermal Growth Factor Receptor 2
hMSCs	Human Mesenchymal Stem Cells
HK-2	Hexokinase 2
IDK1	rat anti-human BSP antibody
IGF	Insulin-like Growth Factor
IL	Interleukin
IM	Inlay Method

ABBREVIATIONS

LC3	1A/1B-Light Chain 3
LDH	Lactate Dehydrogenase
M	media
MAPK	Mitogen-Activated Protein Kinase
MCF	MCF10A
MCT	Monocarboxylate Transporter
MDA	MDA-MB-231
MET	Mesenchymal Epithelial Transition
MMP	Matrix Metalloprotease
mTOR(C)	Mammalian Target of Rapamycin (Complex)
OM	On-Top Method
ON	Over Night
OPN	Osteopontin
P62	ubiquitin-binding protein p62
PARs	Proteinase-Activated Receptors
PBS	Phosphate Buffered Saline
PEG	Polyethylene glycol
PI3K	Phosphatidylinositol-3-Kinase
PFA	Paraformaldehyde
PPPP	Proline-Rich Domain
PR	Progesterone Receptor
PTEN	Phosphatase and Tensin Homolog
RANK(L)	Receptor Activator of Nuclear Factor κ B (ligand)
Ras	Rat Sarcoma – Signaling protein
RGD	Arginine-Glycine-Aspartate motif
RI	Refractive Index
ROI	Region Of Interest
RT	Room Temperature
RUNX2	Runt-related transcription factor 2
S	Supplementary
SD	Standard Deviation
SDH	Succinate Dehydrogenase
SEM	Standard Error of the Mean
SIBLING	Small Integrin-Binding Ligand, N-linked Glycoprotein
SM	Sandwich Method
SNR	Signal to Noise Ratio
SSEE	Casein Kinase II
TAE	Tris-Acetate-EDTA (Ethylenediamine Tetraacetic Acid)
TGF β	Transforming Growth Factor Beta
TIGAR	TP53 (Tumor Protein 53)-Induced Glycolysis and Apoptosis Regulator
TMRM	Tetramethylrhodamin Methyl ester
TOMM20	Translocase Of Outer Mitochondrial Membrane 20
VEGF	Vascular Endothelial Growth Factor
WGA	Wheat Germ Agglutinin

1 INTRODUCTION

The extracellular matrix (ECM) and stromal cells play pivotal roles in cancer biology. In this cumulative work, new cell culture models were established to validate alterations in the ECM-modulated cancer biology. To reproduce cancer cell signal secretion that can induce metastatic niche formation in bone tissue and metabolic coupling with stromal cells undergoing epithelial mesenchymal transition (EMT), different culture settings were tested.

1.1 Properties of the extracellular matrix and its cues

The extracellular matrix (ECM) is composed of water, proteins, and polysaccharides and serves as non-cellular backbone for tissues and organs. Due to its versatile presence in the human body, its assembly is highly dependent on local requirements, making the ECM one of the most complex structures to be defined for the modeling of physiological properties. A myriad of influencing factors on the cellular behavior must be addressed to close the gap between *in vitro* investigations and actual *in vivo* biology (Frantz et al., 2010).

The most apparent purpose of the ECM is to provide the overall tissue structure. Cell adhesion might be mediated by specific binding sites like integrins, glycoprotein branching, or receptors lacking kinase activity, but also unspecific alignments based on ionic interactions mediate their settlement. All these interdependencies can be mediated by the abundant protein, collagen, that is ubiquitously present in mammalian ECM (Leitinger and Hohenester, 2007). That group of at least 28 different triple helix polypeptides is expressed by 42 highly conserved genes resulting in repetitive Glycine-X-Y chains. They do not only provide tissue structure, but also guide migration, differentiation, morphogenesis, and wound healing. The glycine residues in collagens support stable packing of the trimer, while hydroxyprolines serve as stabilizers (Veit et al., 2006). Overall, collagens can be classified based on their supramolecular assembly into fibrils, fibril-associated collagens with interrupted triple-helices (FACITs), networks, hexagonal networks, beaded filaments, and anchoring fibrils defining the tissue morphology (Ricard-Blum, 2011). All of them might be crosslinked with lysyl oxidases that are mainly responsible for the resulting stiffness (Myllyharju and Kivirikko, 2004). Incorporated thrombospondin can maintain tissue homeostasis, since modulation of collagen structure, cell morphology and migration, as well as proliferation and apoptosis are regulated by its binding partners (Tan and Lawler, 2009). Collagen is often linked to fibronectin, another fibrillar structure that is composed of dimers. Fibronectin primarily ensures tissue integrity, since it provides binding sites for itself, but also for collagen, integrins exposed at cellular surfaces, and other ECM components. Therefore, collagen and fibronectin are the key players in setting the basic layout of soft tissue (Pankov and Yamada, 2002).

ECM tension and mechanical signal transduction are key regulating factors for tissue homeostasis. These properties are not only dependent on the ECM scaffold and embedded cells, but also on proteoglycan structures. These molecules further support the tissue architecture through the glucosaminoglycan chains linking protein cores and water attracted by hydroscopic sugar chains. The enclosed liquid helps withstanding compressive forces without severe ECM rupturing and inflammation (Goldoni and Iozzo, 2008). Small leucine-rich proteoglycans, such as lumican, can bind various

cellular receptors such as the epidermal growth factor receptor, insulin-like growth factor 1 receptor and transforming growth factor beta (TGF β) receptors (Schaefer and Iozzo, 2008), thus, blocking or enhancing cellular responses through co-receptor support. Especially on the basement membrane, modular proteoglycans may mediate angiogenesis. Finally, proteoglycans help regulating several pathways dictating the cellular fate based on adhesion, migration, and proliferation (Schaefer and Schaefer, 2010). Therefore, ECM structures are not only crucial for physiological tissue homeostasis, but also play a key role in cancer associated tissue alterations, since not only metabolic activities on single cell level, but also overall tissue stiffness and permeability are altered towards hardened fibril stiffness, which may induce stromal cell aberrations (Erler and Weaver, 2009).

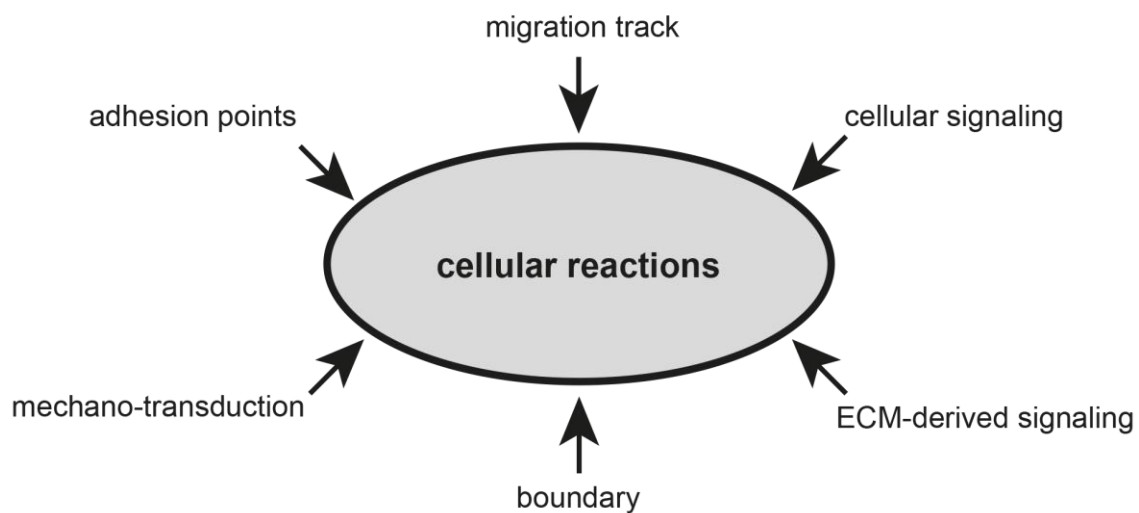


Figure 1. Mechanistic influence of the ECM on cellular reactions. Different properties result in versatile functions of the ECM. Subtissues are defined by cellular polarity based on their anchoring. Therefore, cellular migration is prevented or facilitated dependent on the context. The overall homeostasis is dependent on built-up gradients of incorporated growth-factors and secondary signaling pathways mediated by (co-)receptors may be activated by compound release during remodeling processes including e.g. matrix metalloproteases. Finally, cellular behavior differs based on physical properties provided by the ECM, as stiffness and shear stress can also stimulate protein expression.

Based on structural differences of the ECM, cellular activity can be modulated (Fig. 1). Depending on ECM composition, cells might preferentially adhere to, migrate through, or also react metabolically to signals in the ECM (Lu et al., 2012). Indeed, a major trigger for altered cell responses are fragmented ECM regions. These can result from injury, but also mediated by tissue intrinsic remodeling via enzyme secretion (Ortega and Werb, 2002). EMT and mesenchymal epithelial transition (MET) as counterpart are important processes for the expansion of tissues with multiple types of terminally differentiated cells, since epithelial cells typically exert tissue-specific functions, whereas mesenchymal cells play supporting roles and maintain the structure based on modulating stimuli (Kalluri and Weinberg, 2009). While certain cell types such as stem cells maintain mesenchymal characteristics until a differentiation process is initiated (Rastegar et al., 2010), others undergo EMT and lose their definite polarization in order to migrate towards their destination (Maier et al., 2010). In this process, stromal cells adopt a phenotype that is compatible with metastatic migration (Fig. 2).

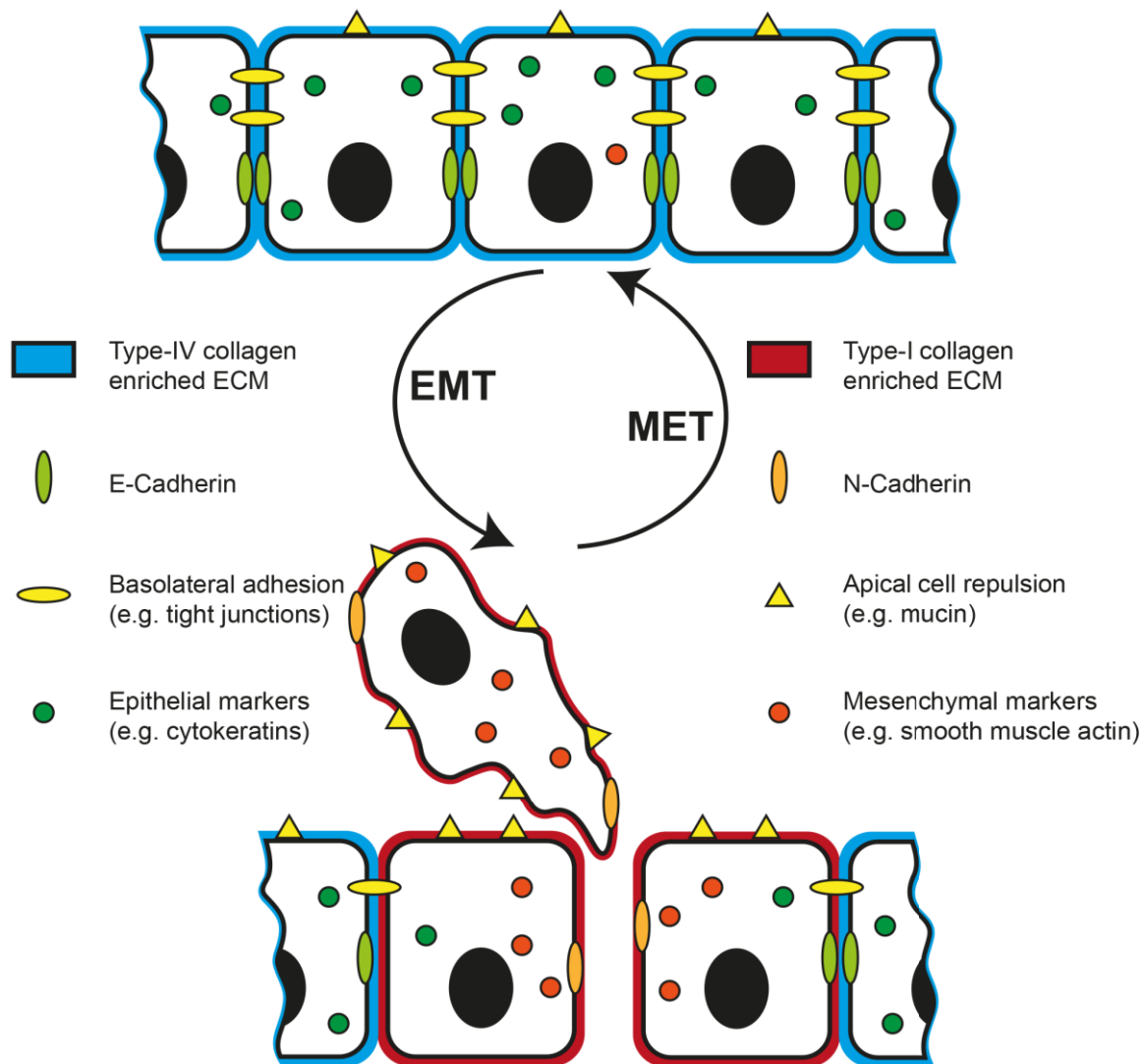


Figure 2. Characteristics of EMT and MET. During EMT, epithelial cells differentiate into a mesenchymal state, losing definite junctions and distinct polarity. Therefore, an increased migratory potential is developed. The opposite process of cells with mesenchymal characteristics incorporating into epithelial arrangements is called MET.

Cell-cell interactions such as cadherin-based tight junctions defining tissue subdomains, or gap junctions mediating intercellular exchange, together with integrin-based cell-ECM adherence (Radisky, 2005) maintain the physiological polarity that is essential for the regulation of cellular proliferation and differentiation (Yeaman et al., 1999). A loss of these anchoring points during EMT induces enhanced motility since increased secretion of MMPs can be associated with decreasing matrix integrity. At the same time, high expression of markers such as smooth muscle actin, epithelial growth factor (EGF) or TGF β correlate with cell migration (Leeb et al., 2002). These processes are crucial during implantation, embryogenesis, and organ development (Type-1 EMT) and wound healing (Type-2 EMT). However, aberrations in its regulation leads to cancer progression and metastasis (Type-3 EMT), since it supports cell transitions into blood vessels and secondary tissues (Kalluri and Weinberg, 2009). A gain of migratory potential is correlating with a loss of adhesion sites and a simultaneous increase of mesenchymal markers. The altered expression profiles vary at different stages of the migratory process and are mostly dependent on TGF signaling

(Huber et al., 2005). During the invasion phase, initiating the migration through the tissue of origin, stationary markers like E-cadherin are downregulated and apical-basal polarity starts to shift towards less defined morphologies. With increasing expression of mesenchymal markers, such as vimentin or smooth muscle actin, cells can start the intravasation into lymph or blood vessels and migrate towards secondary target tissue sites, where they extravasate again. On that secondary tissue site, EMT antagonists such as bone morphogenic protein 7 (BMP-7) induce the MET process with mesenchymal cells adhering to the tissue while regaining distinct polarity (Lee et al., 2006). Indeed, these processes can be related to metastasis and with BMP-7 as member of the TGF superfamily (Meng et al., 2013) being associated with maintained bone homeostasis (Demirkan, 2013), related regulation process should be addressed.

When the ECM is modified, proteinases such as matrix metalloproteases (MMPs) as the major remodeling enzymes are stimulated. These might be universally expressed, but normally their controlled release and activation ensure quick responses to sudden stimuli. Additionally, MMPs help to discriminate between stem cell niches and differentiation zones. Corrupted regulation of MMPs therefore might promote various diseases (Lu et al., 2011). Generally, this class of proteases can be divided into 24 currently known subtypes that all contain specific signal sequences, catalytic sites, and a zinc-2 binding domain. Additionally, a hemopexin domain regulates the specific recognition of the substrate (Roeb et al., 2002) by binding to cellular receptors that mediate their activation, inhibition, and MMP uptake for terminal degradation (Piccard et al., 2007). Further protein binding is mediated by a flexible hinge domain towards the C-terminus (Fig. 3). Finally, fibronectin modules or membrane anchoring domains may increase their affinity to the ECM or to cell surface, respectively (Ozhogina et al., 2001). Since enzymatic functions might be similar between different MMPs (Nagase et al., 2006), a certain crosstalk between specific and unspecific MMP activities cannot be excluded, especially when tissue homeostasis is disturbed in acute alterations such as injury or inflammation (Hardy and Fernandez-Patron, 2020).

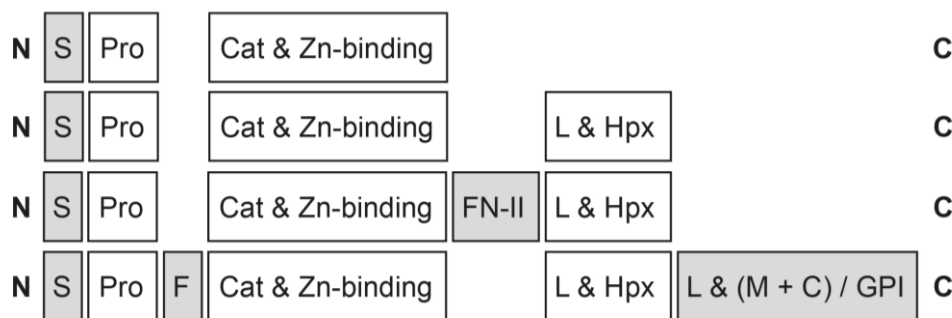


Figure 3. The protein domains of MMPs as scheme. The structure of MMPs can be defined by basic building blocks. Starting at the N-terminus, a signal sequence (S) is followed by a pro-domain (Pro) and a catalytic region (Cat) containing a mandatory zinc-binding domain as well as the contingent motifs of furin (F) in front or a subsequent triplet of fibronectin type II (FN-II). The primarily subtype defining tail towards the C-terminus starts with a linker domain (L) and a hemopexin-like domain (Hpx), followed by an additional hinge linker and either cell-oriented membrane domains (M) continuing with cytosolic tails (C), or alternatively ECM-oriented glycosylphosphatidylinositol anchoring (GPI) domains.

Under physiological conditions, enzymatic breakdown of ECM is highly controlled. One example for such a balanced ECM restructuring is bone remodeling (Fig. 4).

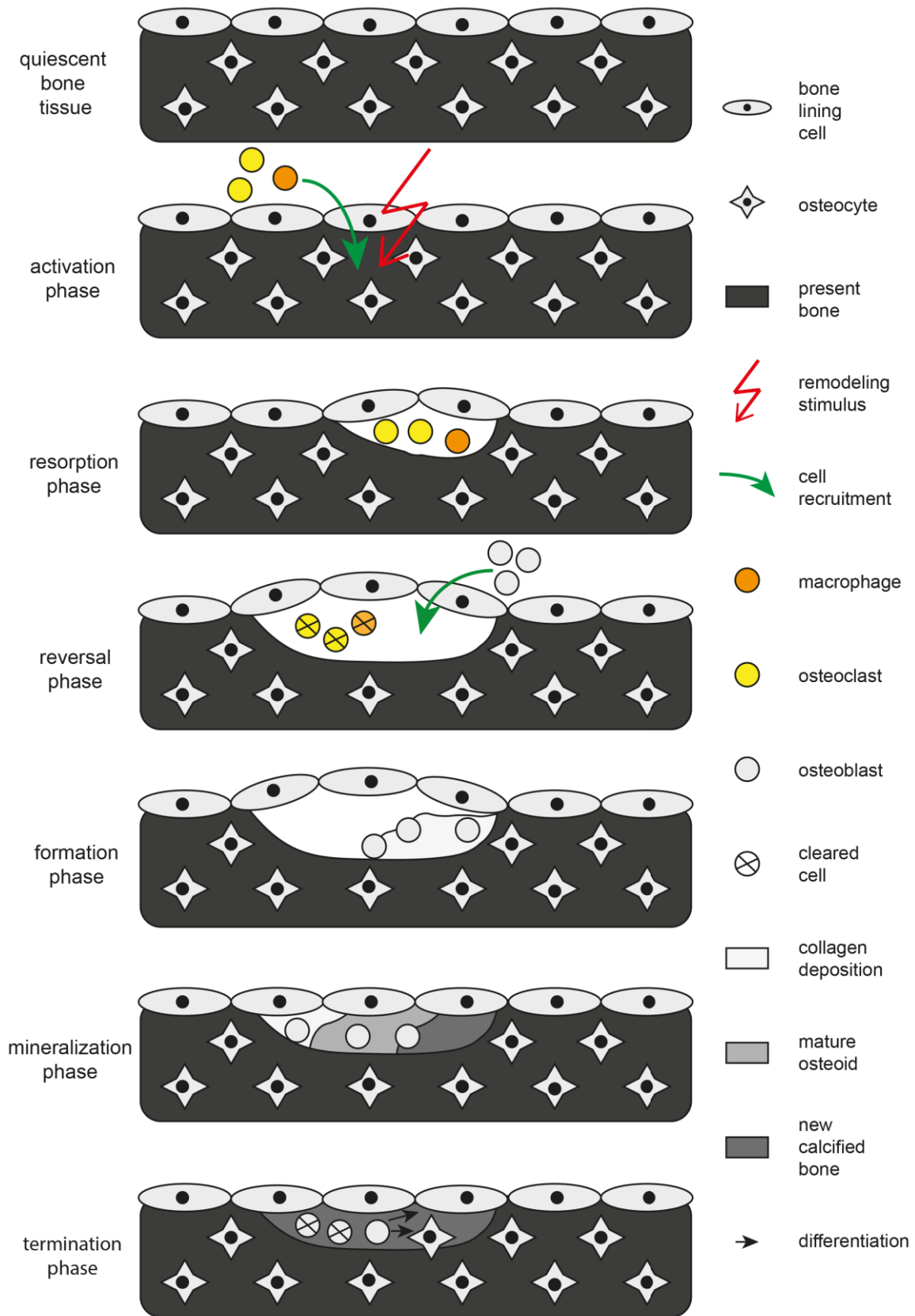


Figure 4. Illustration of the bone remodeling phases. When quiescent bone tissue is activated, osteoclasts are recruited by bone lining cells. Until their reversal, they lyse the bone tissue to establish slots. In the following formation phase, recruited osteoblasts build collagen-rich osteoids that are then mineralized. Finally, while all osteoclasts have undergone apoptosis, some osteoblasts differentiate into osteocytes or bone lining cells.

During this process, bone tissue passes through several phases (Fig. 4), starting with the activation phase. Here, based on stress applied to the overall tissue, osteocytes release osteotropic signals that initiate the formation of resorptive zones through attracted macrophages and osteoclasts (Parra-torres et al., 2013). During the resorption phase, osteoclast activity is regulated by bone lining cells inducing the differentiation of mesenchymal stem cells with the release of various signaling molecules, such as RANKL or TGF β (Tang et al., 2009).

For bone tissue degradation, several MMPs have to be released, due to the multitude of components that have to be digested and a high number of secondary processes mediated by certain members of the protease group. These include the guidance of cellular differentiation, protein maturation, ECM network cleavage and formation, cell recruitment, signal moderation or even their own clearance from remodeling sites. Due to the complexity of their biochemical role and signaling crosstalk within the overall tissue homeostasis, current *in vitro* models are only capable of covering certain aspects, while more complex interactions might still not be discovered (Hardy and Fernandez-Patron, 2020).

After successful bone resorption, osteoclasts undergo apoptosis, and the extended recruitment of osteoblasts is initiated. In this reversal phase, residuals of unstructured bone matrix components are removed and a deposition of collagenous proteins as well as the exposition of a highly mineralized cement line (Philipson, 1965) enhances osteoblast adherence and activation (Gallagher and Sai, 2010). During the following bone formation phase, osteoblasts first deposit Type-I collagen to build up the osteoid. After its maturation, a mineralization phase commences that proceeds until full calcification (Owen and Reilly, 2018). These three steps, collagen deposition, osteoid maturation, and matrix mineralization, are usually performed simultaneously with just short delays within one bone cavity (Hadjidakis and Androulakis, 2006). In the termination phase, excessive osteoblasts are cleared from the bone remodeling site. In addition, some osteoblasts differentiate into osteocytes or adopt a flattened and branched morphology, building the rather quiescent bone lining structure that primarily regulates the calcium flux and releases factors to inhibit both, bone resorption (nitric oxide) and bone formation (sclerostin). This ensures the overall tissue homeostasis until activating stimuli are applied (Bonewald, 2011).

Besides collagen and matrix mineralization, the small integrin-binding ligand, N-linked Glycoprotein (SIBLING) family plays an important role as non-collagenous ECM components in bone formation. Associated members such as dentin matrix protein I (DMP1), osteopontin (OPN), or bone sialoprotein (BSP) are encoded on chromosome 4 and share various similarities, since they are all acidic, secreted proteins with high phosphorylation and sulfation levels (Fig. 5). Although their amino acid sequences are different, their basic domain compositions serve similar purposes. The gene structures of these three SIBLING proteins share the following features (Fig. 5): A non-coding exon is followed by the leader sequence containing the first two amino acids of the mature protein. The third exon contains a consensus sequence for casein kinase II, followed by a proline-rich intermediate domain. After the actual casein kinase sequence, the protein-specific ending is encoded in one or two exons providing the integrin-binding RGD sequence (Fisher et al., 2001). While BSP is rich in glutamic acid, OPN is aspartic acid enriched and DMP1 has a higher molecular weight, since both, glutamic acid and aspartic acid regions are contained (Fisher et al., 2001). Casein kinases can be divided into several subgroups and reversibly phosphorylate substrates

interfering with signal transduction linked to cell proliferation, differentiation, and overall metabolism (Schitteck and Sinnberg, 2014).

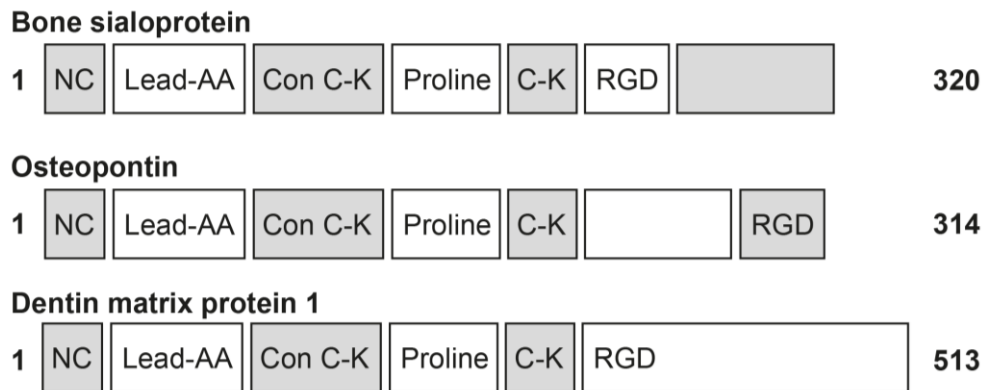


Figure 5. The coding exons of *SIBLING* proteins reveal similarities of their genetic structure. A non-coding exon (NC) is followed by the leader sequence (Lead-AA) containing the first two amino acids of the mature protein. The third exon contains a consensus sequence for casein kinase II (Con C-K), followed by a proline-rich intermediate domain (Proline). After the actual casein kinase sequence (C-K), the unique ending is encoded in one or two exons providing the integrin-binding RGD sequence. All proteins are depicted with the number of included amino acids.

BSP was addressed in particular in this thesis. It is comprised of 320 amino acids and the core protein has a molecular mass of 33.6 kDa (Oldberg et al., 1988). Normally, BSP is highly glycosylated (Fig. 6). N-glycosylation as well as O-glycosylation are implemented as post-translational modifications (Xu et al., 2017).

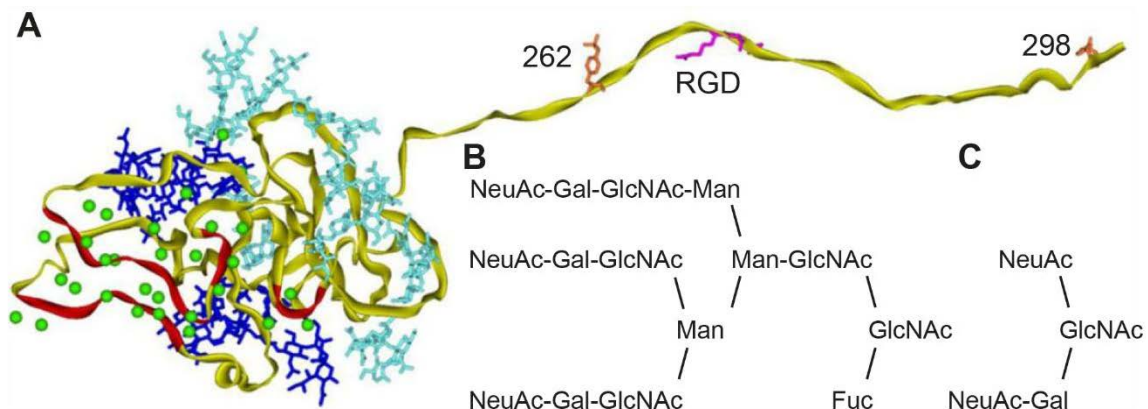


Figure 6. Model of the BSP protein structure. A) Schematic overview of the protein backbone (yellow), including regions of five or more contiguous acidic residues (including phosphoserines / red), N-glycans (dark blue), O-glycans (light blue), RGD motif (magenta), and sulfated tyrosines (orange). Green spheres illustrate Ca^{2+} ions and H atoms are omitted for clarity. Glycosylated sidechains of N- glycan (B) and O-glycan (C) are depicted including *N*-acetyl neuraminic acid (NeuAc), galactose (Gal), *N*-acetyl-d-glucosamine (GlcNAc), mannose (Man), fucose (Fuc), and *N*-acetyl-d-galactosamine (GalNAc). Adapted from Vincent (Vincent and Durrant, 2013) based on license number 5126491096522, ©2013 Elsevier Inc.

Dependent on its carbohydrate sidechains, BSP might reach molecular masses of 70-80 kDa (Diel et al., 1999). As a prominent protein on bone formation sites (Bouleftour et al., 2014), BSP is considered as a regulator that could serve as target to prevent bone metastatic niche formation. In fact, anti-BSP antibody application on MDA-MB-231-derived nude rat xenografts already led to an inhibited tumor growth and expanded the lifespan of these rodents, compared with the control group (Zepp et al., 2010). The enzymatically active coil of BSP can nucleate hydroxyl apatite formation in the bone mineralization process, while its protein-chain tail may mediate adherence to either collagen, or to cells binding to the integrin affine Arginine-Glycine-Aspartate (RGD) motif (Vincent and Durrant, 2013). Therefore, BSP might recruit tissue mineralizing cells and at the same time mediates the orientation of soluble and non-soluble bone components during the formation process. Altogether, BSP could be defined as a connecting link between the bone remodeling process and metastatic cancer progression. Therefore, this work focuses on models containing cell lines that express BSP and might be connected to metastatic tissue.

1.2 Cell Lines chosen to study intercellular signaling that is mediated by the ECM

The human breast cancer cell line, MDA-MB-231, was chosen as the starting point for the studies due to its high potential for EMT. MDA-MB-231 cells are often used as model for triple-negative breast cancer tumors. These are characterized by a lack of three important diagnostic and therapeutic marker proteins, i.e. epidermal growth factor receptor 2 (HER2), the oestrogen receptor (ER), and the progesterone receptor (PR) at once. For this reason, triple-negative breast cancer tumors are particularly hard to treat, as they are not responsive to any of the currently available antibody-based therapies (Holliday and Speirs, 2011). In addition, these cancers are associated with slow proliferation compared with other subtypes. Thus, cytostatic therapeutics like cyclophosphamide, paclitaxel, or 5-fluorouracil as remaining prevalent treatment options have only moderate prospects of success, even if unspecific carrier absorption is reduced by surface modifications such as PEGylation (Fisusi and Akala, 2019). With bone as distinct primary metastatic site, tumor cells are expected to present a broad range of features related to the corresponding ECM and MDA-MB-231 served as triple-negative breast cancer model.

To evaluate the compatibility of MDA-MB-231 with non-malignant cells, MCF10A breast epithelial cells were tested. It is a widely used model line and its basal-like phenotype might help with the modeling of breast tissue for cancer cell homing studies. However, its morphology and expression pattern linked to differentiation might be dependent on the cell culture properties (Qu et al., 2015) and therefore the compatibility with a standardized model for tumor tissue heterogeneity had first to be evaluated.

HT-29 human colon cancer cells were used as second malignant cell line, since it is known to exhibit tumor-stroma interactions and therefore a certain ECM modulation capacity (Ouahoud et al., 2020). These dependencies are underlined by findings that link EMT with altered stromal gene expression profiles rather than epithelial tumor cells (Calon et al., 2015). Linking this with increasing evidence, that tumor progression might equally be dependent on the longtime postulated Warburg signaling as on the rather lately discussed reverse Warburg effect, a novel model was desired that puts these cell types together to give insights in the direct interactions of subpopulations. Using the properties of HT-29 cells forming colonies (Shafiee et al., 2016), it was assumed,

that a morphological classification could help to discriminate cancer cell and stromal cell compartments to enable cell type specific analysis on bordering regions.

Based on the reverse Warburg hypothesis (Pavrides et al., 2012), cancer cells modulate the metabolic behavior and secretion of stromal fibroblasts and cancer cell subpopulations based on a metabolic shift from oxidative phosphorylation towards aerobic glycolysis (Martinez-Outschoorn et al., 2010). In this context, reactive oxygen species are secreted and the overall redox status changes, inducing oncogenesis based on cancer associated fibroblasts (CAFs) entering autophagy and changing their expression as well as secretor profile (Chiavarina et al., 2010). Furthermore, this alteration is also induced in a subpopulation of cancer cells (Fig. 7). The resulting interaction of cancer cells and CAFs then stimulates angiogenesis, migration, and acidification based on hypoxia (Wallace, 2012).

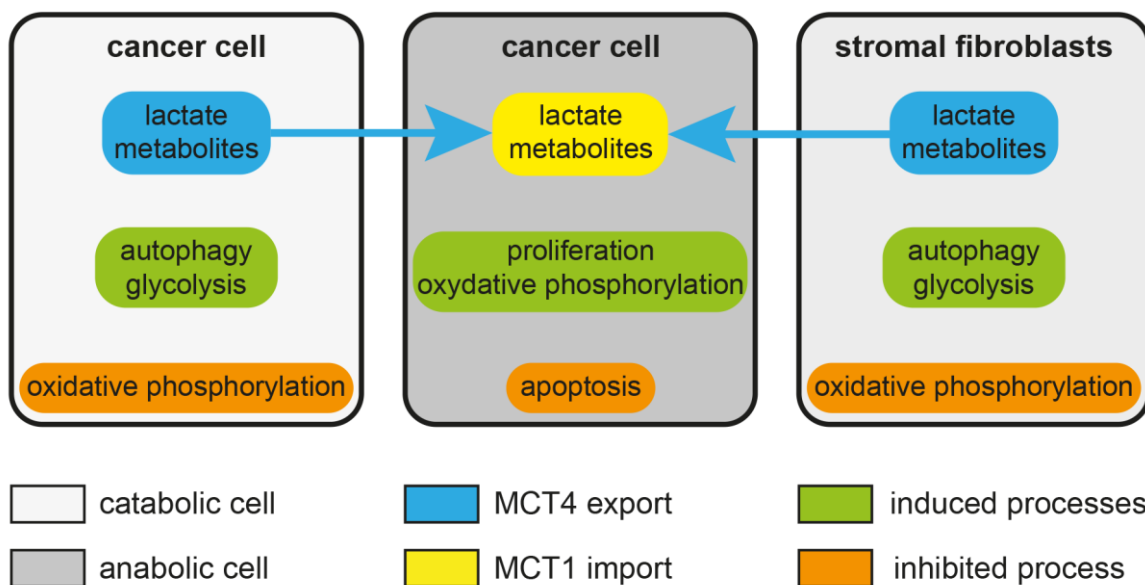


Figure 7. The reverse Warburg signaling induces metabolic alterations in cancer cells and stromal fibroblasts. Starting from the release of reactive oxygen species (ROS) by cancer cells, a change in metabolic state is induced in surrounding cell populations such as stromal fibroblasts. Oxidative stress and corresponding hypoxia can result in mitophagy and aerobic glycolysis that lead to an accumulation of lactate, ketone bodies, and glutamine which catabolic cell populations therefore release into the ECM. By the terminal uptake of available metabolites, tumor progression is promoted in anabolic cancer cells with increased proliferation rates and survival.

As key player in both, ECM secretion and reverse Warburg signaling, fibroblasts were chosen as stromal population that was to be represented by the human fibroblast cell line CCD-1137Sk. It was already known that it has strong signaling capacities that could also help discriminating these cells from other phenotypes (Stines et al., 2004). Since experiments of cancer cells with stromal populations indicated a beneficial effect for melanoma cells being surrounded by fibroblasts (Klicks et al., 2019), similar effects were anticipated when instead adding colorectal cancer cells. Those cells secrete various ECM compounds that are not restricted to structural proteins. Therefore, tumor-stroma-interdependencies might be mimicked by fibroblast-based models, since other complex processes such as wound healing, inflammation or angiogenesis have also been addressed by those (Kendall and Feghali-Bostwick, 2014).

1.3 Primary ECM as a cell culture material

In the *in vivo* situation, evolving tumors are surrounded by a stroma that consists of various factors that have initially been secreted by randomly present stromal cells such as fibroblasts, endothelial cells, and immune cells. The ECM is modified based on the aberrant cellular signaling that is initialized by the presence of cancer cells. *In vitro*, 3D-co-cultures either develop a random cellular distribution, or incorporated subtypes establish self-assembled structures with reproducible accumulations on defined positions (Achilli et al., 2012). Structured seeding protocols (Klicks et al., 2019) or joining pre-assembled spheroids (Hajdu et al., 2011) might help to obtain specific cell type distributions within 3D-cell models.

Further, since not every cell type that might be interesting for the desired model is capable of secreting a sufficiently complex ECM necessary for the basic integrity of 3D-cell cultures, additional materials have been introduced in research approaches. A widespread method to provide a comprehensive matrix composition is the supplementation with extracts of the basal lamina (BME) such as Matrigel. BME is a complex extract of the ECM harvested from the Engelbreth-Holm-Swarm sarcoma (Swarm, 1963) as primary source (Kibbey, 1994). Its biggest advantage is a complexity that enables the application in various cell culture models. But due to its' origin, the composition does not necessarily mimic the stimuli present in a specific tissue, even though this is often assumed. For example, laminin is enriched in the ECM provided with Matrigel, therefore enhancing cell adhesion and growth factor preservation (Hernández et al., 2007). The only present subtype, laminin-111, plays an important role in early embryogenesis, but usually is not present in mature tissue (Uriel et al., 2009). At the same time, all insoluble factors, such as fibrin or elastin (Halper and Kjaer, 2014) are negligible (Czyz and Wobus, 2001) and instead, non-fibrillar (Fig. 8) Type-IV collagen (Velez and Howard, 2012) and growth factors are increased, thus supporting pathological signaling. Since the ECM consists of a lot of components and BME is a complex biogenic extract, many of them might be included in small amounts, depending on the quality of the production. Therefore, BME can replace stromal cells and other ECM compound supplementations in various applications. Nevertheless, the user must consider that BME and Matrigel might induce alterations from physiological metabolism. Therefore, in addition, alternative approaches should be used to confirm conclusions drawn from experiments relying on BME/Matrigel (Kleinman et al., 2003).

To better suit adhesive ECM in mature tissue, collagen is often the material of choice to form protein-based hydrogels with high affinity to various cells. These cells specifically bind to the contained Glycine-Phenylalanine-Hydroxyproline-Glycine-Glutamic Acid-Arginine (GFOGER) protein sequence and the overall conformity can be tuned with covalent crosslinking of the fibrillar collagen structures. However, a main weakness of collagen hydrogels compared to other materials is a comparably low mechanical strength (Davidenko et al., 2016). The quality of the collagen is dependent on the primary source, the processing during extraction, and purification. These factors, and, in addition, age and condition of the donor might change solubility, crosslinking capabilities, and contamination with growth factors or pathogens (Zeugolis et al., 2008). Therefore, the batch-to-batch variances of primary Type-I collagen – the major collagen subtype harvested from tendons – must be considered. Since current artificial proteins still lack some crucial properties due to altered protein morphology on the hetero-trimer, plants for recombinant collagen production are under investigation (Willard et al., 2013). If cost efficacy can be improved, these collagens are promising

for future research and patient compatibility as they might have a superior homogeneity compared to animal-derived extracts (Shoseyov et al., 2013).

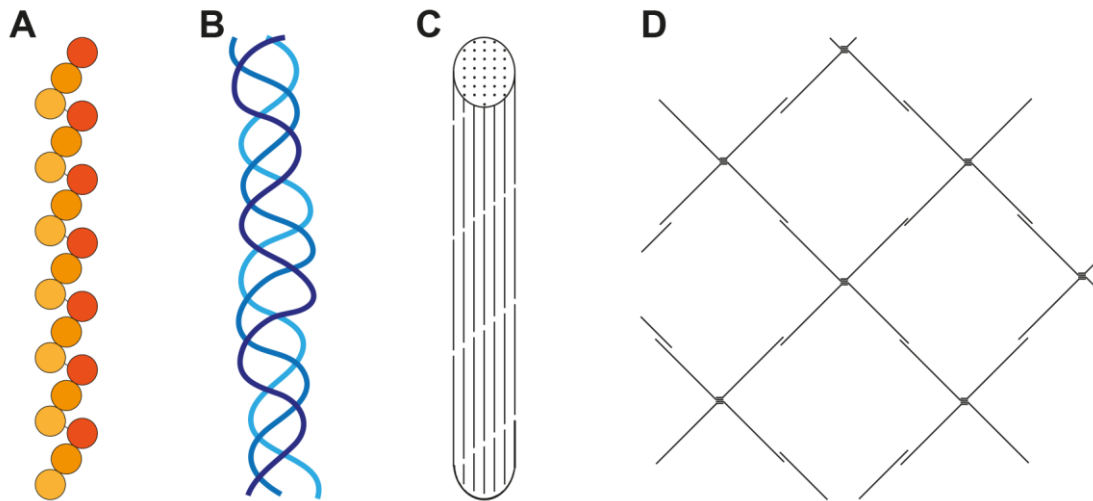


Figure 8. Overview of basic collagen structures. Repeated amino-acid sequences of Glycine-X-Y (A) commonly build up collagen trimers (B). These trimers align to fibrillary Type-I collagen (C). Alternatively, Type-IV collagen is composed of trimers containing non-collagenous domain endings that result in small rectangular macro-structures (D).

So far, BME and Type-I collagen have been the prevalent matrices to support cell cultures in 3D since their versatility has not been met by other supplements. Nevertheless, more defined products with properties fitting a certain task are desired and different protein modifications and non-animal investigations have led to alternatives for cell culture modeling. Often, they benefit from decreased immune response and the absence of bioactive inducing factors while still providing sufficient cell adherence (Campuzano and Pelling, 2019).

Gelatin, for example, consists of denatured collagen that is easier to handle due to its more robust chemical properties. It can be enzymatically crosslinked with the application of transglutaminases and then provides more definite structures (Paguirigan and Beebe, 2006). However, cellular binding is less specific since fewer and different integrins bind the coil conformity (Davis, 1992). To tune their mechanical properties, natural products like gelatin often undergo alternating processing to further optimize their applicability for 3D-printing and customized mold formation. For example, methacrylic anhydride is added to gelatin to result in gelatin-methacryloyl (GelMA), that can easily be crosslinked due to a lack of stability in the added side chain. With photo initiators, ultraviolet light exposure or even gamma irradiation, GelMA structures can easily be preserved (Jaipan et al., 2017).

Further materials like chitosan are rather known for specialized applications. Chitosan is a deacetylated chitin that has been modified to render a more homogeneous polymer structure for simplified polymerization. Due to its biodegradability, it is used in wound healing and in different 3D-cell culture approaches, despite its comparably low stability (Croisier and Jérôme, 2013). Chitosan might be combined with alginate to obtain more favorable mechanical properties in a bio-adhesive environment. While this ensures a rapid formation of hydrogel scaffolds, the release of cells for harvesting is especially

harsh, requiring a 30 min incubation with 55 mM sodium citrate (Shakibaei et al., 2015). In general, the mechanical properties of the linear alginate polymer can be precisely tuned compared to other biomaterials. Physical properties are dependent on the ratios of β -D-mannuronic acid and α -L-guluronic acid. With increasing molecular mass and guluronic acid proportion, gels become more rigid since this side chain enhances ionic gelation based on divalent non-magnesium cations (Andersen et al., 2015).

Cellulose as well as the methylcellulose derivate have been used in diverse approaches due to its versatility with simultaneously strong processability (Varma et al., 2014). It can be modified to obtain certain mechanical properties and at the same time the biocompatibility is tuned by fusing the material with other compounds providing RGD sequences or tissue specific insoluble materials. Without supplementation, methylcellulose might serve as cell-repellent surface coating as well. Therefore, successfully established structures tend to be highly specific for engineered tissue models (Courtenay et al., 2018).

Finally, if complex structures with high robustness and little cross-reactions with cells are needed, synthetic polymers might be the material of choice due to their mechanical properties, tunable biological activity and longer shelf lives compared to any natural compound. Depending on their surface energy, the bioactive properties of synthetic materials differ a lot. For example, the resulting structure establishes a rather low binding-capacity for proteins, if it is made of poly(tetrafluoroethylene) or polyurethane (Lih et al., 2015). Similarly, highly hydrophilic material such as poly-HEMA or poly(ethylene glycol) establish cell-repellent water barriers that also prevent protein adsorption and make them beneficial as anti-fouling surface modification on medical devices (Wei et al., 2015). To adjust cell-adhesiveness, polymers are often modified with incorporated peptide structures such as the well-known RGD sequence. Alternatively, nature-derived matrix components like collagen may be added to the overall mesh, or specific coatings are used to promote the cellular adherence to the surfaces (Chen et al., 2018).

1.4 Cell culture modeling

Several considerations affect the choice and layout of cell culture models. First, based on the provided ECM supplementation, cell culture architecture can be altered and tuned to be fitting for a desired purpose. Further, the complexity of a model is usually dictated by two opposing parameters. On the one hand, the more complex a cell culture, the higher the chance to really simulate complex physiological actions. On the other hand, an easy system might be desired to enable a higher throughput, easier automation, and finer analysis of target readouts. Finally, it is difficult to mimic physiological conditions for cells. Indeed, numerous influencing factors are changing dynamically, and even slight alterations might turn a beneficial cellular phenotype into pathologically relevant aberrations. Therefore, changes interfere with the preservation of the desired homeostasis and can even turn tumorigenic (Scadden, 2006).

1.4.1 2D-derived cell culture modeling as method of choice for basic screening

The impact of 2D-culture models on cellular research have thoroughly been discussed and numerous reviews compare this method with recent 3D-culture conditions (Jensen and Teng, 2020). Since standard 2D-cultivation on polystyrene or glass has been used

since the early 20th century, it is known that cellular behavior might be dramatically changed due to a lack of cell-cell interactions. In addition, rigid surfaces, and limitless access to provided media further differ from a physiological situation. Nevertheless, 2D-cell culture helped to understand myriads of metabolic processes, and its ease in usability combined with a cost-efficient and automatable application still makes it the method of choice for high-throughput screening studies. Additionally, morphological properties might enhance readout resolution and traceability in image-based analysis. New approaches have emerged that include further aspects of physiology such as adapted surface composition. Since cells can integrate into coatings and obtain a rather 3D-morphology, some attempts do not strictly fit the intuitive definition of a mono-layered 2D-cell culture. Providing a certain topography while adding a cell-supportive coating to the inert base material might help with a more physiological expression profile. For example, 2D-cultures of adipocyte precursor cells on poly-L-lactide patterned surfaces appeared to differentiate slower compared to controls in polystyrene dishes, but their production of lipids was enhanced. Since uniform coating resulted in moderate lipid production, surface material and topography both may influence cellular behavior in 3D (Chaubey et al., 2008). Besides topographic alterations, also mechanistic properties of the surface are important, especially for cells that do not differentiate before seeding. Indeed, mesenchymal stem cells cultured on top of polyacrylamide-gels of different stiffness, all coated with the same Type-I collagen, resulted in the distinct expression of various terminal differentiation markers. In detail, cultures on soft gels with an elasticity of 0.1-1 kPa similar to brain tissue exhibited neuronal marker expression, 8-17 kPa led to the expression of myogenic factors commonly present in muscle tissue, and matrices with even higher stiffness of 25-40 kPa induced expression of osteogenic factors (Engler et al., 2006).

Eventually, also in 2D-approaches, the surface area provided to the cells is crucial. Human mesenchymal stem cells (hMSCs) cultured on small fibronectin stamps with an island size of approximately 1,000 μm^2 almost completely differentiated into adipocytes, while 10,000 μm^2 islands resulted in a differentiation shift towards osteoblasts. Fittingly, 2,000 μm^2 big areas showed intermediate results with both cell types based on mechanical tension regulations (McBeath et al., 2004). While keeping the mono-layered cellular structure, sandwich approaches may provide better mechanical support and therefore enable cells to retain a rather round shape that might be beneficial for mechano-transduction and contact-dependent signaling. This can additionally be supported by local gradients since oxygen limitation was linked to higher survival rates for neuronal cell cultures: compared to the number of living cells after 2 days with atmospheric oxygen concentration, a 4-fold higher amount of primary hippocampal cells endured for 5 days *in vitro* when only 9 % oxygen was provided. Covering 2D-cultures on lysine-coated dishes with glass obtained similar effects, indicating that limited diffusion can be beneficial for cell physiology (Brewer and Cotman, 1989). Similar experiments with primary liver cells revealed a decreased transcriptional activity for albumin within 2 weeks when they were cultured directly on collagen coated dishes in 2D. In contrast, RNA levels for albumin expression were constant when the cells were additionally covered with another collagen layer (Dunn et al., 1992). Explanations for that could be linked with morphological integrity on a single cell level, since in 2D-hydrogels an increased expression for cell structuring genes, proliferation and differentiation have been observed. At the same time, in cells provided with a rather three-dimensional morphology within a sandwich approach, the expression for genes involved in transporting mechanisms was induced (Mabry et al., 2016). Bridging findings to 3D-cell culture models, all investigations primarily relying

on cellular interactions should ensure a non-flattened overall cellular morphology. Intercellular signaling is strongly dependent on carrier proteins and more guidance for the culture conditions is needed to accurately fit tissue conditions (Duval et al., 2017).

1.4.2 3D-cell cultures with additional finetuning for specific physiological analysis

Culturing cells in 3D provides them with all around contacts to other cells and matrices, but also introduces variable properties for distinct subpopulations. Outer regions have rather free access to media and oxygen and therefore possess higher proliferative potential. In contrast, internal regions may accumulate waste products and be subject to stronger contact inhibition signaling. Depending on metabolic sensitivity, cells then become quiescent or build a necrotic core. Frequently, no supportive material like additional ECM is provided to the culture, but still cells can interact with their surrounding in a tissue-alike conformity with overall suitable morphology. Therefore, different 3D-cell culture methods have been established for investigations on tumor modeling, pathway analysis, tissue engineering and transplantation therapy. Each kind of 3D-culture (Fig. 9) has its own beneficial properties and therefore fit their task (Ryu et al., 2019).

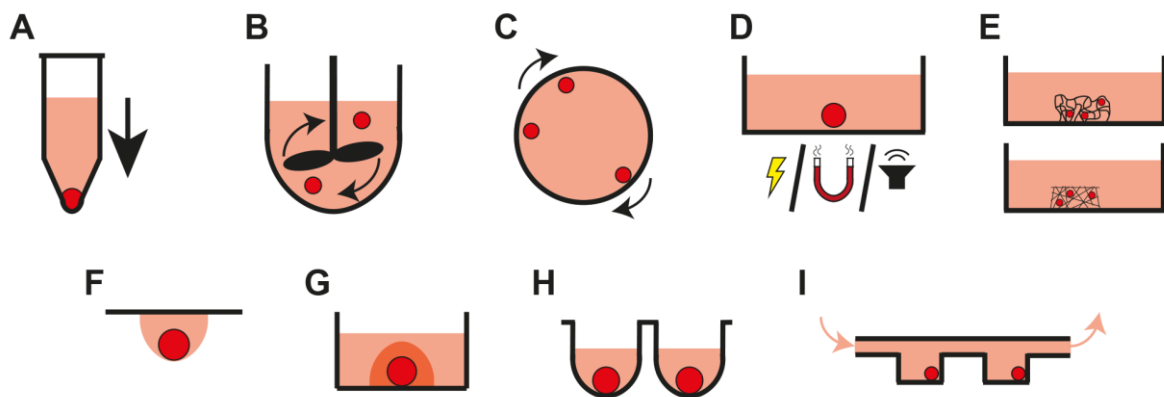


Figure 9. Schematic overview of 3D-spheroid culture techniques. Simplified illustrations of common methodology with pellet (A), spinner culture (B), rotating vessel (C), forced (electrical, magnetic, or acoustic) spheroid formation (D), macro-porous (voided polymerization or micro-spinning) hydrogels (E), hanging drop (F), solid hydrogels (G), ultra-low attachment plates (H), and fluidic devices (I).

To make 3D-cultures applicable to specific questions, a defined *in vivo* process should be simulated in a better observable environment. Therefore, various materials are used and combined to obtain the desired properties. In the best case, present biochemical signals are well-known and can be influenced by adding external stimuli that can treat or induce a certain disease (Gu and Mooney, 2016). Therefore, based on cell adhesion properties, mechanical features, and effector diffusion, 3D-cell culture could significantly influence cellular behavior and promote more physiologically relevant results (Baker and Chen, 2012). In the following, 3D-cell cultures were divided in spheroids, hydrogel-based cultures, and cultures with defined morphology based on polymer structures.

Spheroid cultures

Spheroids are frequently used since they are easy to produce and still guarantee to study effects of intercellular contact. To form spheroids, different methods have been used. Especially in early days, the hanging drop procedure was frequently applied since its application is quite cheap and straightforward. A defined number of cells is trapped in a droplet of media with a certain volume hanging from a lid that forces the single cells to either aggregate to each other, or to remain singularized. The resulting spheroids develop very uniform morphologies, and the process can be automated to achieve high throughputs. The hanging drop has excessively been used due to its wide range of possible applications, but its' rate is declining, since their fragile setup complicates long-term culturing and intermediate analyses of the structures with limited sizes based on its surface tension dependency (Kelm et al., 2003).

Spinner culture spheroids rely on the convection of a stirrer. Their application is rather specific since the 3D-formation is dependent on the energy input to the model. Slow stirring may not lead to sufficient circulation, while faster rotation speed may destroy the spheroids or even harm cells. Alternatively, rotating a vessel that contains a cell suspension leads to similar results in a more delicate way since the cells are not able to adhere to a surface and therefore aggregate to each other. Here, the drawbacks are limited supplies with oxygen and a lack of reproducibility (Kim, 2005). Both methods result in inhomogeneous spheroid morphologies and lack the possibility of easily tracing a specific 3D-structure development over a certain time, since tracking down a single spheroid during the continuous rearrangement of numerous subpopulations is hard in a permanently moving culture. Instead, they are applied in drug production processes. Another easy way to initiate spheroid formation, is to pellet a desired number of cells and concentrate them together by force. These high-density cultures have been utilized for bone-marrow modeling (Zhang et al., 2010), but the high mechanical stress prohibits a broad range application. Still, a careful centrifugation is frequently used in different spheroid approaches to enhance cell aggregation.

Niche applications use the acoustic force method that relies on shockwaves established by externally set membranes to force cells into direct proximity and overall shape (Chen et al., 2016b). A bit more widespread is the so-called magnetic force model in which a certain polarization is applied on the culture to guide the cells (Bae et al., 2011). This method, as well as a protocol of applying electrical force with submerged electrodes (Sebastian et al., 2006), often rely on metallic beads incorporated by the cells to enhance their aggregation based on a magnetic or electric field. All these three methodologies might damage the cells through the applied forces or cytotoxicity of supplemented particles. Additionally, if the formed 3D-structure lacks sufficient intrinsic stability, its integrity might be lost when the forces are removed for harvesting the constructs.

Currently, liquid overlay of cell suspensions on ultra-low attachment material is maybe the most wide-spread spheroid production technique. Repellent surfaces are formed by specific plastic conditions or coating with e.g. agarose or hyaluronic acid. This method allows the production of homogeneous spheroids with a defined cell number and positioning. The application is feasible, no matter if standardized molds or prevalent well-plate formats are supporting the spheroid assembly. Unfortunately, all spheroid cultures lack surface receptor binding sites and therefore can still lead to issues with cancer cell cultures, since anchoring proteins (Yoshimaru et al., 2017) or specific mechano-transduction processes (Baptiste et al., 2007) might be missing.

Mechano-transduction and cellular interactions profoundly affect cellular physiology and thus may often influence outcomes of drug treatment studies (Carvalho et al., 2017). To avoid these issues, media supplementation and overall spheroid size could be adapted to reduce the size of affected subpopulations and a pre-selection based on morphology can help with homogenization of the resulting data (Zanoni et al., 2016). Nonetheless, spheroids might be a fine screening model, but more complex structures may improve the biological accuracy of resulting analyses.

Hydrogel cultures

Besides the intrinsic spheroid forming capacity, the 3D-structure can be facilitated by the addition of ECM components. Compounds like collagen, hyaluronic acid, or chitosan, but also more complex supplements like agar and whole ECM extracts as Matrigel or basal membrane Extract (BME) are added to help singularized cells sticking together after seeding. Since cadherin expression crucial for cell-cell binding is enhanced after initial cell-ECM contact mediated by integrins, supplementation can lead to a faster and more homogeneous spheroid compaction (Cui et al., 2017). This leads to inaccuracies in culture technique classification since it is predominantly dependent on the amount of provided ECM. If appropriate compounds are provided in high concentrations, sufficient mechanical support might be provided for 2D-cultures to establish 3D-phenotypes, while spheroids are encapsulated and start to outgrow their defined spherical structure. Hydrogel cultures rely on a complete encapsulation of singularized cells or aggregates within a biocompatible gel. Therefore, all around support is given based on crosslinking, physical junctions, and entanglements of the ECM proteins (Slaughter et al., 2009). In non-porous hydrogels, the tissue-alike water content protects contained cells from mechanical stress while nutrients can easily diffuse through the gel. Therefore, this method is beneficial for delicate cultures such as organoids. Organoids are defined as cultures that resemble relevant properties of an organ tissue, since most of the cell types and matrix components are contained. While historically, the terminology referred to cultured primary biopsies only, nowadays often complex cultures of e.g. differentiated pluripotent stem cells fit into that definition as well (de Souza, 2017). The small mesh size of continuous hydrogels in the nanometer to micrometer range often limit proliferation and migration of cells that were added before the gelation (Duval et al., 2017). Therefore, enzymatically degradable polymers are preferred since they allow a certain motility over time (Benton et al., 2009). With appropriate supplementation, organoids can maintain complex expression profiles resembling *in vivo* physiology (Rosenbluth et al., 2020). But poor reproducibility and high costs compared to other culture methods limit their application.

If firm cellular environments are undesired for the cell culture mode, macro-porous hydrogels could be beneficial. They also provide three-dimensional support for micro-tissue modelling while the size of lacunae does not limit cellular migration and spreading. Initially, these sponge-alike structures consisted of polymers that have been dissolved in low concentrations prior addition of crosslinking agents (Oxley et al., 1993). Later, polymers as e.g. poly(ethylene glycol) diacrylate were frozen together with a liquid such as PBS and then thawed after polymerization (Göppert et al., 2016). Other approaches blow gas into the substrate during the gelation or dissolve a contained crystalline salt after that step (Dušková-Smrčková et al., 2021). Since these methods are not meant to include living cells during the manufacturing process, hydrogel performance is dependent on cellular penetration during the seeding, with mechano-transduction and elasticity as biological regulators (Koch et al., 2012). Mechanical properties are meant to be improved with scaffolds produced via

electrospinning that results in a fiber mesh with relatively low density and a high cell affinity to compensate for the reduced compactness (Chen et al., 2016a). Major drawbacks of macro-porous structures are inhomogeneous seeding and again a difficult release of the cells after culturing.

Cultures with more defined morphology based on polymer structures

If the materials have suitable physical properties like viscosity and gelation mode, it is possible to use a 3D-printer to bring them into desired shapes before crosslinking. This introduces new opportunities, turning this method into a promising tool for future investigations (Li et al., 2020). Furthermore, synthetic polymers enable the providing of desired properties that are essential for tissue-alike cell assembly. Then, the basic structure often remains inert and specific coatings such as Type-I collagen provide a desired bioactivity (Nies et al., 2019). Local gradients of temperature, nutrients, oxygen, and waste products are delicate and help or prevent cell reactions dependent on the physiological model. Together with the evidence of mechanical stimuli being crucial for cellular signaling processes, these gradients brought microfluidics into cell culture, since superfusion and perfusion chambers permit further culture customization. Combining the microfluidics with cavities and porous or perforated foils resulted in microreactors that enable miniaturized experiments with desired gradients that can be observed in parallelized populations (Coluccio et al., 2019). Such approaches can be beneficial to simulate complex processes such as vascularization, but the high number of influencing factors require extensive testing for optimization.

If comprehensive cell-cell, cell-surface as well as mechanical support and supplemented ECM-bioagents are considered in microfluidic devices, their complexity may be equated with primary tissue cultivation in a physiological environment. Therefore, in the last decade the high potential “organ-on-a-chip” approaches emerged, meant to accumulate all aspects needed to provide cellular physiology (Huh et al., 2011). Implemented membranes can separate subcultures that are still capable of communicating with each other through secreted factors. The increasing complexity of the models should correlate with cell physiology, making them a promising tool for future cell culture derived breakthroughs (Bhatia and Ingber, 2014). However, due to their complexity exceeding simpler cultures, these experiments are extraordinarily expensive and time consuming.

Although additional methods such as phase separation approaches of cells encapsulated in double-emulsion droplets have also been invented (Chan et al., 2013), further models belong to niche applications and were therefore not further addressed.

1.5 Aims and research questions

The knowledge regarding the role of ECM and stromal cells on tumor niche formation and metabolism is still scarce. Studies in that direction have been hampered by a lack of appropriate experimental models. Therefore, the present dissertation aimed at the establishment of novel two- and three-dimensional mono- and co-culture models to address these questions.

Specifically, MDA-MB-231 human breast cancer spheroid models should be optimized for a three-dimensional cultivation with proper integrity. By applying different ECM components and proteases, such as MMP9 being involved in tissue remodeling,

mutual interactions between cancer cells and their microenvironment should be examined. Therefore, the secretion of BSP, a protein associated with bone remodeling and metastatic growth, should be assessed.

To study, metabolic coupling of cancer cells and proximate fibroblasts mediating alterations of the ECM composition, co-cultures of HT-29 human colon cancer cells and CCD-1137Sk human fibroblasts should be established and explored. The reverse Warburg effect should be modeled in 3D-microarray cultures (Fig. 10) that enabled to mimic major aspects of this aberrant metabolism. A dependency of cellular interface with membrane shuttling, metabolic state, and proliferation should be investigated with additional cultures in 2D- and 3D-morphology.

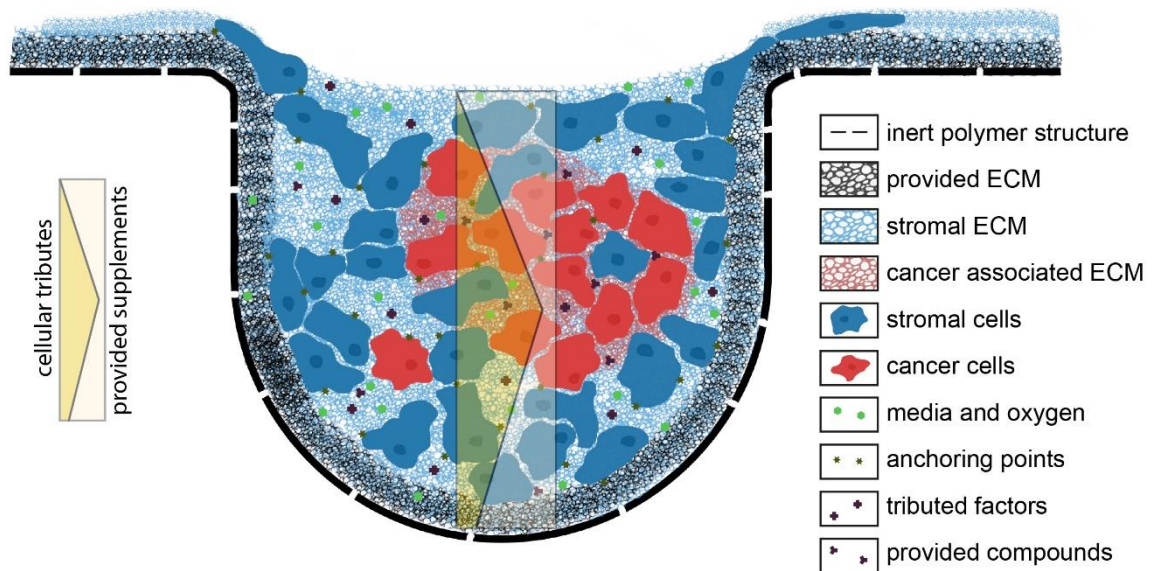


Figure 10. Schematic overview of the terminal microarray co-culture model.

The inert polymer structure provides mechanic structure and defines the overall dimension. While entrapping of added cells into its cavities, media diffusion is still ensured through pores. Provided ECM helps cells to adhere to the cavity walls. Stromal cells build up the basic ECM and assemble a cellular scaffold that supports the homing of cancer cells with less ECM secretion capacity. The cancer cells interact with their surroundings, inducing alterations in their direct proximity, such as the reverse Warburg effect. Through different cellular densities, diffusion barriers, and culture depth, gradients are built with decreasing nutrient and oxygen supply towards the center and simultaneous accumulation of cellular tributes. The overall ECM structure ensures mechanical support through variable anchoring, resulting in various cellular polarities. Added compounds could diffuse based on built-up gradients.

Taken together, two aspects of cancer progression were shown to be mediated by the composition of the ECM. First, EMT on primary tumor sites was induced by the metabolic coupling of cancer cells and stromal fibroblasts. On the other hand, metastatic niche formation was likely induced by cancer cells secreting BSP. Therefore, future studies should include the testing of distinct co-culture composition and corresponding ECM compounds to clarify the origin of alternating findings.

2 ARTICLE 1: BONE SIALOPROTEIN SHOWS ENHANCED EXPRESSION IN EARLY, HIGH-PROLIFERATION STAGES OF THREE-DIMENSIONAL SPHEROID CELL CULTURES OF BREAST CANCER CELL LINE MDA-MB-231

An adapted version of this chapter has originally been published as open-access article distributed under the terms of the Creative Commons Attribution License (CC BY): “Rustamov, V., Keller, F., Klicks, J., Hafner, M., and Rudolf, R. (2019). Bone Sialoprotein Shows Enhanced Expression in Early, High-Proliferation Stages of Three-Dimensional Spheroid Cell Cultures of Breast Cancer Cell Line MDA-MB-231. *Front. Oncol.* 9, 36” (Rustamov et al., 2019); doi: 10.3389/fonc.2019.00036.

As personal contribution, MDA-MB-231 mono-cultures and co-cultures with CCD-1137Sk human fibroblast cells were prepared, stained, and imaged with brightfield and confocal scanning (Fig. 12 and 14). Furthermore, support was given to improve the experimental design that initially was provided. Finally, obtained data were analyzed and interpreted for finalizing this article.

In this project, a suitable model for investigations on ECM compounds related to bone metastasis was developed. The MDA-MB-231 human breast cancer cell line is not establishing a spheroid structure with proper integrity without the support of added extracellular matrix (Ivascu and Kubbies, 2006). However, cells not provided with similar stimuli may falsify readout analysis for markers associated with matrix remodeling. With BSP as target protein related to the bone remodeling process, different cell culture conditions and additives were tested. This study revealed that MDA-MB-231 breast cancer spheroids on cell-repellent U-bottom wells can serve as robust 3D-culture model when basal membrane extract is added. Thus, BSP expression was increased compared to 2D-cell culture and elevated levels decreased between 7 d and 21 d after seeding, making it a worthwhile target for the correlation of cancer progression, growth, and ECM modulation.

2.1 Abstract

Normally, bone sialoprotein (BSP) is an important contributor to bone micro-calcification. However, it is also highly expressed in bone-metastatic malignancies, including prostate, lung, and breast cancer. In these disorders, BSP correlates with poor prognosis. Its expression in triple-negative breast cancer cells is enhanced by the transcription factor RUNX2, and both, BSP and RUNX2 are under control of IGF1 and TGF β 1. Knockdown of BSP or its inactivation by specific antibodies were found to reduce the metastatic potential of MDA-MB-231 triple-negative breast cancer cells in xenografts. While the role of BSP in bone metastasis was studied using such *in vivo* models, valid *in vitro* test systems to investigate BSP biology in a three-dimensional environment have been lacking. Here, we have developed a long-term 3D-spheroid culture model using MDA-MB-231 cells in a sandwich approach. This allowed consistent growth of spheroids for more than 21 days. Also, co-culturing of MDA-MB-231 with CCD-1137Sk fibroblasts yielded stably growing spheroids, suggesting the importance of extracellular matrix in this process. In addition, we have set up a novel and simple open-source analysis tool to characterize protein expression in 2D-cultures and spheroids by immunofluorescence. Using this approach in combination with

Western blot analysis, we analyzed the expression profile of BSP. This was enriched at the rims of spheroids, both in mono- and co-cultures and its abundance in general correlated with that of TGF β 1 under different conditions, including spheroid maturation, cytostatic treatment, and fibroblast co-culture. Conversely, IGF1 and BSP correlation was limited to mono-culture time course profiles. In conclusion, we present novel tools to study the regulation of gene expression in combination with cell proliferation and apoptosis in a long-term 3D-model of breast cancer and find dynamic abundance profiles of the metastasis-relevant protein BSP and its regulators in spheroids versus 2D-culture.

2.2 Introduction

Breast cancer is the most frequent neoplastic lesion in women. When associated with distant metastasis, the overall prognosis for breast cancer is poor with a five-year survival in stage IV of about 27 % (Siegel et al., 2018). Breast cancer can be subdivided into four molecular subtypes: positive for either luminal A, luminal B, or Her-2, and triple-negative (Harbeck and Gnant, 2017; Wu et al., 2016). Metastasis is frequent in breast cancer and typically affects liver, bone, lung, or a combination of these (Chen et al., 2017; Savci-Heijink et al., 2015; Wu et al., 2016), with bone being the most frequently targeted organ of breast cancer metastasis (Langley and Fidler, 2011). This might be due to bone's rich depots of nutrients, growth factors (TGF β , IGF, VEGF, M-CSF, FGF, MCP, BMP2) and fine blood supplies (Mundy, 2002). Furthermore, bone contains a special type of capillaries called sinusoids, which are characterized by slow blood circulation and porous endothelial walls, that facilitate the extravasation of metastatic cells into the bone marrow (Raymaekers et al., 2015). Mortality is positively correlated with bone metastasis (Arneson et al., 2012; Chen et al., 2010; Coleman, 2001; Liu et al.; Mundy, 2002; Obenauf and Massagué, 2015) and develops in 65-75 % of patients with advanced breast cancer (Coleman, 2006). Metastatic injury of bone leads to failure of bone homeostasis (Kingsley et al., 2007). Indeed, while bone remodeling processes (Raggatt and Partridge, 2010) are normally characterized by a balance between osteoblast and osteoclast activities, breast cancer metastases often stimulate the osteolytic process (Macedo et al., 2017). Metastatic cancer cells produce special enzymes, such as matrix metalloproteases (MMPs), cytokines (IL-6, IL-8, IL-11), parathyroid hormone-related protein (PTHrP), chemokine receptor (CXCR4), osteopontin (OPN), and bone sialoprotein (BSP) which help to invade bone marrow (Bellahcène et al., 1996; Esquivel-Velázquez et al., 2015; Kakonen and Mundy, 2003; Kang et al., 2003; Köhrmann et al., 2009; Merdad et al., 2014; Zhao et al., 2018). In most cases, bone metastases are associated with bone pain, hypercalcemia, pathologic fractures, spinal instability, and total bone marrow infiltration. Furthermore, progression of tumor invasion into bone marrow and long-term complications of chemo- and radiation therapy complicate blood diseases such as anemia, neutropenia, leukopenia, and pancytopenia (Shao et al., 2013; Shiozawa et al., 2015). Therefore, strategies which could reduce the incidence and morbidity of bone metastases are of great clinical importance.

BSP is a non-collagenous phosphorylated glycoprotein which was originally isolated from calf bone (Herring, 1972). It is a member of the SIBLING (Small Integrin-Binding Ligand, N-linked Glycoprotein) protein family which also contains osteopontin (OPN), dentin sialophosphoprotein (DSPP), dentin matrix protein 1 (DMP1), and matrix extracellular phosphoglycoprotein (MEPE). Generally, SIBLING proteins function in

adhesion, migration, and spreading of cells through interaction with multiple binding partners such as MMPs, CD44, and integrins (Bellahcène et al., 2008; Fisher and Fedarko, 2003). Normally, they exert functions not only in mineralized tissues such as bone and dentin (Fisher et al., 2001), but in soft organs, too (Ogbureke and Fisher, 2004, 2005). However, in cancer they are differentially regulated in tumor invasion, cell survival and proliferation. This suggests an essential role of SIBLING proteins in tumorigenesis and cancer progression (Ogbureke et al., 2007). Accordingly, BSP is not only expressed in healthy bone, cartilage, teeth, and trophoblasts of the placenta, but also in primary and secondary tumors (Bianco et al., 1991; Oldberg et al., 1988). It is used as an early marker for osteoblast differentiation (Hattar et al., 2005) and accelerates differentiation of mesenchymal cells from bone into osteoblasts (Mizuno et al., 2000). On SDS-PAGE, BSP, with a molecular mass of the core protein of 33.6 kDa, runs at 70-80 kDa due to glycosylation. These smaller and larger forms were termed hypo-glycosylated BSP (hypo-BSP) and high-glycosylated or mature BSP (mature-BSP), respectively (Zepp et al., 2018). Moreover, literature has also shown a band at 45-52 kDa (Wuttke et al., 2001; Zepp et al., 2018). BSP contains an RGD integrin recognition sequence which may facilitate adhesion of tumor cells to the bone surface, especially through $\alpha_v\beta_3$ and $\alpha_v\beta_5$ integrin receptors (Raynal et al., 1996; Sung et al., 1998). Beyond that, the RGD-integrin complex was found to interact with MMP-2 and human complement factor H, which mediates a block of tumor cell lysis during metastasis (Fedarko et al., 2000; Karadag et al., 2004). Therefore, patients with preoperatively elevated serum BSP levels are at high risk of subsequent bone metastases in the first years after primary surgery (Diel et al., 1999). Thus, there seems to be a connection between ectopically formed BSP and the development or progression of osseous metastases in breast cancer. Indeed, in primary breast cancer, BSP expression correlated in with a bad prognosis and the development of bone metastases (Loibl et al., 2006). Downregulation of BSP through antisense oligonucleotides reduced the formation of colonies of MDA-MB-231 breast cancer cells and of osteolytic metastases in nude rats (Adwan et al., 2004). Furthermore, use of an anti-BSP antibody led to decreased proliferation, colony formation, and migration of breast cancer cells *in vitro* and reduced osteolysis in a nude rat cancer model (Bäuerle et al., 2006). These findings suggest that BSP plays an important role in breast cancer bone metastasis and might serve as useful marker protein. Expression of BSP is mediated by the transcription factor RUNX2 (Ducy et al., 1997). RUNX2 expression, in turn, is regulated by TGF β 1 (Lee et al., 2002, 2000) and its DNA-binding activity appears to be induced by ERK- and/or AKT-dependent phosphorylation as a consequence of IGF1 binding (Cohen-Solal et al., 2015; Qiao et al., 2004). Fittingly, BSP expression was also found to be downstream of TGF β 1 (Ogata, 2008; Ogata et al., 1997) and IGF1 (Nakayama et al., 2006).

Until today, experiments related to BSP were either performed in conventional two-dimensional (2D) cell cultures or using *in vivo* rodent models. Although culturing of cells in 2D and their use for studying drug effects are easy to achieve, 2D-models show significant limitations in reproducing the complexity and pathophysiology of *in vivo* tumor tissue (Pampaloni et al., 2007). Therefore, three-dimensional (3D) cell culture systems are of increasing interest in cancer research since tissue architecture and the extracellular matrix (ECM) significantly influence tumor cell responses to micro-environmental signals (Nath and Devi, 2016). The 3D-systems display several characteristics of tumor cells *in vivo*. These include gradients of oxygen and nutrients, with according cellular subpopulations showing proliferative, quiescent, or apoptotic/necrotic behavior. Consequently, models that better mimic tumor

heterogeneity and intercellular contact were found to exhibit more representative responses to drug therapies (Kim, 2005; Yamada and Cukierman, 2007). Here, we set up a sandwich approach for long-term 3D-cell culture which allows consistent growth of spheroids made of triple-negative MDA-MB-231 breast cancer cells for more than 21 days. We characterized the expression profiles of hypo-BSP and mature-BSP in 2D- and 3D-cell culture systems and explored a new non-commercial anti-hypo-BSP monoclonal antibody. This revealed a correlation of BSP expression with cell proliferation.

2.3 Material and Methods

2.3.1 Cell line and cell culture

The human MDA-MBA-231 breast cancer cell line and the non-cancerous human breast epithelial cell line MCF10A, prostate cancer cell line PC-3 and the foreskin fibroblast cell line CCD-1137Sk were purchased from American Type Culture Collection (ATCC, Manassas, VA, USA). MDA-MB-231 and PC-3 cells were maintained as mono-layers in RPMI 1640 medium with L-glutamine (Capricorn Scientific GmbH, Germany) supplemented with 10 % fetal bovine serum (FBS, Gemini Bioproduct Inc., Woodland, CA, USA) and 1 % penicillin/streptomycin (Capricorn Scientific GmbH, Germany) at 37 °C in an incubator with 5 % CO₂. MCF10A cells were cultured in a 1:1 mixture of Dulbecco's modified Eagle's medium and Ham's F12 medium (DMEM/F12) (Capricorn Scientific GmbH, Germany) supplemented with 5% horse serum (Sigma Aldrich, Germany), hydrocortisone (0.5 µg / mL) (Sigma Aldrich, Germany), insulin (10 µg / mL), epidermal growth factor (20 ng / mL) (Sigma Aldrich, Germany), and 1 % penicillin/streptomycin. The medium was changed every two to four days. After the mono-layer of cells became 80 % confluent, subcultivation was carried out using 0.05 % Trypsin-EDTA in DPBS (1x) (Capricorn Scientific GmbH, Germany). CCD-1137Sk cells were maintained as mono-layers in Iscove's Modified Dulbecco's Medium (ATCC, Manassas, VA, USA) and 1 % penicillin/streptomycin (Capricorn Scientific GmbH, Germany) at 37 °C in an incubator with 5 % CO₂.

2.3.2 Tumor spheroid formation and cytostatic treatment

MDA-MB-231 and PC-3 3D-cancer cell cultures were generated using four different methods described below and summarized in table 1. For co-cultures with CCD-1137Sk cells, 10,000 cells of each type were mixed and then seeded on ultralow attachment plates with U-bottom (Greiner bio-one, Frickenhausen, Germany) in MDA-MB-231 medium. The cell numbers of mono-layer cell cultures were determined using a Vi-CELL XR cell counter and cell viability analyzer (Beckman Coulter, Fullerton, CA). In order to examine the effects of different 3D-techniques on long term culture, MDA-MB-231 cells were seeded at day *in vitro* (DiV) 0 with 10,000 cells per well. For cytostatic treatment, six days old spheroids were cultivated for 48 h in either 1 µM Paclitaxel (Sigma Aldrich, Germany) in 0.5 % of DMSO or just in 0.5 % of DMSO as control. Then, samples were harvested, fixed, and prepared for staining.

Hanging drop technique (HD)

20 µL of cell suspension per well were applied into a 72-well Terasaki plate from Greiner Bio-One, Germany. The hanging drop plate was then carefully rotated upside

down and placed into a 100 mm × 20 mm plate. Into the same plate also a 60 mm tissue culture dish without lid was placed and supplied with 5 mL of double-distilled water (ddH₂O) on the bottom of the dish to keep the humidity in the plate constant. At the end, the lid of the 100 mm × 20 mm plate was closed and incubated at 37 °C in a humidified atmosphere at 5 % CO₂. Daily monitoring of the 3D-cell cultures was performed after four days under an inverted phase-contrast microscope (Axiovert 25, Zeiss). Medium was changed every other day by adding 2.5 µL fresh medium per well.

Inlay method (IM)

This method was essentially performed as described before in detail (Longati et al., 2013). Briefly, 7.2 g of methylcellulose (MC) powder (Sigma-Aldrich, Germany) were autoclaved together with a magnetic stirrer. 300 mL of 60 °C warmed RPMI 1640 medium were added to the MC powder, then resulting MC solution were stirred for 20 min. Thereafter, 20 % FCS were added, and the solution was mixed again overnight at 4 °C under sterile conditions. The solution was aliquoted in 15 mL tubes, centrifuged at 5,000 x g for 2 h at 23 °C, and the supernatant was stored at -20 °C. The corresponding cell suspension was mixed well at the rate 4:1 with pre-warmed MC solution at room temperature and 150 µL cell suspension was pipetted per 96-well (Greiner Bio-one, Frickenhausen, Germany). The final concentration of MC was 0.36 % per well, respectively. Spheroid formation was induced by centrifugation of the plates at 800 x g for 15 min before incubation in a humidified atmosphere at 37 °C and 5 % CO₂. For subgroups IM2 and IM3 (Tab. 1) cell-repellent surface plates (CELLSTAR®) were used. In all groups, the 3D-cell cultures were observed for 24 DiV of culturing and medium was changed every other day by replacing 50 % of the medium.

On-top method (OM)

To avoid cell attachment to the plate bottom and to stimulate 3D-cell culture generation, 96-well F-bottom plates (Greiner Bio-one, Frickenhausen, Germany) were coated with pre-warmed SeaPlaque® GTG (Cambrex Bio Science Rockland, Rockland, ME) agarose or with MC solution as described below. For the OM1 subgroup the MC 1,5 % solution was prepared as described for the IM method, but FCS was not included. For the OM2 subgroup, sea plaque agarose (SPA) was diluted in RPMI 1640 medium with L-glutamine without FCS to a final concentration of 1.5 % and then autoclaved together with a magnetic stirrer. Thereafter, for the OM1 subgroup 96 well F-bottom plates (Greiner Bio-one, Frickenhausen, Germany) were coated with 50 µL per well of pre-warmed 1.5 % MC solution. For the OM2 subgroup 96 well F-bottom plates (Greiner Bio-one, Frickenhausen, Germany) were coated with 50 µL per well of pre-warmed 1.5 % SPA solution, respectively. After the first layer had been allowed to solidify, a single-cell suspension containing 10⁴ cells per 150 µL was plated in complete growth medium into each well. The plates were centrifuged at 800 rpm for 15 min to allow cell-cell contact and incubated in a humidified atmosphere at 37 °C and 5 % CO₂. The 3D-cell cultures were observed for 24 DiV of culturing and medium was changed every other day by replacing 50 % of the medium.

Sandwich method (SM)

Here, we describe an improved version of a technique that was previously published by others (Debnath et al., 2003; Friedrich et al., 2009; Ivascu and Kubbies, 2006; Li et al., 2011). The first layer for the sandwich technique was prepared as described for the OM method. The plates were then allowed to cool down under laminar flow for 60 min

at room temperature. Thereafter, 50 μ L of cell suspension containing 10^4 cells were added per well and the plates were then centrifuged at 800 rpm for 10 min to initiate spheroid formation. As basement membrane-like extracellular matrix extracts, we used Matrigel (Cat. No: 354234, BD Biosciences) or BME (Cat. No: 3445-010-01, Cultrex[®] 3-D Culture MatrixTM Reduced Growth Factor Basement Membrane Extract, PathClear[®], Amsbio). Matrix stock solutions were thawed overnight on ice at 4 °C and then mixed on ice with cell culture medium to reach a final concentration of 10 %. 50 μ L of 10 % Matrigel or BME solution were then gently added to each well. Subsequently, spheroids were cultured statically under standard culture conditions (5 % CO₂, 37 °C). The spheroids were observed for 24 days of culturing and medium was changed every other day by replacing 50 % with fresh medium.

Table 1. Overview of experimental 3D-culture design

Method	Subgroup	Initial seeding density	Medium	Coating type
Hanging drop technique (HD)	–	10,000 cells/well	RPMI 1640	–
Inlay method (IM)	IM1	10,000 cells/well	Methylcellulose 0,3%	–
	IM2		RPMI 1640	Cell repellent surface
	IM3		Methylcellulose 0,3%	Cell repellent surface
On top method (OM)	OM1	10,000 cells/well	RPMI 1640	Methylcellulose 1,5%
	OM2			Sea plaque agarose 1,5%
Sandwich method (SM)	SM1	10,000 cells/well	RPMI 1640 + Matrigel 10%	Methylcellulose 1,5%
	SM2			Sea plaque agarose 1,5%
	SM3			RPMI 1640 + BME 10%
	SM4	5,000 cells/well	Sea plaque agarose 1,5%	

(Rustamov et al., 2019)(CC BY)

2.3.3 Analysis of tumor spheroids

To determine the long-term growth kinetics of 3D-cell cultures under each condition, the spheroid/aggregate sizes were examined at DiV 4-24 using an inverted phase-contrast microscope (Axiovert 25, Zeiss). The digitalized images were then processed and analyzed by measuring the area of the 3D-cell cultures using ImageJ (V 1.48) software. In contrast, many previous studies reported the volumes of spheroids (Chen et al., 2014; Friedrich et al., 2009; Ivanov et al., 2014; Piccinini, 2015; Piccinini et al., 2015). These volume values were mostly derived from measured areas, diameters, or perimeters of the spheroids in the 2D-projection. Such a procedure might be useful for perfectly round-shaped 3D-cultures. However, here we obtained many non-circular 3D-cell aggregates, and this made it impossible to get the volume values for 3D-cultures. Therefore, we measured the areas of 3D-cultures to compare morphological characteristics and growth kinetics.

2.3.4 Immunoblotting

For immunoblotting, about 180-190 spheroids were accumulated in 15 mL conical tubes and allowed to sediment. Supernatant was discarded by gentle aspiration and the spheroids were washed twice with PBS (Capricorn Scientific GmbH, Germany). After washing, all spheroids were transferred to an ice cold 0.1 mL micro tissue grinder

glass (Wheaton, USA) and 100 μ L of NP-40 lysis buffer (PMFS 1:100; inhibitor cocktail 1:100) were added. The spheroids were grinded manually and incubated for 15 min on ice. Afterwards, lysates were centrifuged at 10,000 rpm for 15 min at 4 °C and the supernatants stored at -25 °C. Cell lysates from 2D-cultures were also prepared using 100 μ L NP-40 lysis buffer. Protein concentrations were measured using a BCA Protein Assay kit (Pierce). After determining protein concentration, samples were mixed with 2 x Laemmli buffer (Laemmli, 1970) and boiled for 5 min. 30 μ g of protein and standard marker (NIPPON Genetics Europe, Germany) were resolved on 8 % SDS-PAGE, transferred to nitrocellulose transfer membrane (Protran[®], Schleicher & Schuell Bioscience GmbH) and blocked with 5 % milk in TBS–Tween 20 (0.1 %, Sigma). The membranes were probed with primary antibodies for 16 h at 4 °C and then incubated with HRP-conjugated secondary antibodies for 2 h at room temperature. Non-commercial human recombinant carbohydrate deficient bone sialoprotein (CD-BSP (aa 108-122)) and commercially available rat CD-BSP (Cat. No: 4217.VP) primary monoclonal antibodies (mAb) were received as gifts from Immundiagnostik AG, Germany. Additional information about antibodies and dilutions used in the study are shown in supplementary table 1. Blots were visualized by chemiluminescence (Westernbright chemiluminescent substrate sirius; Biozym Scientific GmbH) and imaged using the Syngene G-Box (Syngene, Frederick, MD, USA). Band intensities were quantified using the analysis software Image J as relative intensities of bands of interest divided by the intensities of the corresponding GAPDH bands.

2.3.5 Immunofluorescence

For immunofluorescence, spheroids were accumulated in 15 mL conical tubes and allowed to sediment. Supernatant was discarded by gentle aspiration and the spheroids were washed twice with sterile PBS. After washing, 4-5 spheroids were transferred to a 1.5 mL tube. After sedimentation, the supernatant was gently removed, 4 % paraformaldehyde (PFA) was added, and all placed on an orbital shaker at 1,000 rpm for 2 h at room temperature. Then, PFA was removed, and spheroids were washed twice with PBS. Afterwards, PBS was removed, spheroids were soaked in 10 % sucrose and placed on an orbital shaker at 1,000 rpm for 15 min at room temperature. After 15 min, the sucrose was gently aspirated and then new 10 % sucrose solution was added. Subsequently, a sucrose gradient was applied by incubating 15 min each in increasing sucrose densities (mix 2:1; 1:1; 1:2 with 30 % sucrose). To prepare cryosections, 4-5 spheroids were transferred into Tissue-Tek (Cryomold[®]), embedded with frozen section compound (Leica) and frozen at -25 °C. The blocks were cut on a cryostat (Leica CM 1950) at 10 μ m thickness. The slides were kept frozen at -25 °C until being stained. Mono-layer cell cultures were fixed with 4 % PFA for 15 min and then washed twice with PBS. Fixed sections were permeabilized with 0,1 % Triton X-100 for 5 min and then washed twice with PBS. To avoid unspecific staining, the sections were incubated with blocking solution (10 % horse serum, 0.2 % fish skin gelatin in 1 x PBS) and incubated for 20 min at room temperature. Then, sections were incubated with the primary antibodies overnight at 4 °C in a humidified chamber. Sections were then washed twice with blocking solution for 20 min each. Then, they were incubated with secondary antibodies for 1.5 h at room temperature and subsequently washed twice with blocking solution and PBS. After drying, the samples were covered with 10 % Mowiol[®] (Sigma Aldrich) and allowed to dry overnight in dark storage boxes at room temperature. Slides were imaged on a Leica SP8 confocal laser-scanning microscope with HP PL APO 20x/0.75 IMM CORR oil immersion

objective. The antibodies and dyes used in this study are summarized in supplementary table 1.

2.3.6 Analysis of confocal images

All images were analyzed using the image processing software ImageJ (<https://imagej.nih.gov/ij/>). For automated image-based analysis and to generate high accuracy of measurements, we developed a multistep segmentation routine on the basis of ImageJ. This comprised of the following steps (Fig. S1): First, images were duplicated and on these, noise-pixels were removed with a median filter (radius 1.0). Images were adjusted for brightness/contrast to distinguish relevant structures against the background. Resulting images were binarized and dilated. Next, these binarized images were processed with auto threshold, watershed, and all objects larger than 50 pixels were detected using the analyze-particles function and imported into the ROI manager. Afterwards, all images were checked by visual inspection. Furthermore, a manual check was done by the detection of unspecific ROIs, which were located outside of the spheroid sections. Subsequently, all ROIs were overlaid on the original raw file and measurements were performed on these without any quality loss. Finally, all data were calculated with Microsoft® Excel for Mac OS (Version 16.0). For determination of enrichment of BSP in outer versus inner cells of co-cultures, each spheroid was separated into an inner area (= inside) and an outer area (= outside). The BSP channel was segmented, and the sum of the total spheroid signal and the sum of the outside signal was measured. Each sum was then divided by the number of total ROIs and outside ROIs, respectively, to get the mean of total spheroid BSP signal and outside BSP signal, respectively. The sum of the inside signal was measured by the sum of total signal minus the sum of outside signal. The mean of the inside BSP signal was then measured by dividing the sum of inside signal by the number of inside ROIs.

2.3.7 Statistical analysis

Statistical analysis employed Graph Pad Prism V7.0 (Graph Pad Software Inc., USA). Two-way ANOVA with Tukey's multiple comparisons post hoc test (confidence level 95 %) was used for comparison among 3D-culture systems and growth kinetic of MDA-MB-231 spheroids/aggregates by considering the different 3D-cell culture methods and the time as two factors. Statistical significance of data from western blot and immunofluorescence experiments was evaluated using one-way Analysis of Variance (ANOVA) with Tukey's post hoc test or using unpaired two-tailed t-tests. Normal distribution and homo-/heteroscedasticities of data were probed using Kolmogorov-Smirnov test and F-test, respectively. Graphs are presented as mean \pm standard deviation (SD). P-values were indicated as * ($P < 0.05$), ** ($P \leq 0.01$), *** ($P \leq 0.001$) or **** ($P \leq 0.0001$) and $P > 0.05$ was considered not significant ("ns").

2.4 Results

2.4.1 Influence of 3D-cell culture protocols on aggregate/sphere formation and on growth of MDA-MB-231 cells

First, we compared and refined different previously described 3D-culture protocols for MDA-MBA-231 cells to develop a consistent, reproducible long-term spheroid culture. Therefore, cells were grown under four different conditions, i.e. hanging drop (HD), inlay (IM), on top (OM), and sandwich methods (SM) (for details of culture conditions, refer to Materials and Methods section and Tab. 1).

Figure 11A shows representative microscopic images to illustrate morphological changes of 3D-cell aggregates and spheroids during an observation time period of 24 DiV. A qualitative and quantitative analysis of these cultures revealed the following results. First, cells in HD, IM, and OM cultures did not form spheroids (Fig. 11A) but remained loose cell aggregates that decreased in size during the observation period of 24 DiV (Fig. 11B). Cell spreading was pronounced in IM cultures and low in HD and OM aggregates (Fig. 11A). In contrast to HD, IM, and OM subgroups, we observed formation of firm spheroids (Fig. 11A) and their permanent growth in all SM subgroups (Fig. 11C). Spheroids sandwiched between 1.5 % SPA and 10 % Matrigel (SM2) grew 1.3-fold more than spheroids located between 1.5 % MC and 10 % Matrigel (SM1). Moreover, cells coated with 10 % BME (SM3 and SM4) showed higher linear expansion of spheroids than those with 10 % Matrigel (SM1 and SM2). To determine the best linear growth and the optimal size of spheroids embedded with 10 % BME, cells were seeded at different seeding densities. Initial seeding densities of 5,000 cells per well (SM4) and 10,000 cells per well (SM3) resulted in similar growth curves of spheroids (Fig. 11C). The borders of SM3-4 spheroids were clearly visible and of round shape in comparison with spheroids of conditions SM1 and SM2. Thus, SM3 yielded the most consistent and clearly defined spheroids. To verify a more general applicability of the SM3 culture protocol, we applied to prostate cancer PC-3 cells, another cell line that is difficult to culture in a spheroid format (Fig. S2). As depicted in supplementary figure 2, this led to round and consistently growing spheroids similar to those of MDA-MB-231 cells.

2.4.2 Spheroid formation upon co-culturing of MDA-MB-231 and CCD-1137Sk fibroblasts

Given that BME as well as Matrigel are rich in ECM components, we wanted to test the effects of ECM supply by fibroblast co-culture. Therefore 10,000 MDA-MB-231 cells were co-seeded with an equal amount of CCD-1137Sk foreskin fibroblasts in the absence of BME and Matrigel on ultra-low attachment plates. Appearance and growth of the resulting cultures were studied. As shown in figure 12A, these co-cultures formed more or less round 3D-cultures of spheroid shape, and they were growing with increased culture time (Fig. 12B). However, in contrast to SM3 mono-cultures of MDA-MB-231 cells, which formed smoothly outlined and almost perfectly round spheroids that were consistently growing after 4. DiV (Fig. 11A and C), the co-cultures displayed a more rugged surface with individual cells outside the spheroid (Fig. 12A) already at 7. DiV. The amounts of cells not adhering to the spheroid increased with culture time and by 21. DiV only about 50 % of the area occupied by the entire co-culture was really found in the spheroid (Fig. 12C). In other terms, these co-cultures increasingly disintegrated with culture time.

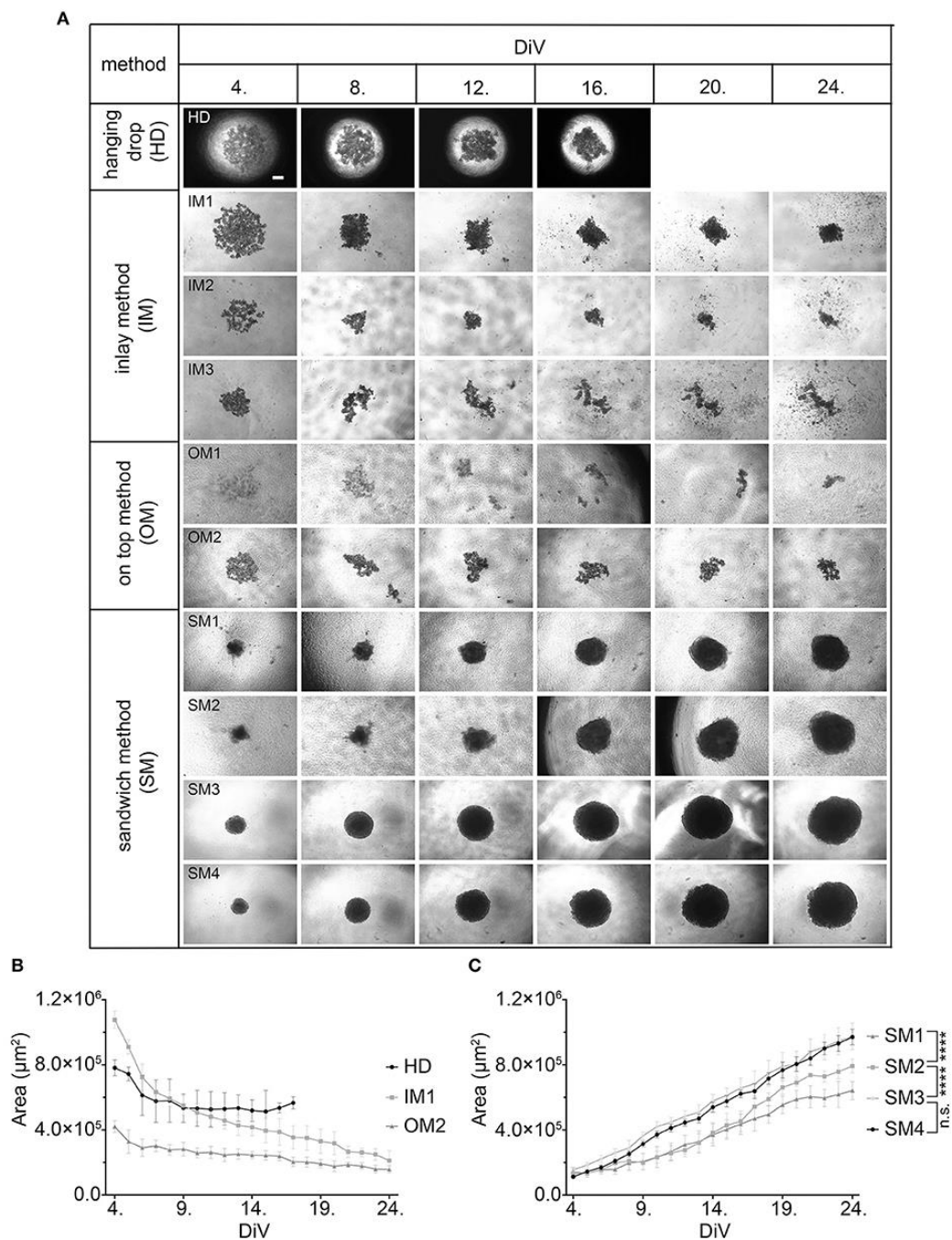


Figure 11. Sandwich method using SPA and BME yields most consistent growth of MDA-MB-231 spheroids. A) Representative phase-contrast microscopy images of MDA-MB-231 3D-cultures. These were generated using four different methods: hanging drop (HD), inlay method (IM1; IM2; IM3), on top method (OM1; OM2), and sandwich method (SM1; SM2; SM3; SM4). From HD to SM3, equal initial seeding densities were used (10,000 cells / well), for SM4 5,000 cells/well were used. Spheroids were cultured until day 24 *in vitro* (DiV). Representative images from DiV 4, 8, 12, 16, 20, and 24 are shown. Scale bars, 200 μm . B-C) Quantitative analysis of 3D-culture growth or shrinkage. Graphs depict areas of 3D-cultures as a function of DiV (mean values \pm SD, $n = 4$ independent experiments with 5 replicates). Statistical analysis was performed using a two-way ANOVA with post-hoc Tukey's multiple comparison test to compare statistically significant differences across methods for each day. Statistical significance values were observed for 24 DiV: (SM1 versus SM2, **** $P < 0.0001$; SM2 versus, SM3 **** $P < 0.0001$; SM3 versus SM4, n.s.). (Rustamov et al., 2019)(CC BY)

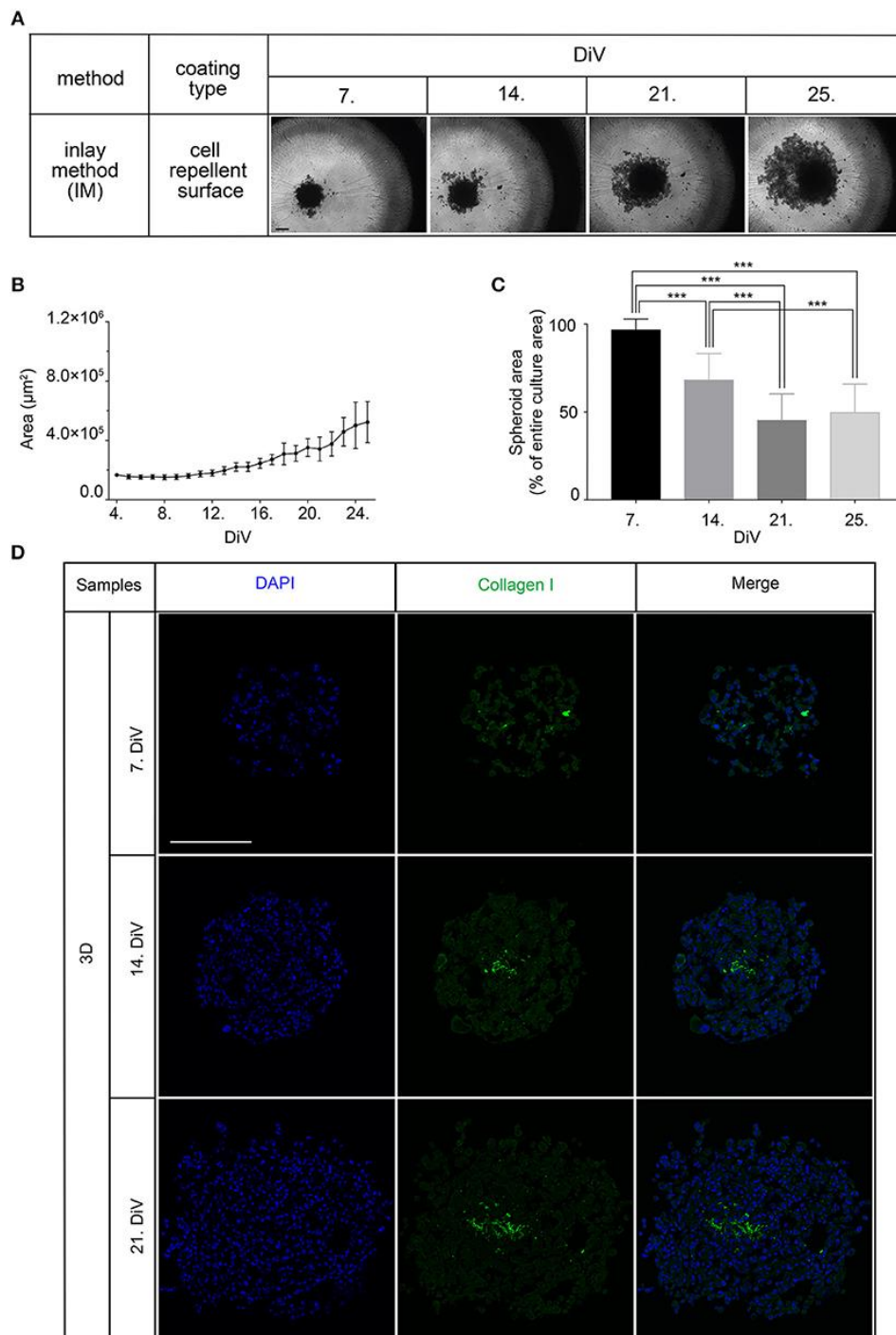


Figure 12. Co-culture of MDA-MB-231 and CCD-1137Sk fibroblast cells yields slowly growing spheroids and extensive outward cell movement. A) Phase-contrast microscopy images of MDA-MB-231 plus CCD-1137Sk 3D-co-cultures. These were generated by co-seeding of 10,000 cells for each type in ultra-low attachment plates. Representative images from DiV 7, 14, 21, and 25 are shown. Scale bars, 200 μm . B) Quantitative analysis of 3D-culture growth. Graphs depict average values of dark compact spheroid areas as a function of DiV (mean values \pm SD, $n = 96$ spheroids). C) Quantitative assessment of outward moving cells. Columns indicate the fraction of the total culture area that was occupied by the dark compact spheroid structures in percent and as a function of DiV (mean values \pm SD, $n = 96$ spheroids; *** $P < 0.001$). D) Slices of co-culture spheroids at 7., 14., and 21. DiV were stained with DAPI for nuclei and anti-Type-I collagen for ECM. Panels show single confocal sections of representative samples. Scale bar, 200 μm . (Rustamov et al., 2019)(CC BY)

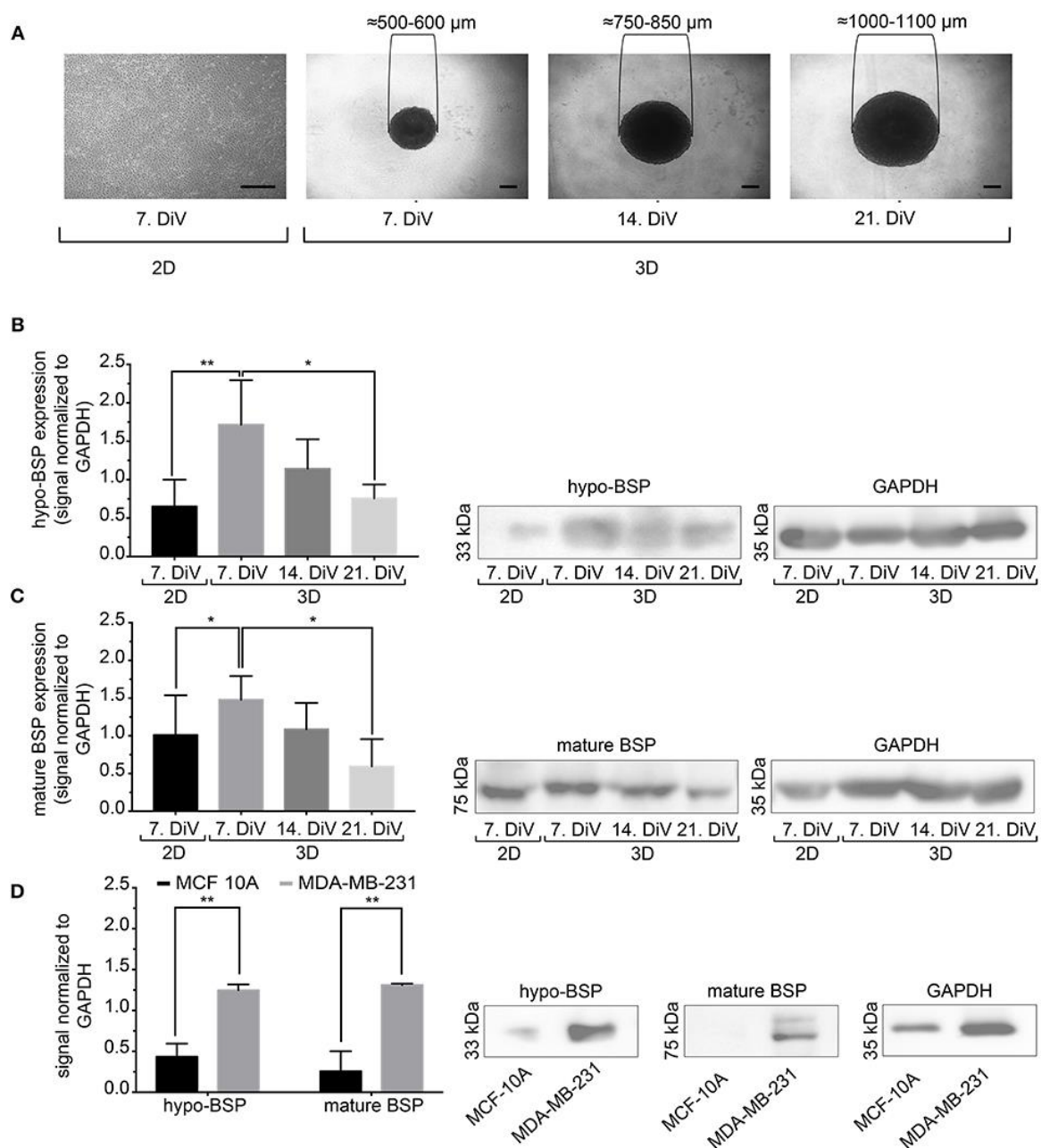


Figure 13. Mature- and hypo-BSP protein levels are increased in 3D- versus 2D-cultures at 7. DiV. A) Wide field images of representative 7. DiV mono-layer cells and 7., 14., 21. DiV old spheroids as used for biochemical analyses. Scale bars, 200 μm. B-C) Equal amounts of protein of lysates from mono-layer cells (2D) and spheroids (3D) were loaded on SDS-PAGE and Western blots were performed. Left panels depict quantitative analyses of Western blot bands as shown for representative cases in right panels. B) Results upon incubation with anti-human CD-BSP (aa 108-122) showing hypo-BSP expression. Statistical analysis was performed with one-way ANOVA followed by Tukey's multiple comparisons test ($n = 6$, $** P < 0.01$, $* P < 0.05$, mean + SD). C) Results upon incubation with anti-rat CD-BSP (aa 108-122) IDK1 indicating expression of mature-BSP. Statistical analysis was performed with one-way ANOVA followed by Tukey's multiple comparisons test ($n = 6$, $* P < 0.05$, mean + SD.). D) Lysates of the non-cancerogenous breast cell line MCF10A were compared to those of MDA-MB-231. Graph shows quantitative analysis of Western blot band intensities as exemplified on the right side. Significant differences between groups were tested using an unpaired, two-tailed t-test ($n = 3$, $** P < 0.01$, mean + SD). (Rustamov et al., 2019)(CC BY)

Notably, Type-I collagen as a major ECM component was found at all spheroid stages throughout the co-cultures, but often enriched in a central region (Fig. 12D). In summary, these data suggest that ECM is a critical component for formation and growth of MDA-MB-231 spheroids, but it appears to be insufficient for maintaining the spheroids compact.

2.4.3 Differential expression of mature- and hypo-BSP in 3D- versus mono-layer cell cultures

Next, we studied the kinetic profile of BSP expression at different times in SM3 MDA-MB-231 mono-cultures. Therefore, 2D-cells were harvested at 7. DiV and spheroid cultures at 7., 14., and 21. DiV for Western blot analysis. Figure 13A shows representative wide field images of these samples. For immunoblotting, 180-190 spheroids were lysed for each trial on 7., 14., and 21. DiV. For each time point, spheroids showed rather homogeneous sizes (Fig. 13A). In the Western blot experiments, we validated a novel human recombinant CD-BSP mAb (aa 108-122 / AF165) against BSP and compared its performance with a commercially available rat recombinant CD-BSP mAb (aa 108-122 / IDK1). The human CD-BSP mAb detected a band at the expected size for hypo-BSP at 33 kDa, as well as a lower one at 25 kDa (Fig. S3). Conversely, the rat CD-BSP mAb primarily detected a band at 75 kDa, which likely reflected mature-BSP, and additionally some weak bands at sizes of 45-50 kDa and 35 kDa, which likely reflected partially glycosylated forms of BSP (Fig. S3). To examine the specificity of both antibodies, we used the non-cancerous human breast epithelial cell line MCF10A as a negative control. This showed a highly significant difference in the expression of both BSP forms. While BSP-specific bands were hardly detectable in MCF10A lysates they were strong in MDA-MB-231 samples (Fig. 13D). Comparison of different MBD-MB-231 cultures revealed that hypo-BSP and mature-BSP expression was significantly higher in 7 DiV 3D-cultures as compared to 2D-mono-layer cultures (Fig. 13B and C). With increasing time in 3D-cultures, expression of hypo-BSP and mature-BSP decreased, and it was significantly lower on 21. DiV as compared to the 7. DiV (Fig. 13B and C).

2.4.4 Increased expression of BSP in young MDA-MB-231 spheroids as revealed by immunofluorescence

To confirm the Western blot findings and to get an insight into the distribution of BSP protein in the spheroids, we next performed immunofluorescence studies with the CD-BSP antibodies. 2D-cultures and 10- μ m thick cryo-sections of spheroids at different DiV were stained. This resulted in immunofluorescence signals as shown in figure 14A. While the rat CD-BSP antibody did not yield any reliable immunostaining (not shown), the human CD-BSP antibody outlined many cell bodies in spheroids with fluorescence intensities being particularly strong at the borders of spheroids (Fig. 14A and S4).

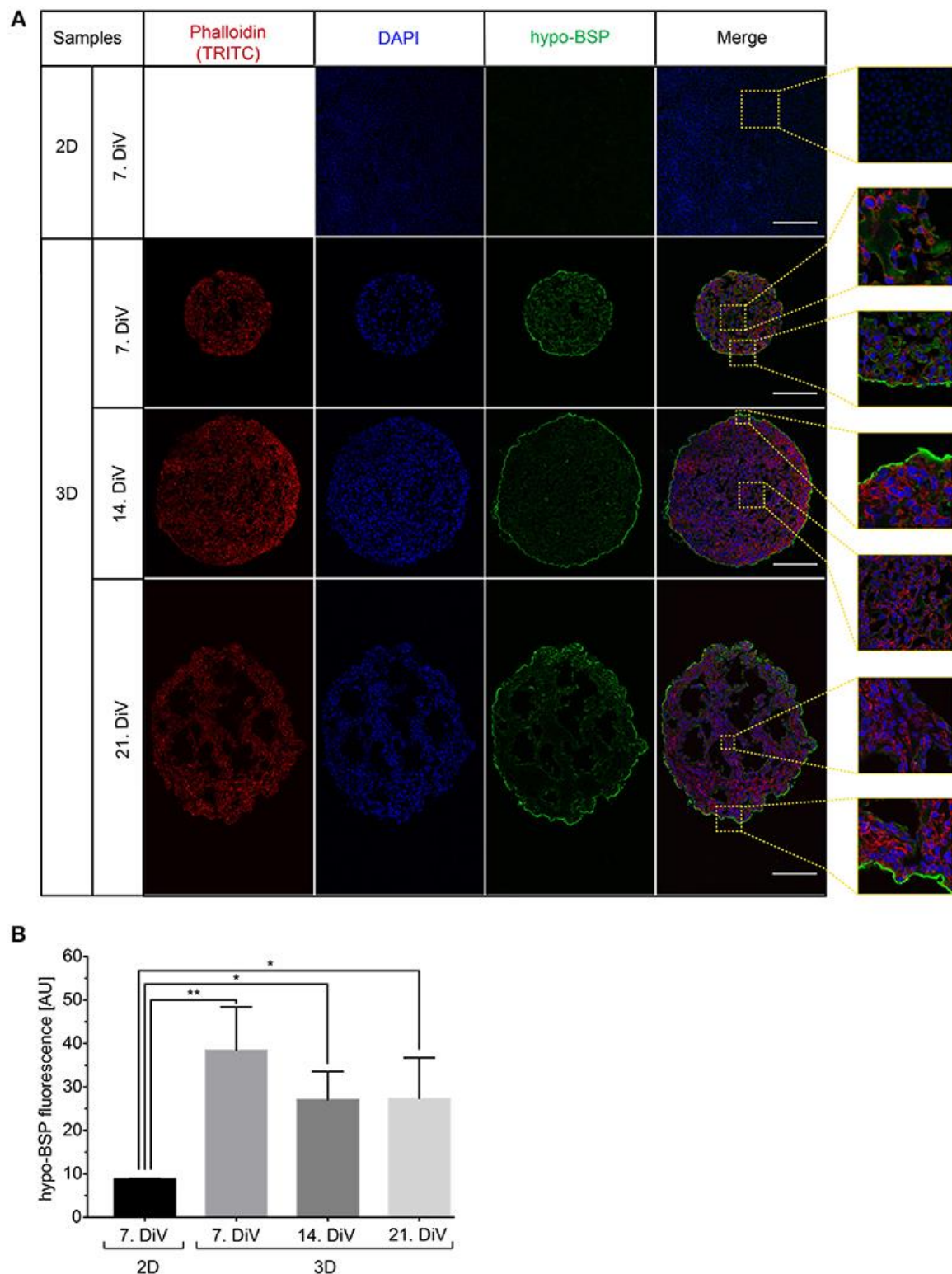


Figure 14. Upregulation of BSP protein levels in young MDA-MB-231 spheroids is confirmed by immunofluorescence analysis. A) 2D-cell cultures were stained with DAPI (blue, cell nuclei) and hypo-BSP antibody (green). 10- μ m thick cryosections of 7, 14, and 21 days old spheroids were additionally labeled with Phalloidin-TRITC (red, actin cytoskeleton). Scale bar, 200 μ m. B) Quantitative analysis of confocal images. The graph depicts antibody fluorescence signals as a function of DiV. Statistical analysis was performed with one-way ANOVA followed by Tukey's multiple comparisons test ($n = 3$ for 2D and $n = 4$ for 3D; a total of 148 confocal images were analyzed; ** $P < 0.01$, * $P < 0.05$, mean + SD). (Rustamov et al., 2019)(CC BY)

To quantify differences in fluorescence intensity on a cellular level, we developed a multistep segmentation routine on the basis of the ImageJ software (<https://imagej.nih.gov/ij/>) and provide this as a convenient and fully annotated ImageJ macro as a supplement to this study. Results of the new macro are schematically outlined and compared to simple threshold-based segmentation in supplementary figure 1. Simple threshold-based segmentation of human anti-CD BSP fluorescence signals was very inefficient and detected primarily the boundaries of spheroids, while the cores of spheroids were hardly segmented (Fig. S1A). Conversely, the multistep segmentation macro yielded more accurate results (Fig. S1C). It involved the following steps. First, the raw image was duplicated, and all subsequent processing changes were done on these duplicates with no changes on raw data. Next, background noise pixels were removed with a median filter and a high level of intensity was adjusted. The adjusted image was then binarized, dilated, and filtered by watershed. After thresholding and the analyze particles command, detected ROIs were overlaid as a mask onto the raw data, resulting in the final, well-segmented image (Fig. S1C, lower right). In comparison to the right panel of supplementary figure 1A, which shows the same image analyzed with simple thresholding, a clear difference in the quality of segmentation is evident: While the novel routine detected most internal cellular borders, the simple method found almost exclusively the strongly stained spheroid border and a couple of noise pixels (indicated by arrowheads in Fig. S1A and C). As shown in supplementary figure 1B, the same algorithm was also useful for segmenting DAPI-stained cell nuclei in the same samples.

By using the new macro, we then quantitatively compared anti-CD BSP immunofluorescence signals from samples taken at different DiV (Fig. 14B). This showed similar trends in hypo-BSP expression as those obtained by Western blotting. Indeed, hypo-BSP immunofluorescence signals were 4.3-fold higher in 7. DiV spheroids than in 2D-cultures (Fig. 14B) and significantly declined in 14. and 21. DiV spheroids as compared to 7. DiV spheroids (Fig. 14B).

2.4.5 Cell proliferation and apoptosis profiles do not correlate to BSP expression

To investigate a potential correlation between BSP expression and physiological processes, we first addressed the occurrence of cell proliferation and apoptosis in 2D- and spheroid samples. Therefore, 2D-cultures and spheroid sections were stained with anti-KI67 (Fig. 15A and C) and anti-Cleaved Caspase 3 antibodies (Fig. 15B and D). Subsequently, the numbers of immune-positive cells were determined using the newly developed ImageJ segmentation macro. This showed more proliferating cells in 2D-cultures of MDA-MB-231 cells as compared to 7. DiV spheroids (Fig. 15C). Moreover, the fraction of proliferating cells decreased significantly from 7. DiV to 14. DiV spheroids and then remained stable (Fig. 15C). Conversely, the number of apoptotic cells was extremely low in 2D-cell culture, increased significantly in 7. DiV spheroids and from there remained similar with slight but significant changes between 14. DiV and 21. DiV (Fig. 15D). In conclusion, neither the profile of numbers of proliferating nor of apoptotic cells fit to the observations for BSP expression.

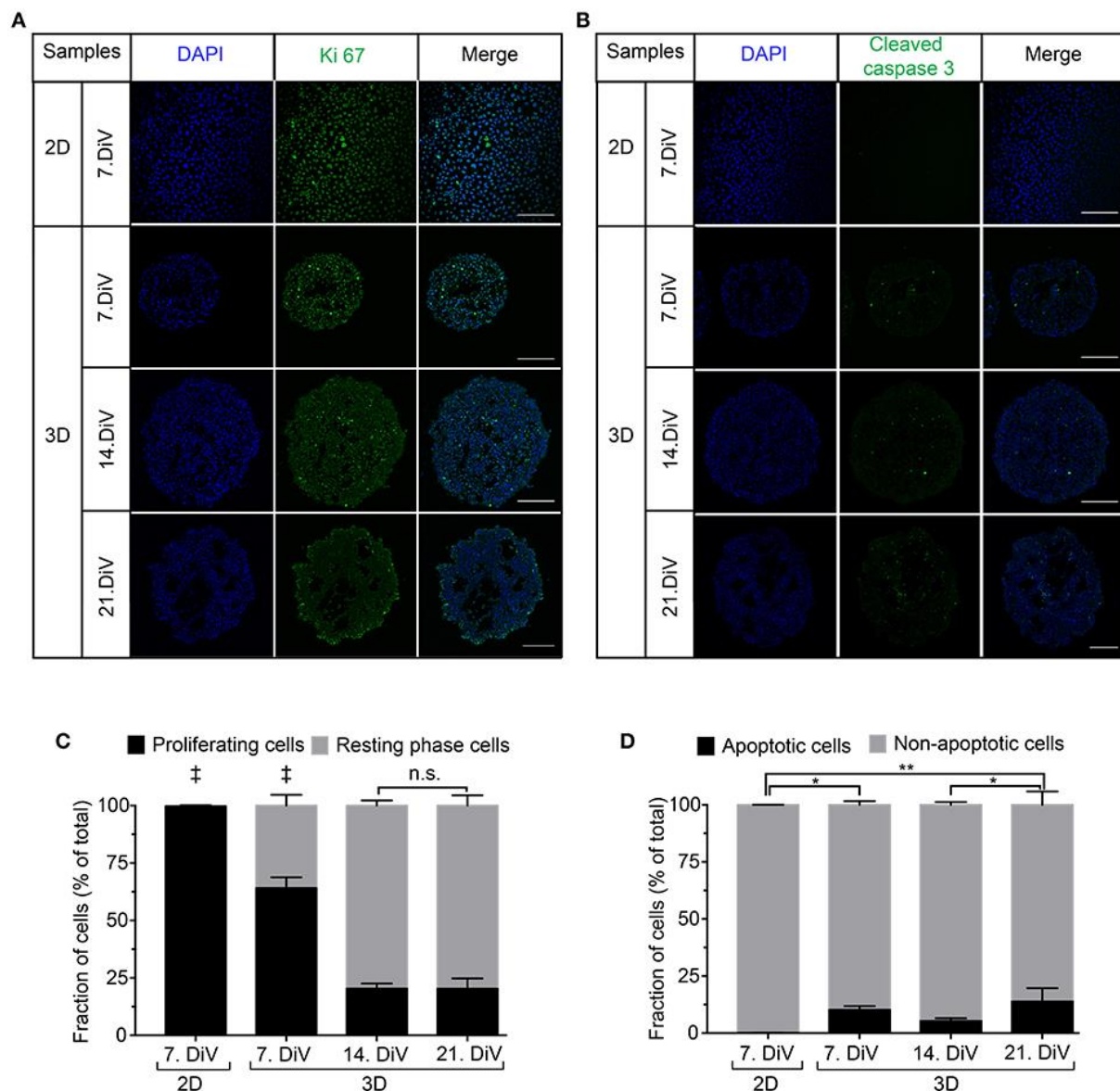


Figure 15. Cell proliferation decreases in MDA-MB-231 spheroids with increasing DiV. A-B) Mono-layer cell culture and 10- μ m thick cryosections of 7., 14., and 21. DiV spheroids were stained with DAPI (blue) and immunolabeled for either Ki 67 (A, proliferation marker, green) or Cleaved Caspase 3 (B, apoptosis marker, green). Images show single confocal slices of representative samples. Scale bars, 200 μ m. C-D) Quantitative analysis of confocal images. Statistical analysis was performed with one-way ANOVA followed by Tukey's multiple comparisons test. C) Graphs depict mean + SD (n = 3 for 2D and 3D; a total of 85 confocal images were analyzed; ‡ = Significant difference from all). D) Graphs depict mean + SD (n = 3 for 2D and 3D; a total of 81 confocal images were analyzed; ** P < 0.01, * P < 0.05). (Rustamov et al., 2019)(CC BY)

2.4.6 Expression of TGF β 1 correlates with that of BSP in different conditions

In breast cancer cells, including MDA-MB-231, BSP expression is mediated by the transcription factor, RUNX2 (Barnes et al., 2003). Further, regulation of RUNX2 abundance and transcriptional activity appear to be under control of TGF β 1 (Selvamurugan et al., 2004) and IGF1 (Nakayama et al., 2006). To address the

regulation of BSP expression from that point of view, three different types of approaches were performed. First, cell lysates were prepared from 7. DiV 2D-cultures as well as from 7., 14., and 21. DiV spheroids and then subjected to Western blotting. As depicted in figure 16A, TGF β 1 signals in the range between 38-50 kDa, likely reflecting different intracellular maturation stages of pre-pro- and pro-TGF β 1 (Gentry et al., 1988), were rather low in the 2D-culture samples, peaked in the 7. DiV spheroids and then declined in older spheroids. Levels of both, presumable pre-pro- (25 kDa) and pro-IGF1 (17 kDa) (Duguay, 1999) were similar in 2D and young spheroids and then decreased with augmenting spheroid age (Fig. 16B).

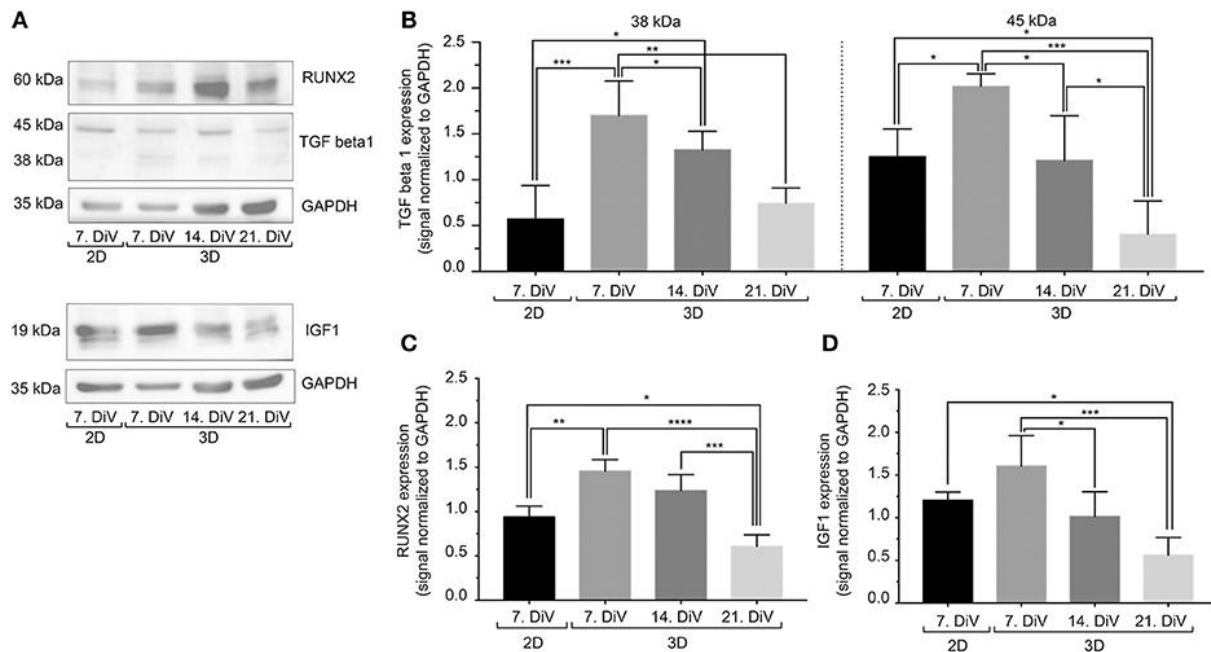


Figure 16. In untreated SM3 spheroids, expression profiles of TGF β 1, IGF1, and RUNX2 are similar to that of BSP. Equal amounts of protein of lysates from mono-layer cells (2D) and spheroids (3D) were loaded on SDS-PAGE and Western blots were performed. (A) Representative Western blot profiles for TGF β 1, RUNX2, IGF1, and GAPDH (loading control). (B-D) Quantitative analyses of Western blot bands. Statistical analysis was performed with one-way ANOVA followed by Tukey's multiple comparisons test (n = 4, *** P < 0.001, ** P < 0.01, * P < 0.05, mean + SD). (Rustamov et al., 2019)(CC BY)

Finally, also RUNX2 followed a similar expression profile (Fig. 16C). Thus, the expression profiles of TGF β 1, IGF1, and RUNX2 correlated well with that of BSP, consistent with the reported signaling axis, under this condition. Second, 6. DiV spheroids were treated for 48 h with 0 μ M or 1 μ M of Paclitaxel. Upon immunofluorescence staining of these samples, the following observations were made. First, Paclitaxel treatment apparently induced apoptosis, but did not alter the fraction of Ki-67 positive cells (Fig. S5). Next, the cytostatic reduced the immunofluorescence signals of both, BSP and TGF β 1, but not that of IGF1. Third, the expression profiles were also examined during prolonged culture times of MDA-MB-231 co-culture spheroids with CCD-1137Sk fibroblasts (Fig. S6). Again, both BSP and TGF β 1 levels apparently decreased with increasing DiV, as also observed in the MDA-MB-231 mono-cultures. Conversely, IGF1 signals increased with higher DiV. In summary, these data show a consistent correlation between the expression of BSP and TGF β 1, while IGF1 profiles showed a more erratic behavior. Similar to the SM3 spheroids, also the

co-culture spheroids showed the highest BSP fluorescence signals in the peripheral cells (Fig. S6A). On average, the fluorescence signals were $32.8 \% \pm 9.0 \%$ brighter there than in the spheroid centers.

2.5 Discussion

Accumulating evidence describes BSP as an important protein for tumorigenesis and metastasis in breast cancer (Loibl et al., 2006). However, expression and function of BSP appears to be highly dependent on the appropriate cellular environment. In particular, while abundance of BSP is high in metastatic breast and bone tissues, it is low or absent in 2D-cultures of cells derived from these entities. Therefore, in order to address regulation and function of BSP protein *in vitro*, appropriate 3D-cell culture systems were needed. Here, we first set up and characterized a long-term spheroid cell culture model of MDA-MB-231 breast cancer cells. Then, this model was used to study BSP expression in a 2D- versus 3D-longitudinal model, which revealed a transient upregulation of BSP upon 3D-culturing as well as correlations of TGF β 1 and IGF1 expression to BSP expression and cell proliferation, respectively.

It is well known that cancer cell lines show different characteristics depending on 3D-culture conditions (Hagemann et al., 2017; Ivascu and Kubbies, 2006; Raghavan et al., 2016). Previous studies reported that the ratio between hydrogel and Matrigel (Carey et al., 2017; Cavo et al., 2018) or the stiffness of the mixture (Cavo et al., 2016) could influence 3D-cell growth and morphology. MDA-MB-231 cells are no exception and they were found to form different types of 3D-aggregates, e.g. round (Ivascu and Kubbies, 2006) or stellate (Kenny et al., 2007). Here, we concentrated on culture protocols for reaching regularly round, linearly growing, and long-term stable spheroids. Of the ones tested, a sandwich-type culture protocol was optimal to mediate consistent growth of large-sized spheroids for more than one month (depicted here is up to 24. DiV). These results and the similar findings we have made in this study for the prostate cancer cell line, PC-3, corroborate our previous work, where, depending on 3D-cell culture technique and initial seeding density, differently sized spheroids of SCC-4 tongue cancer cells were obtained (Rustamov et al., 2017). With respect to spheroid formation and linear long-term growth kinetics of MDA-MB-231 as well as PC-3 cells, protein-rich BME (14-16 mg / mL) was superior to Matrigel (9-12 mg / mL) in the present study. Both matrices are derived from Engelbreth-Holm-Swarm mouse sarcoma, and contain growth factors (EGF, FGF, TGF β , IGF) (Vukicevic et al., 1992), ECM proteins (laminin, Type-IV collagen, entactin) (Kleinman et al., 1982), proteases (MMP-2, MMP-9) (Gillette et al., 2003), and perlecan (Kibbey, 1994). Yet, BME and Matrigel yielded differently sized spheroids of LNCaP prostate cancer cells (Edmondson et al., 2016). Furthermore, cancer cells injected with high-protein content Matrigel displayed significantly accelerated tumorigenesis *in vivo* when compared to low concentrated Matrigel (Fridman et al., 1991). In accordance with previous studies, our SM3 spheroid culture model showed similar growth characteristics as tumor nodules *in vivo*, which were generated by injection of MDA-MB-231 breast cancer cell suspension mixed with 100 μ L Matrigel (Christensen et al., 2015). Notably, during the entire observation period, SM3 spheroid growth was almost linear although the number of proliferative cells decreased after 7. DiV. To explain this apparent discrepancy, two aspects might be relevant. First, although cell proliferation significantly dropped after 7. DiV, it still slightly outweighed the fraction of apoptotic cells. Thus, considering these as the principal sources for cell number, there should be a net increase in spheroid

size even at 14. and 21. DiV. Second, the growth curves in figure 11C simply reported the spheroid area from the outside. As can be seen in figures 14 and 15, though, the inside of the older SM3 spheroids increasingly displayed empty regions, which were likely due to cell death or outward movement of cells away from the core zone. In combination, we think, these two points could well account for the observed linear growth of SM3 culture spheroid areas.

The relevance of an appropriate ECM for the 3D-growth of MDA-MB-231 cells was further supported by our co-culture data, where MDA-MB-231 cells were grown in 3D together with ECM producing CCD-1137Sk foreskin fibroblast cells. Although spheroid condensation took longer in these co-cultures as compared to the SM3 model and although many migrating cells were observed, spheroids from the co-culture model exhibited steady long-term growth over the test period of 25 DiV. Potentially, such a model could be used to study tumor-stroma interactions, but it would also bear the drawback that biochemical analyses will be based on a mixed cellular composition. Interestingly, in both, SM3 as well as co-culture spheroids, BSP was enriched in or on the external cells. Since these cells were well aligned in the SM3 cultures and more unordered in co-cultures, peripheral BSP enrichment was more easily seen in the SM3 cultures, but it was present in both types of spheroids. Considering the proposed role of BSP in metastatic cells, i.e. modulating the ECM for niche formation as a function of TGF β 1 (Nam et al., 2006), this peripheral accumulation might serve as diagnostic feature, which would not be available in 2D-cultures. Taken together, our results confirm that the cells cultured in 3D with Matrigel or BME may serve as a reliable *in vitro* model for the study of long-term 3D-growth of breast and prostate cancer cells, with BME SM3 spheroids being on average larger.

Using this model, we demonstrated that BSP expression was upregulated in young MDA-MB-231 spheroids as compared to 2D-cultures. In older spheroids, though, BSP expression returned to lower values. These results were first obtained with Western blot analysis using two different anti-BSP antibodies, which primarily detected either the hypo-glycosylated or the mature form of BSP. For the hypo-BSP recognizing antibody, these findings could be confirmed by immunofluorescence analysis. Previously, conditional knockdown of BSP in 2D-cell cultures was reported to cause increased apoptosis and reduced cell proliferation as well as decreased bone metastasis in a mouse xenograft model (Kovacheva et al., 2014). Thus, we first addressed a putative correlation between BSP expression and apoptosis or proliferation. With respect to apoptosis, almost no Cleaved Caspase-3 positive cells were found in 2D while at all tested spheroid ages, the fraction of apoptotic cells varied between only six and fourteen percent. Thus, there was no similarity to the BSP expression profile arguing against a simple negative correlation between BSP expression and apoptotic cell death. As for cell proliferation, a gradual decline of KI-67 positive cells was found upon prolonged culture in 3D, reminiscent of the BSP expression profile. However, proliferation was highest in the 2D-cultures, when BSP was very low. Therefore, also between BSP expression and cell proliferation a good fit was not evident.

To address further options, we next concentrated on the link between BSP and metastasis. Indeed, knockdown of BSP was shown to reduce metastatic potential of cells to bone (Kovacheva et al., 2014) and lung in mice (Nam et al., 2006). Furthermore, impairment of BSP expression decreased basal and TGF β -stimulated activation of MMPs and reduced degradation of Type-I or Type-IV collagen (Nam et

al., 2006). Amongst other processes, metastasis competence involves epithelial-mesenchymal transition (EMT) enabling migration and extravasation potential of cancer cells, as well as a homing process, where an adequate metastatic niche provides appropriate ECM-based interactions between cancer cells and target tissue. In the context of metastatic breast cancer, IGF1 and TGF β 1 are both known to be important regulators of EMT (Cevenini et al., 2018; Zarzynska, 2014). However, while IGF1 abundance is reported to correlate with both, breast cancer cell proliferation and metastatic potential (Cevenini et al., 2018), TGF β 1 is thought to promote primarily ECM and niche formation, cytoskeletal reorganization, cell motility and invasion (Cevenini et al., 2018; Zarzynska, 2014), but not cell proliferation. Indeed, according to the 'TGF β 1 paradox' concept, this cytokine acts as a potent growth inhibitor in healthy epithelia and during early tumor phases, while at later stages it promotes the metastatic process by supporting invasion of cancer cells and metastatic niche formation (Zarzynska, 2014). The data of the present study are consistent with an axis involving TGF β 1, IGF1, and RUNX2 in the joint regulation of BSP levels. However, while TGF β 1 and BSP showed rather similar expression profiles in SM3 and co-culture maturation as well as upon Paclitaxel treatment of SM spheroids, the IGF1 expression profile was similar to that of BSP only in untreated SM3 cultures. This suggests that differential pathways might be involved in the regulation of BSP expression.

2.6 Conclusion

In summary, we optimized a sandwich method for long-term culture of triple-negative MDA-MB-231 breast cancer cells in 3D and showed the influence of fibroblasts and different extracellular matrix compounds, such as Matrigel and BME, on spheroid formation. A novel human anti-BSP monoclonal antibody was characterized and found to display specificity to hypo-BSP. Using these 3D- mono- and co-cultures in different experimental paradigms, a consistent correlation between the expression of BSP and TGF β 1 could be confirmed, while there was only a partial connection of BSP abundance to apoptosis, proliferation, and IGF1.

Author Contributions

VR, FK, and JK executed, analyzed, interpreted experiments. VR wrote paper. MH and RR planned experiments, procured funding, and wrote paper.

Funding

VR was funded by the "State Program on Education of Azerbaijani Youth Abroad in 2007-2015". This work was funded by the German Federal Ministry of Research (BMBF) as part of the Innovation Partnership M²Aind, project M²OGA (03FH81021A) within the framework "Starke Fachhochschulen – Impuls für die Region" (FH-Impuls). This research project is part of the Forschungscampus M²OLIE and funded by the German Federal Ministry of Education and Research (BMBF) within the Framework "Forschungscampus: public-private partnership for Innovations".

Acknowledgements

We thank Immundiagnostik AG for gifts of BSP antibodies and Dr. Manfred Frey for providing anti-human secondary antibodies for Western blot analysis. We are greatly indebted to Patrick Williams for proofreading this paper.

Conflict of Interest Statement

Immundiagnostik AG provided anti-BSP antibodies used in the present work. This company is active partner in the public private partnership M2OGA (03FH81021A) within the framework “Starke Fachhochschulen—Impuls für die Region” (FH-Impuls) that is funded by the German Federal Ministry of Research. At no point in this study, Immundiagnostik AG interfered or influenced the work; they did not plan the experiments shown and were not involved at any point in data interpretation or writing of the manuscript.

3 ARTICLE 2: TOWARDS OPTIMIZED BREAST CANCER 3D-SPHEROID MONO- AND CO-CULTURE MODELS FOR PHARMACOLOGICAL RESEARCH AND SCREENING

An adapted version of this chapter has originally been published as open-access article distributed under the terms of the Creative Commons Attribution Non-Commercial License (CC BY-NC 4.0): “Keller, F., Rudolf, R., and Hafner, M. (2019). Towards optimized breast cancer 3D spheroid mono- and co-culture models for pharmacological research and screening. *J. Cell. Biotechnol.* 5, 89–101” (Keller et al., 2019); doi: 10.3233/JCB-199001.

As first author, the experimental design and execution, data acquisition and interpretation, as well as original draft and revised writing were done independently under the supervision of Profs. Hafner and Rudolf.

Since the application of basal membrane extract to MDA-MB-231 cultivated on cell-repellent surfaces indicated a correlation of spheroid growth and available nutrients, different media compositions were investigated. To evaluate their transferability towards co-culture modeling, common media for MDA-MB-231 human breast cancer cells and MCF10A human breast epithelial cells were tested. Furthermore, the impact of BME-supplementation on spheroid morphology and size revealed alterations in cell proliferation based on the adaption of intrinsic features of mono-culture protocols.

3.1 Abstract

Background: Reproducibility and physiological relevance are essential features for test systems used in preclinical cancer drug development. In this context, 3D-cell culture models like spheroids or organoids have recently become attractive due to their potential of mimicking native biology. Further, to increase screening throughput and effectiveness, full automation of sample preparation and data analysis is important.

Objective: This work addressed methodological factors of spheroid cell culturing that are of particular relevance for reproducibility and physiological significance in studies investigating metabolic effects of drug treatment, including media composition, extracellular matrix, addition of stromal cells, and the quality of contrast-based readouts.

Methods: Using standardized and enriched media as well as additional basal membrane extract, spheroids were made from MCF10A human breast epithelial cells and MDA-MB-231 human breast cancer cells. In addition, co-culture spheroids of MDA-MB-231 with CCD-1137Sk human fibroblast cells were prepared. Samples were compared in terms of metabolic behavior. Spheroid analysis employed SpheroidSizer software, confocal microscopy, and Western blotting.

Results: Media composition, supportive additives and the co-culture situation can massively alter the growth and metabolic behavior of spheroids. In particular, spheroid integrity was affected by the presence of extracellular matrix components and upon long-term culturing. Due to drug- or culture-induced spheroid disintegration, automated spheroid size analysis data needed careful evaluation.

Conclusion: Media composition, extracellular matrix, addition of stromal cells, and automated readouts are important parameters for standardized spheroid-based drug screening approaches. Contrast-based spheroid size analyses in automated high-throughput screenings need special attention since spheroid-disaggregation or proliferation of surrounding cells may sophisticate the readouts.

3.2 Introduction

Reproducibility and physiological relevance are particularly important for successful preclinical cancer drug development and the basis of efficient clinical trials for drug launches. Unfortunately, the number of approvals per drug entering phase-I clinical studies continuously decreased from 17 % between 1995 and 2000 (Gilbert et al., 2003) to 5 % in 2013. In that year, 409 drugs were approved while 7,872 were entering clinical studies. Presumably, owing to enhanced efforts in early stages of drug development, e.g. by augmented usage of biomarkers in drug target screenings, the success rate was recently increasing again, reaching 13.8 % in 2015 with 733 approvals out of 5,315 clinical candidates (Wong et al., 2019). However, the average cost and time for the development of a novel marketable oncologic drug have still been rising recently to 757 million USD and 7.3 years (range 5.8 - 15.2 years), respectively (Prasad and Mailankody, 2017). These numbers show the high potential for improvements in drug development pipelines. In addition, reproducibility and comparability would also be desirable in basic and applied research. However, highly specialized methods are often used in research studies, thus, creating issues in comparing their outcomes.

In 1973, the MDA-MB-231 cell line was derived from a triple-negative female breast cancer patient upon metastatic relapse that had followed mastectomy four years earlier. These cells exhibit a moderate doubling time compared to other breast cancer cell lines (Brinkley et al., 1980) and since then their culturing has been performed using several different media compositions without a clear standardization. Originally, Leibovitz L15 medium with 15 % fetal calf serum (FCS), insulin, glutathione and gentamicin was used for cultivating MDA-MB-231 cells at 37 °C in air (Brinkley et al., 1980). While the usage of 5 % CO₂ has become a standard, media composition is still diverse including alterations in FCS concentration (10-20 %), supplementation with insulin (0-10 µg / mL), glutamine (0-2 mM) and antibiotics (carbenicillin, gentamicin, amphotericin, penicillin, streptomycin). Also, the basal media have changed from Leibovitz L-15 to more common variants like DMEM or RPMI1640 (Cailleau et al., 1974; Hjortoe et al., 2004; Pillé et al., 2005; Pozo-Guisado et al., 2002; Viola et al., 2017). However, also their composition can be variable from supplier to supplier as they might contain additional amino acids, including L-glutamine (ATCC American Type Culture Collection, 2012; Cell Biolabs Inc., 2009). Finally, there is an acknowledged variability in the added serum, which in MDA-MB-231 cultures is mostly FCS. This could easily influence cellular behavior (Brinkley et al., 1980), since serum contains crucial factors altering proliferation (Rozengurt, 1992), differentiation (Schuldiner et al., 2000), and attachment (Barnes, 1986) of cells. As complex natural compounds, sera display an intrinsic variance (Baker, 2016).

Co-culturing of different cell lines affects the availability of signals and factors and therefore influences cell survival and differentiation (Ehret et al., 2015). It has been known since the 1960s (Slavkin et al., 1968), that cell-cell interactions can alter cell cultures *in vitro*. Thus, to better recapitulate the physiological situation in cell culture

models, co-cultures have always been a desirable experimental approach. However, mono-cultures are more easy to standardize and therefore more widely used to evaluate, for example, proliferative effects (Noreen et al., 2019), drug sensitivity of a tissue entity (Hafner et al., 2017a), or the metastatic potential of cancer cells (Liu et al., 2019). Conversely, co-culturing can reveal important cell-cell communication, leading to unexpected cellular responses compared to controls with single cell types (Picon-Ruiz et al., 2016). For example, co-cultures of osteoblasts with peripheral blood mononuclear cells led to segregation of extracellular matrix components which allowed to replace growth factor supplementation for bone regeneration (Hammerl et al., 2019). In co-cultures of fibroblasts and cancer cells, targeting the tumor microenvironment instead of the cancer cells alone led to improved treatment results (Valkenburg et al., 2018). This suggests that also cancer-associated fibroblasts which support tumor cells by providing metabolites and altering the tissue composition (Martinez-Outschoorn et al., 2010; Pavlides et al., 2012; Wilde et al., 2017), should be considered as drug targets.

While 2D-cell culture models were preferred for decades due to their easy and cheap preparation, 3D-cell culture models have lately experienced rising interest since they promise to better mimic the physiological conditions (Kapałczyńska et al., 2018). In particular, in 3D-cultures, the access of nutrients and oxygen (Breslin and O'Driscoll, 2013), cellular interactions (Bissell et al., 2003), mechanistic support (Mason et al., 2013), and the permeability of drugs (Graf and Boppart, 2010; LaBonia et al., 2016; Liu et al., 2013) are more similar to that in tumors than in classical 2D-cultures. Therefore, these aspects profit from investigations in three dimensions (Griffith and Swartz, 2006).

Due to their sensitivity against mechanical stress, spheroid cultures are often hard to cultivate for long time periods (Lin et al., 2008). Also, they typically exhibit disseminating or dissociated cells not contained within the core spheroid (Hsiao et al., 2012). This is strongly dependent on the method used to develop the 3D-structure of the cultures (Hongisto et al., 2013). Finally, three-dimensional cell culture in general has two major drawbacks: it is more time consuming and expensive compared to 2D-cultivation (Kim et al., 2004). For this reason, operative automation is desired. Depending on the size of enterprise, this involves cell culture handling, drug treatment, data acquisition, and segmentation-based data evaluation. While data quality is increasing continuously, automated 3D-readouts based on 2D-data achieved with widefield microscopy can lead to erroneous data interpretation. For example, the calculation of spheroid size based on simple image thresholding might overlook effects of cellular dissemination and spheroid disintegration (Boutin et al., 2018; Chen et al., 2014; Härmä et al., 2014).

3.3 Materials and Methods

3.3.1 Cell Culture

MDA-MB-231 human breast cancer cells were passaged in MDA-MB-231 medium (MDA-M) consisting of Dulbecco's Modified Eagle Medium (Capricorn, DMEM-HPA, Lot# CP18-2096) supplemented with 10 % fetal bovine serum (Capricorn, FBS-12B, Lot# CP16-1422), 1 % Minimum Essential Medium Nonessential Amino Acids (Capricorn, NEAA-B, Lot# CP17-1726) and 1 % penicillin/streptomycin (Capricorn,

PS-B, Lot# CP18-2207). CCD-1137Sk human foreskin fibroblasts were passaged in IMDM containing Iscove's Modified Dulbecco's Medium (Capricorn, IMDM-A, Lot# CP18-2245) supplemented with 10 % FBS-12B and 1 % PS-B. MCF10A media (MCF-M) consisted of Dulbecco's Modified Eagle's Medium/Nutrient Mixture F-12 Ham (Sigma-Aldrich, D8062-500mL, Lot# RNBG3907) supplemented with 5 % horse serum (Gibco, Gibco HI Horse Serum, #26050088), 20 ng / mL epidermal growth factor (Miltenyi, EGF, #130.093.825), 500 ng / mL hydrocortisone (Sigma, H-0888, Lot# 86H04185), 100 ng / mL Cholera Toxin (Sigma, C8052-.5MG, Lot# 116M4078), 10 µg / mL Insulin (SAFC, 91077C-1G, Lot# 16A145-C) and 1 % PS-B. All cell lines were passaged at 80 % confluency and seeded with 1×10^6 cells per T75 flask for MDA-MB-231 and CCD-1137Sk, and with 5×10^6 cells for MCF10A. Spheroid formation was achieved using 96-well spheroid microplates (Corning, Ref 4520, Lot# 04618014) through adding the appropriate number of cells and centrifugation for 6 min at 500 rcf. If needed, 2.5 % of basement membrane extract (BME / Cultrex, PathClear No. 3432-005-01, Lot# 41651B18) were added directly after the cells before centrifugation. For each data point, 12 replicates were made.

3.3.2 Brightfield Microscopy and spheroid size evaluation

Brightfield pictures for spheroid size estimation were captured with an Axiovert 25 (Zeiss, objective CP-ACHROMAT, 5x/0.12Ph0). For further processing, the images were exported in TIFF format and analyzed with MATLAB using the SpheroidSizer software (Chen et al., 2014).

3.3.3 Immunostainings and confocal microscopy

Cell Cultures were fixed for 30 min in 4 % paraformaldehyde (PFA) in phosphate-buffered saline (PBS). After permeabilization with 0.4 % Triton-X100 in deionized water, the samples were blocked with 3 % bovine serum albumin fraction V (BSA) in deionized water. Primary antibody incubation was performed over night at 4 °C. After washing with PBS, secondary antibodies together with dyes were applied for 2 h at room temperature. Dyes used were 2-(4-Amidinophenyl)-6-indolecarbamidine dihydrochloride (DAPI / Roche, 10236276001, Lot# 28114320) at 1:1000 dilution, and wheat germ agglutinin was diluted 1:500 (WGA / Biotium, CF488A, # 29022). Primary antibodies were used against PTEN (Proteintech, AB9260, Lot# 2; 1:100), LC3 (CellSignalling, 3868S, Lot# 11; 1:200), MCT4 (SantaCruz Biotechnology, sc-376140, Lot# D3018; 1:400), KI67 (Merck, AB9260, Lot# 3094997; 1:500). Secondary antibodies goat anti-Mouse alexa fluor 488 (Invitrogen, A11001, Lot# 1834337) and goat anti-Rabbit 647 (Invitrogen, A21246, Lot# 55002A) were diluted 1:1000. Confocal microscopy was performed with an inverted Leica SP8 (Leica Microsystems) equipped with HC PL APO 20 x /0.75 IMM CORR and HC PL APO CS2 63 x /1.2 W CORR objectives. The visualization was achieved with the Leica LAS-X 3.3.0 software suite and the image capturing was set to 1024 x 1024 pixels resolution with 3 times frame average and a pinhole of 1 airy unit. Z-step size in 3D-stacks was 1 µm. All images used for direct comparison were taken at the same day with identical settings of laser, gain and pinhole. For the quantification of specific signals, the overall intensity divided by the total area was normalized on the supplement-rich MCF-M without added BME while seeding.

3.3.4 Western Blotting

Protein extraction was achieved with 1 h incubation of trypsinated cells in lysis buffer (50 mM Tris-HCl, 150 mM NaCl, 1 % NP-40 (AppliChem, A1694) with 10 % glycerol, 1 mM EDTA, 1 mM EGTA, 1x protease inhibitor cocktail (Roche, #88665) and 0.5 mM PMSF (AppliChem, A0999) on ice), before heating to 99 °C for 7 min after addition of Laemmli buffer. The amount of protein was measured with a BCA assay (ThermoScientific, 23225, Lot# SI256196) and 30 µg of each probe were subjected to a 10 % SDS-PAGE followed by Western blot analysis. The used primary antibodies were specific for light-chain 3 (1:1000 / LC3 / rabbit anti-LC3B mAb / Cell Signaling, #3868S, Lot# 11) or Glyceraldehyde-3-phosphate dehydrogenase (1:10000 / GAPDH / mouse anti-GAPDH mAb / Thermo Fisher, MA5-15738). Secondary antibodies were diluted 1:10000 and goat anti-rabbit IgG (H+L) HRP (Jackson Immuno Research, 111035003) together with goat anti-Mouse IgG (H+L) HRP (Thermo Fisher, #32430) were utilized. Gels were developed with Western Bright Chemilumineszenz Substrat Sirius (Biozym, 541020, Lot# 180829). Pictures captured with a G:Box (Syngene, model Chemi XX6) and evaluated using ImageJ software (v1.48v). Biological triplicates were made, and each data point was technically analyzed three times.

3.3.5 Statistics

For statistics GraphPad Prism 7 was used applying one-way ANOVA and multiple comparison based on the raw data. Normal distribution and homoscedasticity were tested using Kruskal-Wallis and F-test, respectively. All graphs show mean values and standard deviation. Significance was as indicated (* P < 0.05, **** P < 0.0001).

3.4 Results

To evaluate the effect of different media on the spheroid growth of highly metastatic MDA-MB-231 breast cancer cells and non-tumorigenic MCF10A breast gland epithelial cells, media tests were performed with each cell line. These tests included incubation in poorly or richly supplemented MDA-M and MCF-M media, respectively, and in the absence or presence of BME as extracellular matrix compound. Brightfield microscopy revealed large differences in all culture conditions. First, MDA-MB-231 spheroids were generally larger and more compact than those made of MCF10A cells (Fig. 17A and C). This was particularly true in the presence of BME, where MDA-MB-231 spheroids were perfectly round and solid (Fig. 17A), while MCF10A cultures formed core spheroids with numerous satellite spheroids around (Fig. 17C). In the absence of BME, spheroids of both cell lines were considerably smaller, and the cultures showed numerous disseminated cells. Furthermore, both cell lines displayed the best growth in richly supplemented MCF-M (Fig. 17B and D; Tab. 2). This data suggests that there is a synergistic effect of ECM components and metabolically relevant supplements on spheroid compactness and growth.

To address the effects of media composition on spheroid growth from a metabolic point of view, MDA-MB-231 spheroids cultured under these different conditions were stained for the marker protein Phosphatase and Tensin Homolog (PTEN). This protein is a negative regulator of the phosphoinositide 3-kinase Akt (PI3K / Akt) signaling pathway and, thus, usually correlating inversely with cellular activity (Maehama and Dixon, 1998). As expected, immunofluorescence staining of spheroids cultured nine days *in*

vitro (9 DIV) showed different PTEN gene expression levels depending on media composition and presence of BME within the culture (Fig. 18). Quantitative analysis of PTEN fluorescence signal intensity per area revealed the highest values in spheroids cultured in MCF-M without BME. Upon normalization of this data point to 100 %, PTEN immunofluorescence signal intensities from cultures in MDA-M or MCF-M with BME reached significantly lower numbers, more precisely $37.2 \% \pm 4.4 \%$ (mean \pm SD) or $42.0 \% \pm 8.1 \%$ (mean \pm SD), respectively. In summary, these data suggest that in MDA-MB-231 spheroids PTEN expression is positively and negatively affected by metabolically active supplements and by BME, respectively.

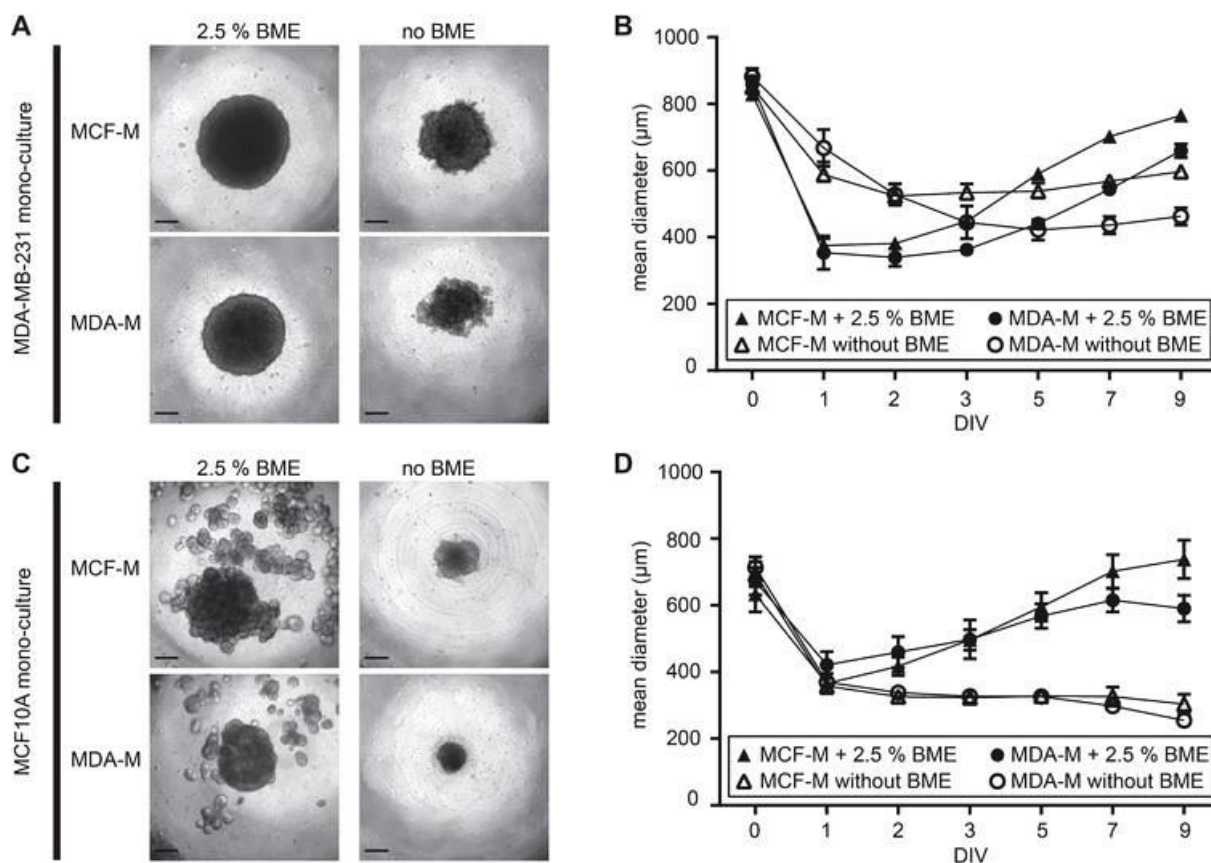


Figure 17. Supplements of media and extracellular matrix components massively alter compactness and growth of breast cancer and epithelial spheroid cultures. MDA-MB-231 breast cancer and MCF10A breast epithelial cells were cultured in ultra-low attachment plates for up to 9 DIV using either rich media designed for MCF10A cells (MCF-M) or poor media for MDA-MB-231 cells (MDA-M) and in the absence or presence of BME. A, C), brightfield micrographs of MDA-MB-231 (A) or MCF10A (C) after 9 DIV. Scale bars, 200 μ m. B, D), quantitative analysis of spheroid-areas. Depicted are mean areas \pm SD as a function of DIV. For each data point, at least 12 spheroids were analyzed. (Keller et al., 2019)(CC BY)

To further deepen the insights into the role of extracellular matrix components on MDA-MB-231 spheroid compactness and to assess the possibility to co-culture these cells with fibroblasts, we next performed comparative assays of MDA-MB-231 mono-cultures and co-cultures with fibroblasts (Rustamov et al., 2019) in the presence or absence of BME. To find an experimental paradigm that allows quantitative comparisons, we first looked for seeding densities delivering approximately equal

spheroids areas right after the condensation and just before the linear growth phase, i.e. at 4 DIV. From 125 to 16,000 seeded cells per well were tested.

Table 2. Comparison of mean diameters in 3D-spheroid cultures at 9 DIV. Spheroid diameters are mentioned in the corresponding condition cell, P-values upon comparison between different culture conditions are shown in crossing fields.

MCF10A				
	MCF-M + BME 738.6±58.0 µm	MCF-M 303.8±29.4 µm	MDA-M + BME 590.1±40.7 µm	MDA-M 254.8±11.2 µm
MCF-M + BME 738.6±58.0 µm		****	****	****
MCF-M 303.8±29.4 µm	****		****	****
MDA-M + BME 590.1±40.7 µm	****	****		****
MDA-M 254.8±11.2 µm	****	****	****	

MDA-MB-231				
	MCF-M + BME 768.4±15.4 µm	MCF-M 596.7±20.4 µm	MDA-M + BME 659.9±19.9 µm	MDA-M 462.5±26.3 µm
MCF-M + BME 768.4±15.4 µm		****	****	****
MCF-M 596.7±20.4 µm	****		****	****
MDA-M + BME 659.9±19.9 µm	****	****		****
MDA-M 462.5±26.3 µm	****	****	****	

(Keller et al., 2019)(CC BY)

Notably, for all used cell densities, co-cultures of MDA-MB-231 cells with fibroblasts were smaller than corresponding MDA-MB-231 mono-cultures using the same amounts of MDA-MB-231 cells. This revealed an ideal seeding density of 8,000 cells per well in mono-cultures and 10,000 cells per type for co-cultures of MDA-MB-231 and CCD-1137Sk (thus, a total of 20,000 cells). A detailed view on spheroids after 4, 7, 14, and 21 DIV revealed clear differences in long-term cultivation (Fig. 19A). While MDA-MB-231 mono-cultures supplemented with BME generated firm and stable spheroids with consistent growth for at least two weeks (Fig. 19A and C), MDA-MB-231 plus fibroblast co-cultures also supported spheroid formation in the absence of BME (Fig. 19A), but albeit the higher initial seeding density, the co-culture spheroids were growing more slowly and into significantly smaller cores (Fig. 19C) with many surrounding disseminating cells (Fig. 19A). In the absence of BME, mono-culture spheroids were fragile and also showed many disseminating or dissociated cells (Fig. 19A). As a consequence of the observed dissemination or dissociation effects, automated spheroid area recognition based on the contrast of brightfield pictures indicated larger spheroid areas compared to manual segmentation in these two conditions (see Fig. 19B for an example of co-culture analysis). This difference

between core spheroid and surrounding dissociated cells increased as a function of DIV. Thus, the spheroid integrity defined as manually segmented core spheroid area divided by automatically segmented area significantly decreased over time, especially for co-cultures (Fig. 19D) and mono-cultures in the absence of BME (data not shown).

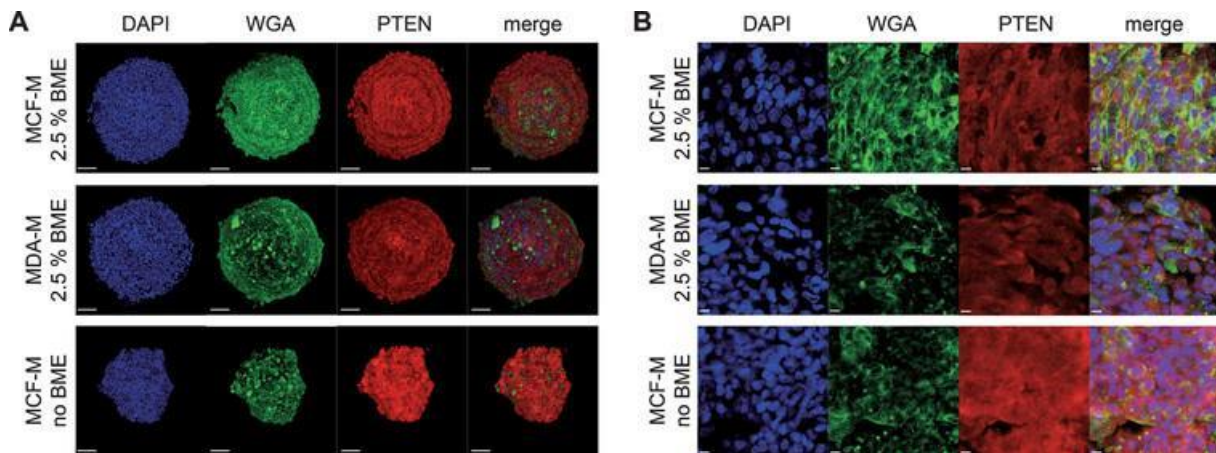


Figure 18. Addition of BME strongly alters PTEN expression level in MDA-MB-231 spheroids. MDA-MB-231 cells were cultured in ultra-low attachment plates for 9 DIV using either rich media designed for MCF10A cells (MCF-M) or poor media for MDA-MB-231 cells (MDA-M) and in the absence or presence of BME. Then, whole mount spheroid staining was done using DAPI, WGA, and anti-PTEN antibodies to label nuclei (blue), cell membranes (green), and PTEN protein (red). Spheroids were then imaged using confocal microscopy. Panels depict maximum-z projections (A) or single optical slices (B) from samples as indicated. (Keller et al., 2019)(CC BY)

To investigate, whether co-culturing also affected metabolic characteristics, we compared the autophagic activity in MDA-MB-231 mono-cultures to that of MDA-MB-231 plus fibroblast co-cultures. Upon normalization to the loading control GAPDH, Western blot analysis of MDA-MB-231 and CCD-1137Sk in 2D-mono- and co-cultures yielded enhanced LC3-II bands (Fig. 20A). LC3-II is a principal active component in cells that undergo autophagy (Kabeya et al., 2000). This finding was confirmed by quantitative analysis, where MDA-MB-231 cells and fibroblasts in mono-culture resulted in ratios of 0.66 ± 0.02 and 0.72 ± 0.01 respectively, whereas co-cultivation of these cell types resulted in ratios of 1.47 ± 0.05 in 2D- and 1.31 ± 0.03 in 3D-spheroid cultures (Fig. 20A and B). Immunofluorescence staining of LC3 and a marker of enhanced lactate shuttling, i.e. MCT4, corroborated the Western blot data. Fluorescence micrographs from the co-culture model showed the highest LC3 and MCT4 signals, followed by cancer cells in mono-culture and fibroblasts (Fig. 20C) with relative signal intensities of 60.4 ± 6.9 % (MDA-MB-231) or 40.8 ± 4.4 % (fibroblasts) for LC3 and 68.4 ± 6.7 % (MDA-MB-231) or 24.2 ± 3.2 % (fibroblasts) for MCT4.

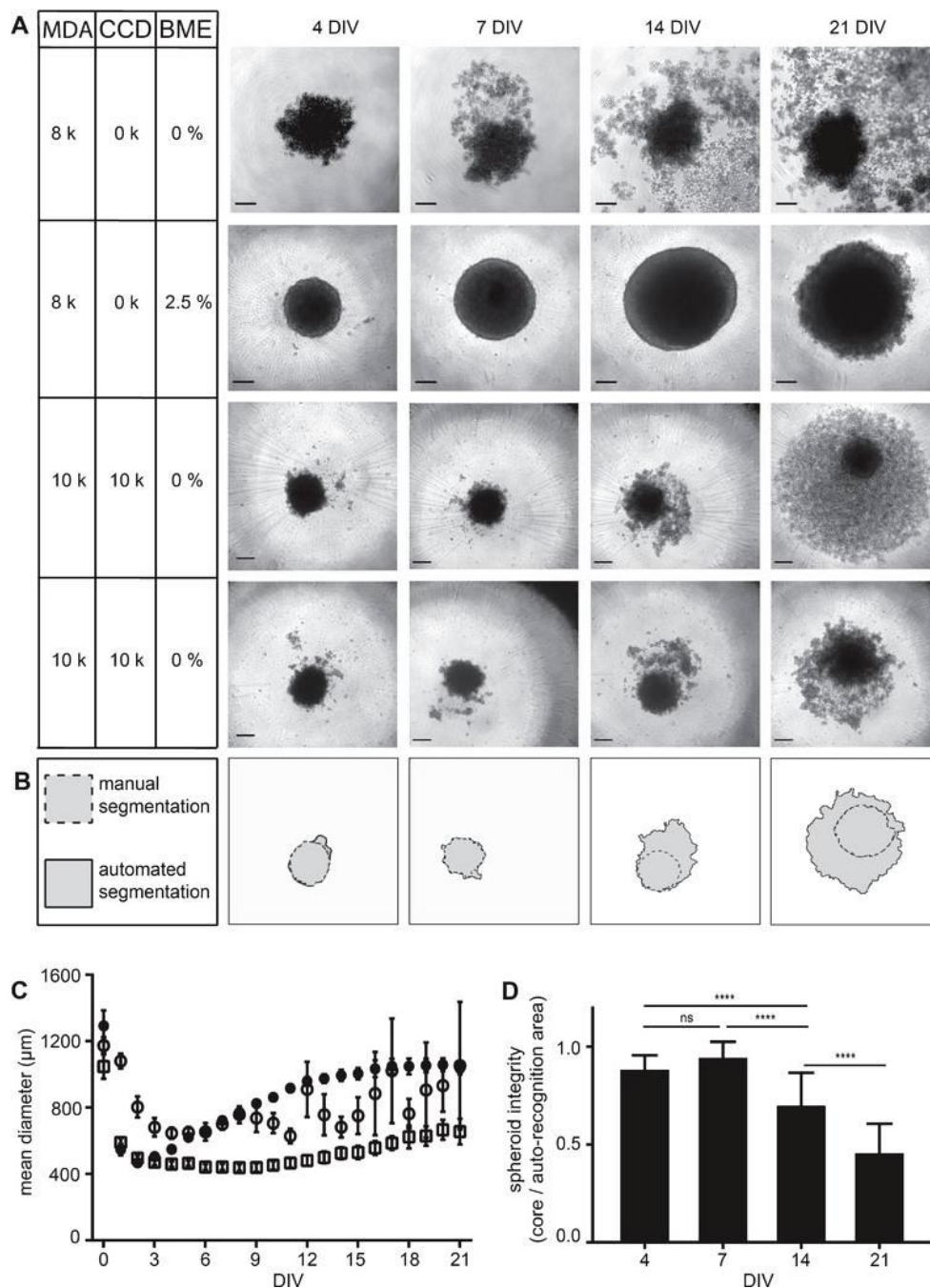


Figure 19. MDA-MB-231 spheroid integrity is preserved in the presence of BME and partially also achieved by co-culturing with CCD-1137Sk fibroblasts. MDA-MB-231 breast cancer cells were either cultured alone in ultra-low attachment plates for up to 21 DIV using MDA-M in the absence or presence of BME or in co-culture with CCD-1137Sk human fibroblasts in the absence of BME. A) Brightfield micrographs of spheroids at 4, 7, 14, and 21 DIV under culture conditions as indicated with cell lines MDA-MB-231 (MDA) and CCD-1137Sk (CCD) supplemented with basal membrane extract (BME). For co-cultures, two data sets are shown to illustrate the variability in spheroid disintegration. Scale bars, 200 μm . B) Difference between automated (solid outline) and manual segmentation (dashed outline) using SpheroidSizer as illustrated on the lower panels in (A). C) Quantitative analysis of spheroid diameters as a function of DIV. Depicted are mean values \pm SD. For each data point, at least 12 spheroids were analyzed. D) Quotient of manually versus automatically segmented spheroid areas as a measure of spheroid integrity. Depicted are mean values \pm SD. For each data point, at least 40 spheroids were analyzed. (Keller et al., 2019)(CC BY)

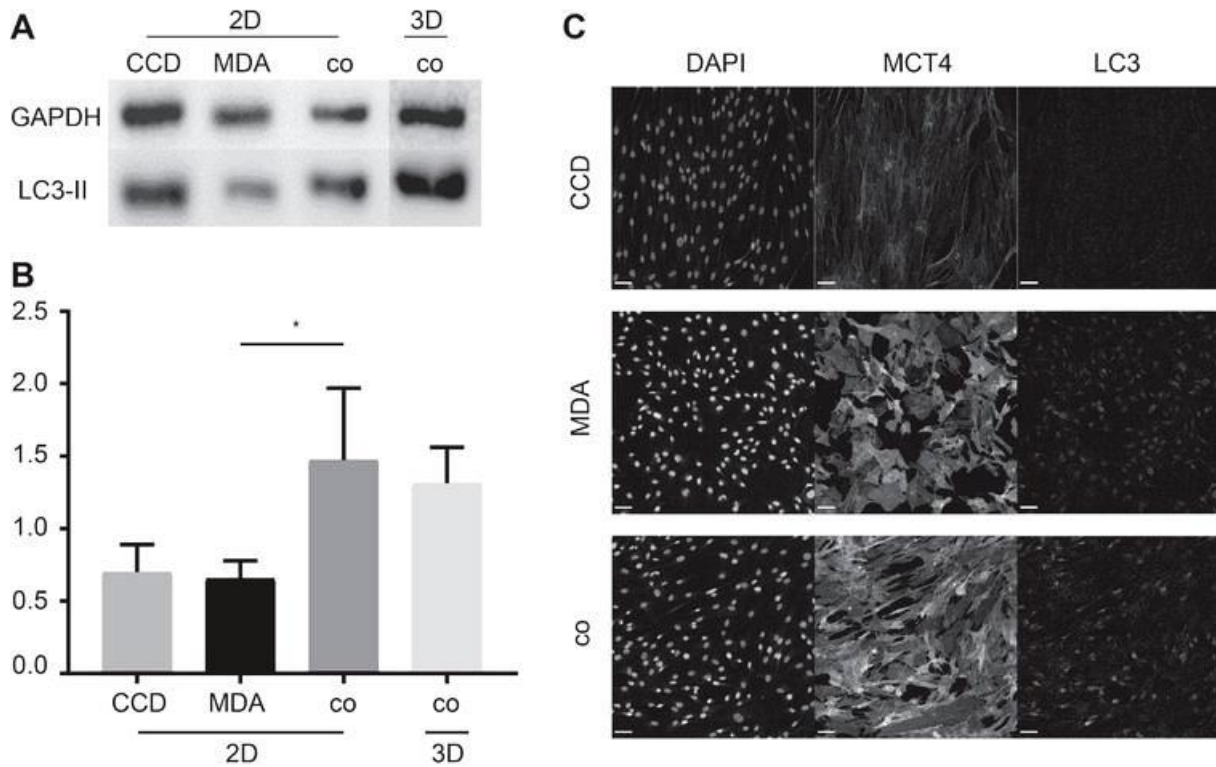


Figure 20. Co-cultures of MDA-MB-231 and CCD-1137Sk cells exhibit higher levels of LC3-II and MCT4 expression. MDA-MB-231 breast cancer cells and CCD-1137Sk fibroblasts were either cultured alone as adherent cultures (2D) or co-cultured in 2D (2D) or in ultra-low attachment plates (3D) for 4 DIV. Then, cells were analyzed by Western blot (A-B) or immunofluorescence (C). A) Representative Western blot bands upon staining against LC3-II or GAPDH. B) Quantitative analysis of LC3-II band intensities upon normalization to GAPDH. Depicted are mean + SD. At least 3 experimental replicates were made. C) Confocal images of representative 2D-regions stained for nuclei (DAPI), MCT4, and LC3. Scale bars, 100 μ m. (Keller et al., 2019)(CC BY)

3.5 Discussion

Tissue-specific cell culture models are crucial for phenotypic drug screenings. In this context, co-culturing cancer cells with stromal cells can increase the physiological relevance of such models, e.g. to achieve different cellular subpopulations that may affect proliferation rates or drug resistance within the whole culture (Burguera et al., 2010; Yamaguchi et al., 2014). Furthermore, 3D-cultures are often considered to better mimic the physiological conditions (Langhans, 2018). Here, we addressed aspects that can help to avoid unwanted heterogeneity of data between different experimental 3D-cell culture paradigms. This showed that media composition, supportive additives, the co-culture situation, and post-processing data analysis are critical features in the setup of 3D-cancer cell models.

First, we focused on the establishment of breast-tissue specific 3D-spheroid models made of, either, the human breast cancer cell line MDA-MB-231 (Cailleau et al., 1974) or the non-tumorigenic breast epithelial cell line MCF10A (Soule et al., 1990). Identification of a media composition that would be useful for both cell lines would have allowed to co-culture these cells and, thus, to test cell type specific activities of drugs or other treatments. With respect to spheroid integrity and size, this showed a strong

dependency of both cell types on the presence of BME, whereas the supplementation with insulin and metabolism-stimulating factors included in the MCF-M appeared to be less critical but only led to subtle size differences. This suggests that co-cultures between MDA-MB-231 and MCF10A cells should be possible upon addition of BME, perhaps because this adds important growth stimuli or due to its delivery of extracellular matrix components.

To differentiate between these two options, we continued to culture MDA-MB-231 cells either as mono-cultures using different media compositions and tested their metabolic activity or co-cultured them with fibroblasts that should be capable of supplying extracellular matrix. With respect to the first approach, the data pointed to a negative correlation between the expression of PTEN and the richness of the tested media. Given that PTEN is a known down-regulator of Akt/mammalian target of rapamycin (Akt / mTOR) signaling pathway, which, in turn, is linked to active metabolism, these results appeared counter-intuitive at first sight. However, they might suggest that strong activating external signals could lead to negative feedback mechanisms, e.g. via USP11, which is known to antagonize Akt/mTOR signaling by upregulation of PTEN (Park et al., 2019). This could improve homeostasis and prevent a tissue from consuming its nutrient stock within a short time (Edinger, 2007). Indeed, previous work showed that PTEN expression can be high in early stages of cancer tissue, while in later stages a down-regulation of PTEN compared to PI3K leads to over-activation of the Akt/mTOR pathway supporting tumor growth and metastasis (Zeleniak et al., 2018). For the present study, the most important conclusion from these results was the confirmation, that it is crucial to check common media compositions with respect to their effects on metabolic activity before co-culturing different cell lines.

The second point, i.e. the role of extracellular matrix for the formation and growth of MDA-MB-231 spheroids, was investigated using co-cultures with CCD-1137Sk fibroblasts. This yielded mixed results. On the one hand, in the absence of BME, the formation of spheroids was superior in co-cultures of MDA-MB-231 and fibroblasts when compared to MDA-MB-231 mono-cultures. On the other hand, fibroblast co-cultures could not compensate for the lack of BME with respect to speed of formation, roundness, growth, and long-term integrity of spheroids. Indeed, in the absence of BME, co-culture spheroids took longer to condense, grew less, and disintegrated more rapidly over time than BME-treated MDA-MB-231 mono-cultures did. This strongly suggests that BME, besides its supply of extracellular matrix components, also delivers further, yet undefined, factors that are beneficial for spheroid morphology. Notably, MDA-MB-231 plus fibroblast co-cultures were smaller than MDA-MB-231 mono-cultures using the same amounts of MDA-MB-231 cells. Indeed, at DIV 4, co-culture spheroids using 10,000 fibroblasts plus 10,000 MDA-MB-231 cells were just roughly the same size as mono-cultures prepared from only 8,000 MDA-MB-231 cells. Since at this early time point, major effects on cell proliferation might not be expected, there are currently three potential scenarios to explain this observation. First, the co-culture could have led to death of MDA-MB-231 cells, but we could not find signs of many dead cells at DIV 4. Second, it could be that MDA-MB-231 cells were hindered by the fibroblast cells to integrate into the spheroid culture, but also for this option we have no indication. Finally, fibroblasts might have led to a higher compaction of MDA-MB-231 cells. To get further insights into these questions, a future study might aim at counting cells per type.

Considering the aforementioned uncertainties with co-cultures, one might argue that it is preferable to use MDA-MB-231 mono-cultures for future drug screening studies. However, although spheroid integrity is certainly an important feature for the ease of data extraction (see below), cellular signaling between different cell types might also be of importance for gauging potential drug efficacy *in situ*. For example, increasing evidence suggests that there is a metabolic interplay between cancer and stroma cells in tumors (Denton et al., 2018) that might serve as a target for metabolism-specific drugs (Fu et al., 2017). One line of research in this field proposes that cellular signaling in tumors can lead to an anabolic switch in stromal fibroblasts, which would result in the production of lactate and its potential export to feed neighboring anabolic cancer cells (Martinez-Outschoorn et al., 2011). This knowledge was recently harnessed for drug-induced metabolic tuning to drive the tumor into a critical energy-depleted state, in which it is more susceptible to low doses of classical chemotherapeutic treatments (Maycotte and Thorburn, 2011). Thus, such combination therapies could exploit tumor-specific metabolic alterations for an enhanced therapeutic efficacy and reduced negative side effects by chemotherapeutics. However, *in vitro* test systems can apparently only mirror such complex interaction if the associating cell types are available. Thus, albeit the aforementioned limitations of cancer cell-fibroblast co-cultures, these can be necessary for the analysis of such combinatorial effects. Indeed, our experiments showing differential levels of LC3-II, a marker of autophagic activity, and of MCT4, a marker of lactate shuttling, in MDA-MB-231 plus fibroblast co-cultures compared to mono-cultures supported this point.

Finally, as for many other studies, also the presented data on spheroid morphology clearly showed gross differences in spheroid integrity, both, over time as well as when comparing different culture modalities. Therefore, we strongly suggest considering spheroid integrity as an indicator for spheroid-based data analysis. One way of dealing with the issue of disaggregation and unmet readout quality could be the implementation of random manually analyzed spot tests of core spheroid segmentations. If the integrity drops below a defined threshold value, this will indicate that fully automated analysis using e.g. SpheroidSizer software or other comparable contrast-based algorithms needs to be critically re-evaluated.

Author Contributions

FK did the experiments and wrote the paper under the supervision of RR and MH that both participated the studies through help at planning and interpretation of the investigations.

Funding

This work was funded by the German Federal Ministry of Research (BMBF) as part of the Innovation Partnership M2Aind (03FH8I01IA) within the framework "Starke Fachhochschulen – Impuls für die Region" (FH-Impuls). This research project is also part of the Forschungscampus M2OLIE and funded by the German Federal Ministry of Education and Research (BMBF) within the "Framework Forschungscampus: public-private partnership for Innovations". At no point in the study did the funding agencies influence the design of the study, the collection, analysis, or interpretation of data, nor the writing of the manuscript.

Acknowledgments

We thank Richard Schneider and Julia Meier-Hubberten of Merck KGaA in Darmstadt, Germany, for providing the cell line MDA-MB-231 and for many fruitful discussions.

Conflicts of Interest

The authors declare no conflict of interest.

4 ARTICLE 3: ROUTINE OPTICAL CLEARING OF 3D-CELL CULTURES: SIMPLICITY FORWARD

An adapted version of this chapter has originally been published as open-access article distributed under the terms of the Creative Commons Attribution License (CC BY): “Nürnberg, E., Vitacolonna, M., Klicks, J., von Molitor, E., Cesetti, T., Keller, F., Bruch, R., Ertongur-Fauth, T., Riedel, K., Scholz, P., et al. (2020). Routine Optical Clearing of 3D-Cell Cultures: Simplicity Forward. *Front Mol Biosci* 7, 20” (Nürnberg et al., 2020); doi: 10.3389/fmolb.2020.00020.

As personal contribution, a stable transfection of ECFP-fluorescent MDA-MB-231 cells was independently acquired and microarray co-cultures together with CCD-1137Sk fibroblasts were established for appropriate testing of the different clearing protocols defined by the equally contributing first authors (E. Nürnberg and M. Vitacolonna). After staining and clearing the corresponding samples, data analysis was realized following the example (Fig. 26) set by the writing authors and interpreting the outcome was supported during group discussions under the supervision of Profs. Hafner and Rudolf.

This work focused on identifying adequate optical tissue clearing protocols for whole mount analysis of 3D-cell cultures. Robust and simple methods that enable cell-specific readouts in thick samples were desired. Optical tissue clearing is a field of life science technologies that turns normally opaque tissue and 3D-cell cultures into optically transparent samples. This enables the qualitative and quantitative analysis of fluorescence signals of an entire 3D-sample using 3D-microscopy and without tedious and error-prone tissue slicing. A major aspect of all optical tissue clearing techniques is to reduce refractive index mismatches inside the sample. This has been achieved by different means, often by replacing water with higher refractive index media. Depending on the used chromophores, thickness of the sample, and cell type composition, different optical tissue clearing protocols might be more adequate. This study revealed that glycerol incubation yielded a fair tissue clearing over a broad range of cell types, chromophores, and culture modes. Therefore, this protocol was used for all subsequent studies.

4.1 Abstract

Three-dimensional cell cultures, such as spheroids and organoids, serve as increasingly important models in fundamental and applied research and start to be used for drug screening purposes. Optical tissue clearing procedures are employed to enhance visualization of fluorescence-stained organs, tissues, and three-dimensional cell cultures. To get a more systematic overview about the effects and applicability of optical tissue clearing on three-dimensional cell cultures, we compared six different clearing/embedding protocols on seven types of spheroid and chip-based three-dimensional cell cultures of approximately 300 μm in size that were stained with nuclear dyes, immunofluorescence, cell trackers, and cyan fluorescent protein. Subsequent whole mount confocal microscopy and semi-automated image analysis were performed to quantify the effects. Quantitative analysis included fluorescence signal intensity and signal-to-noise ratio as a function of z-depth as well as segmentation and counting of nuclei and immunopositive cells. In general, these analyses revealed five key points, which largely confirmed current knowledge and were

also quantified in this study. First, there was a massive variability of effects of different clearing protocols on sample transparency and shrinkage as well as on dye quenching. Second, all tested clearing protocols worked more efficiently on samples prepared with one cell type than on co-cultures. Third, z-compensation was imperative to minimize variations in signal-to-noise ratio. Fourth, a combination of sample-inherent cell density, sample shrinkage, uniformity of signal-to-noise ratio, and image resolution had a strong impact on data segmentation, cell counts, and relative numbers of immunofluorescence-positive cells. Finally, considering all mentioned aspects and including a wish for simplicity and speed of protocols – in particular, for screening purposes – clearing with 88 % glycerol appeared to be the most promising option amongst the ones tested.

4.2 Introduction

In the human body, cells grow in clusters, organizing themselves into function-specific tissues and multifunctional organs in all three spatial dimensions. Since *in vitro* mono-layer cell cultures do not sufficiently reflect this attribute, they have often been considered to be limited in representing the physiology of organs and tissues (Hafner et al., 2017b; Imamura et al., 2015). In two-dimensional (2D) cell culture models, the lack of comprehensive interaction among cells via cell-cell contacts and between cells with their surrounding extracellular matrix (ECM) can lead to non-physiological morphology, gene expression, and cellular behavior (Luca et al., 2013; Zschenker et al., 2012). The absence of nutrient and oxygen gradients, as well as restricted migration potential when grown on a plastic surface, further contribute to a limited representation of physiology in 2D-*in vitro* systems (Duval et al., 2017). During the last decade, there has been a substantial increase in the use of three-dimensional (3D) cell culture models in a large variety of biological fields, ranging from developmental biology (Lancaster et al., 2013) to oncology (Drost and Clevers, 2018; Fong et al., 2016) and drug discovery (Alepee et al., 2014).

Coarsely, 3D-*in vitro* models can be divided into matrix-supported and matrix-free models (Wang et al., 2014). Amongst others, hydrogels, decellularized matrices, porous polymers, and nanofibers might serve as scaffolds in static or dynamic experimental setups that can be designed (Carvalho et al., 2017; Das et al., 2015), e.g. in organ-on-a-chip systems (Bauer et al., 2017; Hübner et al., 2018). With respect to matrix-free 3D-cultures, spheroids are common due to their ease and reliability of production. Currently, numerous 3D-spheroid models for tissues like skin and its pathological conditions (Chiricozzi et al., 2017; Klicks et al., 2019), tumor (Shroyer, 2016), intestine (Pereira et al., 2016), skeletal muscle (Khodabukus et al., 2018) or brain (Lee et al., 2017) are available.

Despite the widespread usage of 3D-cell culture models, there is much potential for optimization in related analytical downstream processes. The analysis of cell type or marker protein distribution in fixed frozen or paraffin-embedded biological 3D-samples typically uses tissue sectioning followed by immunohistological staining, and confocal laser scanning microscopy (CLSM). Due to the time-consuming preparation, potential loss of tissue sections, and the cumbersome reconstruction of spatial 3D-information, such samples are mostly analyzed only partially (Berlanga et al., 2011; Leong, 2004; Marchevsky and Wick, 2015). In addition, this method is destructive and not compatible with high throughput. In samples with homogeneous distribution of cells and effects, this technique might yield representative results (Grootjans et al., 2013; Laugisch et

al., 2019; Roelofs and De Bari, 2019; Rohe et al., 2018). However, heterogeneous distribution of different cell types or effects in more complex *in vitro* culture models, such as tumor co- or tri-cultures or stem cell-derived organoids, might yield non-representative data upon classical sectioning (Renner et al., 2017; Wu and Swartz, 2014). To circumvent these issues, *in toto* immunofluorescence of the intact sample followed by whole mount imaging with confocal or light sheet microscopy can be used (Mertz, 2011). However, penetration of light into biological samples is usually limited to around 50 – 70 μm . Primarily, this is due to light scattering caused by refractive index (RI) mismatches at the interfaces between biological tissue components, such as proteins, water, and lipids (Schmitt and Kumar, 1998). Accordingly, reduction of RI mismatches renders biological tissues optically transparent. Several different optical tissue clearing methods have been developed in the recent years, aiming to improve optical transparency and thus enable fluorescence imaging deep within tissues (Silvestri et al., 2016; Tainaka et al., 2016). Methods based on organic solvents, such as BABB (benzyl alcohol, benzyl benzoate) (Dodt et al., 2007), 3DISCO (3D-imaging of solvent-cleared organs) (Erturk et al., 2012), iDISCO (immunolabeling-enabled three-dimensional imaging of solvent-cleared organs) (Renier et al., 2014) and uDISCO (ultimate DISCO) (Pan et al., 2016) are based on combinations of dehydration, delipidation, and homogenization of RI at around 1.55. Although fast, extensive removal of lipids can be detrimental (Ariel, 2017). Furthermore, tissue shrinkage and the use of toxic chemicals, which can affect fluorophore stability, are of disadvantage. Conversely, water-based high-RI solutions provide a more protein-friendly environment and do not affect fluorophore stability as much as organic solvents. Here, RIs of approximately 1.44 – 1.48 can be achieved by using high concentrations of sugars, such as sucrose or fructose (Hou et al., 2015; Ke et al., 2013, 2016; Tsai et al., 2009). However, these solutions often exhibit a high viscosity. Commercially available ready-to-use tissue clearing products, such as FocusClear (Chiang et al., 2002) and RapiClear (Chen et al., 2019) are convenient but costly. Furthermore, aqueous high-RI solutions often display limited clearing efficiency in larger tissues, making them more adequate for smaller structures, such as spheroids, organoids, or tissue slices (Ariel, 2017). In contrast to these methods, hyperhydrating clearing protocols reduce the RI of tissue to $\sim 1.38 - 1.48$ and often employ removal of lightscattering molecules. For example, the *Scale*-method (Hama et al., 2011) uses a combination of delipidation, maintenance of the aqueous environment, and urea-mediated tissue hydration, which partially denatures and hydrates high-RI proteins (Richardson and Lichtman, 2015). Implementation of amino alcohol-mediated tissue decolorization shortened clearing times, leading to methods such as *Scale*CUBIC (*Scale* clear, unobstructed brain imaging cocktails and computational analysis) (Susaki et al., 2014) and *Scale*S (sorbitol-based *Scale*) (Hama et al., 2015). Detergent-free hyperhydrating clearing methods (Kuwajima et al., 2013) make use of gradients of aqueous formamide solutions (Clear^T), or formamide and polyethylene glycol (Clear^{T2}). To prevent excessive protein-loss by strong detergents or masking of epitopes by protein-denaturation, tissue transformation methods, such as SWITCH (system-wide control of interaction time and kinetics of chemical) (Murray et al., 2015), CLARITY (clear lipid-exchanged acrylamide-hybridized rigid imaging/immunostaining/*in situ* hybridization-compatible tissue-hydrogel) (Chung et al., 2013), and its derivatives (Yang et al., 2014) include embedding of tissue into a gel-like structure. Despite their great clearing performance, clearing time can vary and technical implementation is complex.

While most available clearing methods were established and optimized in whole organs and tissues, they have recently also been implemented into the analytical

pipelines with 3D-cell culture models (Chen et al., 2013, 2019, 2016c; Costa et al., 2018b; Desmason et al., 2018; Dingle et al., 2015; Grist et al., 2016; Kabadi et al., 2015; Masson et al., 2015; Schmitz et al., 2017; Smyrek and Stelzer, 2017; Wenzel et al., 2014). As for organs (Xu et al., 2019), alterations in optical clearing efficiency between different cell types/lines were also observed in 3D-*in vitro* systems (Boutin et al., 2018; Dingle et al., 2015), but systematic studies in that respect have been missing. Therefore, our aim was to compare different optical clearing protocols on a set of spheroids and complex 3D-co-culture systems with respect to maintenance of sample integrity, clearing efficiency, and downstream automated analysis.

4.3 Material and Methods

4.3.1 Cell Culture

To investigate the influence of optical tissue clearing protocols on cells of different origin and 3D-cultivation methods, a total of seven tumorous and non-malignant cell lines was chosen for the generation of mono- and tri-culture spheroids, and a microcavity array-based co-culture model: human keratinocyte cell line HaCaT, human induced pluripotent stem cell-derived neural precursor cells B7_033#1NPC1, human fibroblast cell line CCD-1137Sk, colorectal adenocarcinoma-associated HT-29 cells, human tongue cell line HTC-8, melanoma cell line SK-MEL-28, and the stably transfected, breast cancer-associated cell line MDA-MB-231-ECFP. All cell lines were repeatedly authenticated by phenotypic analysis and regularly tested for mycoplasma.

4.3.2 Spheroid generation

For all mono- and tri-culture spheroids used in this study, the appropriate amounts of cells were seeded onto ultra-low attachment (ULA) 96-well U-bottom plates (Corning) in their corresponding medium and centrifuged at 300 rpm for 5 min. All cells were maintained in a humidified incubator at 37 °C and 5 % CO₂ and, with the exception of a melanoma tri-culture model, kept in culture until reaching a diameter of ~ 300 µm.

HaCaT spheroids

The human keratinocyte cell line HaCaT (B.R.A.I.N. AG) was cultured in Dulbecco's Modified Eagle Medium (DMEM) (Capricorn) supplemented with 1 % penicillin/streptomycin (Pen/Strep, Sigma-Aldrich) and 10 % fetal bovine serum (FBS, Capricorn). For spheroid generation, cells were detached using Trypsin/EDTA (Sigma-Aldrich) and seeded onto 96-well ULA plates at a concentration of 9×10^3 cells per well. A diameter of ~ 300 µm was reached after four days of cultivation.

B7_033#1NPC1 spheroids

The human iPSC-derived B7_033#1 NPC1 line was kindly provided by S. Horschitz (Hector Institute for Translational Brain Research, Mannheim, Germany) and cultured in DMEM/Ham's F12 + GlutaMAX supplemented with 1 % N2 and 2 % B27 supplements, 1 % GlutaMAX, 1 % Minimum Essential Medium Nonessential Amino Acids (MEM-NEAA, all Invitrogen), 1 % Pen/Strep and 20 ng / mL FGF-2_Type 147 (Cell Guidance Systems). For spheroid generation, cells were detached using TrypLE (Invitrogen) and seeded onto 96-well ULA plates at a concentration of 1×10^4 cells per well. A diameter of ~ 300 µm was reached after three days of cultivation.

CCD-1137Sk spheroids

CCD-1137Sk fibroblast cells derived from human foreskin (ATCC) were cultured in Iscove's Modified Dulbecco's Medium (IMDM, Capricorn) supplemented with 10 % FBS and 1 % Pen/Strep. For spheroid generation, cells were detached using Trypsin/EDTA and seeded onto 96-well ULA plates at a concentration of 1×10^4 cells per well. An average diameter of 300 μm was reached after four days of cultivation.

HT-29 spheroids

HT-29 colon cancer cells (ATCC) were cultured in McCoy's 5A medium (Capricorn) supplemented with 10 % FBS and 1 % Pen/Strep. For spheroid generation, cells were detached using Trypsin/EDTA and seeded onto 96-well ULA plates at a concentration of 1×10^3 cells per well. A diameter of $\sim 300 \mu\text{m}$ was reached after three days of cultivation.

HTC-8 spheroids

Human tongue cell line HTC-8 (B.R.A.I.N. AG) was cultured in HTC-medium according to Hochheimer et al. (2014) (Hochheimer et al., 2014). For spheroid generation, cells were detached using Trypsin/EDTA and a concentration of 6×10^3 cells per well were seeded onto 96-well U-bottom plates. An average diameter of 300 μm was reached after five days of cultivation.

Melanoma tri-culture spheroids

Melanoma tri-cultures were generated according to Klicks et al. (2019) (Klicks et al., 2019). Briefly, 1×10^4 cells of CCD-1137Sk cells were seeded, followed by simultaneous addition of HaCaT (1×10^4 cells / well) and SK-MEL-28 (ATCC) (2.5×10^3 cells / well) after three days. For discrimination of individual cell types, HaCaT and SK-MEL-28 cells were labelled with CellTracker Red CMPTX (10 μM) and CellTracker Green CMFDA (10 μM) dye (both Life Technologies), respectively according to manufacturer instructions for 30 min. Tri-culture spheroids were kept in culture for another two days and reached an average diameter of 450 μm .

Dynarray co-culture model

The human breast cancer cell line MDA-MB-231-ECFP was maintained in DMEM supplemented with 10 % FBS, 1 % MEM-NEAA and 1 % Pen/Strep. For co-culture experiments in Dynarrays (300MICRONS), MDA-MB-231-ECFP and CCD-1137Sk cells were used. MDA-MB-231 (ATCC) were stably transfected with ECFP-C1 plasmid (Addgene) using Nucleofector™ II (Lonza) following the manufacturer's protocol. Briefly, ECFP plasmid was linearized by incubating 10 μg / μL DNA with 10 % μL AseI buffer 3.1 (New England Biolabs) and 5 % AseI enzyme (New England Biolabs) for 30 min at 37 °C under gentle shaking with 300 rpm. To keep the construct in linear shape, DNA was incubated with alkaline phosphatase (Invitrogen) for 30 min at 37 °C. 1×10^6 MDA-MB-231 cells were transfected using Nucleofector II and 2 μg linearized ECFP-construct. CCD-1137Sk were labeled with CellTracker Red CMPTX according to manufacturer instructions at a concentration of 10 μM in serum-free medium for 30 min. Prior to cell seeding, Dynarrays were treated with an isopropyl alcohol cascade (100 %, 70 %, 50 %, 30 % of alcohol in purified water for 30 s each). After washing twice with purified water, chips were coated for 1 h at room temperature with 30 μg / mL rat tail Type-I collagen (Roche) in 0.04 % acetic acid and washed once with phosphate-buffered saline (PBS). 2×10^6 MDA-MB-231-ECFP and 2×10^6 CellTracker-labeled

CCD-1137Sk were mixed in 100 μ L media and seeded onto Dynarray chips. Following a 3 h incubation at 37 °C in a CO₂ incubator, 10 mL supplemented DMEM were added and changed every other day for nine days.

4.3.3 Fixation and immunofluorescence

Spheroids were transferred into 200 μ L PCR-tubes, washed 2 x with PBS and fixed with 4 % paraformaldehyde (PFA, Carl Roth) for 1 h at 37 °C, followed by washing twice with PBS containing 1 % FBS, for 5 min each. Then, spheroids were quenched with 0.5 M glycine (Carl Roth) in PBS for 1 h at 37 °C with gentle shaking. With the exception of Sca/eS clearing protocol, all other optical clearing methods contained the following steps for immunofluorescence: after fixation and PFA-quenching, samples were incubated in penetration buffer for 30 min, containing 0.2 % Triton X-100, 0.3 M glycine, and 20 % DMSO (all Carl Roth) in PBS to improve penetration of antibodies and nuclear dyes. Spheroids were then washed twice with PBS / 1 % FBS and incubated in blocking buffer (0.2 % Triton X-100, 1 % bovine albumin serum (BSA, Carl Roth), 10 % DMSO in PBS) for 2 h at 37 °C with gentle shaking. After blocking, samples were incubated with primary antibody overnight (ON) at 37 °C with gentle shaking. Primary anti-KI67 antibody (Merck, rabbit polyclonal antibody) was diluted 1:300 in antibody buffer (0.2 % Tween 20, 10 μ g / mL heparin (both Sigma-Aldrich), 1 % BSA, 5 % DMSO in PBS). Samples were then washed 5 times for 5 min each in washing buffer (0.2 % Tween20, 10 μ g / mL heparin, 1 % BSA) and stained with secondary antibody and nuclear dyes ON at 37 °C with gentle shaking. Corresponding secondary antibody and nuclear dyes were diluted in antibody buffer with the following concentrations: donkey anti-rabbit AlexaFluor488, 1:800; donkey anti-rabbit AlexaFluor647, 1:800; DRAQ5, 1:1000 (all Invitrogen); DAPI, 1:500 (Sigma-Aldrich). Samples were washed subsequently 5 times for 5 min in washing buffer with gentle shaking and then embedded or cleared according to the following protocols, protected from light to prevent bleaching of fluorophores.

Table 3. Cell lines used in the study.

	Cell line	Cell type	Labeling	Source
Mono-cultures	HaCaT	Keratinocyte	–	B.R.A.I.N. AG
	B7_033#1NPC1	iPSC-derived neural precursor	–	Hector Institute for Translational Brain Research, Mannheim
	CCD-1137SK	Fibroblast	–	ATCC
	HT29	Colorectal adenocarcinoma	–	ATCC
	HTC-8	Human taste bud	–	B.R.A.I.N. AG
Dynarray co-culture	MDA-MB231	Triple-negative breast cancer	ECFP	ATCC
	CCD-1137SK	Fibroblast	CellTracker Red	ATCC
Melanoma tri-culture	HaCaT	Keratinocyte	CellTracker Red	B.R.A.I.N. AG
	SK-MEL-28	Melanoma	CellTracker Green	ATCC
	CCD-1137SK	Fibroblast		ATCC

Cell line, cell type, labeling and source are indicated.

(Nürnberg et al., 2020)(CC BY)

4.3.4 Optical clearing

Embedding in PBS or Mowiol (Sigma-Aldrich) and optical clearing with Glycerol: after immunofluorescence and 24 h prior to imaging, samples were mounted in 18 well μ -slides (ibidi) in either PBS or Mowiol. Glycerol-based RI matching was performed according to Williams et al. (2019) (Williams et al., 2019) by immersion of stained spheroids in an aqueous solution of 88 % glycerol (RI 1.459) ON at RT with gentle shaking, followed by mounting on 18 well μ -slides in the same solution. All procedures

were executed with minimal exposure to light. After mounting, spheroids were always kept in the microscope room for several hours to allow for temperature adjustment prior to microscopy.

Clear^{T2}

This was performed according to Dingle et al. (2015) (Dingle et al., 2015). Briefly, fixed spheroids were incubated for 10 min at RT in a solution of 25 % formamide / 10 % polyethylene glycol (PEG) (both Carl-Roth), followed by a 5 min incubation in a 50 % formamide / 20 % PEG solution. Finally, samples were immersed in fresh 50 % formamide / 20 % PEG and incubated for 60 min at RT and subsequently mounted. All steps were carried out under gentle movement.

CytoVista

After immunofluorescence staining, remaining liquid was carefully removed from samples, followed by ON immersion at RT in 30 μ L of CytoVista Tissue Clearing Reagent (Invitrogen). Then, spheroids were mounted in ibidi 18 well μ -slides in CytoVista reagent. All steps were carried out with gentle movement.

ScaleS

An adapted version of the original *ScaleS* tissue clearing protocol (Hama et al., 2015) for indirect immunofluorescence was used. After fixation, spheroids were immersed ON in S0 solution (20 % (w/v) D-sorbitol (Sigma-Aldrich), 5 % (w/v) glycerol (Carl-Roth), 3 % (v/v) DMSO in PBS, pH 7.2) to avoid sample floating in subsequent steps. Permeabilization involved adaptation in S0, immersion in A2 (10 % (w/v) glycerol, 4 M urea (Sigma-Aldrich), 0.1 % (w/v) Triton X-100 in ddH₂O, pH 7.7) for 24 h at 37 °C, followed by a 24 h incubation in B4(0) (8 M urea in ddH₂O, pH 8.4) at 37 °C and a final incubation in A2 ON at 37 °C. Then, samples were washed for 6 h in PBS at RT and blocked in *ScaleS* blocking solution (2.5 % (w/v) BSA, 0.05 % (w/v) Tween 20, 0.1 % (w/v) Triton X-100 in PBS, pH 7.4) for 24 h at 37 °C. Then, samples were incubated with primary antibody for 24 h at 37 °C, washed two times for 2 h each in fresh *AbScale* (0.33 M urea, 0.1 % (w/v) Triton X-100 in PBS, pH 7.4) at RT and then incubated ON at 37 °C in secondary antibody solution containing nuclear dyes. Next, samples were washed in fresh *AbScale* for 6 h at RT, followed by reblocking twice for 2 h each in *ScaleS* blocking solution. After refixation in 4 % PFA for 1 h at RT, spheroids were washed in PBS ON at 4 °C. For RI matching, samples were incubated in *ScaleS4* solution (40 % (w/v) D-sorbitol, 10 % (w/v) glycerol, 4 M urea, 15 % DMSO in ddH₂O, pH 8.1) ON at RT and mounted in 18-well μ -slides. All steps were carried out under gentle movement to ensure proper immersion of samples. After mounting, spheroids were kept in the microscope room for several hours to allow temperature adjustment.

4.3.5 Image acquisition and analysis

Microscopy

For imaging, the inverted Leica TCS SP8 confocal microscope (Leica Microsystems CMS, Mannheim) equipped with HC PL APO 20 x / 0.75 IMM CORR objective, 405 nm, 488 nm, 561 nm, and 633 nm lasers and Leica Application Suite X software was used. All image stacks were acquired with comparable settings, using Immersion Type F (Leica Microsystems, RI 1.52), at a resolution of 1024 x 1024 pixels, z-step size of 1.5 μ m, a laser intensity of 1 – 1.5 % and a gain between 600 – 750 V, in order to avoid

overexposure of pixels. For comparability of tested clearing methods, image stacks for Figs. 21 – 27 and Figs. S7 – S12 were acquired without z-compensation. Data for Figs. 28 and 29 were acquired with z-compensation. For brightfield microscopy, an Axiovert 25 (Carl Zeiss Microscopy GmbH) was used.

Measurement of spheroid diameter and depth-dependent z-axis profile

The average size of each spheroid before and after fixation was determined by measuring the sample diameter twice in a perpendicular angle using the line tool of FIJI (Schindelin et al., 2012) on maximum z-projections made from image stacks acquired by confocal microscopy. For measuring the depth-dependent signal intensity, a circular region of interest (ROI) with a diameter of 100 µm was placed in the central region of each spheroid. The ROI area was duplicated from the original image stack and the mean signal intensity determined for each single optical section by using FIJI's function to plot a z-axis profile.

Signal-to-noise ratio (SNR)

For the depth-dependent SNR, ROI-stacks for the measurement of signal intensity were used to determine intensity values of background and nuclear signal. Briefly, a median filter (radius 1) was applied to image stacks from a central region of each spheroid and a threshold range was manually set in upper regions of the sample, to cover areas defined as background, and converted into binary masks. ROIs generated from binary masks were used to automatically measure mean background intensity and standard deviation from the initial image stack. For determination of signal intensity of nuclear dyes, an automated thresholding mechanism was applied independently to each optical section and images were converted into binary masks, which were used to measure signal intensities from initial stacks. SNR was calculated for each optical section and defined as:

$$SNR = \frac{\mu_{SIGNAL}}{\sigma_{BACKGROUND}}$$

where μ depicts mean intensity of signal and σ the standard deviation of background intensity. In order to measure excitation wavelength-dependent differences in SNR, DAPI and DRAQ5 were analyzed.

3D-segmentation of nuclei: 3D-confocal data were pre-processed using Fiji. This included image cropping, splitting of multichannel datasets into single channel stacks to segment cell nuclei and antibody staining separately, background correction, conversion into 8-bit format, and export as tiff files. Segmentation and quantification of stacks was performed with a previously published algorithm (Schmitz et al., 2017) which employs 3D-seeded watershed for segmentation. Parameter values were adjusted using the build-in graphical user interface. The median filter range was set to 3 pixels, local threshold range to 10 pixels, and hole filling range to 1 pixel. For seed detection, Laplace of Gaussian (LoG) with a seed range between 9 – 25 pixels was chosen. The other parameters were applied as default. Post-segmented data were exported as different 3D-stacks in tiff format and a XLSX file containing quantitative results.

Statistical analysis: Statistical analysis employed the program GraphPad Prism 8. Data were tested for normal distribution by Kolmogorov-Smirnov test. For statistical analysis

of spheroid size measurements, non-parametric Kruskal-Wallis with Dunn's multiple comparisons test was performed. Analysis of segmentation results was done by one-way ANOVA with Tukey's multiple comparisons test. Significance level α was set to 0.05 with 95 % confidence interval and P-values were adjusted to account for multiple comparisons.

4.4 Results

To analyze the impact of optical clearing methods on different 3D-*in vitro* systems of varying complexity, mono-culture spheroids, co-culture spheroids, and chip-based 3D-co-cultures were compared. Mono-culture spheroids were prepared with an average diameter of 300 μm and made of cell lines derived from human keratinocytes (HaCaT), fibroblasts (CCD-1137Sk), colon cancer-associated cells (HT-29), human tongue cells (HTC-8) and human induced pluripotent stem cell (hiPSC)-derived neural precursor cells (B7_033#1NPC1). The more complex cell cultures consisted of a tri-culture model of skin cancer and a microarray-based co-culture model of human fibroblasts and breast cancer cells (MDA-MB-231). For convenience of implementation into the lab routine, we chose to analyze clearing efficiencies of simple clearing protocols Clear^{T2}, CytoVista, a modified version of Sca/eS, and immersion in Glycerol.

4.4.1 Spheroid clearing affects fluorescence, transparency, and sample volume

First, the optical clearing protocols were applied to all mono-culture spheroids upon triple-labeling with DAPI, DRAQ5, and anti-KI67 antibody. Alternative to optical clearing with Clear^{T2}, CytoVista, Sca/eS and Glycerol, spheroids were embedded in PBS or Mowiol. As shown in Fig. 21 for HaCaT spheroids (for an overview of the other cell types, see Fig. S7), the brightness of DAPI signals varied strongly between the tested clearing methods. In particular, it was decreased in PBS, Clear^{T2}, and Sca/eS samples, whereas Mowiol, CytoVista, and Glycerol retained bright DAPI signals. Fluorescence intensities of KI67 and DRAQ5 signals did apparently not differ strongly (Fig. 21). Orthogonal volume projections (Fig. 21, right panels for each dye) revealed a superior improvement of imaging depth upon clearing with Sca/eS and Glycerol. Small spheroid volumes were seen with Clear^{T2} and CytoVista (Fig. 21). In the following, the observed changes were analyzed quantitatively.

4.4.2 Volume changes of spheroids are minimal with Sca/eS and Glycerol

To determine the effects of clearing procedures on sample volume, spheroid diameters were determined from confocal image stacks. Additionally, original sample size and potential post-fixation changes of spheroid diameters were determined from bright field images taken before and after fixation. Fig. 22 demonstrates that Mowiol, Clear^{T2}, and CytoVista caused significant reductions of HaCaT spheroid diameters, with the strongest effect for CytoVista (44.8 % \pm 0.7 % loss). Conversely, Sca/eS and Glycerol did affect spheroid sizes only to a minor extent and compared to the diameters right after fixation, these were unaltered (Fig. S8). Similar results were obtained for all other cell lines and tri-culture spheroids (Fig. S9), although shrinkage was less pronounced for HT-29 and HTC-8 cells. B7_033#1NPC1 cells showed a slight volume increase.

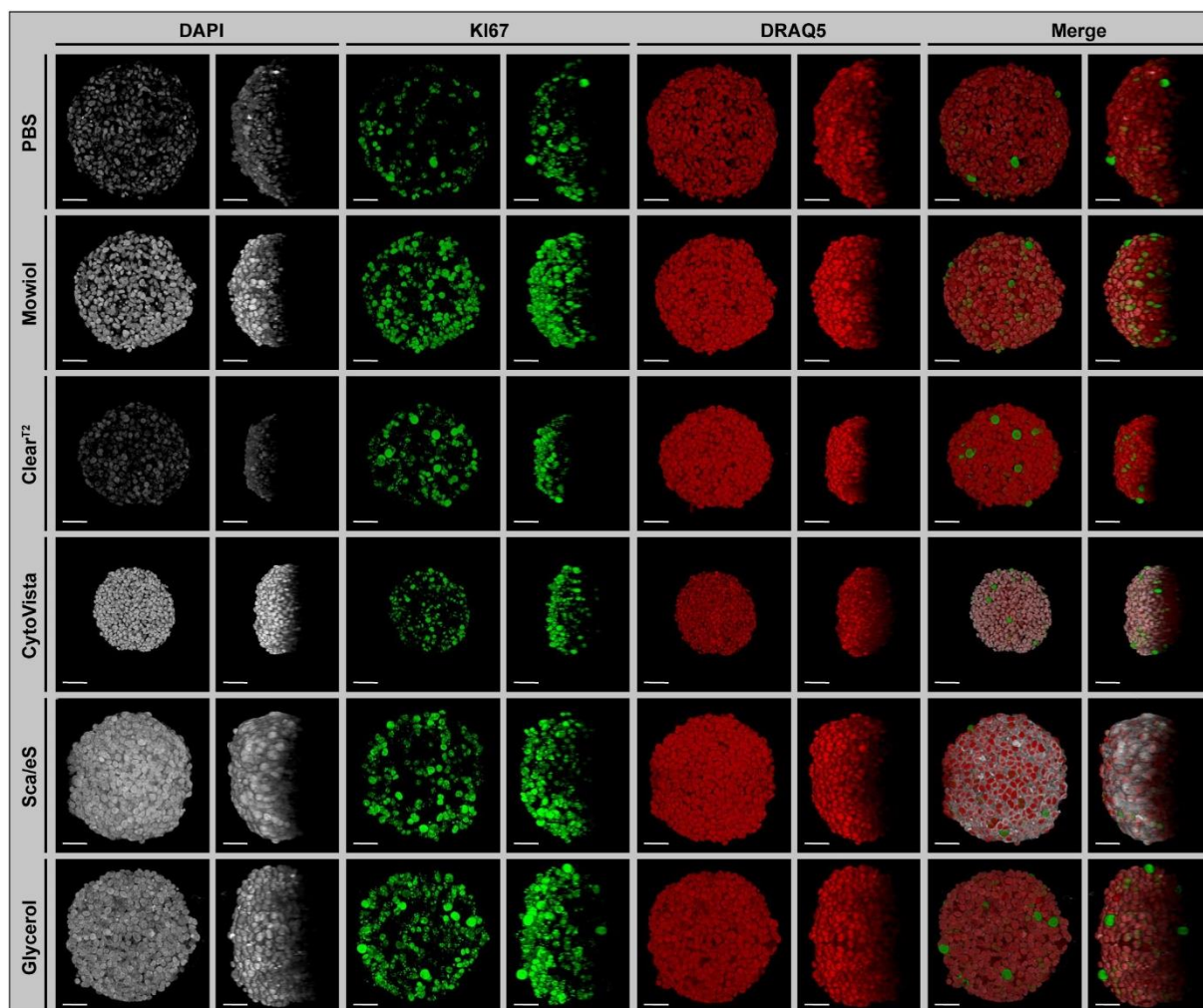


Figure 21. Preservation of fluorescence signal intensity, sample volume and optical transparency is strongly dependent on optical clearing protocol. Upon growth to a diameter of approximately 300 μm , spheroids made of HaCaT keratinocytes were fixed, stained with anti-KI67 (green) and the nuclear dyes, DAPI (gray) and DRAQ5 (red), followed by optical tissue clearing or embedding as indicated and subsequent confocal whole mount microscopy. Images show representative top (Left panels for each staining) and orthogonal (Right panels for each staining) 3D-volume projections of single and merged channels after corresponding clearing method. Scale bars, 50 μm . (Nürnberg et al., 2020)(CC BY)

4.4.3 ScaleS and Glycerol improve light penetration into spheroids

To analyze light penetration into spheroids, single equidistant optical sections were prepared from top to bottom of the samples. Table S3 summarizes the percentage decrease in light penetration of DAPI and DraQ5 stains. In PBS, Mowiol, and Clear^{T2} samples, central regions of the spheroids already darkened at 50 μm of depth and signals were almost completely invisible at ~ 150 μm of depth (Fig. 23A). Conversely, ScaleS or Glycerol clearing preserved signal intensities at 100 μm of depth and central spheroid regions remained visible beyond 150 μm for DRAQ5 and KI67 (Fig. 23A). Ring-like localization of KI67 signals at 100 μm depth and below was as expected, because cell proliferation in HaCaT spheroids is limited to the spheroid rim. Due to the massive shrinkage of CytoVista-cleared spheroids, optical sections were here

analyzed at 25 μm intervals (Fig. 23B). Normalized to spheroid size, light penetration was comparably good for ScaleS, Glycerol, and CytoVista samples.

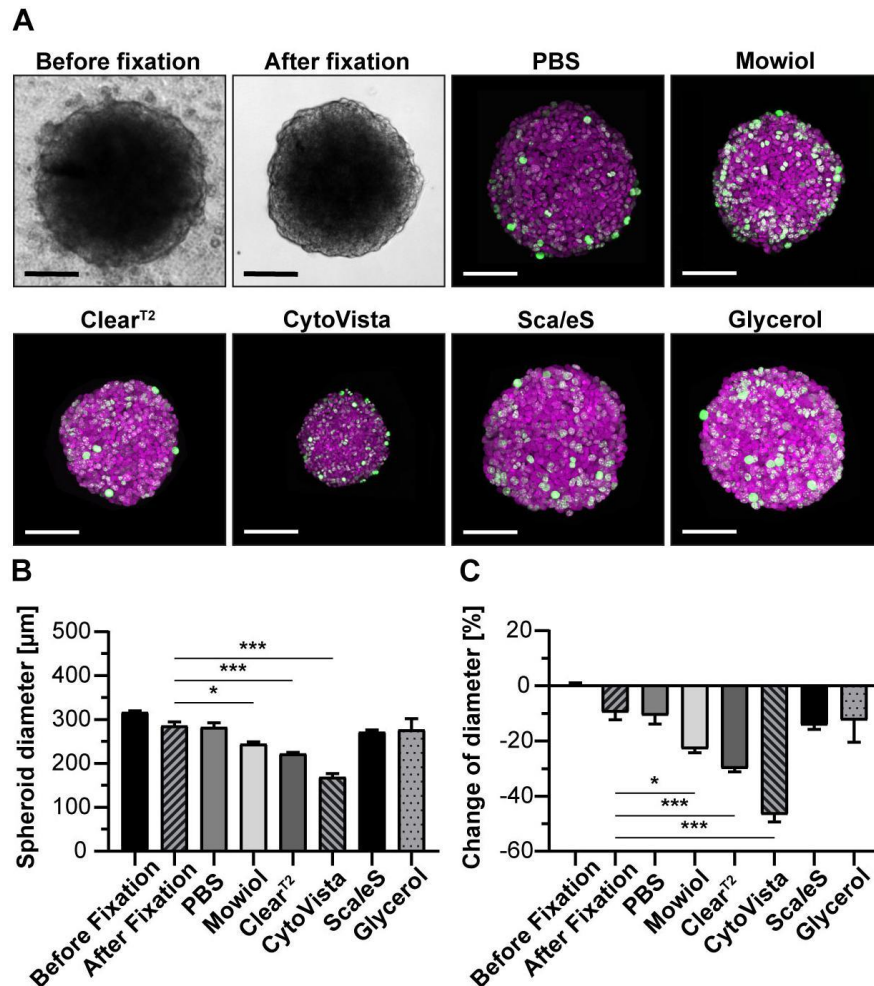


Figure 22. Aqueous clearing methods and detergent-containing hyperhydration prevent massive post-fixation volume changes. Upon growth to a diameter of approximately 300 μm , spheroids made of HaCaT keratinocytes were fixed, stained with anti-KI67 and DRAQ5, followed by optical tissue clearing or embedding as indicated. Spheroid diameters were determined from brightfield images before and after fixation and from confocal microscopy stacks after staining. A) Representative brightfield images of spheroids before and after fixation as well as maximum projections of confocal image stacks upon staining and clearing/embedding as indicated. In the confocal panels, DRAQ5 and KI67 fluorescence signals are shown in magenta and green, respectively. Scale bars, 100 μm . Quantitative analysis of average spheroid diameter (B) and change of average spheroid diameter relative to pre-fixation state (C). Graphs depict mean + standard deviation (SD); $n \geq 9$; * $P \leq 0.05$, *** $P \leq 0.001$. (Nürnberg et al., 2020)(CC BY)

4.4.4 Signal intensity in depth depends on clearing method, cell line, and fluorophore

To quantify the decay of DAPI and DRAQ5 signal intensities as a function of depth, mean intensities at each optical section were measured in circular ROIs placed in the central region of each spheroid. To compensate for clearing-induced volume changes of samples, depth values were normalized to pre-fixation diameters multiplied with the percentage change of swelling or shrinkage (normalized depth).

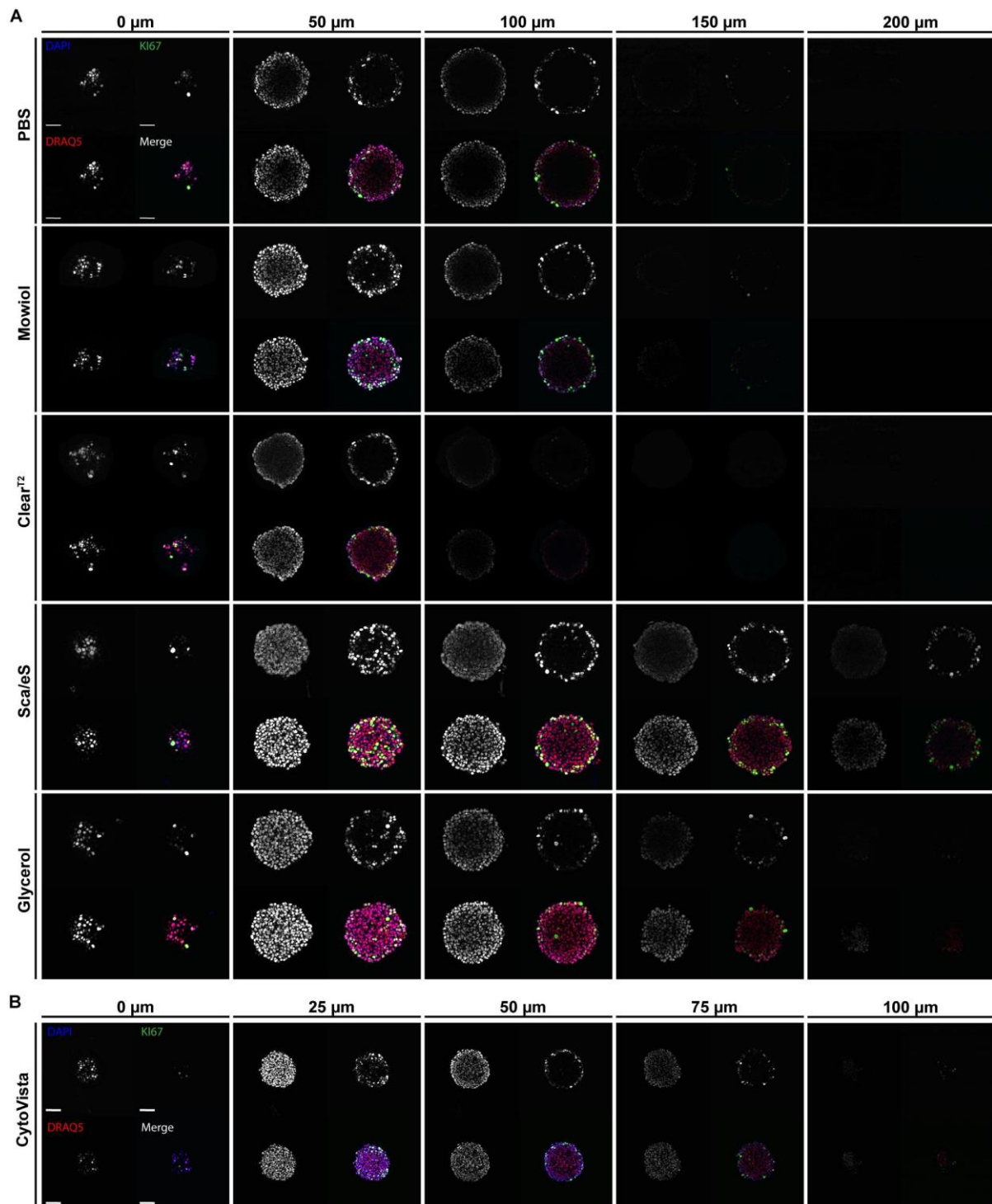


Figure 23. High-refractive index aqueous solutions or detergent-containing hyperhydration improve light penetration into spheroids. Upon growth to a diameter of approximately 300 μm , spheroids made of HaCaT keratinocytes were fixed, stained with anti-KI67, DAPI, and DRAQ5, followed by optical tissue clearing or embedding as indicated and subsequent confocal whole mount microscopy. A-B) Depicted are single optical sections of spheroids at discrete z-depths with fixed intervals of 50 μm (A) or 25 μm (B). Each panel shows DAPI, DRAQ5, and KI67 fluorescence signals, as well as a merge. In merged panels DAPI is shown in blue, DRAQ5 in red, and KI67 in green. Colocalization of DAPI and DRAQ5 appears in magenta, additional colocalization with KI67 in green to white hues. Scale bars, 50 μm . (Nürnberg et al., 2020)(CC BY)

Mean data were plotted for HaCaT spheroids in Fig. 24A and B, and for all other cell lines in Fig. S10. This showed that different clearing protocols can be better suited to either DAPI or DRAQ5, or to a specific cell line. In all spheroids, maximal brightness values were seen in the upper parts of spheroids, followed by exponential decays. As indicated by the 50 % and 90 %-signal decay depths, Glycerol or ScaleS were superior for most of the samples (Tab. S3). CytoVista was good in HT-29 and HTC-8 cells, whereas Clear^{T2} was not superior for any condition. Overall, 50 % loss of signal intensity ranged from 85 to 133 μm of depth for DAPI and from 56 to 127 μm for DRAQ5 (Tab. S3). 90 % loss of signal intensity ranged from 151 μm to 327 μm of depth for DAPI and from 133 μm to 331 μm for DRAQ5 (Tab. S3).

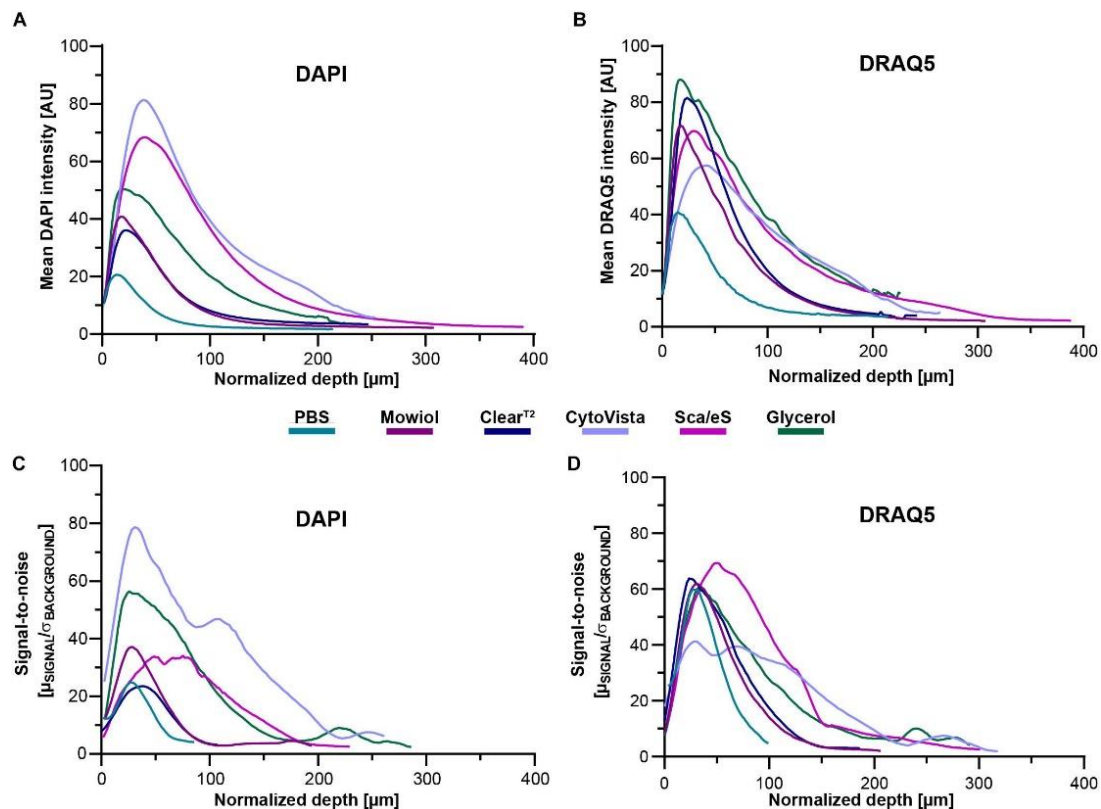


Figure 24. Optical transparency, preservation of fluorescence signals, and depth-dependent SNR are dependent on clearing method and cell line. Monoculture spheroids of HaCaT cells were grown to approximately 300 μm diameter and then fixed. Upon staining of proliferating cells (anti-KI67) and nuclei (DAPI and DRAQ5), spheroids were embedded/cleared as indicated and then imaged *in toto* using confocal microscopy. Analysis of depth-dependent signal intensity of DAPI and DRAQ5 was performed by selecting one circular region of interest (ROI) per sample through the central region of the spheroid followed by mean intensity measurement throughout the entire stack depth. SNR values for DAPI and DRAQ5 were determined by measurement of mean intensity and standard deviation of background and nuclear signal via semi-automated thresholding. Then, SNR was calculated as the ratio of mean signal intensity in identified nuclear regions to the average standard deviation of background intensity ($\mu_{\text{SIGNAL}}/\sigma_{\text{BACKGROUND}}$). To account for volume-changing effects of individual clearing methods, all depth values were normalized by the method-dependent degree of swelling or shrinkage. A-B) Graphs show mean intensities of DAPI and DRAQ5 as a function of normalized z-depth HaCaT spheroids. C-D) Graphs show mean SNR values for staining with DAPI and DRAQ5 as a function of normalized z-depth for HaCaT spheroids. All mean values were calculated from $n \geq 7$ spheroids per condition. (Nürnberg et al., 2020)(CC BY)

4.4.5 Depth-dependent decline of signal-to-noise ratio varies with cell type

Next, SNR was calculated by the ratio of mean signal intensity and the corresponding standard deviation of the background. SNR values were then plotted as a function of normalized depth (Fig. 24C and D) and the depth up to which the Rose criterion (SNR > 5) was met was determined (Tab. S4). In HaCaT spheroids, maximal SNR values of 79 and 72 were reached for DAPI and DRAQ5 in the upper parts of spheroids, followed by more or less rapid decays. Similar as for signal intensities, the depth for reaching the Rose criterion was mostly the largest in Glycerol or ScaleS samples, but also CytoVista showed good performance and was superior for DAPI in HaCaT, HT-29, and HTC-8 cells, and for DRAQ5 in HaCaT cells (Fig. S11, Tab. S4). For DAPI, the normalized depths to reach Rose criterion ranged from 122 to 219 μm , for DRAQ5 from 233 to > 332 μm .

4.4.6 Complexity of 3D-cultivation systems affects optical clearing efficiency

Although mono-culture spheroids are being used in many 3D-cell culture applications, more sophisticated approaches with different cell types in one model gain in importance. To evaluate the efficiency of tissue clearing for more complex co-cultures, we included a recently published tri-culture spheroid melanoma model (Klicks et al., 2019) as well as a chip-based microarray co-culture of fibroblasts and breast cancer cells into our analysis. In addition, these models allowed to test the influence of optical clearing on the performance and stability of frequently used markers in cell culture, i.e. CellTracker dyes and stably expressed fluorescent protein. First, we examined the clearing with the melanoma model. This consisted of a CCD-1137Sk fibroblast core, surrounded by HaCaT keratinocytes and clusters of SK-MEL-28 melanoma cells, the latter two labeled with CellTracker Red and Green, respectively. Additionally, samples were stained with DAPI and anti-KI67 (Fig. 25A). Embedding, optical clearing, and analyses were performed in analogy to mono-culture spheroids. Here, we observed similar post-fixation volume changes as for mono-culture spheroids, showing significantly reduced sample volumes for Mowiol, Clear^{T2}, and CytoVista (Fig. S8 and S9). For all tested methods, fluorescence of the different dyes was preserved, although to varying extent (Fig. 25B). The DAPI signal was best preserved with CytoVista, followed by Mowiol and Glycerol. With respect to Rose criterion, Glycerol performed best (Tab. S5), but none of the methods resulted in an absolute SNR cutoff depth higher than 89 μm (Tab. S5). Notably, this value was much less than those obtained for mono-culture spheroids of HaCaT cells (153 μm , Table S4) and CCD-1137Sk fibroblasts (175 μm , Tab. S4). For CellTracker Green, Mowiol worked best and none of the tested clearing methods could improve depth penetration for this dye. Likely, this was due to the primary spatial localization of CellTracker Green-labeled SK-MEL-28 cells in the peripheral region of the tri-cultures.

Next, we addressed optical clearing in microarray chip-based co-cultures of CCD-1137Sk fibroblast and MDA-MB-231-ECFP breast cancer cells. Here, cells were grown in collagen-coated cavities with a diameter of 300 μm and a depth of 200 μm . Fibroblasts and cancer cells were labeled with CellTracker Red and stably expressed ECFP, respectively. Additionally, cells were stained with DRAQ5 and anti-KI67 (Fig. 26A and B). Except determination of clearing-induced volume changes and corresponding normalization of depth values, which were omitted, analyses were done as for spheroids. This revealed a particular sensitivity of ECFP to clearing.

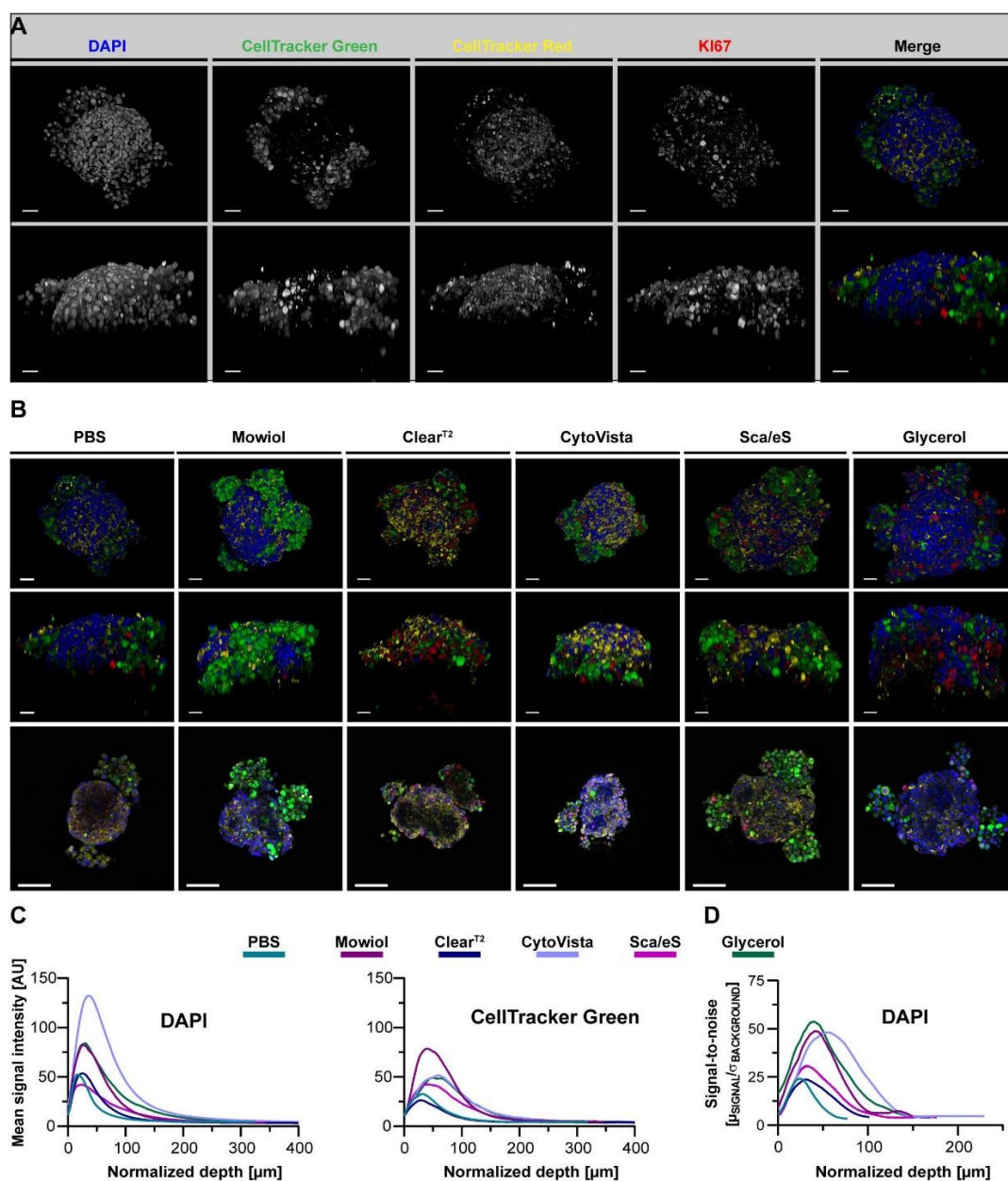


Figure 25. Optical clearing efficiency is affected by complexity of a spheroid-based tri-culture model. Melanoma tri-culture spheroids were generated starting with formation of a core spheroid of CCD-1337Sk fibroblasts, followed after 72 h by simultaneous addition of HaCaT keratinocytes labeled with CellTracker Red and SK-MEL-28 melanoma cells marked with CellTracker Green. After another two days of cultivation, spheroids were fixed, stained with anti-KI67 and DAPI, and then embedded or cleared as indicated. Confocal 3D-imaging of whole spheroid cultures was performed. A) Representative top and orthogonal 3D-volume projections of fluorescence signals (indicated) of a PBS-embedded spheroid are shown in upper and lower panels, respectively. In the merge, DAPI appears in blue, CellTracker Green in green, CellTracker Red in yellow, and KI67 in red. Scale bars, 50 μm . B) Depicted are representative images of tri-culture spheroids after different types of embedding/clearing as indicated. Top and side view maximum projections are shown in upper and middle panels. Lower panels show single optical sections at 75 μm of imaging depth. Scale bars, 50 μm in upper and middle row, 100 μm in lower row. Quantitative analysis of mean signal intensity of DAPI and CellTracker Green (C) and SNR of DAPI signals (D) as a function of normalized depth. Mean of $n = 10$ spheroids per condition. (Nürnberg et al., 2020)(CC BY)

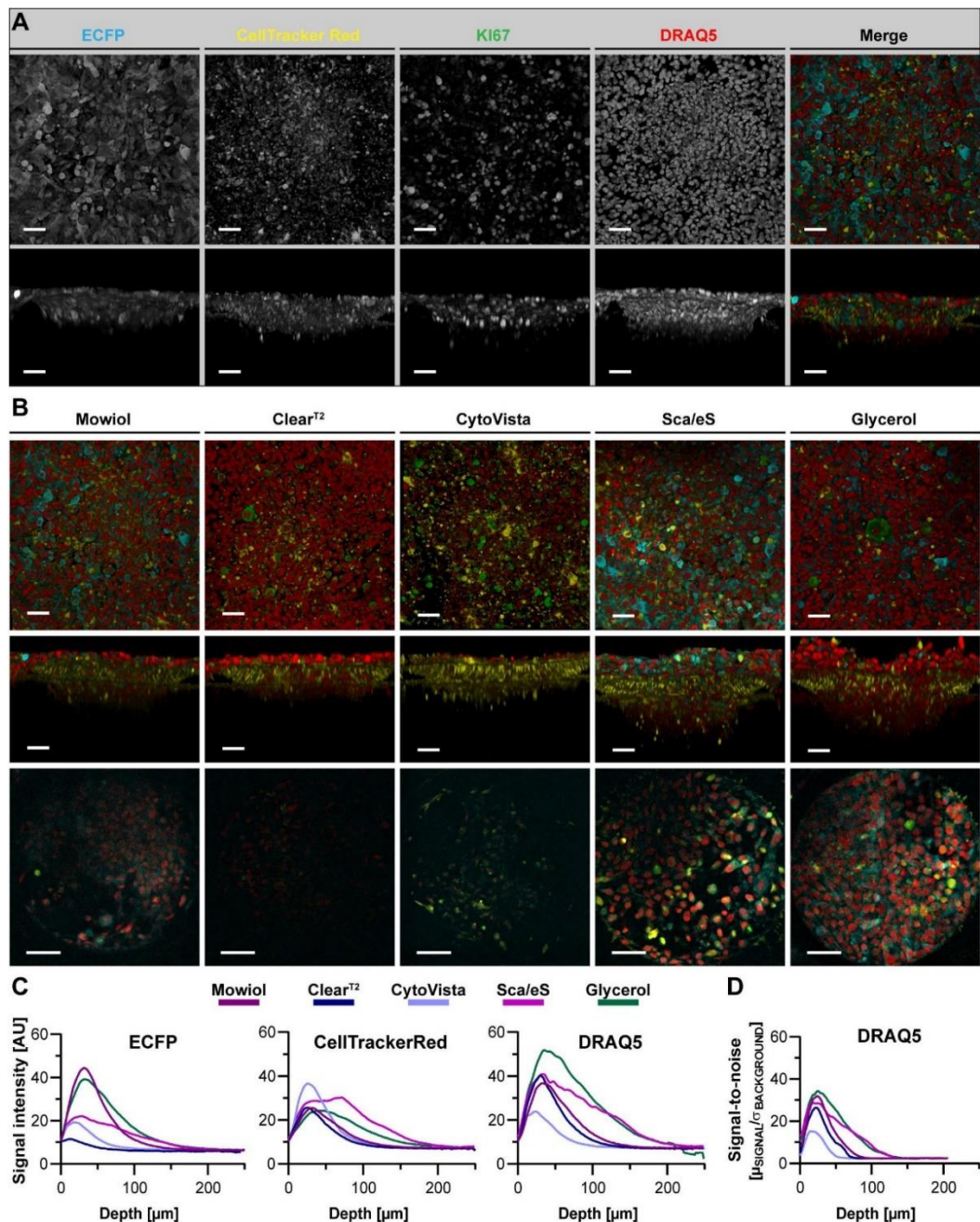


Figure 26. ECFP fluorescence is maintained by Glycerol-RI matching in a chip-based co-culture model of breast cancer cells and fibroblasts. ECFP-expressing MDA-MB-231 breast cancer cells were co-seeded with CellTracker Red labeled CCD-1337Sk fibroblasts into Dynarray chips with 300 μm wide cavities. After 9 days of cultivation, chips were fixed, stained with anti-KI67 and DRAQ5, and then embedded or cleared as indicated. A) Representative top and orthogonal 3D-volume projections of fluorescence signals (indicated) of Mowiol-embedded chip cavities are shown in upper and lower panels, respectively. In the merge, ECFP appears in cyan, CellTracker Red in yellow, KI67 in green, and DRAQ5 in red. Scale bars, 50 μm . B) Depicted are representative images of chip cavities after different types of embedding/clearing as indicated. Top and side view maximum projections are shown in upper and middle panels. Lower panels show single optical sections at 75 μm of imaging depth. Scale bars, 50 μm in upper and middle row, 100 μm in lower row. C-D) Quantitative analysis of mean signal intensity of ECFP, CellTracker Red, and DRAQ5 (C) and SNR of DRAQ5 signals (D) as a function of depth. Mean of $n = 10$ cavities per condition. (Nürnberg et al., 2020)(CC BY)

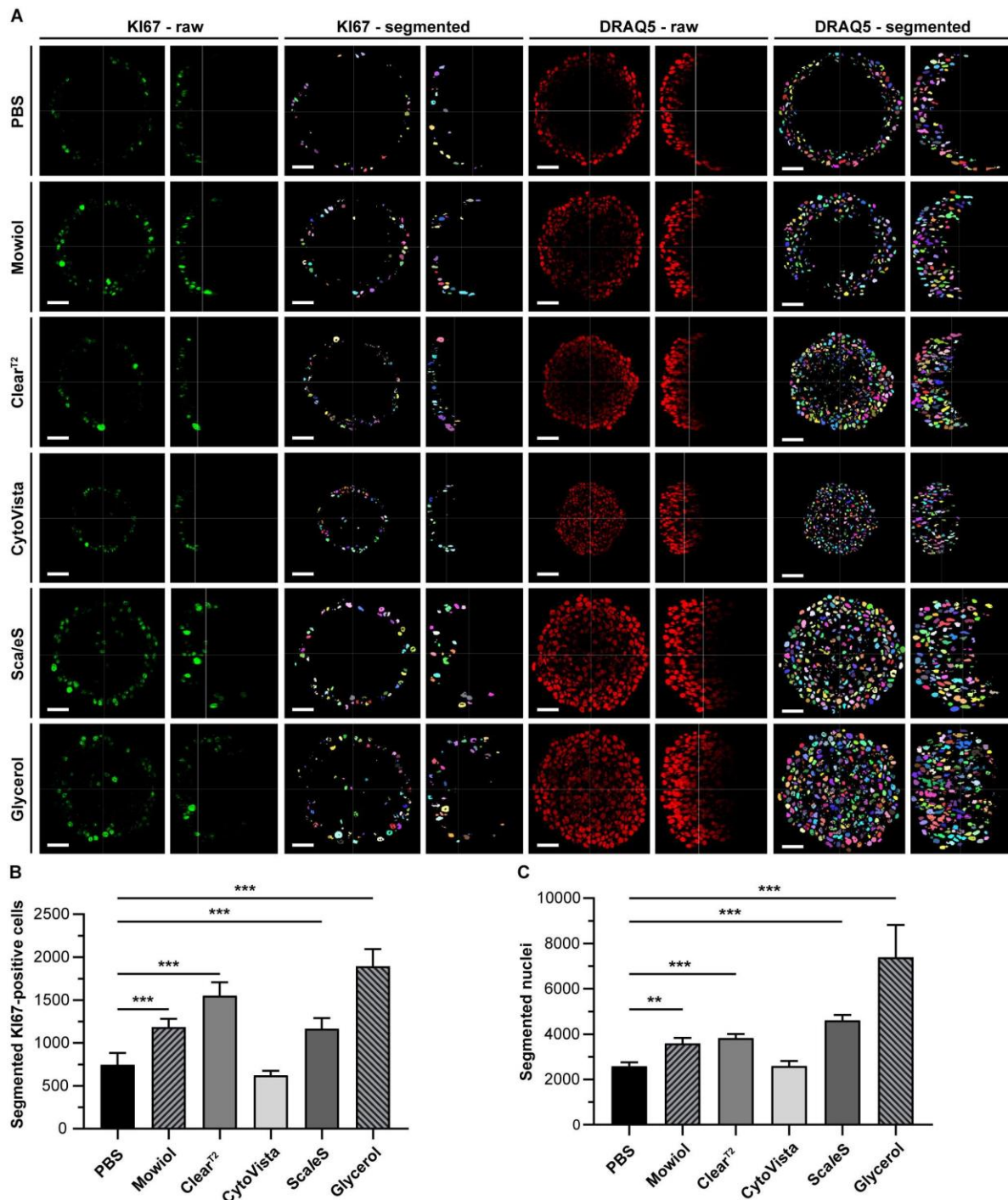


Figure 27. Optical clearing of HaCaT spheroids with Glycerol improves detection and quantification of cell nuclei. Upon growth to a diameter of approximately 300 μm , spheroids made of HaCaT keratinocytes were fixed, stained with anti-KI67 and DRAQ5, followed by optical tissue clearing or embedding as indicated and subsequent confocal whole mount microscopy. Semi-automated image segmentation was performed to detect and count KI67⁺ and DRAQ5⁺ nuclei. A) Depicted are raw single optical sections and orthogonal views from central regions for both markers (KI67 – raw; DRAQ5 – raw) and corresponding segmented images (KI67 – segmented; DRAQ5 – segmented). In raw images, fluorescence signals of KI67 and DRAQ5 are shown in green and red, respectively. Different colors of segmented nuclei were used for better visual discrimination. Scale bars, 50 μm . B-C) Quantitative analysis of KI67⁺ (B) and Draq5⁺ nuclei (C) as a function of clearing/embedding protocol. Data show mean + SD; $n \geq 9$; ** $P \leq 0.01$; *** $P \leq 0.001$. (Nürnberg et al., 2020)(CC BY)

While Mowiol and Glycerol maintained ECFP signals, the other tested protocols led to a loss of signal intensity (Fig. 26C). This was particularly pronounced for Clear^{T2}, which abolished ECFP fluorescence almost completely. Signal loss was less dramatic for the other dyes, but overall, only Mowiol, ScaleS, and Glycerol yielded a balanced maintenance of fluorescence for all dyes. While ScaleS and Glycerol led to an improvement of signal intensity in greater depth of the cavities, Mowiol performed badly in this aspect. The depth-dependent Rose criterion cutoff of DRAQ5 signals was met for ScaleS and Glycerol at approximately 110 μm of depth (Fig. 26D, Tab. S5). In summary, these data revealed that complex 3D-cultivation systems pose an increased challenge for clearing protocols.

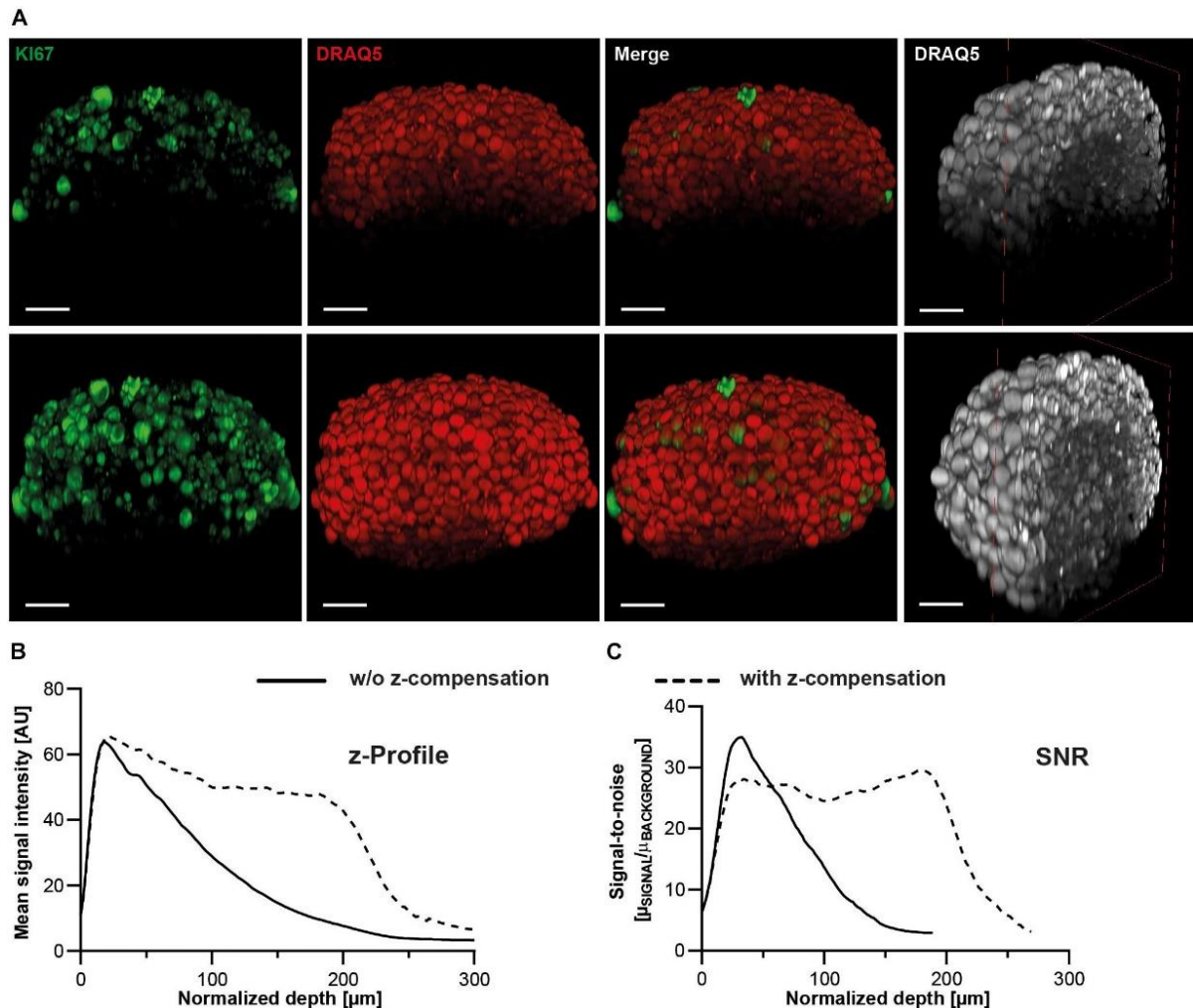


Figure 28. Z-profiles of signal intensity and SNR remain more stable upon z-compensation. Upon growth to a diameter of approximately 300 μm , spheroids made of HaCaT keratinocytes were fixed, stained with anti-KI67 and DRAQ5, followed by optical tissue clearing with Glycerol and subsequent confocal whole mount microscopy. A) Depicted are orthogonal maximum projections (left three columns) and a clipped projection to visualize the spheroid core (right column) of the same spheroid imaged in the absence (upper panels) or presence of z-compensation (lower panels). In the left panels, fluorescence signals of KI67 and DRAQ5 are shown in green and red, respectively. The right panels show only DRAQ5 signals in gray. Scale bars, 50 μm . Graphical representations of z-profiles for DRAQ5 channel signal intensity (B) and SNR (C) in a z-extended column through the central region of the spheroid. (Nürnberg et al., 2020)(CC BY)

4.4.7 Optical clearing and z-compensation improve data segmentation

To evaluate the effects of clearing on quantitative image analysis of 3D-datasets, the segmentation efficiencies of the different clearing methods were compared. Therefore, DRAQ5-stained nuclei and KI67⁺ cells were segmented and counted for all samples. This revealed a high variance between different clearing protocols and cell lines (Figs. 27 and S12).

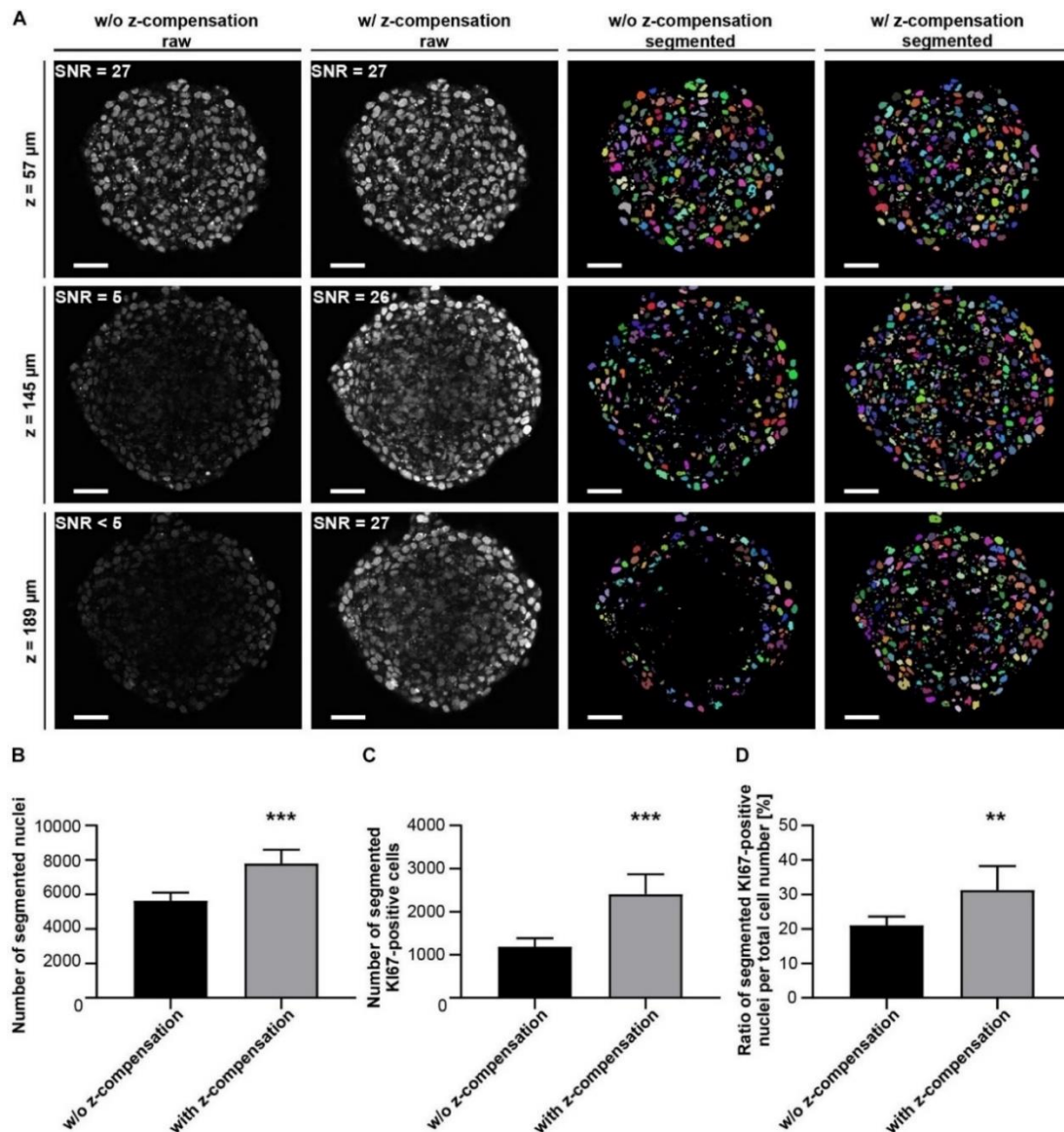


Figure 29. Z-compensation improves semi-automated segmentation of nuclei. Upon growth to a diameter of approximately 300 μm, spheroids made of HaCaT keratinocytes were fixed, stained with anti-KI67 and DRAQ5, followed by optical tissue clearing with Glycerol and subsequent confocal whole mount microscopy. A) Depicted are single raw confocal images (left two columns) and corresponding segmented nuclei (right two columns) at different z-depths showing DRAQ5 signals in gray and segmented nuclei in different colors. The corresponding image stacks were taken in the absence or presence of z-compensation, as indicated. SNR values measured in the shown raw images are given in their upper left angles. Scale bars, 50 μm. Quantitative analysis of Draq5⁺ nuclei (B), KI67⁺ nuclei (C), and ratio of KI67⁺/DRAQ5⁺ nuclei (D) in the absence or presence of z-compensation. Data show mean + SD; n ≥ 9; ** P ≤ 0.01; *** P ≤ 0.001. (Nürnberg et al., 2020)(CC BY)

While nuclei in HaCaT spheroids could only be detected in the outer spheroid regions in PBS samples, Mowiol, Clear^{T2}, ScaleS, and Glycerol allowed improved segmentation of nuclei and KI67⁺ cells towards the spheroids core (Fig. 27A). Correspondingly, quantitative data showed significantly more nuclei and KI67⁺ cells with all clearing methods except for CytoVista as compared to PBS controls (Fig. 27B and C). Depending on the quality of signal preservation, depth penetration, and SNR, similarly enhanced segmentation results were also obtained for the other cell types (Fig. S12). Overall, the most consistent improvements were observed for Glycerol and ScaleS.

Notably, for all previous experiments, image acquisition was performed without depth-dependent adjustment of laser intensity or detection gain (z-compensation), in order to ensure comparability of methods. To test potential improvements of data quality and analysis by z-compensation, Glycerol-cleared HaCaT spheroids were imaged \pm z-compensation by stepwise linear increase of excitation laser intensity, followed by quantification of depth-dependent signal intensity, SNR (Fig. 28), and segmentation (Fig. 29). Contrary to the data taken with static image acquisition parameters, z-compensation yielded almost constant levels for signal intensity (Fig. 28B) and SNR throughout the central region of the entire spheroid (Fig. 28C). This also affected segmentation of nuclei, which was clearly improved in deeper spheroid layers upon z-compensation (Fig. 29A). As a consequence, counts of nuclei and KI67⁺ cells increased (Fig. 29B). Likely, because cell proliferation was enriched in the peripheral spheroid layers, the rise in nuclei and KI67⁺ cell counts occurred in a disproportional manner, leading to an altered percentage of KI67 positive cells.

4.5 Discussion

Recently, the increasing relevance of 3D-*in vitro* models in biomedical research has expanded the utilization of optical clearing methods from tissues and organs to 3D-cell cultures. However, investigations on cell type- and dye-dependent effects of optical clearing techniques have been sparse and not systematic. Ideally, a suitable optical clearing protocol should be easy to integrate into daily lab routine and manageable without specialized, cost intensive equipment or harmful chemicals. Moreover, sample integrity should be preserved and flexibility in the type of fluorescence labeling should be retained. Here, we compared simple clearing protocols with a range of cell types, dyes, and 3D-culture conditions and found that soft clearing procedures such as RI-matching in Glycerol can work rather well for many applications.

4.5.1 Effects of clearing on sample shrinkage

Clearing-induced changes in sample volume can be desired in some cases. For example, expansion microscopy relies on increased sample dimensions to resolve objects that are normally below the optical resolution limit (Chen et al., 2015). However, this also leads to massive increase in time and resources needed for imaging, data processing and storage. In addition, expansion microscopy might affect sample or epitope integrity. On the other end, sample shrinkage might be advantageous for saving scanning and image processing time (Pan et al., 2016), but there is a risk of losing spatial resolution and segmentation of densely packed structures for automated quantification becomes more difficult (Jonkman et al., 2014). Thus, in most instances, preservation of sample volume is preferred for reasons of quantification,

reproducibility, and structural integrity. Our results showed, that *ScaleS* and Glycerol were able to maintain post-fixation sample size, whereas Mowiol, Clear^{T2}, and CytoVista led to consistent further spheroid shrinkage, which was likely due to dehydration during tissue clearing (Pan et al., 2016). The strongest alteration of sample volume was observed with CytoVista followed by Clear^{T2}. Previously, CytoVista was reported to cause only minor shrinkage. However, these studies referred to the clearing of tissues and not to small 3D-structures such as spheroids (Bossolani et al., 2019; Hama et al., 2015; Ke et al., 2016). Also, with Clear^{T2}, spheroids of human dermal fibroblasts (Costa et al., 2018c) and rodent-derived glioblastoma or neural stem cells (Dingle et al., 2015) showed no significant alterations of sample size. In contrast, constant monitoring of sample volume in an on-chip approach of optical clearing revealed an initial reduction of spheroid area by 20 % (Grist et al., 2016). These diverse findings may result from different protocols employed for immunostainings, pointing towards the influences of sample processing on the outcome of sample volume. In contrast to Clear^{T2} and CytoVista, optical clearing by our modified version of *ScaleS* did not alter the post-fixation sample volume. This is consistent with recent observations, where RI matching of spheroids used only *ScaleS4* solution (Boutin et al., 2018).

4.5.2 Effects of clearing on dye preservation and SNR

Further principal factors in the selection of an appropriate clearing protocol are preservation of fluorescence signal intensity and its accentuation against a background of autofluorescence, with the latter being particularly critical for segmentation purposes. While all tested procedures yielded analyzable signal intensities at the upper object layers for DAPI, DRAQ5, AlexaFluor488, and CellTracker dyes, ECFP fluorescence was compromised with *ScaleS* and CytoVista and almost completely abolished by Clear^{T2}. On tissue sections, this effect of Clear^{T2} was already observed for GFP and YFP and attributed to the formamide-induced non-aqueous micro-environment which is part of this method (Li et al., 2017b; Yu et al., 2016). As for SNR, the maximum values were mostly higher for DRAQ5 than for DAPI regardless of cell type and clearing protocol. However, for both dyes, SNR decayed at a similar depth below the Rose criterion in non-z-compensated image stacks. Importantly, z-compensation had a rather beneficial effect on keeping both, signal intensity and SNR, high over the entire spheroid range. This demonstrates that proper z-compensation is a critical component for quantitative segmentation approaches, and it suggests that SNR is dependent on fluorescence signal intensity even in confocal microscopy.

4.5.3 Effects of sample complexity on clearing efficacy

Clearing of complex 3D-co-culture systems revealed that optical clearing is becoming less effective with increasing sample intricacy. Compared to respective mono-culture spheroids, a tri-culture model of fibroblasts, keratinocytes, and peripheral melanoma cells showed decreased sample transparency and depth-dependent image quality for all tested clearing methods. Similarly, the chip-based co-cultures of fibroblast and breast cancer cells were penetrated in an incomplete manner. We suggest, that not only cell type-specific characteristics, but also the interaction between different cell types affects efficiency of optical clearing, most likely due to altered compactness (Desmaison et al., 2018) and additional scattering sources such as extracellular matrix (Senthebane et al., 2018). This is of particular importance when intracellular (e.g.

keratins) or extracellular protein composition change during naturally occurring differentiation and stratification processes, like in skin 3D-models.

Table 4. Summarized evaluation table of all clearing methods and assessed parameters regardless of cell type-specific variations.

		PBS		Mowiol		ClearT ²		CytoVista		ScaleS		Glycerol	
Monoculture	Sample preservation	++		-		--		---		+++		++	
		DAPI	DRAQ5	DAPI	DRAQ5	DAPI	DRAQ5	DAPI	DRAQ5	DAPI	DRAQ5	DAPI	DRAQ5
	Signal intensity	---	---	--	-	---	--	+++	+++	++	++	++	++
	SNR	---	---	-	-	---	--	+++	+	+	++	++	+++
	Segmentation	---		--		--		--		++		+++	
Co-/Tri-culture	Signal intensity	CellTracker Green											
		---		-		-		--		-		-	
		CellTracker Red											
		-		--		--		++		++		++	
		Nuclear dye											
		---		-		--		-		++		+	
	Segmentation	---		-		--		-		++		+++	

The color coding and the number of plus or minus signs corresponds to the overall ranking of clearing methods from worst (red, ---) to best (dark green, +++).

(Nürnberg et al., 2020)(CC BY)

4.5.4 Effects of clearing on segmentation

Precise segmentation of 3D-microscopy data is fundamental to quantify changes between experimental groups at the single cell level, e.g. after treatment with a therapeutic agent. The image analysis pipeline used here combined a number of different pre-processing algorithms with a marker-controlled three-dimensional watershed segmentation approach that could reach an F-score of 0.88 (Schmitz et al., 2017). However, to obtain high segmentation accuracy, excellent raw data quality is of paramount importance (Bassel, 2015; Roeder et al., 2012). Notably, we observed gross differences in the number of segmented nuclei for the same samples cleared with distinct protocols. In addition, z-compensation during image acquisition proved to ultimately enhanced data quality. Principal factors that determined image fineness were here found to be i) high SNR, ii) uniformity of SNR in xy and z, and iii) appropriate resolution and packing of objects. Importantly, it is the combination of all three parameters that needs to be project-dependently optimized, because these will mutually affect each other.

Ad i): as noted earlier, decent SNR values were obtained in the superficial layers of image acquisition for all clearing protocols and cell types. But even with the best clearing protocol, it tended to decay rapidly for all samples, if no z-compensation was used. Accordingly, data segmentation was accurate at the beginning of a data stack and deteriorated deeper within. Our analysis showed that segmentation was reliable at SNR around 20, while at the Rose criterion, i.e. SNR = 5, it was already insufficient. This does not necessarily mean that data with Rose level of SNR could not be properly analyzed. Indeed, we suggest that the algorithm used here would have still been able to detect most nuclei well. But given that the settings were optimized to segment robustly in a higher SNR range, the automated processing underperformed at lower

SNR values. Thus, while a certain minimal SNR is needed, variability of SNR appeared to pose a critical major limitation, as well.

Ad ii): a general challenge with the imaging of 3D-biological specimens is the non-linear scattering of light. As observed also in this study, that leads to an exponential loss in signal intensity beyond a certain depth. Furthermore, since biological specimens have mostly round shapes, peripheral parts of these objects are covered by thinner layers of scattering material than central, or core regions. Hence, signal quality and brightness are higher in the periphery than in the core. Z-compensation as used here, can result in overexposure of peripheral zones, but fortunately, at least for the present study it did not pose a problem. Conversely, z-compensation not only amended the loss of SNR in depth but also the variation of SNR within one optical layer from border to center. In conclusion, z-compensation is highly recommended to obtain higher quality image stacks with 3D-cell cultures.

Ad iii): at high cell densities or low resolution, nuclei tend to overlap. Regularly, separation of such dense objects is a big challenge for segmentation algorithms (Jonkman et al., 2014). For example, segmentation based on a 3D-seeded watershed algorithm detects regional differences in brightness. Diffuse and incomplete edges due to poor image quality will impede accurate and consistent object detection, especially if the nuclear staining is not homogeneously distributed (Toyoshima et al., 2016). Sample shrinkage is a further factor that affects the segmentation accuracy adversely since the cell nuclei are more densely packed with more overlapping objects. This may lead to under-segmentation, and hence to a lower number of detected nuclei compared to the original sample (Blin et al., 2019). It is likely, that the high variance in cell numbers between different clearing protocols as observed in the present study is at least partially due to sample shrinkage in combination with high cell density.

4.6 Conclusions

In summary, we showed that inherent characteristics of cell lines influence the outcome of optical clearing and that protocols should be chosen in a sample-dependent manner. Factors to consider include size, complexity, and composition of 3D-cultures. In our hands, the hyperhydrating method *ScaleS* and the aqueous high-RI solution *Glycerol* provided the best results concerning their ability to preserve fluorescence of applied dyes and proteins, while maintaining sample integrity. Furthermore, the choice of the clearing method and z-compensation also strongly influence quantitative image analysis and should be considered in experimental planning.

Author Contributions

EN, MV, MH, RR conceptualized and wrote the paper. EN, MV, JK, EvM, TC, FK, RB produced and analyzed experimental data. TEF, KR, PS, TL, RS, JM contributed materials, conceptual ideas and participated in writing of the manuscript.

Funding

This work was funded by the German Federal Ministry of Research (BMBF) as part of the Innovation Partnership M²Aind, project M²OGA (03FH81021A) within the framework *Starke Fachhochschulen—Impuls für die Region (FH-Impuls)*. This research project is part of the *Forschungscampus M²OLIE* and funded by the German Federal Ministry of

Education and Research (BMBF) within the Framework Forschungscampus: public-private partnership for Innovations. EN was funded by the Graduiertenkolleg TASCDDT of the MWK Baden-Württemberg. RB was funded by Carl-Zeiss Foundation.

Acknowledgments

We thank Dr. Knebel (Leica Microsystems, Mannheim) for fruitful discussions.

Conflict of Interest

Authors TEF, KR, and PS were employed by the company B.R.A.I.N. AG. Authors RS and JM were employed by the company Merck Healthcare KGaA. The remaining authors declare that the research was conducted in the absence of any commercial or financial relationships that could be construed as a potential conflict of interest.

5 ARTICLE 4: EXTRACELLULAR MATRIX COMPONENTS REGULATE BONE SIALOPROTEIN EXPRESSION IN MDA-MB-231 BREAST CANCER CELLS

An adapted version of this chapter has originally been published as open-access article distributed under the terms of the Creative Commons Attribution (CC BY) license: “Keller, F., Bruch, R., Clauder, F., Hafner, M., and Rudolf, R. (2021). Extracellular Matrix Components Regulate Bone Sialoprotein Expression in MDA-MB-231 Breast Cancer Cells. *Cells* 10” (Keller et al., 2021); doi: 10.3390/cells10061304.

As first author, for this article the conceptualization was done together with R. Rudolf. Furthermore, experimental methodology, validation, and investigation was done independently. R. Bruch helped with computer applications for data analysis. After autonomous original draft writing, the supervisors Profs. Hafner and Rudolf and co-authors helped with review and editing. More precise contributions are honored in the article.

After a direct connection of basal membrane supplementation and enriched media composition with spheroid growth was observed, and since BSP expression further correlated with MDA-MB-231 proliferation in 3D, mechanistic regulations of certain ECM compounds were tested. Thereby, proteolytic stimuli of Dispase and MMP-9 were shown to enhance BSP signal intensity and cycloheximide treatment of permeabilized and non-permeabilized cultures indicated correlating protein neogenesis. This induced protein expression was consistent with the activation of ECM-contained latent TGF β and MMPs.

5.1 Abstract

Bone sialoprotein (BSP) has become a target in breast cancer research since it is associated with tumor progression and metastasis. The mechanisms underlying the regulation of BSP expression have been largely elusive. Given that BSP is involved in the homing of cancer cells in bone metastatic niches, we addressed regulatory effects of proteolytic cleavage and extracellular matrix components on BSP expression and distribution in cell culture models. Therefore, MDA-MB-231 human breast cancer cells were kept in 2D- and 3D-spheroid cultures and exposed to basement membrane extract in the presence or absence of matrix metalloproteinase 9 or the non-polar protease, Dispase. Confocal imaging of immunofluorescence samples stained with different antibodies against human BSP demonstrated a strong inducing effect of basement membrane extract on anti-BSP immunofluorescence. Similarly, protease incubation led to acute upregulation of anti-BSP immunofluorescence signals, which was blocked by cycloheximide, suggesting *de novo* formation of BSP. In summary, our data show that extracellular matrix components play an important function in regulating BSP expression and hint at mechanisms for the formation of bone-associated metastasis in breast cancer that might involve local control of BSP levels by extracellular matrix degradation and release of growth factors.

5.2 Introduction

Breast cancer is one of the most lethal illnesses for women and the most common type of malignancy besides skin cancer. Only 26 % of women with distant malignancies survive a 5-year time-period after diagnosis (Howlader et al., 2020). 65-75 % of metastases spread into bone tissue (Macedo et al., 2017) and develop features that lead to either osteolytic osteoporosis, osteoblastic sclerosis, or both. In osteolytic regions, niche formation for metastatic apposition is a common mechanism (Selvaggi and Scagliotti, 2005). According to current knowledge, bone resorption is not mediated by the cancer cells themselves, but primarily involves osteoclast activation (Taube et al., 1994). Mechanistically, some evidence suggests a role of growth factors such as transforming growth factor beta (TGF β), vascular endothelial growth factor (VEGF) and interleukins, such as interleukin-6 (IL-6), in the underlying remodeling processes at osteolytic metastatic sites (Bussard et al., 2008). However, the origin of these factors and the rationale for their release are still largely elusive. Investigations in nude mice indicate that homing and niche formation of breast cancer cells are independent of estrogen receptor status (Capietto et al., 2016) and thus, the mode of action might be transferable to different breast cancer types. Regularly, breast cancer lesions are located within trabecular bone regions that are rich in osteoblasts and micro-vessels and may overlap with the hematopoietic stem cell niche (Allocca et al., 2019). Although trabecular bone has the same lamellar structure as compact bone (Reznikov et al., 2015), slight differences in remodeling processes of these two bone types may give a hint why trabecular bone is preferred for metastasis. Indeed, while general features of bone extracellular matrix (ECM) are similar, such as the presence of collagenous (Type-I, Type-III and Type-V collagen) and non-collagenous proteins (proteoglycans, glycoproteins and glycoposphoproteins) as well as inorganic ECM (hydroxyapatite) (Lin et al., 2020), trabecular bone shows, in addition, increased levels of Wnt3a, β -catenin, osteocalcin and RANK-L (Li et al., 2017a). Consequently, interference with these pathways was found to have a huge impact on both, osteoblastic bone formation and osteoclastic bone resorption. For example, inhibition of β -catenin-mediated canonical Wnt-signaling (McCrea and Gu, 2010) led to decreased osteoblast differentiation and induced resorption of bone mass (Huang et al., 2007). In addition, RUNX2-mediated signaling cascades regulated expression of small integrin-binding ligand, N-linked glycoproteins (SIBLING) in early-stage bone formation processes (Kirkham and Cartmell, 2007), making them a crucial component of the ECM.

While bone-related cancer treatments often start at late stages by e.g. interfering with RANK-L signaling, the disturbance of bone homeostasis that leads to niche formation presumably starts early in the tumor development (Shupp et al., 2018). Physiologically, bone remodeling is a 5-stage process, consisting of quiescent, activation, resorption, formation, and mineralization phases (Owen and Reilly, 2018). Osteoclasts are key players in the bone resorption phase, during which small lacunae are formed through the removal of pre-existing mineral and organic components like hydroxyapatite and collagens. To that end, osteoclasts express various matrix metalloproteases (MMPs) that do not only participate in initial lacuna formation, but also serve additional functions such as cell recruitment (MMP-9), survival (MMP-9), ECM degradation (MMP-12), macrophage fusion and adhesion (MMP-14) or maturation (MMP-7 and MMP-14 through RANK/RANK-L guidance) (Hardy and Fernandez-Patron, 2020). Thus, MMPs are capable of interfering with various ECM components. Especially, osteopontin and bone sialoprotein (BSP), members of the SIBLING glycoprotein family, are known to have multiple MMP-related binding partners that might interfere with bone tissue

homeostasis to support metastatic niche generation (Bellahcène et al., 2008). Both proteins are markers for osteoblast differentiation (Hattar et al., 2005) and they are crucial for bone-tissue remodeling under physiological and tumor-associated conditions. Notably, tumor cells and their microenvironment synergistically interact with each other during cancer progression and this involves positive feedback-loops that can trigger severe effects based on minimal alterations of cancer and stroma cell interactions (Polyak et al., 2009). Unfortunately, in currently available cell-culture models, these small changes might be masked by undefined supplements, such as Matrigel or Basal Membrane Extract (BME). These biomaterials contain not only structurally important proteins, such as collagens, but also largely undefined mixes of signaling molecules with significant batch to batch variances (Prestwich, 2007). To address potential mutual interactions between tumor cells and their microenvironment, this work focused on effects of extracellular matrix components and proteases on cellular responses, with a focus on the SIBLING protein, BSP.

5.3 Materials and Methods

5.3.1 Cell Culture

To cultivate the MDA-MB-231 human breast cancer cell line, Dulbecco's Modified Eagle Medium (Capricorn; DMEM-HPA; Lot CP18-2096) was supplemented with 10 % fetal bovine serum (Capricorn; FBS-12B; Lot CP16-1422), 1 % penicillin/streptomycin (Sigma-Aldrich; P4333-100ML; Lot #91675) and 1 % Minimum Essential Medium Nonessential Amino Acids (Sigma-Aldrich; M7145-100ML; Lot RNBj0616). Passaging was done twice a week with seeding densities of 1×10^6 cells / T75 flask.

For two-dimensional cell analysis, circular cover slips (12 mm; VWR; ECN 631-1577; Lot #43395 819) were sterilized and placed in culture dishes (Greiner; 100x20 PS; 664 160) prior seeding. Then, 1.2×10^6 cells were cultured in 10 mL of media with appropriate supplements for 4 days prior fixation.

3D-cell culture was based on spheroids grown in 96-well cell-repellent microplates (Greiner; PS U-bottom; 650970; Lot E20063QS). Therefore, 4.000 to 10.000 breast cancer cells were set into one well with a total volume of 150 μ L and supplemented with 2.5 % BME (Biotechne; Cultrex; BME Pathclear; 3432-005-01; Lot 1514944) or 5 mM Type-I collagen (Roche Diagnostics; 11179179001; Lot #38429220) as required. To ensure a complete integration of all cells into the spheroids, cell aggregation was supported by initial centrifugation for 6 min at 500 rcf.

Dispase (EMD Millipore; SCM133; Lot #3168044) treatment studies were accomplished after 4 days of culturing. Culture controls were fixed directly prior treatment. For mode of action studies, cultures were washed twice with phosphate buffered saline (PBS), then exposed to Dispase for different time periods (2-10 min), rinsed with FCS-contained media to stop enzymatic induction, washed again twice and then either fixed or contingently further cultivated in media that ranged from common culture media to secondary treatment supplementing with 5 μ M cycloheximide (Sigma-Aldrich; Cycloheximide Solution; 18079-10X10ML-F; Lot #BCCB2943). The elapsed time from stop of protease treatment to fixation was about 2-4 min. Additionally, treatment controls were handled in parallel to the secondary treatment studies with common media exchanges and no added drugs.

400 ng / mL MMP-9 (abcam; ab168863; Lot GR3381311-1) treatment, stopping, washing and further processing – including timelines – were as for Dispase exposure. The culture was kept in MMP-9-containing FCS-free media for appropriate time periods (2-12 min), then rinsed with FCS-containing media, washed twice with PBS, and further cultivated for a total cultivation time of 25 min after first MMP-9 contact. Then all samples were fixed at once.

5.3.2 Sample preparation

For immunostaining analysis, samples were washed in PBS, fixed with 4 % paraformaldehyde in PBS (PFA) and washed again prior further handling.

2D-samples are permeabilized (0.4 % Triton X-100 in deionized water / 5 min) and blocked with bovine serum albumin fraction V (BSA; Carl Roth; 8076.3; Lot 479289436) buffer (3 % in PBS / 1 h) at room temperature (RT). Primary antibodies were diluted in BSA buffer and applied overnight (ON) at 4 °C, while secondary antibodies were incubated at RT (2 h). For intermediate washing, PBS was used (3 * 5 min / RT). Finally, samples were mounted using 10 % Mowiol (Sigma-Aldrich).

Whole mount spheroid samples were stained and cleared with Glycerol as published earlier (Keller et al., 2020; Nürnberg et al., 2020). In brief, fixed samples were permeabilized with 2 % Triton X-100 (2 min / RT) following an incubation with penetration buffer (10 % DMSO, 0.3 M glycine and 0.2 % Triton X-100 in PBS / 2 h). Blocking buffer (10 % DMSO, 1 % BSA and 0.2 % Triton X-100 in PBS / 2 h) was applied prior staining through appropriate immunoglobulin incubations in antibody buffer (5 % DMSO, 1 % BSA, 0.2 % Tween 20 and 10 µg / mL heparin in PBS / ON). Washing buffer (0.2 % Tween 20 and 10 µg / mL heparin in PBS) was applied three times after each antibody incubation step. For terminal clearing, samples were incubated with 88 % Glycerol in deionized water with the refractive index of 1.458 for 24 h. All buffer and clearing incubations were performed on a roller mixer at 37 °C. For storage, stained samples were kept dark at 4 °C.

5.3.3 Antibodies and dyes

Primary antibodies used had the following dilutions and specifications: AF165 (1:250; Immundiagnostik; AF165 (a-BSP); human monoclonal; Lot RP-SZ_423/03), FP21 (1:250; Immundiagnostik; FP21 (a-BSP); mouse monoclonal; Lot AK679/01B.2), IDK1 (1:100; Immundiagnostik; IDK1 (a-BSP); rat monoclonal; Lot AK606/05B.4), GM130 (1:400; BD Bioscience; 610822; mouse monoclonal; Lot #262), IGF1 (1:250; Invitrogen; PA5-27207; rabbit polyclonal; Lot TK2672961D), MMP-9 (1:250; abcam; ab38898; rabbit polyclonal to MMP9; Lot GR3204084-22), RUNX2 (1:500; Cell Signaling; D1L7F; rabbit monoclonal; Lot #2), TGFβ (1:500; abcam; ab92486; rabbit polyclonal to TGF beta 1; Lot GR3237963-2).

Secondary antibodies were incubated together with nuclear dye as follows: Anti-Rat 488 (1:500; Invitrogen; Alexa Fluor 488 donkey anti-rat; A21208; Lot #1810471), Anti-Mouse 555 (1:1000; Invitrogen; Alexa Fluor 555 goat anti-mouse IgG (H+L); A21424; Lot #2123594), Anti-Mouse 647 (1:1000; Invitrogen; Alexa Fluor 647 donkey anti-mouse IgG (H+L); A31571; Lot #2045337), Anti-Human 488 (1:1000; Invitrogen; Alexa Fluor 488 goat anti-human IgG (H+L); A11013; Lot #2110842), Anti-Human 647

(1:1000; Invitrogen; Alexa Fluor 647 goat anti-human IgG (H+L); A21445; Lot #2160390), Anti-rabbit 647 (1:1000; Invitrogen; Alexa Fluor 647 goat anti-rabbit IgG (H+L); A21246; Lot #55002A), DAPI (1:1000; Roche Diagnostics; 10236276001; Lot #28114320).

5.3.4 Data acquisition and analysis

Before starting the imaging, samples were stored within the same room to match the temperature. Confocal scans (Leica SP8, objectives HC PL APO 20 x /0.75 IMM CORR and HC PL APO CS2 63 x /1.2 W CORR, software Leica LAS-X 3.3.0) were captured with a resolution of 1024 x 1024 pixels when using 20x and 2048 x 2048 pixels for 63x objective pictures. Z-step size was set to 0.4 μm for 2D-analysis and 1 μm in case of whole mount spheroid investigations. To reduce the impact of glass surface related background, only signals above the nuclei center were included for quantifications. Therefore, we automatically segmented the DAPI signal and averaged their morphological centers as stack borders to remove all lower planes. Data analysis was performed using ImageJ software (v1.52) for either summed up or mean signal intensity measurements within cell culture contained regions of interest within confocal scans.

For statistics, GraphPad Prism 7 software was used. Normal distribution was ensured with the Kolmogorov-Smirnov test. One-way ANOVA with Holm-Sidak multiple comparison was applied. For the analysis, an appropriate number of experiments was executed (see corresponding figure legend) and 10 random cells were analyzed per experiment. The mean of means ensured a gaussian distribution in this case and multiple comparison t-tests without assumptions were applied. Significance was defined based on P-values (* $P < 0.05$, ** $P < 0.01$, *** $P < 0.001$, **** $P < 0.0001$).

5.4 Results

5.4.1 BME and Type-I collagen enhance BSP expression in MDA-MB-231 spheroids

Earlier investigations suggested a high impact of media composition on growth and morphology of MDA-MB-231 spheroids (Keller et al., 2019). Since here we wanted to gauge the role of ECM components on breast cancer cell growth and BSP expression, 3D-culture conditions with different extracellular supplements were compared. Therefore, 8,000 MDA-MB-231 cells were seeded on ultra-low attachment plates and supplemented with either 2.5 % BME, 5 $\mu\text{g} / \text{mL}$ Type-I collagen or nothing. Spheroid growth and BSP expression were analyzed after four days of culturing, because at later time points, cultures in the absence of either collagen or BME started to disintegrate. Thus, whole mount confocal imaging of fixed and permeabilized spheroid samples was performed upon staining with DAPI and two different anti-BSP antibodies, AF165 and FP21. To visualize the entire upper half of each spheroid, samples were optically cleared. For quantitative assessment, the sum of immunofluorescence signal per spheroid was normalized to the corresponding DAPI fluorescence. Qualitative analysis revealed that the subcellular localization of BSP immunofluorescence signals differed between AF165 and FP21 staining (Fig. 30A). Specifically, they appeared to label cell boundaries and perinuclear regions, respectively. Yet, despite the differential subcellular localization, the general trend of signal intensities was similar between the two antibody staining groups (Fig. 30B). Indeed, for both markers, BME

supplementation led to the highest signal increase compared to the condition without supplement. Type-I collagen resulted in an intermediate effect: compared to non-supplemented cultures, there were slightly rising levels of FP21 signals and unaltered AF165 signals, but signal intensities were lower than with BME.

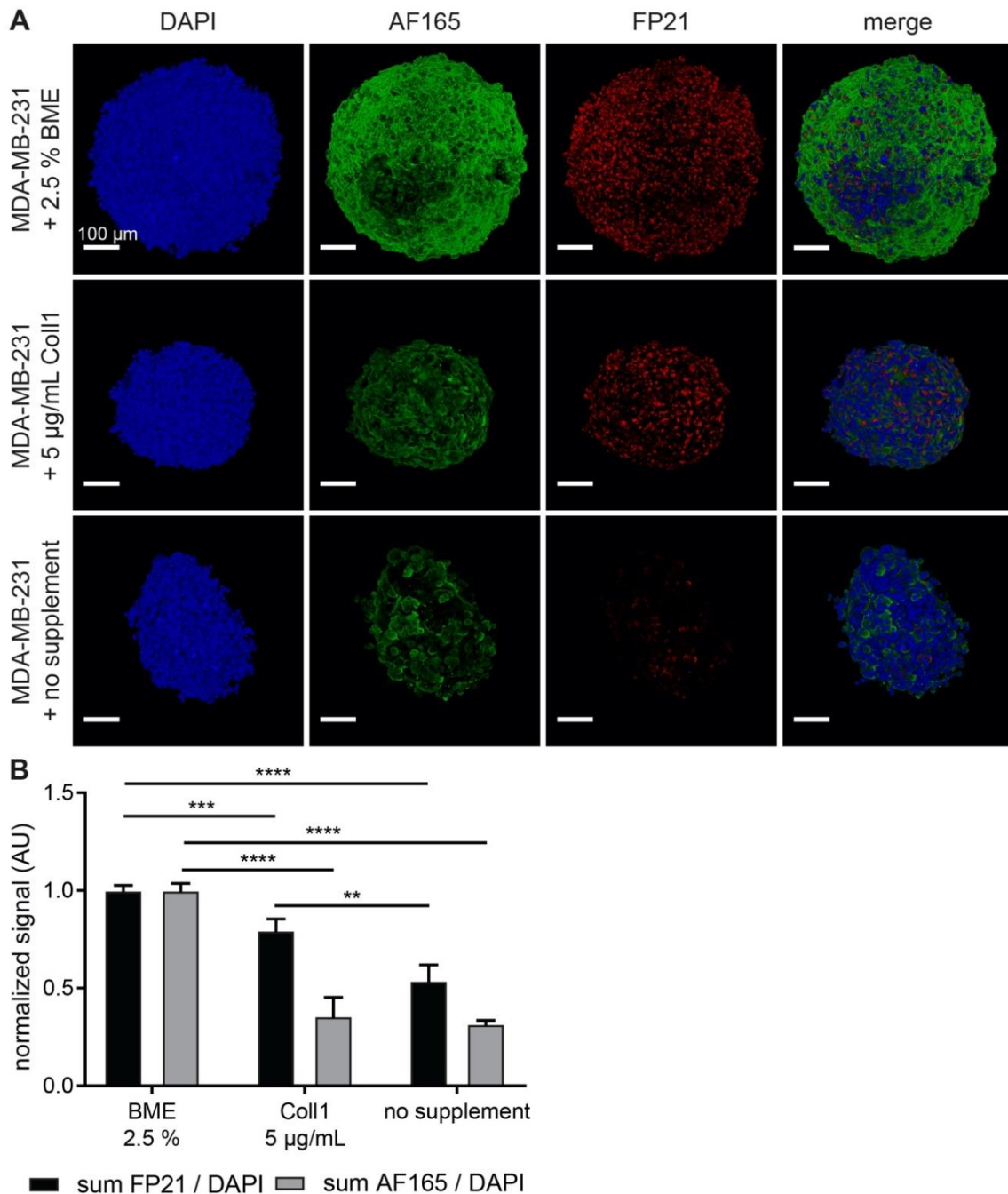


Figure 30. BME and Type-I collagen enhance anti-BSP immunofluorescence signals in MDA-MB-231 spheroids. 8,000 MDA-MB-231 cells were seeded in mono-culture spheroids and supplemented with 2.5 % BME, 5 µg / mL Type-I collagen, or no additive upon seeding. After 4 days, spheroids were fixed and stained for DAPI and BSP (AF165 and FP21) as indicated. A) Representative confocal image stacks of individual spheroids depicted as volume projections. B) Graphs showing quantitative analysis of fluorescence intensities normalized with DAPI. Mean + SD (n = 4; ** P < 0.01, *** P < 0.001, **** P < 0.0001). (Keller et al., 2021)(CC BY)

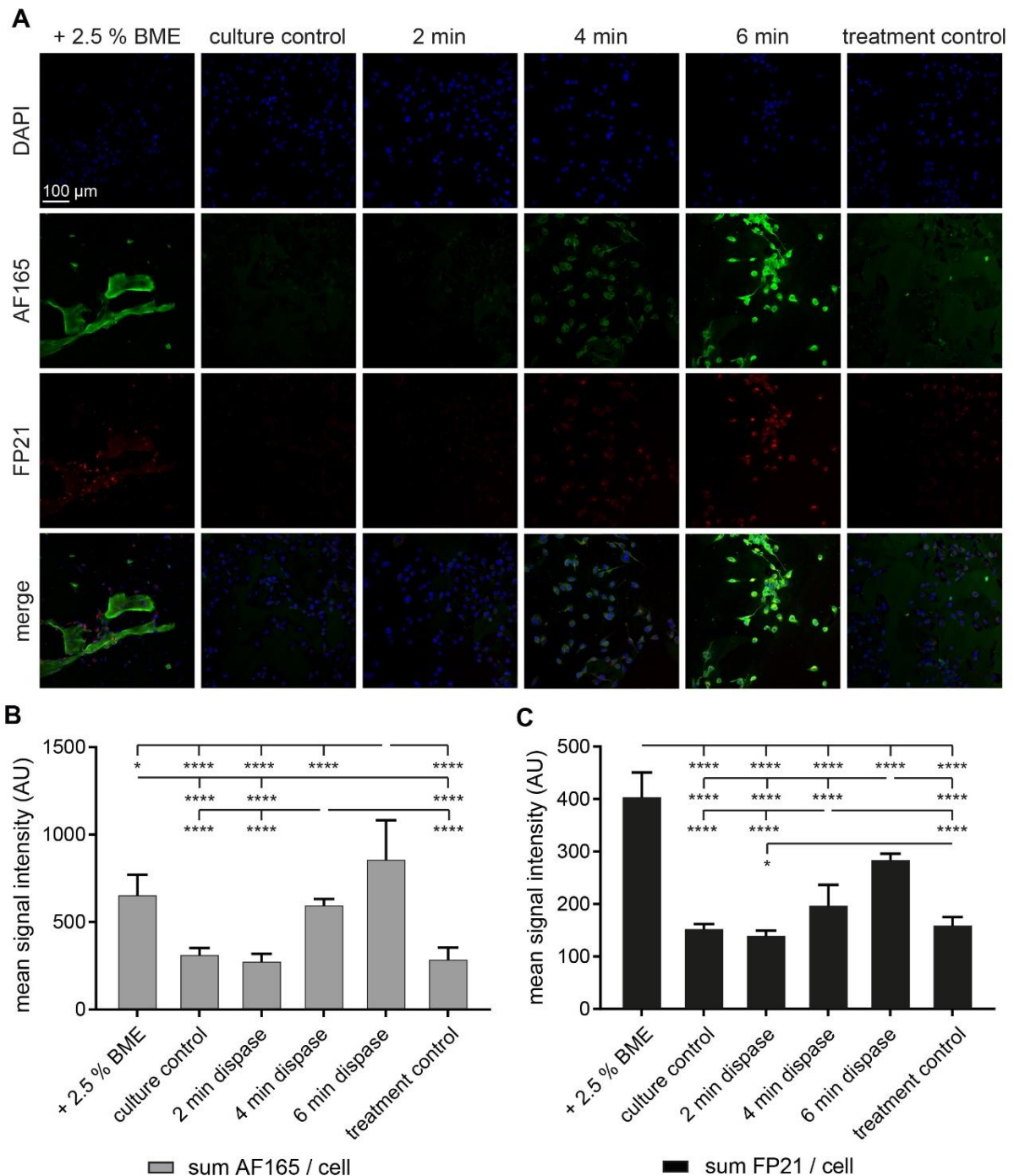


Figure 31. BME and short-term protease treatment enhance BSP immunofluorescence. 1,200,000 MDA-MB-231 cells were seeded in petri dishes containing glass cover slips. After 2 days, one culture was supplemented with 2.5 % BME within the media. Alternatively, no BME was added and after 4 days, cultures were treated with either Disperse for exposition times as indicated, or with fresh media as treatment control. Then, all cover slips were fixed and stained for DAPI and human BSP (AF165 and FP21). A) Representative confocal images in sum projections. B-C) Graphs showing quantitative analysis of fluorescence intensities per cell. Mean + SD (n = 3; * P < 0.05, **** P < 0.0001). (Keller et al., 2021)(CC BY)

5.4.2 Both BME and short-term protease treatment enhance BSP immunofluorescence

To investigate the effects of BME on BSP expression in MDA-MB-231 spheroids in more detail, further experiments in the absence and presence of BME were made, but now in 2D-adherent cultures. As for spheroids, also adherent cultures of MDA-MB-231 cells showed significantly higher fluorescence intensity signals for both, AF165 and FP21, in the presence of BME (+ 2.5 % BME, Fig. 31) than in its absence (culture control, Fig. 31). Next, since it is known that local proteolytic activities occur during metastatic niche formation, we also assessed whether these could be mimicked *in vitro* and might affect BSP expression. Therefore, Dispase treatments were set up to digest the ECM of the 2D-culture without inducing cell detachment. Thus, after four days in 2D-culture – in the absence of BME – MDA-MB-231 cells were exposed to Dispase for up to 6 min. This time range was chosen, because longer incubation resulted in a complete cell loss (data not shown). Then, samples were fixed, stained with anti-BSP antibodies, AF165 and FP21 (Fig. 31A), and mean signal intensities of confocal scans were quantitatively analyzed. On average, the time from stop of Dispase treatment to fixation of the cells lasted about 3 min. As shown in Fig. 31B and C, this revealed increased immunofluorescence signal intensities at the cell level for both antibodies upon Dispase treatment. The amount of induction correlated with Dispase exposure times and was independent from operative stress since treatment controls with parallel washing and media lacking Dispase did not result in enhanced immunofluorescence signals.

5.4.3 Dispase appears to induce BSP biosynthesis in MDA-MB-231 cells

To understand, whether the enhanced BSP immunofluorescence signals in the presence of Dispase were due to increased biosynthesis, BSP exocytosis, or both, additional tests were performed. Specifically, to test the effect of Dispase on BSP secretion, MDA-MB-231 2D-cultures were treated with or without Dispase for 6 min, incubated with normal medium or cycloheximide for 0 or 4 h, and then fixed. Subsequently, samples were immunostained in the absence of permeabilization with the two anti-BSP antibodies, AF165 and IDK1 (Fig. 32A). In this and the following experiment, IDK1 anti-BSP antibody was used instead of FP21, because FP21 showed an intracellular fluorescence signal (Fig. S13 and S14), and this was incompatible with the analysis of BSP release of non-permeabilized cells. Conversely, both, AF165 and IDK1 yielded extracellular signals and were, therefore, both employed here to consolidate the findings. Representative images of this test are shown in Fig. 32A. Quantitative analysis of the data revealed for AF165, that Dispase treatment resulted in a significant decrease of signal intensity per cell when comparing the culture control with treated conditions (Fig. 32B). The same trends were observed for IDK1, but no significances could be found with this antibody (Fig. 32C). A schematic of the experimental plans is depicted in Fig. 32D.

Next, to address the effect of Dispase on BSP expression, the same experiments as in figure 32 were carried out, but cells were now permeabilized upon fixation to reveal also intracellular BSP species. As illustrated with representative images in Fig. 33A, confocal image analysis showed that Dispase exposure for 6 min resulted in enhanced AF165 signal intensity per cell and this further increased upon 4 h of post-incubation in media (Fig. 33B, compare bars 1, 2, and 3). Application of cycloheximide blocked any such signal increase (Fig. 33B, bar 5). Similar trends resulted from IDK1-signal

quantification, although all differences were less pronounced (Fig. 33C). A schematic of the experimental plans is depicted in Fig. 33D.

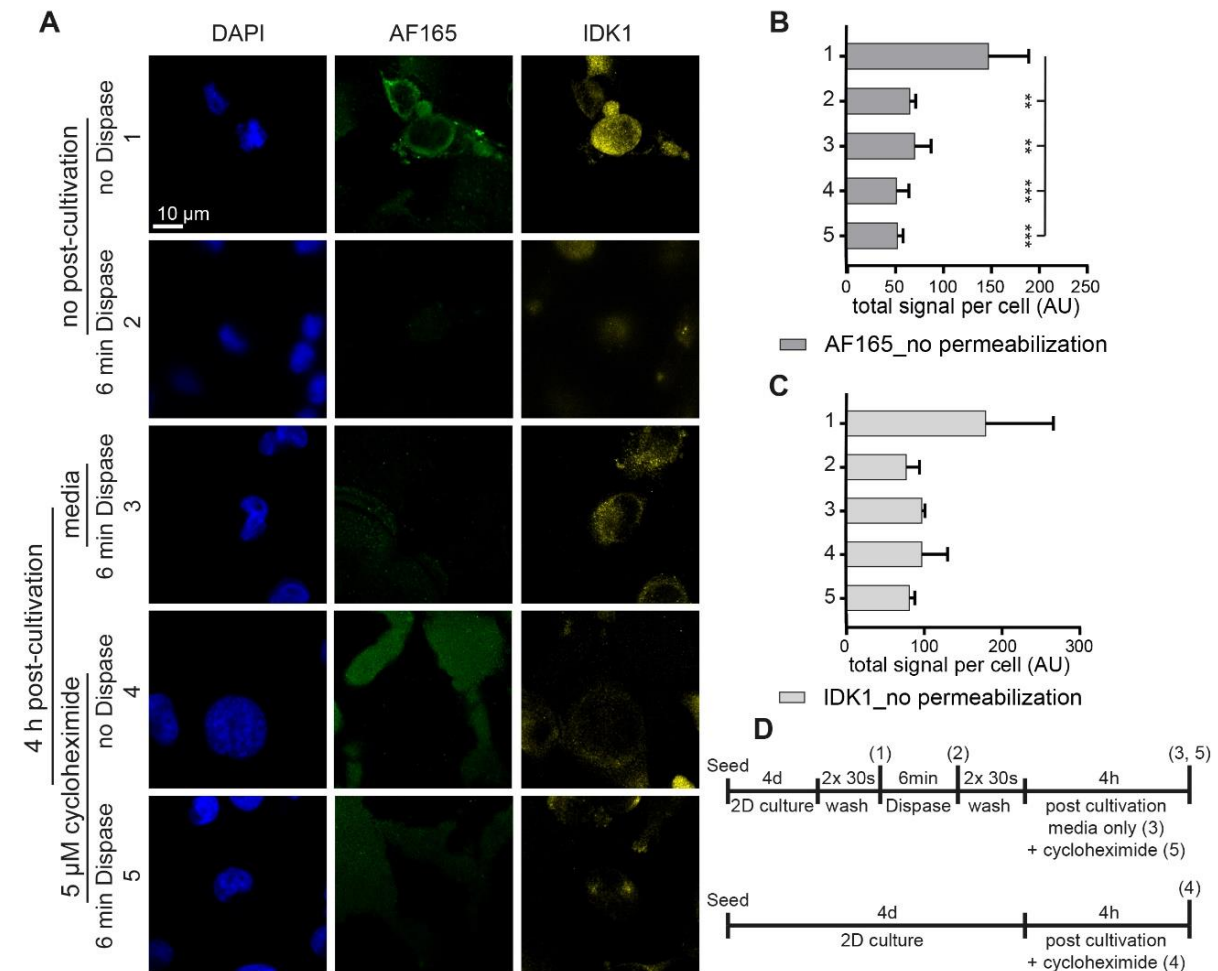


Figure 32. In the absence of permeabilization, BSP immunofluorescence levels are diminished upon Dispase exposition. 1,200,000 MDA-MB-231 cells were seeded in petri dishes containing glass cover slips. After 4 days, cultures were treated with Dispase and partially further cultivated with media or for secondary treatments with cycloheximide after washing, as indicated. PFA fixed and non-permeabilized samples were stained for DAPI and human BSP (AF165 and IDK1). A) Representative confocal images in sum projections. B-C) Graphs show quantitative analysis of fluorescence intensity per cell. See (D) for methodology. Mean + SD (n = 3; ** P < 0.01, *** P < 0.001). (Keller et al., 2021)(CC BY)

5.4.4 Regulatory markers are consistent with Dispase-induced BSP expression

To corroborate *de novo* BSP protein expression upon Dispase treatment, markers connected to BSP expression pathways were also examined. Thus, after Dispase treatment for 6 min, cells were fixed, permeabilized, and stained for nuclei (DAPI), BSP (AF165, FP21) and, in addition, for IGF1, RUNX2, TGFβ, or MMP-9. As illustrated in Fig. 34, TGFβ and MMP-9 revealed a signal increase, similar to signals of AF165 and FP21. Furthermore, while RUNX2 showed a similar rising trend upon Dispase treatment, IGF1 remained unchanged under these conditions.

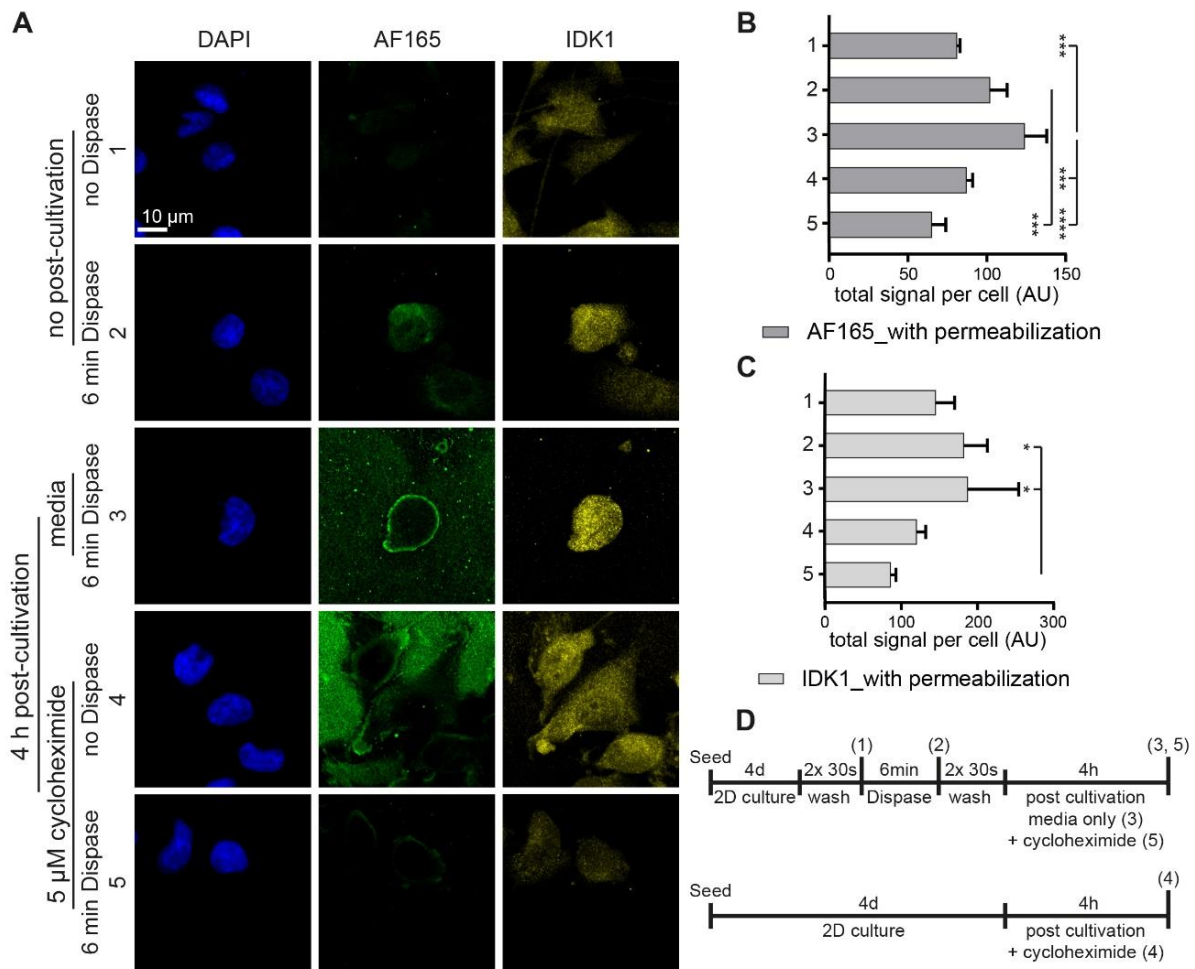


Figure 33. Dispace induces BSP biosynthesis in MDA-MB-231 cells. 1,200,000 MDA-MB-231 cells were seeded in petri dishes containing glass cover slips. After 4 days, cultures were treated with Dispace and partially further cultivated with media or for secondary treatments with cycloheximide after washing as indicated. PFA fixed samples were permeabilized and then stained for DAPI and BSP (AF165 and IDK1). A) Representative confocal images in sum projections. B-C) Graphs showing quantitative analysis of fluorescence intensity per cell. See (D) for methodology. Mean + SD (n = 3; * P < 0.05, *** P < 0.001, **** P < 0.0001). (Keller et al., 2021)(CC BY)

5.4.5 Dispace leads to an increase of BSP levels in MDA-MB-231 spheroids

Next, both BME and Dispace were applied to the MDA-MB-231 spheroid model. 4,000 MDA-MB-231 cells were seeded into ultra-low attachment plates and supplemented with 2.5 % BME to form spheroids. After four days in 3D-culture, spheroids were exposed to Dispace for up to 10 min. Then, samples were fixed, stained with AF165 and FP21 antibodies, and with DAPI. After optical tissue clearing, half of each spheroid was scanned by confocal imaging (Fig. 35A). For quantification, the sums of immunofluorescence signals were normalized to that of DAPI. For AF165, this revealed an increase in signal intensity after 2 min and 4 min of Dispace exposition, while longer incubation times returned signals to levels comparable to non-treated controls (Fig. 35B). For FP21, similar trends were observed, but only the differences between signal intensities after 2 min and 4 min Dispace treatment with 10 min exposed samples were significant (Fig. 35C). As a further control, the sum of DAPI signal per spheroid was

quantified to proof the integrity of the spheroids throughout investigation. This revealed no significant changes over the course of Disperse treatment (Fig. 35D). However, qualitatively, spheroid integrity and roundness started to decrease after 10 min of Disperse. A schematic of the experimental plan is depicted in Fig. 35E.

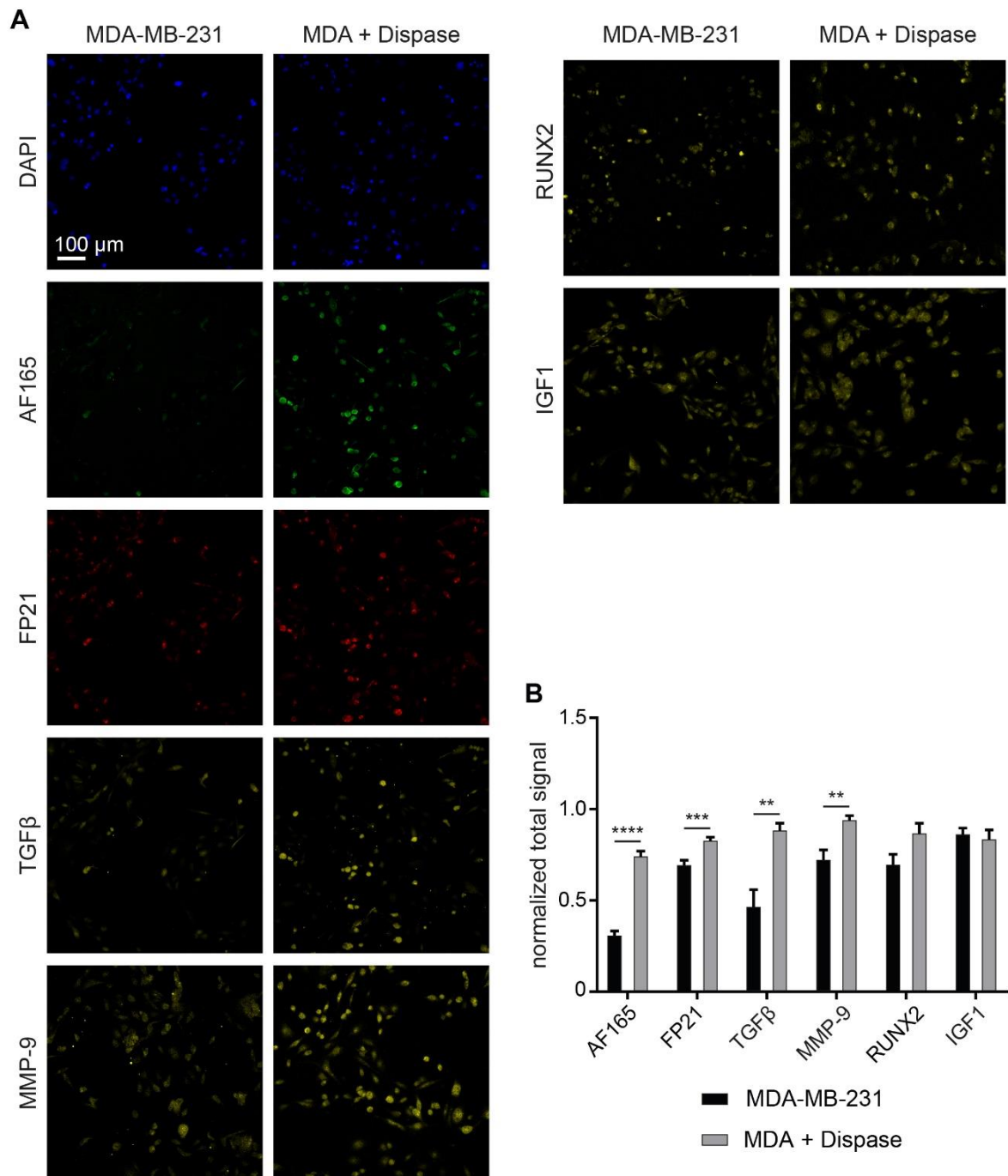


Figure 34. Immunofluorescence signals of regulatory markers are consistent with induced BSP expression. 1,200,000 MDA-MB-231 cells were seeded in petri dishes containing glass cover slips. After 4 days, cultures were treated with Disperse for 6 min. PFA fixed samples were permeabilized and then stained for DAPI, BSP (AF165 and FP21), and one additional regulatory marker (TGFβ, MMP-9, RUNX2, or IGF1). A) Representative confocal images in sum projections. B) Graph showing quantitative analysis of fluorescence intensity per cell. Mean + SEM (n = 6 for TGFβ, MMP-9, RUNX2, IGF1; n = 24 for AF165, FP21; ** P < 0.01, *** P < 0.001, **** P < 0.0001). (Keller et al., 2021)(CC BY)

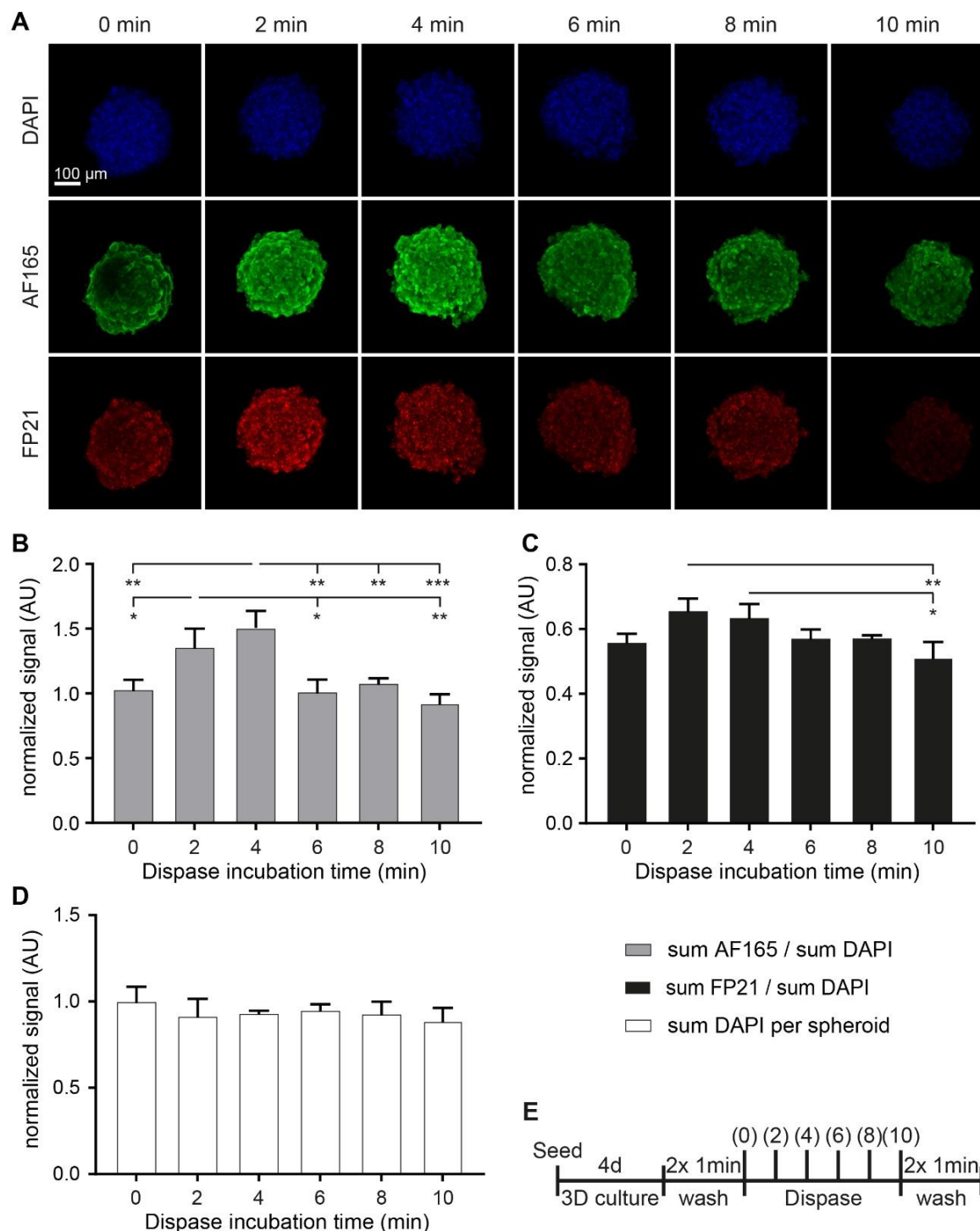


Figure 35. Dispase leads to a transient increase of anti-BSP immunofluorescence in MDA-MB-231 spheroids. 4,000 MDA-MB-231 cells were seeded in mono-culture spheroids and supplemented with 2.5 % BME upon seeding. After 4 days, spheroids were exposed to Dispase for different incubation times up to 10 min as indicated. PFA fixed spheroids were stained for DAPI and human BSP (AF165 and FP21). A) Representative confocal images in volume projections. B-D) Graphs show quantitative analysis of sum immunofluorescence intensities over the entire spheroid normalized to sum fluorescence intensities of DAPI (B-C) or sum of DAPI fluorescence signal per spheroid (D). E) Methodological overview. Mean + SD (n = 3; * P < 0.05, ** P < 0.01, *** P < 0.001). (Keller et al., 2021)(CC BY)

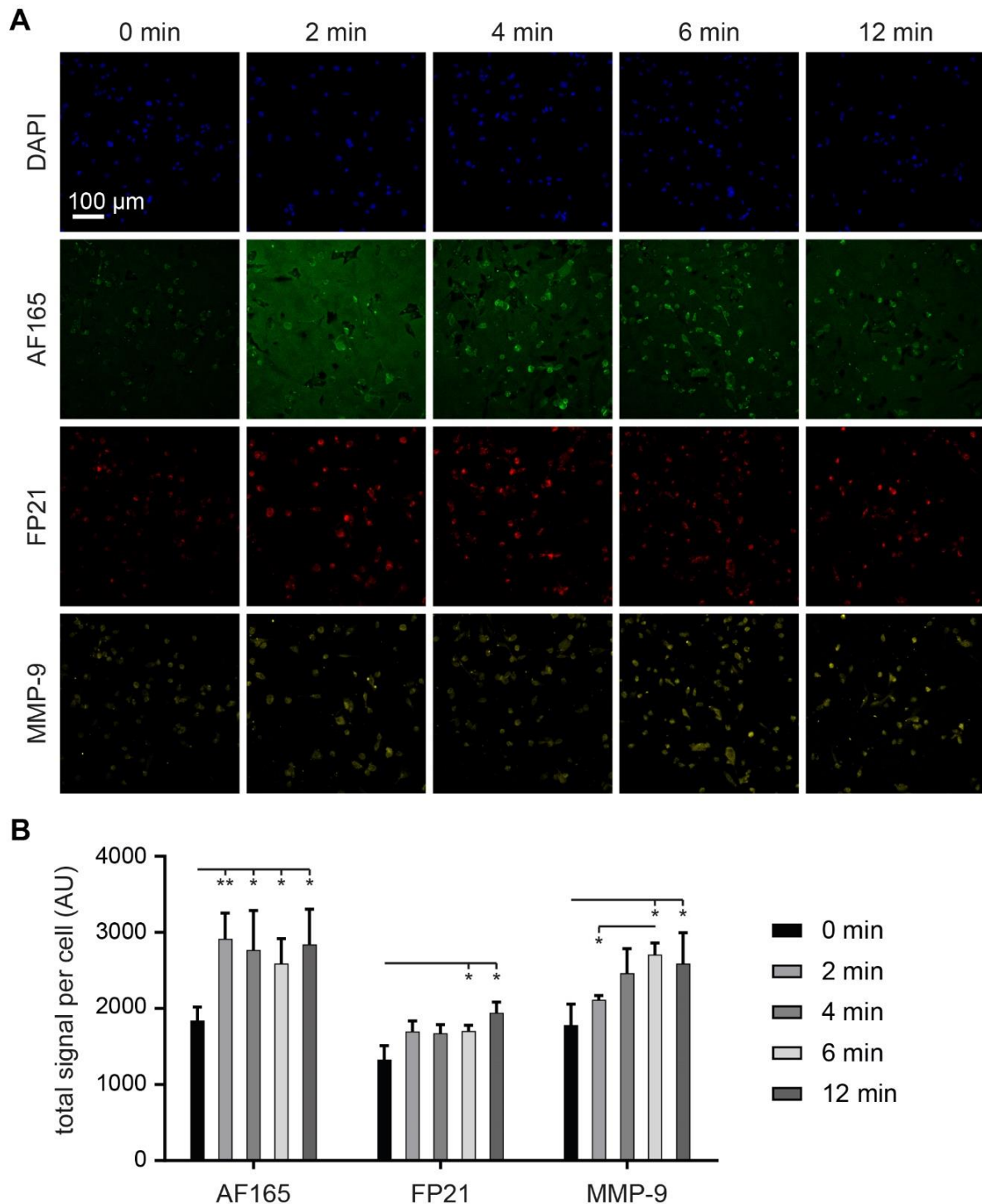


Figure 36. Incubation with MMP-9 protein enhances anti-BSP immunofluorescence. 1,200,000 MDA-MB-231 cells were seeded in petri dishes containing glass cover slips. After 4 days, cultures were treated with 400 ng / mL MMP-9 in FCS-free media for exposition times as indicated, or with fresh media as 0 min control. Then, samples were fixed and stained for DAPI and human BSP (AF165 and FP21) as well as MMP-9. A) Representative confocal images in sum projections. B-C) Graphs showing quantitative analysis of fluorescence intensities per cell. Mean + SD (n = 3; * P < 0.05, ** P < 0.01). (Keller et al., 2021)(CC BY)

5.4.6 3.6. MMP-9 exposure increases BSP signals in adherent MDA-MB-231 cultures

Finally, to substantiate the finding of a proteolysis-induced regulation of BSP levels with a physiologically relevant protease, we also tested the effect of MMP-9 incubation on anti-BSP fluorescence signal levels. Therefore, MDA-MB-231 cells were cultivated as adherent cultures for 4 days and then incubated with active human MMP-9 protein for up to 12 min. After washing, fixation, and permeabilization, samples were stained for BSP (AF165 and FP21) as well as for MMP-9 and with DAPI. As shown by representative images (Fig. 36A) and quantification of total intensity per cell (Fig. 36B), anti-BSP fluorescence signals increased significantly after 2 min and 6 min of MMP-9 treatment for AF165 and FP21, respectively. Similarly, also anti-MMP-9 fluorescence signals augmented after 6 and 12 min of incubation.

5.5 Discussion

Cancer cell homing and niche formation are critical steps in metastasis. Enhanced levels of BSP correlate with the development of bone lesions (Loibl et al., 2006). To better understand the interaction between BSP and metastatic niche formation in bone, we here addressed the effects of ECM components and extracellular proteolysis on BSP expression in breast cancer cells.

The present study showed that supplementation of MDA-MB-231 seeds with Type-I collagen enhanced spheroid formation and BSP expression compared to similar cultures without any addition of ECM components. This suggests that structural support by a collagen mesh might affect cell-cell interaction and protein expression patterns. These effects were excelled by BME. Although BME, being a biological supplement, is known to show considerable batch to batch variability (Benton et al., 2011), it contains the major structural ECM components, collagen and laminin (Kleinman et al., 1982), as well as a less defined mix of growth factors. These include fibroblast growth factor (FGF), transforming growth factor beta (TGF β), insulin-like growth factor (IGF), and epithelial growth factor (EGF) (Vukicevic et al., 1992), all known to strongly affect cellular behavior and to interfere with BSP expression (Midha et al., 2016). However, effects of adding either TGF β or IGF1 to the culture media in the absence of BME were inconsistent regarding BSP expression (not shown).

Next, given that BME and/or Matrigel contain also proteolytic activity (Gillette et al., 2003), and considering that cancer-cell homing is characterized by proteolytic preparation of the niche ECM (Mishra et al., 2011), we hypothesized that these processes might directly or indirectly affect also the expression pattern of cancer cell-derived BSP. Fittingly, acute incubation with the proteases, Dispase as well as MMP-9, the latter being a major protease expressed by metastatic cancer cells (Huang, 2018), led to an enhanced immunofluorescence staining signal upon use of different anti-BSP antibodies. The different anti-BSP antibodies employed in this study were chosen to validate each other by parallel use on the same samples. This was possible due to their different host origins: human, mouse, and rat for AF165, FP21, and IDK1, respectively. Since AF165 staining appeared primarily at the outside of the cells and the rim of spheroids, thus, exposed to extracellular receptors (Fig. S13 and Fig. S14), we hypothesize that the BSP species detected by this antibody participated in intercellular signaling. The same might be true for IDK1, because its staining was also localized to the membrane and its clinical relevance was suggested with MDA-MB-231 xenografts in nude rats: treatment with IDK1 led to decreasing tumor volumes (Zepp

et al., 2018). In contrast, FP21 signals were primarily located in the Golgi apparatus, and they were found in most cells throughout spheroids (Fig. S14). This might indicate the ubiquitous and continuous presence of BSP-mRNA in MDA-MB-231 cells. One may speculate that BSP species recognized by FP21 were early forms undergoing processing in the Golgi apparatus, while those labeled by AF165 and IDK1 were more mature forms and secreted. However, further proof would be needed to confirm such assumption. Currently, we can only speculate, whether and to what extent these data correlate to the observed effects of BME on the increase of anti-BSP immunofluorescence signals. Also, it remains elusive, which proteolytic activity on BME or in a cancer niche might be relevant here. Yet, for MMP-9, it is known that it is poorly expressed in intact tissue but strongly upregulated upon injury (Gordon et al., 2009) and relevant in bone resorption processes (Qian and Huang, 2010) through its role in osteoclast differentiation (Sundaram et al., 2007). Increased levels of MMP-9 could simulate wounds and therefore stimulate various associated actions (Manicone, Anne M.; McGuire, 2008), such as activating substrates like VEGF (Bergers et al., 2000) or TGF β (Yu and Stamenkovic, 2000). These, in turn, could further increase the amount of MMPs within direct cell proximity through triggering their expression (Yao et al., 2001) and might be relevant for regulating BSP expression.

Notably, the overt increase of BSP immunofluorescence signals upon acute Dispace treatment was blocked by cycloheximide. Given that cycloheximide inhibits translational processes in general (Schneider-Poetsch et al., 2010), this result suggests that proteolytic activities in the immediate vicinity of breast cancer cells might trigger feedback mechanisms that favor their homing and niche formation through a signal-transduction cascade that increases acute protein expression and/or release of BSP. This was corroborated by the basal availability of FP21 labeling throughout the spheroid, as this suggested constant BSP expression. Thus, assuming the presence of BSP mRNA in the cell and an average translation elongation speed of 4-6 amino acids per second (Stein and Frydman, 2019), *de novo* formation of BSP protein should be possible within roughly 1 min. This could be compliant with the timeline of upregulation of anti-BSP immunofluorescence upon Dispace and MMP-9 after only few minutes, as observed in the present study. In reality, some more minutes might have elapsed under these conditions, since protease inactivation, washing, and fixation steps might have summed up to an additional 2-3 min. Furthermore, it cannot be excluded, that the protease treatment also led to a partially enhanced accessibility of the anti-BSP antibodies to their epitopes, at least for the extracellular signals of AF165 antibody.

Assuming a proteolytic activation of BSP expression, this might be linked to protease activated receptors (PAR). These can be cleaved by trypsin, but also by ECM-contained enzymes like proteinase 3 or MMP-9. They may activate various signaling pathways such as ion channels, ERK or Ras via G-Protein signal transduction and therefore have also been studied as targets for tumor treatment (Heuberger and Schuepbach, 2019). MDA-MB-231 cells express the PAR2-receptor, and its activity has been linked to fast cellular responses. Upon PAR-2 activation, induced migration of MDA-MB-231 cells was shown to start within 2 min. Furthermore, within 5 min, trypsin-mediated protein synthesis based on pERK induction was observed. (Ge et al., 2004). Also, further patho-physiological effects have been linked to proteolytic activity. For example, in human bronchial epithelial cells, EGFR and TGF signaling were induced by protease exposure (Oguma et al., 2011) and MMP-9 proenzyme induced angiogenesis via FGF activation (Ardi et al., 2009). Furthermore, MMP-9 supported

pre-metastatic niche development upon induced overexpression in tumor stroma (Deryugina and Quigley, 2010) and, thus, can be related to ECM-mediated stimuli. Therefore, IGF1 (Ochiai et al., 2012), RUNX2 and TGF β (Ogata, 2008), as well as MMP-9 were studied in this context. The fast upregulation of BSP observed in the present study is consistent with proteolytic activation of latent pro-enzymes of TGF β (Shi et al., 2016) and MMP-9 (Toth et al., 2003), or with PAR-mediated signal transduction. Thus, this study points at how quickly local availability and activity of associated factors might change upon ECM induction.

5.6 Conclusions

In summary, this study reports that BSP protein expression in MDA-MB-231 breast cancer cells is enhanced upon incubation with Type-I collagen, basement membrane extract, and short-term proteolytic treatment using Dispase or MMP-9. These findings are consistent with a mutual interaction between cancer cell and lesion site that could favor feedforward and feedback mechanisms during cancer cell homing and/or niche formation.

Author Contributions

Conceptualization, F.K. and R.R.; methodology, F.K. and R.B.; validation, F.K.; formal analysis, F.K. and R.B.; investigation, F.K.; writing – original draft preparation, F.K.; writing – review and editing, F.K., R.B., F.C., M.H., R.R.; supervision, M.H. and R.R.; project administration, M.H. and R.R.; funding acquisition, M.H. and R.R. All authors have read and agreed to the published version of the manuscript.

Funding

This work was funded by the German Federal Ministry of Education and Research (BMBF) as part of the Innovation Partnership M²Aind, projects SM²all (03FH8I01IA) and M²OGA (03FH8I02IA) within the Starke Fachhochschulen-Impuls für die Region (FH-Impuls).

Conflicts of Interest

Immundiagnostik AG provided anti-BSP antibodies used in the present work. This company is active partner in the public private partnership M2OGA (03FH8I02IA) within the framework “Starke Fachhochschulen—Impuls für die Region” (FH-Impuls) that is funded by the German Federal Ministry of Research. At no point in this study, Immundiagnostik AG interfered with or influenced the work.

6 ARTICLE 5: A SCAFFOLD-FREE 3-D CO-CULTURE MIMICS THE MAJOR FEATURES OF THE REVERSE WARBURG EFFECT IN VITRO

An adapted version of this chapter has originally been published as open-access article distributed under the terms and conditions of the Creative Commons Attribution (CC BY) license: “Keller, F., Bruch, R., Schneider, R., Meier-Hubberten, J., Hafner, M., and Rudolf, R. (2020). A Scaffold-Free 3-D Co-Culture Mimics the Major Features of the Reverse Warburg Effect In Vitro. *Cells* 9, 1900” (Keller et al., 2020); doi: 10.3390/cells9081900.

As first author, conceptualization, experimental methodology, validation, data analysis and interpretation, writing, and editing were done under the supervision of Profs Hafner and Rudolf. Support was taken for computer applications during data analysis from R. Bruch. More precise contributions of all co-authors are honored in the article.

After the proof of altered cellular activity of cancer cell mono-cultures depending on stimuli contained in their provided ECM, direct cell-cell interactions were investigated. Since distinct mechano-transduction processes were estimated for co-culture spheroids based on their compact structures and the lack of stronger physical support, an array-based 3D-culture system was established. To ensure the transferability of breast cancer-based findings to other entities, fibroblasts were cultured together with HT-29 human colon cancer cells. Analyzing alterations in the metabolic activity of both, ECM producing fibroblasts and cancer cells, revealed signature interactions associated with the reverse Warburg effect as milestone for metabolic coupling. Membrane carrier expression was increased upon co-cultivation and metabolic markers showed a shift towards aerobic glycolysis. These properties are possible targets for treatment studies and refer to cancer progression. Therefore, a promising tool for preclinical trials has been established.

6.1 Abstract

Most tumors consume large amounts of glucose. Concepts to explain the mechanisms which mediate the achievement of this metabolic need have proposed a switch of the tumor mass to aerobic glycolysis. Depending on whether primarily tumor or stroma cells undergo such a commutation, the terms ‘Warburg effect’ or ‘reverse Warburg effect’ were coined to describe the underlying biological phenomena. However, current *in vitro* systems relying on 2D-culture, single cell type spheroids, or basal-membrane extract (BME/Matrigel)-containing 3D-structures do not thoroughly reflect these processes. Here, we aimed to establish a BME/Matrigel-free 3D-microarray cancer model to recapitulate the metabolic interplay between cancer and stromal cells that allows mechanistic analyses and drug testing. Human HT-29 colon cancer and CCD-1137Sk fibroblast cells were used in mono- and co-cultures as 2D-mono-layers, spheroids, and in a cell-chip format. Metabolic patterns were studied with immunofluorescence and confocal microscopy. In chip-based co-cultures, HT-29 cells showed facilitated 3D-growth and increased levels of Hexokinase-2, TIGAR, Lactate dehydrogenase, and TOMM20, when compared with HT-29 mono-cultures. Fibroblasts co-cultured with HT-29 cells expressed higher levels of Mono-carboxylate transporter 4, Hexokinase-2, Microtubule-associated proteins 1A/1B light chain 3, and

Ubiquitin-binding protein p62 than in fibroblast mono-cultures; they did so in both, 2D-culture, and chips. TMRM live-cell imaging of chip co-cultures revealed a higher mitochondrial potential in cancer cells than in fibroblasts. The findings demonstrate a crosstalk between cancer cells and fibroblasts that affects cellular growth and metabolism. Chip-based 3D-co-cultures of cancer cells and fibroblasts mimicked features of the reverse Warburg effect.

6.2 Introduction

The human colon adenocarcinoma cell line HT-29 is frequently used as a model for colorectal cancer. Colorectal cancer is one of the most frequent malignancies in the Western world. Although annual rates declined over the last decades, in 2017 the life-time risk of disease in the USA was at 4.6 % and 4.2 % for men and women, respectively, with a death rate of roughly 38 % (Siegel et al., 2017). Upon surgical removal of colorectal adenoma, 3 % of patients develop colorectal cancer within a median follow-up of 7.7 years (Løberg et al., 2014). Thus, effective treatment options are still needed. To decrease the median development time and cost, efficient pre-clinical screening methods are being investigated by researchers and developers worldwide (Sensi et al., 2018).

Like in many other malignancies, also colorectal cancer exhibits an extraordinarily high demand of energy, which is due to excessive metabolic activity and proliferation (Wilde et al., 2017). Therefore, total energy intake and macronutrient consumption serve as risk indicators (Sun et al., 2012). Furthermore, the characteristic of exuberant glucose uptake of colorectal lesions has been regularly exploited for diagnostic purposes in clinical molecular imaging by using ¹⁸F-fluorodeoxyglucose as a biomarker to identify metastatic sites (Benz et al., 2010). However, metabolic interactions within tumors are complex and involve heterogeneous tumor cell populations ranging from anabolic to catabolic forms that must be considered for the establishment of reliable cancer models (Xiao et al., 2019). Furthermore, also stromal components, such as mesenchymal cells, might participate in the metabolic interplay (Martinez-Outschoorn et al., 2014). While the increased overall glucose consumption in a tumor indicates an altered metabolic activity with a tendency towards aerobic glycolysis (Gatenby and Gillies, 2004), it is debated if all cells in a tumor undergo such a metabolic switch, or whether this occurs primarily for either, tumor or stromal cells. According to the Warburg hypothesis, it is the cancer cells that do so (Otto, 2016). However, this is in conflict with the observation that *in situ*, tumor cells often display intact mitochondria (Vyas et al., 2016). Thus, a reverse Warburg hypothesis was formulated that proposes the occurrence of a signaling from cancer cell to stromal fibroblast which modulates the metabolic behavior in the fibroblast and induces its shift to aerobic glycolysis (Martinez-Outschoorn et al., 2010). This may lead to the production of reactive oxygen species and a general change in redox status. Accordingly, extensive alterations within tumor tissue sites (Chiavarina et al., 2010), such as angiogenesis, migration, acidification, and hypoxia are the consequence (Wallace, 2012).

While cancer cells eventually enter a neoplastic state through reduced restrictions of proliferative potential (Porporato et al., 2018), a metabolic shift of fibroblasts can bring these cells from a suppressive to a cancer supportive state (Costa et al., 2018a). These stromal cells are usually referred to as cancer-associated fibroblasts (CAFs) and exhibit a strongly altered expression profile (Augsten, 2014), including overexpression of Smooth muscle actin or Vimentin (Shiga et al., 2015) and downregulation of

Caveolin 1. In addition, CAFs show enhanced autophagic activity, leading to higher expression levels of Microtubule-associated proteins 1A/1B light chain 3 (MAP1LC3, short LC3) and Ubiquitin-binding protein p62 (P62), both markers for autophagosome formation (Klionsky et al., 2016), and a loss of mitochondria through mitophagy (Pavlidis et al., 2012). This further favors a shift to aerobic glycolysis and accumulation of short carbon-rich metabolites like lactate, that can be shuttled to surrounding cancer cells (Wu et al., 2018). Therefore, Mono-carboxylate transporters (MCT) play an important role (Park et al., 2018), with MCT4 and MCT1 being principal exporters and importers, respectively. While MCT4 is often upregulated in CAFs, MCT1 expression is typically abundant in tumor cells (Whitaker-Menezes et al., 2011). The increased lactate levels can enhance metabolic activity in oxidative cancer cells (Fu et al., 2017; Pérez-Escuredo et al., 2016) and metabolic plasticity of tumor cell mitochondria is essential for adequate processing of nutrients available on a non-regular basis (Cannino et al., 2018). Such metabolic interactions can be instrumental for tumorigenesis, drug resistance, and tumor relapse (Fu et al., 2017).

Current metabolic models often either originate from primary tissue biopsies (Katt et al., 2016) or include xenograft tissues (Georges et al., 2019) relying on Matrigel or basal membrane extract (BME) as supporting material (Benton et al., 2011). However, a major issue here is that approaches based on primary cells are time consuming, expensive, and prone to low reproducibility due to intrinsic variability of the patient material itself. On the other hand, commonly used two-dimensional mono-cultures often lack important components of intercellular signaling, which are crucial for drug testing (Riedl et al., 2017). Therefore, Matrigel as naturally derived hydrogel scaffold for 3D-cell cultures that are more homogeneous compared to biopsies or xenografts have been the gold standard for a wide range of cell types (Fang and Eglen, 2017). These hydrogels provide biophysical cell-adhesive properties and can contribute to cell viability and growth (Nunes et al., 2019), but they also contain an ill-defined mixture of growth factors that influences cellular behavior in an unpredictable way due to batch-to-batch variances (Li and Kumacheva, 2018), potentially obliterating the examination of delicate alterations in short-term cultures.

We aimed to model the reverse Warburg effect using 2D- and 3D-co-cultures of human HT-29 colon cancer cells and human CCD-1137Sk fibroblasts. While Dynarray cell chip microarray cultures reflected major aspects of the reverse Warburg effect, 2D-cultures partially reproduced these findings but lacked effects on HT-29 cells. Conversely, spheroid co-cultures did not show enhanced growth, suggesting a lack of efficient metabolic advantage under this condition.

6.3 Materials and Methods

6.3.1 Cell Culture

CCD-1137Sk human fibroblasts were kept in Iscove's Modified Dulbecco's Medium (Capricorn; IMDM-A; Lot #CP18-2245) supplemented with 10 % fetal bovine serum (Capricorn; FBS-12B; Lot #CP16-1422), and 1 % penicillin/streptomycin (Capricorn; PS-B; Lot #CP18-2207). HT-29 human colon cancer cells were cultivated in McCoy's 5a media (Capricorn; MCC-A; Lot #CP19-2689), supplemented with 10 % FBS-12B and 1 % PS-B. The media for MDA-MB-231 human breast cancer cells consisted of Dulbecco's Modified Eagle Medium (Capricorn; DMEM-HPA; Lot #CP18-2096) supplemented with 10 % FBS-12B, 1 % PS-B and 1 % Minimum Essential Medium

Nonessential Amino Acids (Capricorn; NEAA-B; Lot #CP17-1726). All cell lines were passaged twice per week with a seeding density of 1×10^6 cells / T75 flask. 2D-cell culture analysis was based on cover slips (12 mm; VWR; ECN 631-1577; Lot #43395 819) placed in cell culture dishes (Greiner; PS; 664 160) before seeding a total of 1.2×10^6 cells in appropriate ratios and culturing for four days.

6.3.2 Spheroid Formation

To analyze growth behavior, the spheroid formation was performed with a total of 6,000 cells seeded per well within different mono- and co-culture ratios using 96-well cell-repellent microplates (Greiner; 650970; Lot #E2001347). BME dependency of the spheroid metabolism was analyzed setting 250 HT-29 or 4,000 CCD-1137Sk cells in mono-culture condition. Additionally, 250 cancer cells were co-cultivated together with 500 fibroblasts. This ensured a more homogeneous spheroid mean diameter distribution around 300 μm after four days, preventing size dependent effects from influencing the cellular biology approach. Appropriate amounts for 2.5 % or 10 % BME dissolved in media were added immediately after the culture suspensions. Cell aggregation was enhanced by centrifugation for 6 min at 500 rcf.

6.3.3 Dynarray Preparation

For Dynarray (300MICRONS; Dynarrays MCA-C300-300-PC) seeding, the microarrays were sterilized with 100 %, 70 %, 50 %, and 30 % isopropanol for 1 min, respectively, before washing twice in sterile deionized water. Then, 100 μg / mL Type-I collagen (Roche; rat tail Collagen; 11179179001) dissolved in 150 μL sterile deionized water was incubated 1 h on top of the cavities at room temperature for coating the microarray. The cancer cells and fibroblast cells were seeded at appropriate ratios to result a density of 4,000 cells per cavity. The Dynarrays were placed in cell culture dishes and after 4 hours at 37 °C and 5 % CO_2 , 10 mL of media was added. After fixation in 4 % PFA / PBS, Dynarrays were either stained, cleared, and imaged as whole mounts, or orthogonal Dynarray slices were made. In brief, chips were embedded in 2 % agarose (Roche; Agarose MP; 11 388 983 001) dissolved in TAE buffer (0.04 M tris base, 0.02 M acetic acid, 0.01 M EDTA) and 50 μm thick slices were collected using a vibratome (Leica Biosystems; Vibratome Model VT1000S). To label the cells with CellTracker, mono-type suspensions of either HT-29 or CCD-1137Sk cells were incubated 1 h in FBS-free media (37 °C / 5 % CO_2) and washed with PBS directly before co-seeding. For live-cell analysis, Dynarray cultures were incubated in TMRM-containing complete media (30 min / 37 °C), washed 3 times with PBS and transferred into 25 mM HEPES buffer to ensure steady pH conditions throughout the imaging process.

6.3.4 Antibodies and Dyes

Primary antibody incubation was performed in a static incubation (ON / 4 °C) for 2D and on a roller mixer (ON / 37 °C) for 3D-samples. Secondary antibodies were used for 1 h at room temperature for flat and as the primary antibodies for spheroid and Dynarray preparation. Antibody or dye details and concentrations were as follows. Anti-Carcino Embryonic Antigen CD66e (CEA; Thermofisher scientific; MIC0101; Lot #VD2969991; dilution 1:250), Anti-Type-I Collagen (Collagen 1; Rockland; 600-401-

103-0.5; Lot #41250; dilution 1:100), Anti-Type-IV Collagen (Coll4; Rockland; 600-401-106-0.5; Lot #40995; dilution 1:100), CellTracker Deep Red (CTdr; Lifetechnologies; C34565; Lot #1781143; stock 2 mM; dilution 1:1000), CellTracker Green (CTg; Lifetechnologies; C7025; Lot #1913919; stock 10 mM; dilution 1:1000), DAPI (Roche; 10236276001; Lot #28114320; 1 mg / mL; dilution 1:1000), Anti-Hexokinase II (HK-2; abcam; ab209847; Lot #GR3220265-2; dilution 1:100), Anti- Microtubule-associated proteins 1A/1B Light Chain 3 (LC3; CellSignalling; 3868S; Lot #11; dilution 1:200), Anti-Lactate dehydrogenase (LDH; abcam; ab47010; Lot #GR3307117-1; dilution 1:1000), Anti-Monocarboxylate Transporter 1 (MCT1; Sigma-Aldrich; Anti-SLC16A1; Lot #C114705; dilution 1:500), Anti-Monocarboxylate Transporter 4 (MCT4; SantaCruz Biotechnology; sc-376140; Lot #D3018; dilution 1:400), Anti-Ubiquitin-binding protein p62 protein (P62; Progen; GP62-C; Lot #703241-03; dilution 1:100), Anti-Succinate Dehydrogenase (SDH; Thermofisher scientific; 459200; VC296863; dilution 1:200), Anti-TP53-induced glycolysis and apoptosis regulator (TIGAR; abcam; ab37910; Lot #GR3210648-2; dilution 1:500); Anti-Tetramethylrhodamine (TMRM; Invitrogen; T-668; 500 μ M; dilution 1:2000), Anti-Translocase of outer mitochondrial membrane 20 (TOMM20; Sigma-Aldrich; HPA011562-100UL; Lot #4450; dilution 1:400), Goat α -mouse AF 488 (M; Invitrogen; A11001; Lot #1834337; dilution 1:1000), Donkey α -rabbit AF 488 (R; Invitrogen; A21206; Lot #176375; dilution 1:1000), Goat α -guinea pig AF 555 (GP; Invitrogen; A21435; Lot #2015338; dilution 1:1000), Goat α -rabbit AF 647 (R; Invitrogen; A21246; Lot #55002A; dilution 1:1000).

6.3.5 Data Acquisition

Brightfield (Zeiss Axiovert 25 / objective CP-ACHROMAT, 5x/0.12Ph0) and confocal (Leica SP8, objectives HC PL FLUOTAR 10x /0.30, HC PL APO 20 x /0.75 IMM CORR and HC PL APO CS2 63 x /1.2 W CORR) microscopy and the evaluation of spheroid size (Chen et al., 2014) were conducted as published earlier (Keller et al., 2019). For confocal analysis, pictures with a resolution of 1024 x 1024 pixels were taken with 1 μ m z-steps for 3D-stacks. Whole mount staining was enhanced by a clearing procedure based on the Glycerol clearing protocol as published (Nürnberg et al., 2020). Briefly, samples were immersed in an aqueous glycerol solution with a refractive index of 1.459 containing 88 % of glycerol (ON / 37 °C) on a roller mixer. Microscopy was performed in the same solution. Therefore, samples were fixed in 4 % PFA / PBS, treated with 2 % Triton X-100 (2 min / RT), incubated in penetration buffer (0.2 % Triton X-100, 0.3 M glycine, 20 % DMSO in PBS / 30 min / 37 °C), blocked with bovine albumin serum (1 % BSA, 0.2 % Triton X-100, 10 % DMSO in PBS / 2 h / 37 °C) and stained with antibodies incubated in appropriate buffer (0.2 % Tween 20, 10 μ g / mL heparin, 1 % BSA, 5 % DMSO in PBS / ON / 37 °C). For intermediate washing steps, a buffer containing 0.2 % Tween 20 and 10 μ g / mL heparin in PBS was used.

6.3.6 Data Analysis

2D-image analysis and assembly were done with ImageJ software (v1.48v) and based on signal intensities in split channels. In 2D, regions of interest were set based on DAPI and CEA channel threshold.

For 3D-image analysis and corresponding data visualization, a dedicated Python script was established. Each stack was divided into a set of small non-overlapping regions with x, y, and z dimensions of 32, 32, and 16 voxels, respectively. To minimize the

influence of background signals, the images were first segmented based on their nuclei channel. Therefore, the DAPI signal of an image volume was smoothed using three-dimensional Gaussian blur and then segmented using a threshold value calculated by Otsu's method (Smith et al., 1979). To also include adjacent regions outside the nuclei, high sigma values of 4, 4, and 0 for the x, y, and z dimension were used for Gaussian smoothing. An exemplary sum-projection of a segmentation including the visualization of the region borders can be seen in Fig. 42C. Only regions with more than 50 % foreground based on segmentation were included. For the remaining regions, the average foreground intensity of the voxels was calculated for DAPI, CEA and the corresponding marker channel. For visualization, composite results of 5 cavities for each culture type were assembled.

Statistics were calculated with GraphPad Prism 7. For direct comparison of two data points within immunofluorescence evaluation, significance was defined based on the P-values (* $P \leq 0.05$; ** $P \leq 0.01$; *** $P \leq 0.001$; **** $P \leq 0.0001$) in multiple comparison t-test analysis without assumptions. Normal distribution and homoscedasticity were tested with the Kolmogorov-Smirnov procedure. For testing of co-localization, the Coloc2 algorithm of ImageJ was used with a PSF of 3.0 and 10 randomizations. The Pearson's correlation (R) above threshold was evaluated. Furthermore, one-way ANOVA with Holm-Sidak multiple comparison was performed for the growth curve comparisons. Significance was defined based on P-values (* $P \leq 0.05$; ** $P \leq 0.01$; *** $P \leq 0.001$; **** $P \leq 0.0001$).

6.4 Results

6.4.1 MCT4 as well as markers for glycolysis and autophagy are upregulated in CCD-1137Sk fibroblasts upon co-culture with HT-29 cells

First, we investigated whether co-cultures of HT-29 cells and CCD-1137Sk fibroblasts exhibited an altered expression of lactate transporters as compared to the respective mono-cultures. Therefore, 2D-mono- and co-cultures were set up and cultured at a confluency of up to 80 % for four days. Then, immunofluorescence staining was first done for MCT1 and MCT4, as markers for lactate influx and efflux, respectively. While both, MCT1 and MCT4, were stronger expressed in HT-29 tumor cells than in fibroblasts, only MCT4 increased significantly in the fibroblasts upon co-cultivation (Fig. 37A – C). Conversely, MCT1 remained low in fibroblast cells under all conditions (Fig. 37A – C). Discrimination between HT-29 and CCD-1137Sk cells was done on the basis of three criteria. First, HT-29 consistently grew in dense islets, both, in mono- and co-culture, whereas CCD-1137Sk typically showed a spindle-shaped morphology and grew in between the HT-29 islets in co-cultures. Second, molecular markers, Carcinogen embryonic antigen (CEA) (Tiernan et al., 2013) and Type-IV collagen (Coll4) (Pastor-Pareja, 2020), were primarily expressed in either HT-29 or CCD-1137Sk cells, respectively (Fig. S15). These served as additional confirming features for the cell type selection. Finally, DAPI staining of CCD-1137Sk cell nuclei was mostly darker than that of HT-29 cells and showed a more elongated and larger area. This trait was also used for the later analyses of 3D-data sets.

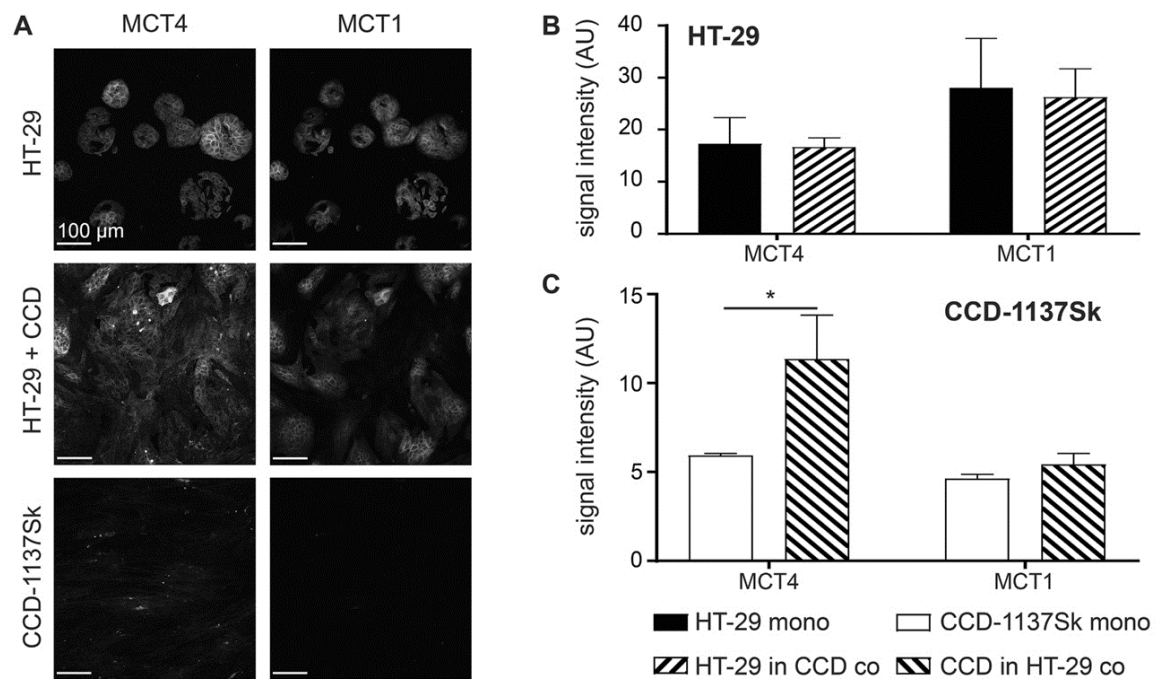


Figure 37. Mono-layer co-cultures of HT-29 and CCD-1137Sk show enhanced expression of MCT4 in fibroblasts. HT-29 and CCD-1137Sk cells were either seeded alone or in co-culture and grown to a subconfluent state for four days. Then, cells were fixed and stained with DAPI as well as antibodies against MCT4 and MCT1 as markers for nuclei, lactate export, and lactate import, respectively (A–C). A) Representative confocal images of fluorescence staining for markers and cultures as indicated. B–C) Graphs show quantitative analysis of fluorescence intensity values for markers and cell type as indicated. Mean + SEM (n = 3 experiments; * P < 0.05). (Keller et al., 2020)(CC BY)

Next, the effects of co-culturing of HT-29 and CCD-1137Sk cells on their metabolic profiles were addressed. Therefore, immunofluorescence staining of the cultures as those mentioned in Fig. 37 was done for Hexokinase-2 (HK-2), Lactate dehydrogenase (LDH), TP53 Induced Glycolysis and Apoptosis Regulator (TIGAR), Succinate dehydrogenase (SDH), and Translocase of outer mitochondrial membrane 20 (TOMM20), as markers for glucose breakdown, pyruvate-lactate metabolism, negative glycolysis regulation, oxidative phosphorylation, and mitochondrial content, respectively (Fig. 38A – C) (Wilde et al., 2017). While HT-29 cells did not show any significant change in any of these markers, CCD-1137Sk cells displayed altered expression levels consistent with an upregulation of glycolysis and a downregulation of oxidative phosphorylation. Indeed, HK-2 went up, whereas TIGAR and TOMM20 decreased. LDH and SDH remained unaltered under these conditions.

The data on lactate transporters and metabolic markers were consistent with a co-culture induced switch of the CCD-1137Sk cells towards a catabolic phenotype. To further corroborate this possibility, expression of markers for autophagy, namely LC3 and P62, were assessed under mono- and co-culture conditions. As shown in Fig. 39, both proteins were upregulated in CCD-1137Sk in co-culture with HT-29 cells. Conversely, no alteration of LC3 or P62 levels were found in HT-29 cells upon co-culturing with fibroblasts.

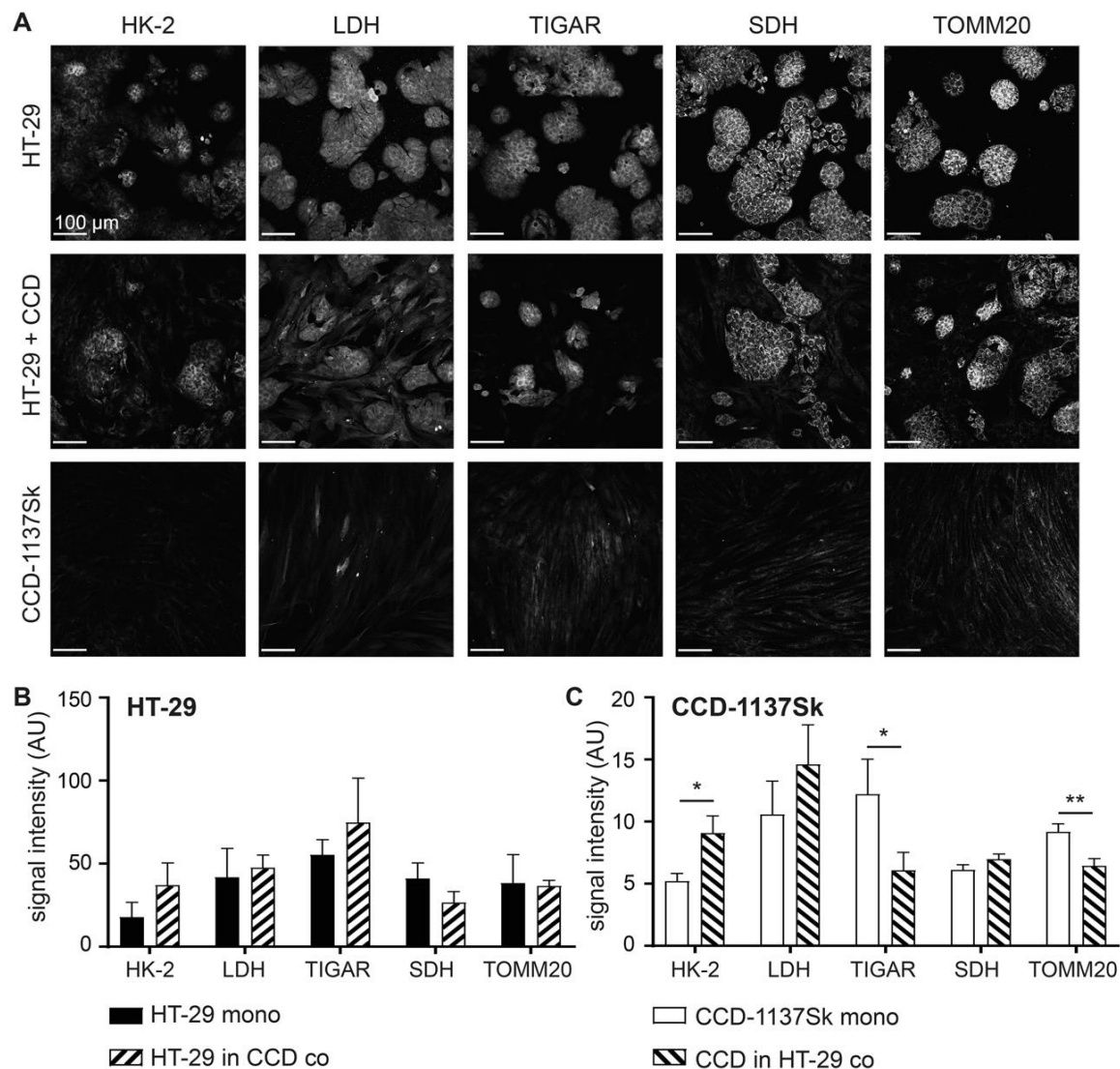


Figure 38. Fibroblasts in mono-layer co-cultures of HT-29 and CCD-1137Sk show enhanced glycolytic and reduced oxidative phosphorylation markers. HT-29 and CCD-1137Sk cells were either seeded alone or in co-culture and grown to a subconfluent state for four days. Then, cells were fixed and stained with DAPI as well as antibodies against HK-2, LDH, TIGAR, SDH, and TOMM20 as markers for nuclei, glucose breakdown, pyruvate-lactate metabolism, negative glycolysis regulation, oxidative phosphorylation, and mitochondrial content, respectively (A–C). A) Representative confocal images of fluorescence staining for markers and cultures as indicated. B–C) Graphs show quantitative analysis of fluorescence intensity values for markers and cell types as indicated. Mean + SEM (n = 3 experiments; * P < 0.05, ** P < 0.01). (Keller et al., 2020)(CC BY)

Finally, to investigate whether the observed modifications of fibroblast metabolism were exclusively related to the co-culture with HT-29 cells, analogous experiments were carried out with the human breast cancer cell line MDA-MB-231 in mono- and co-culture with CCD-1137Sk fibroblasts. As shown in supplementary Figs. S16 – S18, the overall results were essentially the same: upon co-culture with MDA-MB-231 cells, CCD-1137Sk cells showed enhanced levels of MCT4, HK-2, LC3, and P62 and reduced presence of TIGAR and TOMM20. In contrast, the breast cancer cells did not show any such alteration.

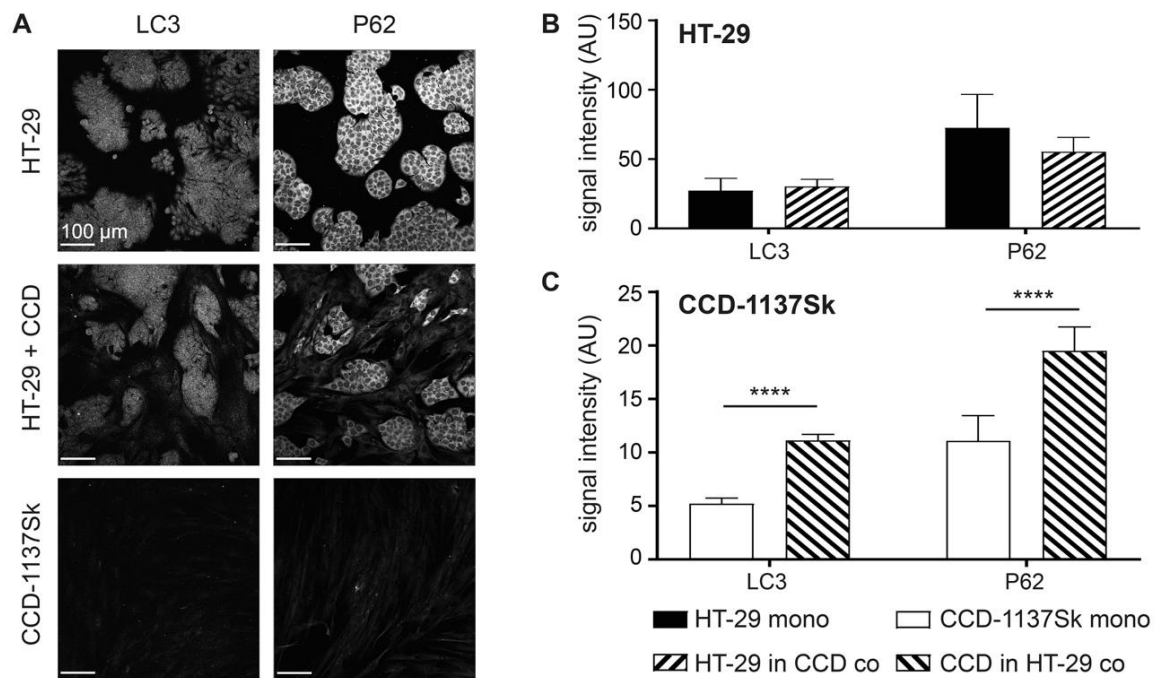


Figure 39. Fibroblasts in mono-layer co-cultures of HT-29 and CCD-1137Sk display enhanced levels of autophagy markers. HT-29 and CCD-1137Sk cells were either seeded alone or in co-culture and grown to a subconfluent state for four days. Then, cells were fixed and stained with DAPI as well as antibodies against LC3 and P62 as markers for nuclei and autophagy (A–C). A) Representative confocal images of fluorescence staining for markers and cultures as indicated. B–C) Graphs showing quantitative analysis of fluorescence intensity values for markers and cell type as indicated. Mean + SEM (n = 3 experiments; **** P < 0.0001). (Keller et al., 2020)(CC BY)

6.4.2 Addition of CCD-1137Sk fibroblasts does not alter growth of HT-29 spheroids

Although 2D-cultures are ideal for quantitative analyses, they often lack gradients of drugs, oxygen, waste products, and nutrients as they are present *in vivo*. Therefore, we next established three-dimensional spheroid co-cultures with CCD-1137Sk fibroblasts and HT-29 colon cancer cells. To test the best conditions for a homogeneous distribution of both cell types in spheroids, different ratios of cancer cells and fibroblasts were either seeded together or sequentially in ultra-low attachment plates and allowed to grow for up to 30 days. Every seeding procedure resulted in rather round spheroids. Since the condensation of the first cell population into a spheroid was typically accomplished within two days (Fig. 40A), the secondary seeding in the sequential protocols was performed on that day. Size measurements of the mean diameters revealed, that neither the different tested cell-line ratios, nor seeding sequences altered assembly or growth of spheroids (Fig. 40B). Indeed, all spheroids with cancer cells alone or cancer cells plus fibroblasts showed a very similar behavior: after an initial condensation phase, which led to a minimal mean diameter of spheroids at two to three days, they followed an asymptotic growth curve and reached a maximal spheroid diameter of approximately 1,000 μm (Fig. 40B). Thus, CCD-1137Sk fibroblasts did not contribute to any major change in growth of HT-29 spheroids. Accordingly, fibroblast mono-culture spheroids remained small and did not increase in size over time (Fig. 40B). Examination of the distribution of Coll4 and CEA proteins on

optical slices from co-culture spheroids suggested, that fibroblasts remained rather confined to small islets (Fig. 40C, arrowheads). Thus, it appeared that there was a limited crosstalk between both cell types, suggesting that the spheroid model was not ideal to study mutual interactions between HT-29 cancer cells and CCD-1137Sk fibroblasts.

6.4.3 Growth of CCD-1137Sk and HT-29 co-cultures is enhanced in Dynarray chips

Reasoning that the spherical arrangement with its observed strict spatial separation between HT-29 and CCD-1137Sk cells might have contributed to the lack of an effect of co-culturing on spheroid growth, we switched to chip-based 3D-Dynarrays. These have cavities of 300 μm in diameter and depth and their inner surfaces can be coated with extracellular-matrix components or gels. Furthermore, the walls of the cavities are porous, allowing the passage of nutrients. HT-29 and CCD-1137Sk cells were either seeded as mono- or co-cultures into Type-I collagen coated Dynarray chips and cellular growth was assessed. In all cases, 4,000 cells were seeded per cavity, i.e. either 4,000 HT-29 or CCD-1137Sk cells in the mono-cultures or 2,000 cells of each type for the co-cultures. In this format, the fibroblast marker Type-I collagen was widely distributed throughout the co-cultures (Fig. 41A), suggesting a better mixing of both cell types than in spheroids. MCT4 fluorescence signals were comparable in both HT-29 and CCD-1137Sk cell areas of the co-culture chips (Fig. 41A). Furthermore, the growth behavior of HT-29 cells in Dynarray chips was influenced by the presence or absence of fibroblasts. While HT-29 cells in mono-culture were adhering to the inner chip walls and growing in only few flat layers (Fig. 41B), co-cultures with fibroblasts filled out the entire chip cavities and were even often growing beyond (Fig. 41B). Total cell counts increased in co-cultures by 55 % as compared to HT-29 mono-cultures after four days in culture (Fig. 41C). This demonstrates that the growth behavior of CCD-1137Sk and/or HT-29 cells can be modulated by 3D-co-culturing and that this is dependent on the type of 3D-culture system.

6.4.4 Fluorescence staining of CEA, Coll4, and DAPI show different intensities in HT-29 and CCD-1137Sk cells

To assess potential effects of co-culturing on metabolic markers in Dynarray cultures of HT-29 and CCD-1137Sk cells, we sought cell type specific features that could later serve as discriminators. Thus, in analogy to the 2D-cultures, chips were stained with DAPI, anti-CEA, and anti-Coll4, and were then visualized by 3D-confocal microscopy. This revealed a high density of nuclei (Fig. 42A), impairing an instance segmentation of individual cells. Yet, a correlative quantitative voxel analysis could be implemented to determine relative staining intensities. Therefore, 3D-image stacks were subdivided into voxel cubes as shown in Fig. 42C and the average fluorescence intensity per cube was determined after nuclei segmentation and background subtraction. This showed the following principal features. First, in mono-cultures, HT-29 cells showed brighter CEA and darker Coll4 signals than CCD-1137Sk cells (Fig. 42B). In this and all following graphs, a red vertical line marks the CEA brightness range that contains 95 % of all CCD-1137Sk voxel cubes in mono-culture. Second, also in mono-cultures, DAPI fluorescence was much brighter in HT-29 cells than in CCD-1137Sk cells (Fig. 42B, color code). Third, in co-cultures, the Coll4 vs. CEA distribution looked more similar to the HT-29 mono-culture than to the CCD-1137Sk mono-culture distribution (Fig. 42B), suggesting that most cells in co-cultures were HT-29 cells.

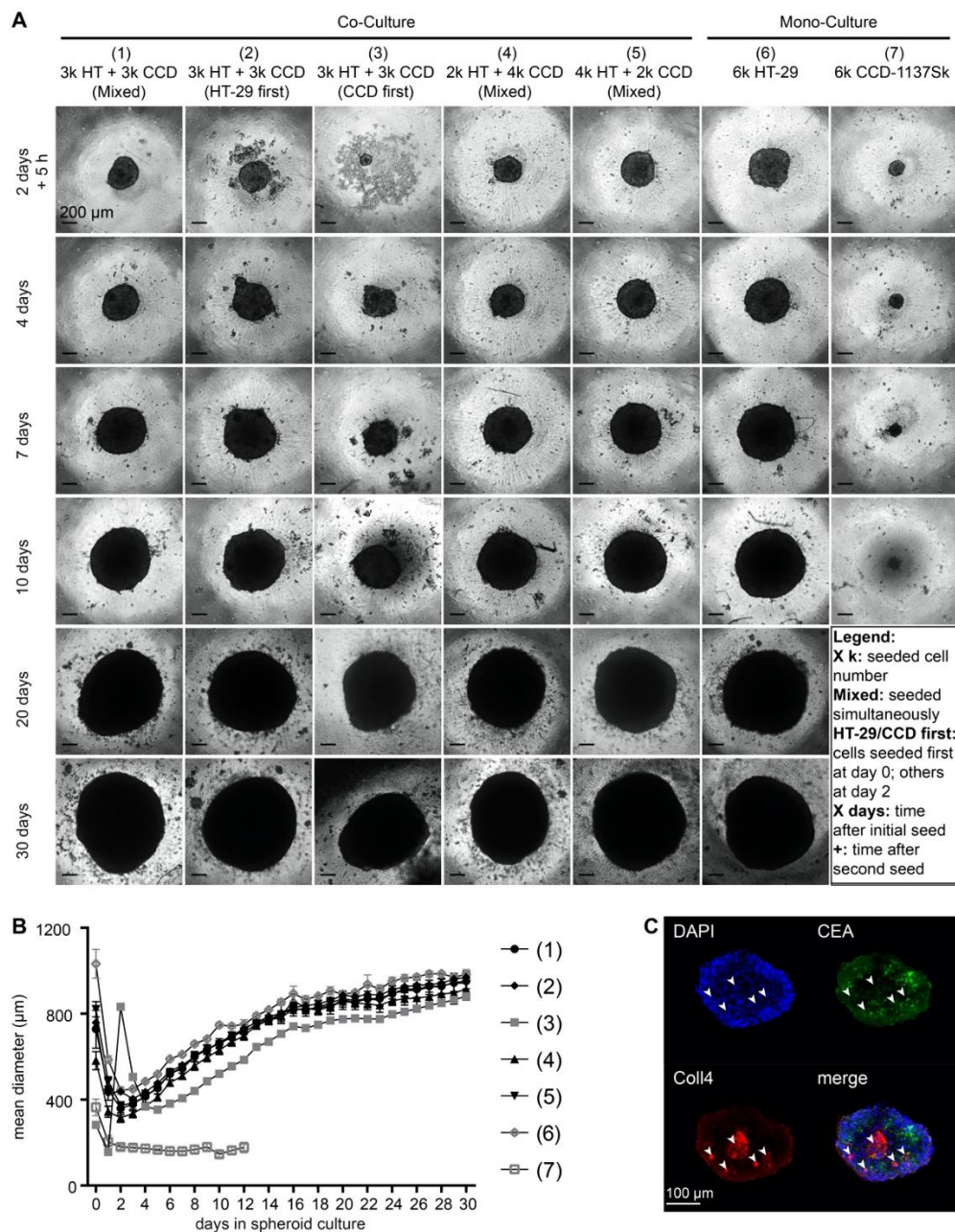


Figure 40. Growth of HT-29 spheroids is unaffected in the presence of CCD-1137Sk cells. Human HT-29 or CCD-1137Sk cells were seeded into ultra-low attachment plates to form spheroids, following different seeding orders (Mixed, HT-29 first or CCD-1137Sk first) and cell numbers (ranging from 2,000 to 6,000 cells per type) as indicated. From 0 to 30 days in culture, brightfield images were taken to perform spheroid-size analysis based on the mean diameter (A–B). Additionally, co-culture spheroids with 250 HT-29 cells together with simultaneously seeded 500 CCD-1137Sk cells were fixed after four days and stained with DAPI as well as with anti-CEA and anti-Coll4 antibodies as markers for nuclei, HT-29 cells, and fibroblasts, respectively (C). A) Representative brightfield images of HT-29 and CCD-1137Sk mono- and co-culture spheroids seeded in different ratios and orders, as depicted. B) Graph shows a quantitative analysis of mean diameters of mono- and co-culture spheroids at different time-points as indicated. Mean + SEM ($n = 5 - 9$ experiments). C) Representative optical slice of DAPI (blue), anti-CEA (green), and anti-Coll4 signals (red). Arrowheads, exemplary clusters of Coll4-positive areas. Bottom right panel shows an overlay image of all three channels. (Keller et al., 2020)(CC BY)

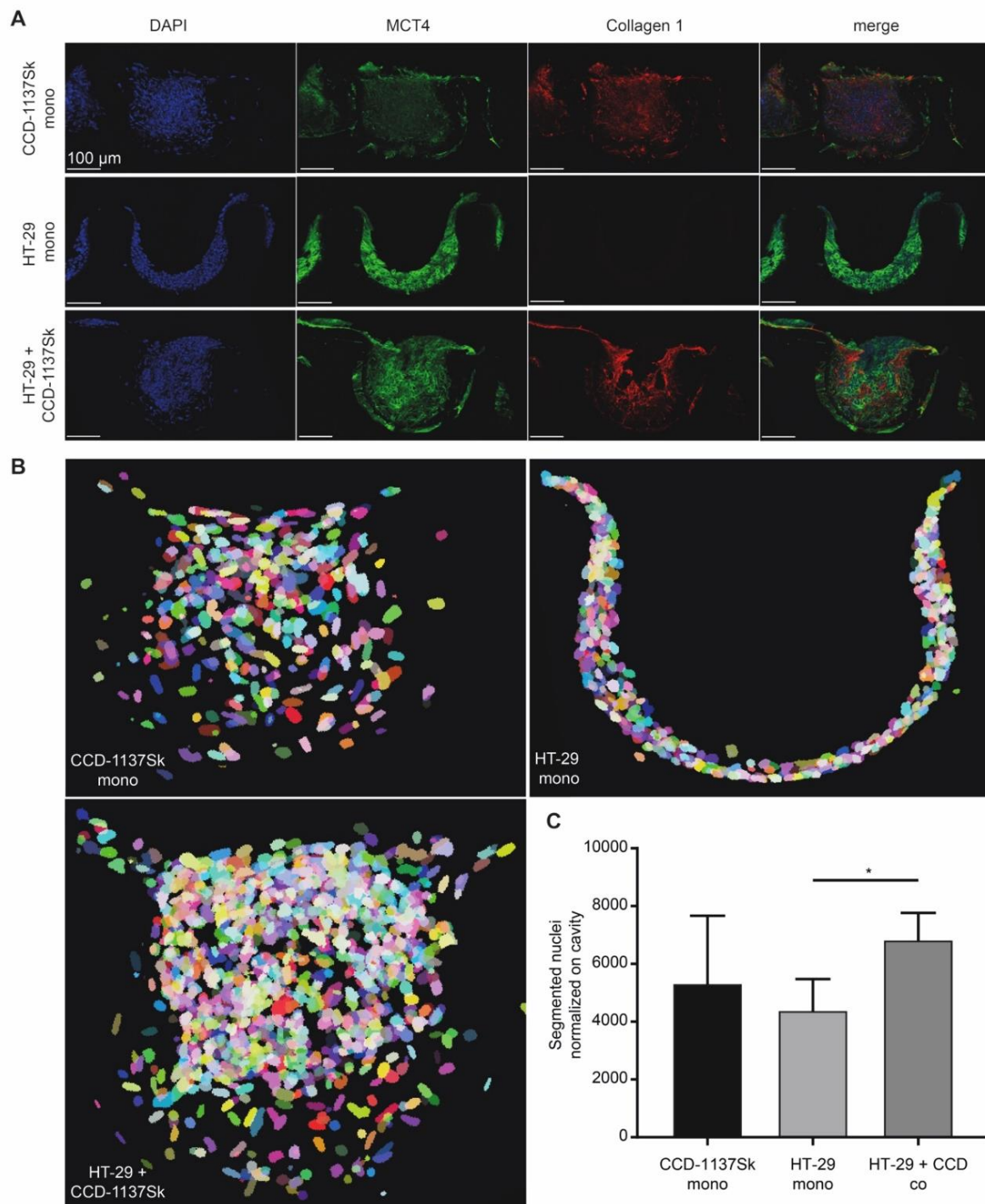


Figure 41. Chip-based 3D-cultures reveal morphological and metabolic changes upon co-cultivation of HT-29 and CCD-1137Sk cells. A total of 4,000 cells per chip cavity were seeded to yield either mono- or co-cultures of HT-29 and CCD-1137Sk cells. In case of co-cultures, 2,000 HT-29 cells were co-seeded with 2,000 CCD-1137Sk cells per well. After four days, chips were fixed, transversally sectioned, and then stained with DAPI as well as antibodies against MCT4 and Type-I collagen as markers for nuclei, lactate export, and ECM, respectively. Subsequently, sections were imaged with confocal microscopy. A) Representative maximum-z projections. B) Representative display of segmented nuclei from different culture conditions as indicated. Pseudo-colors were chosen to discriminate between individual nuclei. They do not indicate different cell types. C) Quantitative analysis of nuclear counts. Mean + SEM (n = 3 experiments). (Keller et al., 2020)(CC BY)

However, a limited number of signals in the lower left quadrant of the co-culture distribution showed a combination of low DAPI and CEA signals on the one hand and higher Coll4 signals on the other hand, suggesting that these could indicate the fibroblast population (Fig. 42B). Altogether, a picture emerged that by using this kind of voxel-based analysis the two cell populations could be differentially assessed with respect to their marker expression, at least under the assumption that in co-cultures the marker expression did not alter in a confounding manner. However, it appeared also, that either the fibroblast population in the co-cultures was rather small and/or that signals from HT-29 cells were preferentially detected in co-cultures using this approach. In the following, we used CEA and DAPI staining as discriminators to address the expression of metabolic markers in the two cell types.

6.4.5 Fluorescence signals of metabolic marker proteins show differential regulation in Dynarray co-cultures

Given that the voxel-cube analysis was promising to distinguish relative marker-protein expression levels in 3D-cultures, we wanted to assess a potential metabolic crosstalk between HT-29 and CCD-1137Sk cells in chips. Therefore, Dynarrays were seeded with mono-cultures of HT-29 or CCD-1137Sk cells or with co-cultures of both cell lines as described before and grown for four days. Then, chips were fixed, cleared, and stained with DAPI and anti-CEA to segregate the cell types from each other. In addition, the samples were labeled with antibodies against metabolic marker proteins HK-2, LDH, TIGAR, or TOMM20. 3D-confocal microscopy of stained specimens was done, and image stacks were quantitatively analyzed using the voxel-cube approach. As already evident from simple sum-z projections (Fig. 43A), all metabolic-marker proteins exhibited different intensities, within a given culture, between the two cell types, and in the mono- vs. co-culture condition. The quantitative analysis of all individual voxel cubes gave the following major results: First, comparing mono-cultures of HT-29 and CCD-1137Sk, CEA signals were always extending more to the brighter values range for HT-29 than for CCD-1137Sk cells; in co-cultures, the CEA brightness was further right-shifted. Second, for markers HK-2 and TIGAR, the fluorescence distribution in HT-29 mono-cultures was bimodal with a low and a high intensity cluster, suggesting the presence of two subpopulations of cells with either low or high abundance of HK-2 and TIGAR; this was not correlating to the expression of CEA. In co-cultures, the same kind of bimodal distribution was found, but here, both, CEA and metabolic-marker protein fluorescence signals were higher, leading to an overall shift of the data cloud to the upper-right part of the graphs; this was more pronounced for HK-2 than for TIGAR. Third, CCD-1137Sk cells in mono-cultures showed no bimodal distribution for any of the markers, but rather displayed a continuous range of fluorescence intensities for all four tested markers. However, while TIGAR and LDH were reaching high values in CCD-1137Sk mono-cultures compared to HT-29 mono-cultures, intensities of HK-2 and TOMM20 signals were similar or lower in CCD-1137Sk than in HT-29 cells. Finally, while LDH and TOMM20 were apparently going up in the HT-29 population of co-cultures (right from the red line), TIGAR and LDH were seemingly downregulated in CCD-1137Sk cells upon co-cultivation. Though, the latter effect might have been also caused by a potential skew towards HT-29 cells of the analysis method.

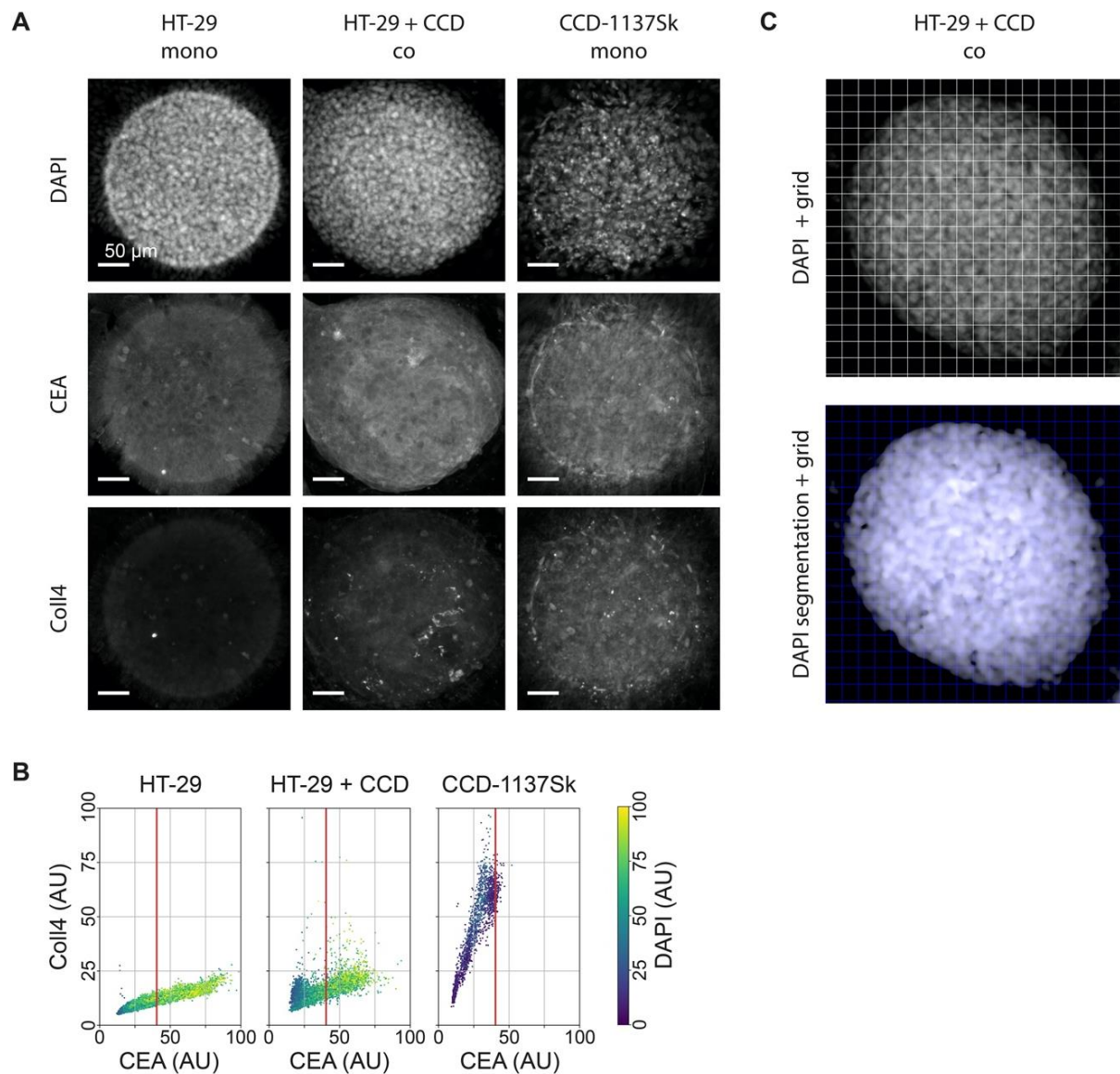


Figure 42. DAPI, CEA, and Coll4 staining jointly discriminate HT-29 and CCD-1137Sk cell populations in 3D-Dynarray co-cultures. A total of 4,000 cells per chip cavity were seeded to yield either mono- or co-cultures of HT-29 and CCD-1137Sk cells. In case of co-cultures, 2,000 HT-29 cells were co-seeded with 2,000 CCD-1137Sk cells per well. After four days, chips were fixed, cleared, and stained with DAPI and antibodies against CEA and Coll4 as markers for nuclei, cancer cells, and fibroblasts, respectively. Subsequently, samples were imaged with 3D-confocal microscopy. A) Representative sum-z projections. B) Scatter plots showing anti-Coll4 intensity distribution as a function of anti-CEA intensity for HT-29 mono-cultures (left), HT-29 + CCD-1137Sk co-cultures (middle), and CCD-1137Sk mono-cultures (right). Each dot shows the average intensity of a Voxel cube in a total of five Dynarray cavities. Red vertical line, CEA brightness range that contains 95 % of all CCD-1137Sk voxel cubes in mono-culture. C) Exemplary images showing the voxel-cube grid used for quantification of average fluorescence intensities. Upper panel, raw sum-z projection of DAPI signal; lower panel, sum-z projection upon nuclei segmentation and background subtraction. (Keller et al., 2020)(CC BY)

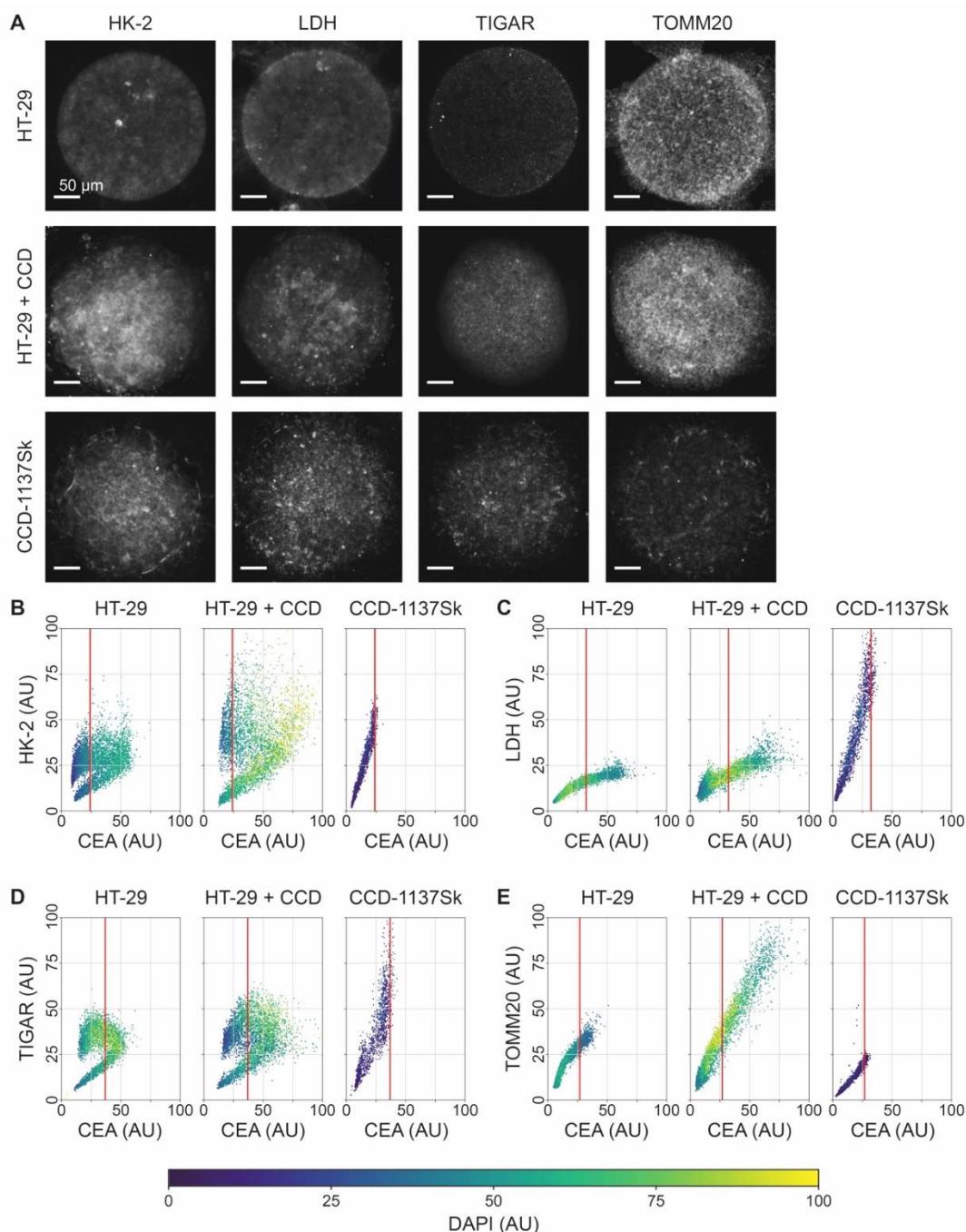


Figure 43. Expression of relevant metabolic marker proteins is altered upon co-culturing of HT-29 and CCD-1137Sk cells in Dynarrays. A total of 4,000 cells per chip cavity were seeded to yield either mono- or co-cultures of HT-29 and CCD-1137Sk cells. In case of co-cultures, 2,000 HT-29 cells were co-seeded with 2,000 CCD-1137Sk cells per well. After four days, chips were fixed, cleared, and stained with DAPI and antibodies against CEA as well as HK-2, LDH, TIGAR, or TOMM20 as markers for nuclei, cancer cells, and different metabolic activities, respectively. Then, samples were imaged with 3D-confocal microscopy. A) Representative sum-z projections. B–E) Scatter plots showing fluorescence intensity distributions of anti-HK-2 (B), anti-LDH (C), anti-TIGAR (D), or anti-TOMM20 (E) as a function of anti-CEA intensity for HT-29 mono-cultures (left), HT-29 + CCD-1137Sk co-cultures (middle), and CCD-1137Sk mono-cultures (right). Each dot shows the average intensity of a voxel cube in a total of five Dynarray cavities. Red vertical line, CEA brightness range that contains 95 % of all CCD-1137Sk voxel cubes in mono-culture. (Keller et al., 2020)(CC BY)

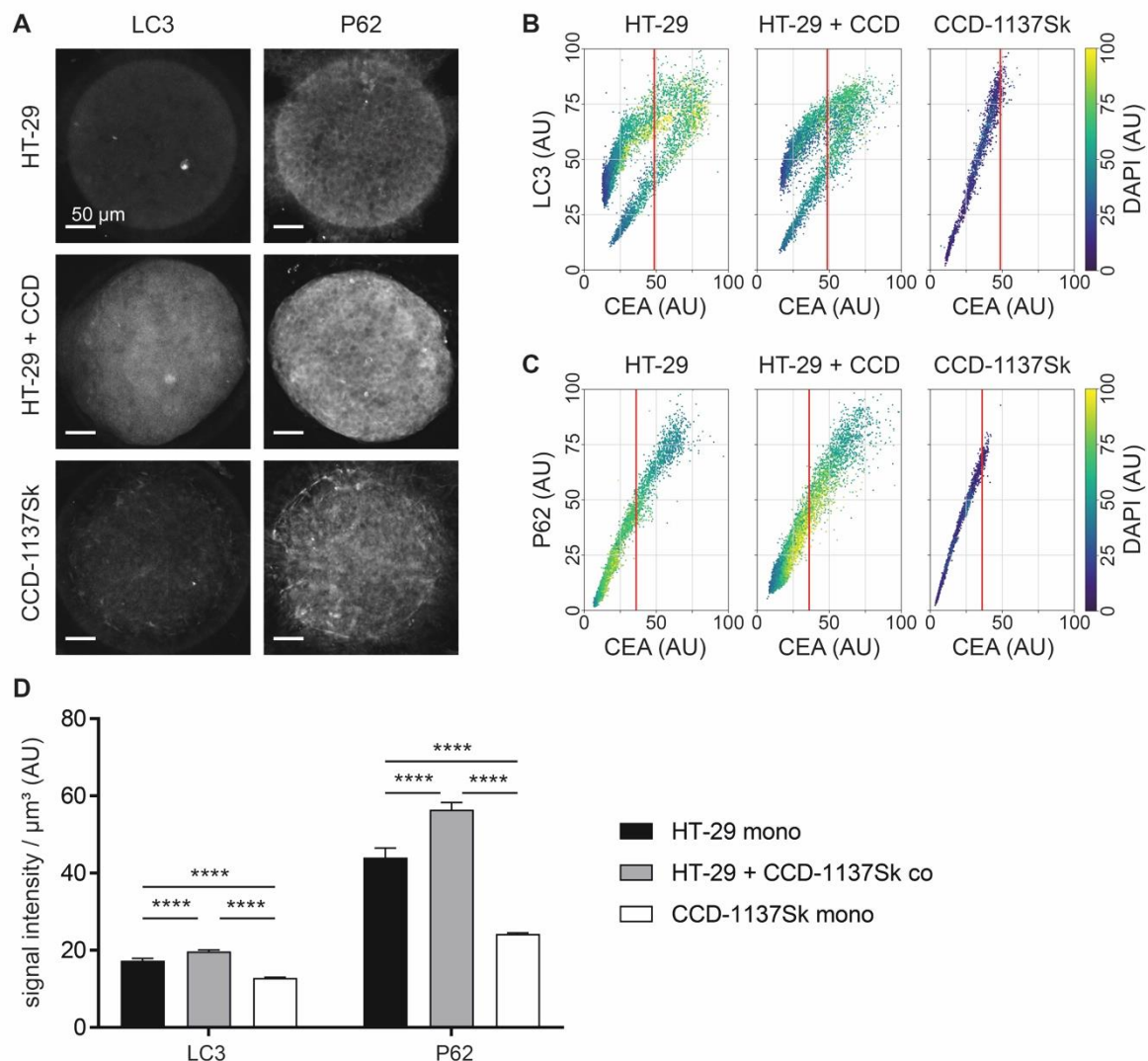


Figure 44. Co-culturing of HT-29 and CCD-1137Sk cells in Dynarrays leads to a rise of autophagic markers. A total of 4,000 cells per chip cavity were seeded to yield either mono- or co-cultures of HT-29 and CCD-1137Sk cells. In case of co-cultures, 2,000 HT-29 cells were co-seeded with 2,000 CCD-1137Sk cells per well. After four days, chips were fixed, cleared, and stained with DAPI and antibodies against CEA as well as LC3 or P62 as markers for nuclei, cancer cells, and autophagy, respectively. Then, samples were imaged with 3D-confocal microscopy. A) Representative sum-z projections. B–C) Scatter plots showing fluorescence intensity distributions of anti-LC3 (B) or anti-P62 signals (C) as a function of anti-CEA intensity for HT-29 mono-cultures (left), HT-29 + CCD-1137Sk co-cultures (middle), and CCD-1137Sk mono-cultures (right). Each dot shows the average intensity of a voxel cube of a total of five Dynarray cavities. Red vertical line, CEA brightness range that contains 95 % of all CCD-1137Sk voxel cubes in mono-culture. D) LC3 and P62 fluorescence intensity per μm^3 . Mean + SEM (n = 5 experiments). (Keller et al., 2020)(CC BY)

6.4.6 Autophagy is enhanced in Dynarray co-cultures of HT-29 and CCD-1137Sk cells

Next, the voxel-cube approach was used to assess a potential regulation of autophagy in 3D-chip cultures. Therefore, mono- and co-cultures of HT-29 and CCD-1137Sk cells

in Dynarrays were fixed after four days, cleared, and stained with DAPI and anti-CEA as before. To study the presence of autophagy, samples were co-labeled with anti-LC3 or anti-P62. Although a first look on the sum-z projections suggested that the fluorescence intensity of both, LC3 and P62, was higher in co-cultures than in mono-cultures of either HT-29 or CCD-1137Sk (Fig. 44A), the voxel-cube analysis did not confirm this. Rather it seemed, that the brightness distributions of both, LC3 (Fig. 44B) and P62 (Fig. 44C), were rather similar, when comparing HT-29 mono-cultures and co-cultures. For HT-29 mono- and co-cultures, LC3 signals showed a bimodal distribution, similar to the ones observed for HK-2 and TIGAR. Conversely, CCD-1137Sk cells in mono-culture again showed simple continuous ranges of LC3 and P62 fluorescence intensities. Since the lack of higher LC3 and P62 values in co-cultures upon voxel-cube analysis did not well reflect the sum-z projections and there was a suspicion, that the voxel-cube approach might have a skew towards HT-29 signals, the data were additionally analyzed by fluorescence-intensity measurements per μm^3 regardless of cell type. As depicted in Fig. 44D, this corroborated the qualitative impression of the sum-z projections. Indeed, using this approach, LC3 and P62 signals were highest in the co-cultures and lowest in the CCD-1137Sk mono-cultures. Of course, this did not allow a cell type specific statement, but in consideration of the whole picture, a major contribution of fibroblasts to the high autophagy marker values in co-cultures is appeared likely.

6.4.7 In microarray chip co-cultures, CCD-1137Sk fibroblasts show low mitochondrial membrane potential

Cells undergoing Warburg- or reverse Warburg-based metabolic switches are expected to vary greatly with respect to mitochondrial activity. Thus, to test the presence of active mitochondria, live-cell imaging was performed using the red-fluorescent vital dye, TMRM. This accumulates in mitochondria depending on their membrane potential. To be able to differentiate between the cell types in live-cell imaging, CCD-1137Sk and HT-29 cells were loaded with either CellTracker DeepRed (CTdr) or CellTracker Green (CTg), respectively. Then, they were co-cultured in Dynarray chips for four days. 30 min after loading with TMRM, 3D-live cell confocal microscopy was performed. At this point it is necessary to say, that in control experiments the CellTracker staining itself enhanced also LC3 expression primarily in CCD-1137Sk cells of HT-29 co-cultures (data not shown). Therefore, we cannot completely exclude, that the TMRM data shown here were partially affected by the experimental procedure itself. However, as observed upon immunostaining against Type-I collagen and CEA (see Fig. 41A), also CellTracker signals revealed clusters of fibroblasts interspersed within the HT-29 colony (Fig. 45A). While CTg-positive HT-29 cells exhibited variable but mostly bright TMRM fluorescence, CTdr-positive CCD-1137Sk cells were almost completely devoid of such signals. Co-localization analysis of TMRM with the labeling intensity for each CellTracker dye using Pearson's coefficient measurements confirmed this observation (Fig. 45B). This suggests that HT-29 cancer cells were present in different states of mitochondrial activity, while fibroblasts were mostly lacking a consistent mitochondrial membrane potential. Moreover, additional immunostaining of co-culture chips showed that regions outside the circular entry of the chip cavities, which were primarily populated by fibroblasts, were strongly positive for MCT4 but not for MCT1 (Fig. 46). Conversely, the circular body within the 3D-cavities, which was composed of mixed HT-29 and CCD-1137Sk populations, exhibited variable amounts of MCT1 and MCT4, showing a prevalence for either one or the other kind of transporter.

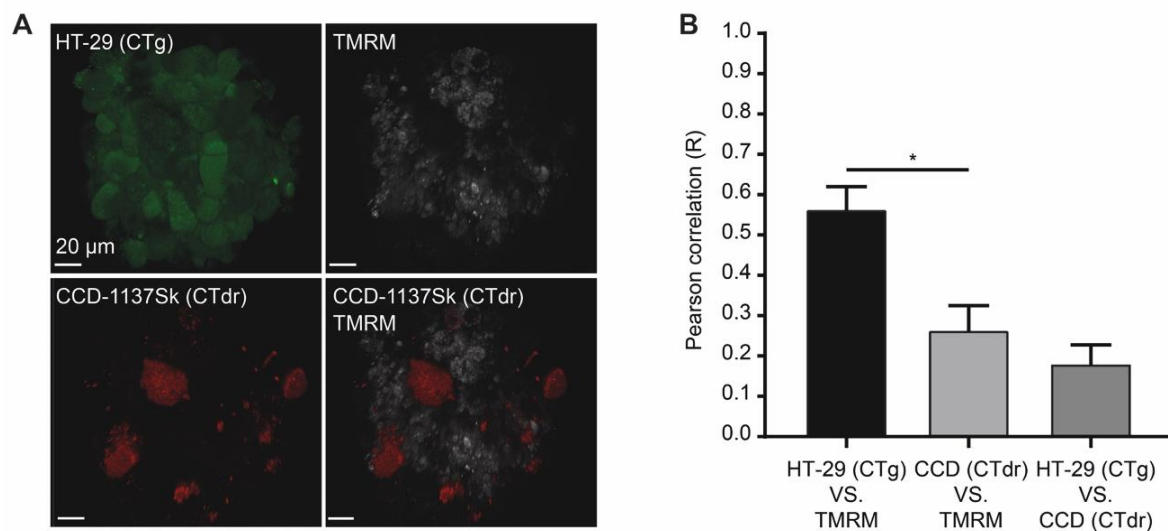


Figure 45. Chip-based 3D-cultures reveal low mitochondrial membrane potential in fibroblasts upon co-cultivation of HT-29 and CCD-1137Sk cells. Human HT-29 and CCD-1137Sk cells were live stained with CTg and CTdr, respectively, and then co-seeded in Dynarray chips for four days. To evaluate the mitochondrial membrane potential, TMRM was analyzed in 3D-live cell imaging. A) Representative maximum-z projections of fluorescence signals for CTg, CTdr, and TMRM, as indicated. B) Quantitative analysis of Pearson's correlation between CT-dyes and TMRM as a measure of cell type specific TMRM fluorescence intensity. Mean + SEM (n = 3 experiments). (Keller et al., 2020)(CC BY)

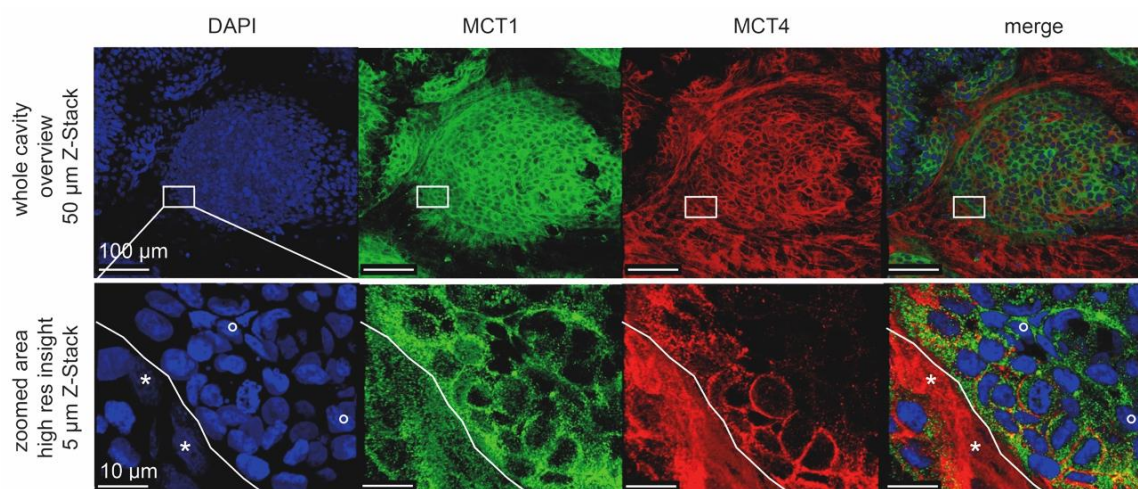


Figure 46. High-resolution confocal images reveal differential cell type-specific expression of lactate shuttle proteins upon co-cultivation of HT-29 and CCD-1137Sk cells. Per chip cavity, 2,000 HT-29 and 2,000 CCD-1137Sk cells were co-seeded. After four days, cultures were fixed, cleared, and then stained with DAPI as well as antibodies against MCT4 and MCT1 as markers for nuclei, lactate export, and lactate import, respectively. Subsequently, samples were imaged with confocal microscopy. Shown are representative maximum-z projections with indicated thickness. Lower panels were taken from the same specimen region as boxed in the upper panels. White solid lines in the lower panels indicate the border between a zone primarily populated by CCD-1137Sk (lower left) and HT-29 cells (upper right). Asterisks and open circles point to typically dim and large nuclei of CCD-1137Sk vs. bright and small nuclei of HT-29 cells. (Keller et al., 2020)(CC BY)

6.5 Discussion

Since a few years, mutual interactions between cancer and stromal cells have emerged as major contributors to tumor metabolism (da Cunha et al., 2019). Paracrine and autocrine signaling of growth factors, proteases, inhibitors, and extracellular matrix components might lead to a wide-spread crosstalk between cancer cells and their surroundings. This influences the metabolism of all cells involved (Mueller and Fusenig, 2004) and has become a widely studied target for cancer treatment. However, cell model systems with desired properties in terms of both, fast and easy usability, as well as sufficient physiological complexity including effects within tumor populations of cancer and stromal cells for drug treatment investigation, are rare.

Current *in vitro* model systems for cancer studies mostly employ either cell lines or primary tumor cells and these are either cultured on planar surfaces or, using different methods, in 3D. Regarding the choice of 'cell line' versus 'primary cells', the latter appear superior for personalized medicine (Ginsburg and Phillips, 2018) and for a higher physiological relevance (Pan et al., 2009). However, since primary cells are derived from a limited amount of tumor material and since genotype and phenotype are variable not only between any two patients but also within the tumor population of a given patient, primary cells exhibit major inherent variability in terms of availability and genetic constitution (Sasaki and Clevers, 2018). Therefore, while *in vitro* models derived from primary cells might be advantageous for personalized medicine and advanced stages of drug testing, also the use of cell lines can still be an option for the study of more fundamental cell-biological phenomena and principles of cellular signaling due to their unlimited availability and relative phenotypic robustness. With respect to culturing in 2D or 3D, the former is still widely used due to its unbeatable applicability and analytical amenability, in particular, in the context of image-based assays (Kapałczyńska et al., 2018). Nevertheless, signaling processes mediated by cell-cell contact or paracrine mechanisms might be reliably addressed in such adherent cell cultures. However, since contact via the entire cell surface as well as the establishment of physiological cell organization, of gradients of drugs, oxygen, waste products etc. can only be obtained in 3D-cell cultures, the latter gained increasingly in importance in recent years. Therefore, spheroids and, particularly, tumor organoids have become key to *in vitro* cancer studies (Chaicharoenaudomrung et al., 2019). Spheroids are mostly based on the self-assembly of immortalized cells by impairing their settlement on any non-cellular surface. In contrast, tumor organoids involve the use of primary tumor-derived cells and their embedding in hydrogels formed by extracellular-matrix extracts, typically Matrigel, BME, or similar. Models of intermediate complexity use Matrigel in combination with cell lines, in particular, for obtaining 3D-cultures from cell lines that otherwise hardly form such cultures (Keller et al., 2019; Rustamov et al., 2019). Although Matrigel/BME-based tumor organoids have been seen as a 'gold standard' for *in vitro* cancer research, the use of Matrigel has also important draw-backs. For example, there is a considerable lot-to-lot variability, Matrigel is derived from tumor tissue, and it inherently adds specific physicochemical matrix properties (Cruz-Acuña and García, 2019). Furthermore, it has a significant autofluorescence in the green wavelength range (Shen et al., 2018; Solanki et al., 2020), rendering its use in marker-specific microscopic analyses less efficient. We have compared 3D-cultures made with and without BME and experienced issues of autofluorescence. On top, BME-based cultures were much less regular and condensed, leading to increased size of 3D-data stacks, an issue that requests more efforts on data acquisition time, storage, and analysis (Fig. S19A – C). Most worrying,

though, were the differences observed in terms of marker expression. For example, in CCD-1137Sk mono-cultures, the presence of BME increased the fluorescence signals obtained for CEA and decreased those for LC3 (Figure S19D).

Recapitulating, different model systems might be superior to others for certain aspects, but the choice of an appropriate condition will likely depend strongly on the research topic. In this context, we here used yet another assay system, i.e. the Dynarray chip. From a purely technological point of view, these can be an interesting option for mechanistic studies where both, intrinsic cell-cell interactions as well as a defined surface composition should be guaranteed. These chips feature equally-spaced and equally-sized cavities made by an optically transparent polymer, which can be coated with any material of interest, e.g. Matrigel, BME, collagen, or also Poly-L-lysine, to enhance interaction between chip and cells. We chose Type-I collagen to allow for a defined support and avoiding potentially interfering signaling molecules that might come with Matrigel/BME. Indeed, at least in 2D-cultures, coating with Type-I collagen did not affect the expression of any of the tested markers at the level of immunofluorescence (Fig. S20). In Dynarray co-cultures of HT-29 or MDA-MB-231 cells with CCD-1137Sk fibroblasts, the latter were typically making most of the contacts to the collagen surface and the morphology of these peripheral cells was often spindle-shaped, forming bridges between the chip wall and the mass of the co-culture. Conversely, in the centers of the cavities, cells were better mixed, although some segregation of fibroblasts and tumor cells into nests was also observed like in spheroids. Altogether, this mediated a high homogeneity of 3D-cultures between different cavities and different chips. Another technical advantage of the chips over the spheroid cultures was their spatial regularity, which eased automated microscopic acquisition and subsequent data analysis.

Regarding the metabolic interactions, the 2D-cultures and Dynarrays revealed good consensus for fibroblasts. Indeed, in both systems, data were consistent with a higher level of HK-2 and autophagy markers as well as a loss of TIGAR and TOMM20 in CCD-1137Sk cells upon co-culturing with HT-29. With respect to the metabolic profile of HT-29 cells, 2D-cultures did not reveal any significant change, while in Dynarrays, data showed an upregulation of HK-2, TIGAR, LDH, and TOMM20. This could indicate that the signaling interplay in the 3D-cultures was more extensive, leading to a clearer response of the HT-29 cells. Furthermore, the lactate export carrier MCT4 was upregulated in fibroblasts in 2D upon co-cultivation and it showed a prevalence over MCT1 in fibroblasts within Dynarray cultures. Mitochondrial membrane potential, as measured by TMRM fluorescence intensity, was mostly low in fibroblasts. In contrast, TMRM signal was higher but variable from cell to cell in HT-29 cells. Finally, chip-based 3D-co-cultures of HT-29 and CCD-1137Sk cells grew more robustly than corresponding mono-cultures, although it was not possible to unequivocally attribute this to one of the two cell types. Altogether, these data pointed to a metabolic crosstalk between cancer and fibroblast cells in co-cultures, which primarily affected the metabolic behavior of the fibroblasts, but in Dynarrays also of HT-29 cells. This result is most consistent with a scenario in which HT-29 cells induce CCD-1137Sk cells to switch to a glycolytic and autophagic state, to lose mitochondrial activity, and to gain lactate export capabilities. Conversely, HT-29 cells apparently remained mixed in terms of mitochondrial activity and expression of lactate importers and exporters, suggesting the presence of both, catabolic and anabolic states. This was nicely corroborated by the bimodal expression patterns of HK-2, TIGAR, and LC3. Similar features, likely to be responsible for differential susceptibility to drug treatment, were

previously observed in mouse models and tumor tissue (Blank et al., 2018; Sharick et al., 2019). In particular, metabolic heterogeneity of malignant cells (Schcolnik-Cabrera et al., 2017) and bad prognosis together with decreased overall survival upon enhanced MCT4 expression of tumors are fitting to the present study (Bovenzi et al., 2015). Finally, HT-29 in Dynarray co-cultures also gained in HK-2, TIGAR, LDH, and TOMM20, being consistent with a combination of high glucose and lactate metabolism capability (Cannino et al., 2018) that could jointly fuel production of pyruvate and oxidative phosphorylation.

While the metabolic interaction patterns were observed in mono-layer and chip-based co-cultures, no effect of co-culturing was evident on spheroid growth. This might be explained by three, not mutually exclusive, scenarios: First, fibroblasts remained rather isolated and encapsulated in spheroid co-cultures while they were more loosely interspersed in the chip-based co-cultures. Thus, one might speculate that distribution of paracrine signals between tumor and fibroblast cells was not comparable between the two culture conditions. Second, it might be that the relatively large spheroids of up to 1,000 μm diameter created more profound gradients of oxygen, nutrients, and waste products than the 300 μm wide Dynarray-chip cultures. This might have intrinsically changed the basic metabolic profile of these cells or their propensity to react to each other. Finally, it cannot be completely excluded that the measurement of spheroid diameter was insufficient to detect metabolic alterations induced upon co-cultivation. For this reason, seeding densities in experiments focusing on the metabolic aspects of spheroid cultures had to be altered in a way that ensured homogeneous size distribution as compared to the 300 μm Dynarray cavities. More analysis should be undertaken to reveal changes in the metabolic state of the cells. However, even if these existed, they were apparently so subtle, that they had no robust effect on cell growth as observed in the chip format.

6.6 Conclusion

In summary, this work describes different cellular co-culture models to mimic mutual metabolic interactions between HT-29 cancer and CCD-1137Sk fibroblast cells. In particular, the differential expression patterns of MCT1, MCT4, HK-2, TIGAR, TOMM20, LC3, and P62 in HT-29 and CCD-1137Sk cells, as well as the low mitochondrial membrane potential in fibroblasts as observed in mono-layer 2D- and chip-based 3D-co-cultures were consistent with reverse Warburg type interactions. Together with the additional synergistic effects of co-culturing on cell proliferation in Dynarray chips, these features were comparable to those observed in tumor tissue. In contrast, spheroid co-cultures were not showing such effects. In the future, the presented models might be employed for addressing basic molecular signaling and cell physiology aspects as well as for testing metabolic modifiers in combination with anti-cancer drugs for treatment of neoplastic disorders.

Author Contributions

Conceptualization, F.K. and R.R.; methodology, F.K. and R.B.; validation, F.K.; formal analysis, F.K. and R.B.; investigation, F.K.; resources, R.S. and J.M.H.; writing - original draft preparation, F.K.; writing - review and editing, F.K., R.S., J.M.H., M.H., R.R.; supervision, M.H., R.R.; project administration, R.S., J.M.H., M.H., R.R.; funding

acquisition, M.H., R.R. All authors have read and agreed to the published version of the manuscript.

Funding

This work was funded by the German Federal Ministry of Education and Research (BMBF) as part of the Innovation Partnership M²Aind, projects SM²all (03FH8I01IA) and M²OGA (03FH8I02IA) within the framework Starke Fachhochschulen–Impuls für die Region (FH- Impuls).

Conflicts of Interest

The funders had no role in the design of the study; in the collection, analyses, or interpretation of data; in the writing of the manuscript, or in the decision to publish the results.

7 CONCLUSIVE DISCUSSION

Cancer progression is strongly dependent on niche formation and the metabolic state of the malignant cell population. Both these processes are tightly connected to the ECM and cellular signaling. So far, studies addressing these features largely relied on animal models with relatively high intrinsic read-out variance (Slifko et al., 2002), or cell culture models with flaws regarding of cell morphology and model setup (Hoarau-Véchet et al., 2018). In particular, investigations on 2D-cultures, tissue slices and small biopsies may lack crucial information from off-site interactions (Wu and Swartz, 2014). Therefore, this work transferred *in situ* effects of primary tumors to defined cell line-based cultivation studies. Through the implementation of in-process controls such as spheroid integrity measurements and the usage of tissue clearing protocols for confocal imaging of targeted microarray cultures, a comprehensive reflection of cell type specific reactions was achieved. With a special focus on the cancer cell secretion of the bone-metastasis marker, BSP, and metabolic coupling between cancer and fibroblast cells, metastasis-related cellular behavior was investigated.

7.1 Cancer cell homing and metastatic niche formation are induced by the secretion of ECM-modulating factors

Enriched media and excessive ECM supplementation induced cancer cell proliferation and stimulated spheroid formation in cell culture modeling (Keller et al., 2019). Furthermore, co-cultivation with stromal fibroblasts led to a metabolic interaction between stroma and cancer cells (Keller et al., 2020). Increased secretion rates might alter the composition of the ECM and corresponding tissue aberrations promote cancer progression (Jinka et al., 2012). As proliferating cancer cell populations facilitate ECM alterations, and since released growth factors can furthermore induce cancer cell homing and niche formation, links between metabolic coupling and bone-related metastasis were studied in targeted 2D- and 3D-cell cultures. In that context, a first target to be addressed was TGF β , a major regulator of EMT. Indeed, although depending on the tissue and involved cell types, EMT regulation can be different (Thiery et al., 2009), TGF β signaling is involved in most cases. TGF β signaling includes canonical transcription regulations with SMAD-translocation, but also other targets such as MAPK, AKT, JNK, ERK, and ROCK can mediate proliferation, differentiation, migration, angiogenesis, invasion, and therefore EMT (Bierie and Moses, 2006). In MDA-MB-231 breast cancer cells, increased levels of TGF β correlated with the expression of MMP-9 (Duivenvoorden et al., 1999). Fittingly, the application of MMP-9 induced BSP secretion and provided proteolytic activity led to a degradation of built-up ECM (Keller et al., 2021).

While TGF β mediates growth inhibition in non-malignant cells, aberrant signaling supports tumor progression through the loss of growth inhibitory control, increased cellular invasiveness and the evasion of immune response (Thomas and Massagué, 2005). These effects are not restricted to direct cellular interaction, but also mediated by the ECM. For example, adding TGF β protein to MCF-7 cells, a low-metastatic breast cancer line, slightly stimulated their migration and expression profiles towards a loss of E-cadherin and increased SMAD signaling. If these cells were grown on the decellularized ECM of highly metastatic MDA-MB-231 cultures, the EMT-related alterations were more prominent (Brandão-Costa et al., 2020). Since that effect was not observed when conditioned media were applied, relevant factors were rather

deposited in the matrix and more aggressive cancer cells showed the capacity of indirectly inducing EMT in secondary cell lines in heterogeneous tumors (Brandão-Costa et al., 2020). The altering effect of supplemented ECM for inducing the expression of proteins associated with tumor progression was not restricted to complete extracts like BME, but it was also observed in other primary compounds such as Type-I collagen (Keller et al., 2021). An important experimental restriction of all such experiments with primary biological materials is, that they are impure and, indeed, contain varying amounts of ECM components, including growth factors (Vukicevic et al., 1992) and MMPs (Gillette et al., 2003). These enzymes might not only promote EMT, but additionally induce cancer cell niche formation. Matrix metalloproteases are activated by applied proteolytic activity, such as furin or other MMPs, or by ECM acidification connected to oxidative stress. In total, these processes initiate matrix remodeling and cellular migration, therefore promoting EMT (Kessenbrock et al., 2010).

Next, following a loss of tissue integrity, metastatic niche formation can be initiated. Here, proteinase-activated receptors (PARs) play a crucial role. Physiologically, PARs are associated with local inflammation processes, but their increased expression in cancer was reported. PAR activation in cancer cells and fibroblasts both correlated with invasiveness in MDA-MB-231 and therefore a promoted migration towards the MMP source was estimated (Boire et al., 2005). PARs are associated with zones of high metabolic turnover (Ge et al., 2004), explaining their association with cancer cell homing on bone remodeling sites. Indeed, at these sites, osteoclasts secrete MMPs during bone resorption (Zhu et al., 2020), and thus attract cancer cells. With primary tumor-related properties such as ROS secretion likely being preserved, the bone tissue becomes acidified. Bone tissue acidity again is associated with increased osteoclast differentiation and survival (Yuan et al., 2016). With BSP secretion related to physiological osteoblast differentiation (Al-Bari and Al Mamun, 2020), two key aspects of bone tissue homeostasis can be interfered by cancer cells. Thereby both, osteolytic osteoporosis and osteoblastic sclerosis can be manifestations of induced niche formation with cancer-mediated feedback regulation.

7.2 Metabolic interactions with ECM-providing stromal cells support cancer progression

The BSP secretion correlated with MMP-9 as well as with regulation markers TGF β (Keller et al., 2021), RUNX2, and IGF1 (Rustamov et al., 2019). Since also proliferation rates and overall spheroid integrity correlated with BSP signaling (Keller et al., 2019), metastatic potential of MDA-MB-231 cells seemed to be highly dependent on their metabolic activity. However, as the composition of the ECM varies in different tissues, interactions with additional cell types providing structural molecules and metabolites have to be considered under co-culture conditions. To enable statements that are not restricted to the MDA-MB-231 cell line, HT-29 colon cancer cells were used in parallel to assess additional cancer-stroma interactions with CCD-1137Sk fibroblasts. Here, it was advantageous that HT-29 cells grow in rather distinct islets. This property simplified to trace down subcultures and their interfering border regions in cell type specific analysis for both, 2D- and 3D-conditions (Keller et al., 2020).

To address metabolic interplay between HT-29 colon cancer and CCD-1137Sk fibroblast cells, expression of markers associated with the corresponding metabolic pathways were investigated. Therefore, based on previous studies (Wilde et al., 2017),

import carrier expression in cancer cells and secretion of metabolites by cancer associated fibroblasts were examined and correlated with markers for glycolysis, oxidative phosphorylation, and autophagy. H⁺-coupled symporter monocarboxylate transporter 4 (MCT4) was enhanced in fibroblasts upon co-cultivation with cancer cells. Since HT-29 cells also expressed the import carrier MCT1, they were appreciated as rather incorporating counterpart of this stromal cell secretion. Typically, MCT4 is highly expressed in metastatic tumors, and it is important for glycolysis in the context of the Warburg effect. Besides product removal, cytosolic alkalization, and NADH recycling in cancer cells, this transporter plays a major role in the acidification of the cancer cell environment, supporting tumor invasiveness and immune response evasion (Liberti and Locasale, 2016). MCT4 is exclusively able to transport lactate against high gradients, but also transports pyruvate which again is the main target for the primarily importing carrier protein MCT1 (Contreras-Baeza et al., 2019).

With respect to the overall energy consumption dependency, the appropriate metabolic pathways have to be considered. Aerobic glycolysis yields in 2 molecules of adenosine triphosphate (ATP) per processed glucose unit. Conversely, oxidative phosphorylation generates up to 36 ATP units per processed glucose molecule. While being less efficient in total ATP production, glycolysis provides this energy carrier at a faster rate (Pfeiffer et al., 2001). Anyways, pure energy consumption cannot be the lone reason for glycolysis, since its ATP contribution has been shown to be highly dependent on the cellular context, ranging from 0.31 % for L-929 mouse fibrosarcoma cells to 64 % for Novikoff Hepatoma rat liver cells based on the cohesive analysis of oxygen uptake and lactate excretion in cancer cells (Zu and Guppy, 2004). With ATP not being the limiting factor for cell proliferation under conditions containing adequate amounts of glucose, further aspects are considered. Glucose as the starting reagent has been reported to be a major source for nucleotides and therefore glycolysis is necessary for DNA synthesis (Lunt and Vander Heiden, 2011). Glutamine as alternative carbon source is also processed in proliferating cells, but without glucose, cells are not able to proliferate, due to interdependencies of growth factor activations (Wellen et al., 2010). Furthermore, glucose can be converted into cytosolic acetyl-CoA as a carbon source for cell membrane creation if it is not metabolized during oxidative phosphorylation. Based on aerobic glycolysis-related signaling, glucose uptake is increased, and the higher level of pyruvate enriches citrate concentration within mitochondria. This is then transported into the cytosol based on the built-up gradient, where it is processed to acetyl-CoA and oxaloacetate by the ATP citrate lyase (ACL). Inhibition of ACL activity correlates with inhibited proliferation in cancer cells establishing aerobic glycolysis and might therefore proof its importance in the providing of cellular building blocks (Hatzivassiliou et al., 2005). This was consistent with observed signal increase for TIGAR, HK-2, and TOMM20 in HT-29 cancer cells while co-cultivated fibroblasts showed enhanced MCT4 export carrier expression.

The third aspect of aerobic glycolysis is the resulting acidification of the cellular environment based on lactate excretion. With lactate being the major product of provided glucose in human glioma cells (DeBerardinis et al., 2007), this aspect is contradictory to the hypothesis of glucose primarily being a carbon source. Therefore, lactate might further be used to regenerate NAD⁺ for the glycolytic flux, while in parallel changing the composition of the ECM. Lactate and associated oxidative stress may therefore inhibit immune responses through autologous T-cell stimulation, while enhancing cancer cell motility through induced angiogenesis. Furthermore, the acidified cellular environment is again associated with increased MMP-9 expression

(Kato et al., 2013). All this contributes to an enhanced metastatic potential through ECM modulation.

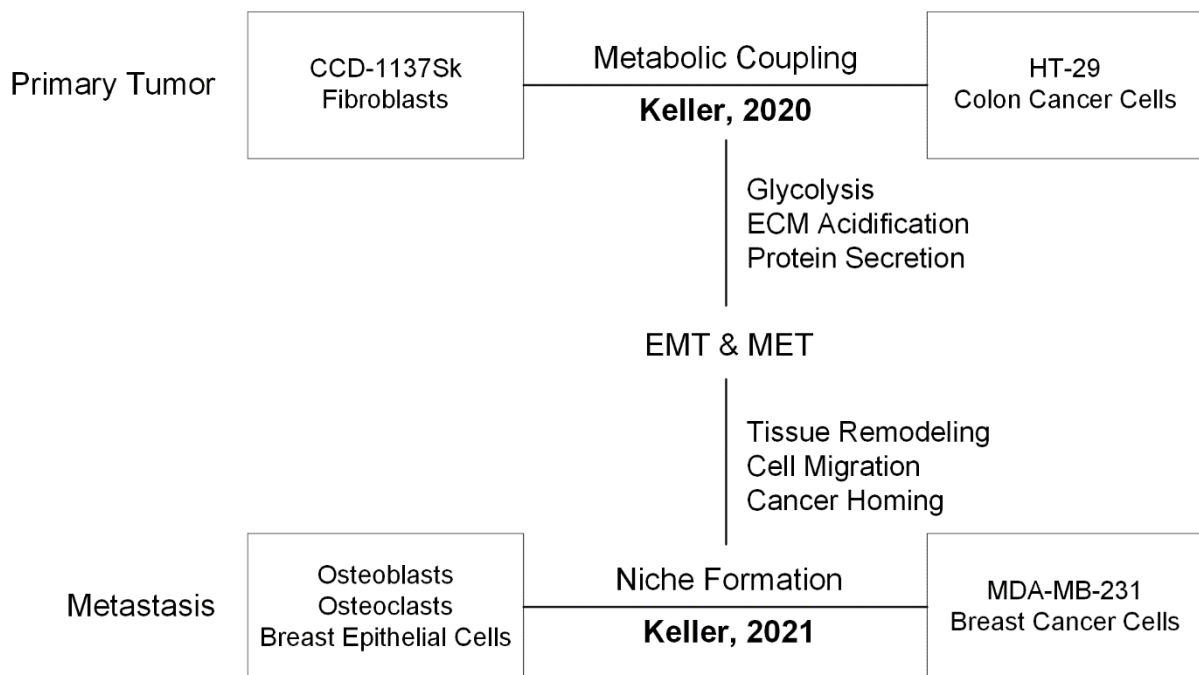


Figure 47. The extracellular matrix modulates EMT and MET during cancer progression. The metabolic coupling on primary tumor site and metastatic niche formation on metastatic site are linked via ECM-modulating epithelial mesenchymal transition and mesenchymal epithelial transition as depicted. Reverse Warburg signaling leads to an acidification of the primary tissue and induces EMT. During bone remodeling, released factors attract cancer cells and induce MET. Cancer cell homing then interferes with bone tissue homeostasis and facilitates metastatic growth.

With this, the current work was brought to a full cycle since the metabolic coupling of cancer cells and stroma was associated with similar markers as the ECM-mediated cancer cell secretion profile for BSP (Fig. 47). While reverse Warburg signaling induces a tissue acidification based on aerobic glycolysis known to include excessive lactate secretion, this milieu is further associated with increased MMP expression and cancer cell homing during bone remodeling. Although it was not possible to clarify a causal relationship between metabolic coupling and BSP secretion, their mutual crosstalk was further tested. Preliminary data showed similar profiles for BSP secretion in both, the HT-29 colon cancer and MDA-MB-231 breast cancer cells, when comparing 3D-spheroid and Dynarray cultures with 2D-cultures. Similarly, signatures of a reverse Warburg signaling were observed in fibroblast co-cultures with HT-29 as well as with MDA-MB-231 cells. Furthermore, application of MCT4 inhibitors mitigated fibroblast-induced higher proliferation rates of MDA-MB-231 cancer cells and decreased the release of lactate and VEGF into the supernatant. Future studies with membrane lactate carrier inhibitors and measurements of BSP expression may reveal direct connections between bone-associated cancer cell homing and stroma-dependent metabolism. To complete the analysis of ECM-mediated alteration in cancer progression, further tissue specific set-ups should be tested. Therefore, the substitution of the human skin fibroblast used so far with bone cells such as osteoblasts and added-up immune cells may be beneficial to improve the recreation of physiological properties.

7.3 Technological advances improve cell culture and data acquisition quality to obtain comprehensive information on classified populations

Scientific progress is highly dependent on the quality of available data acquisition methods. To enable the desired classified findings of wholesome samples, targeted improvements had to be established in terms of cell culture methodology to prevent distorting effects of detached subpopulations on the resulting read-out.

Depending on the 3D-culture condition, cancer cell lines establish different characteristics in terms of morphological structure and drug sensitivity (Raghavan et al., 2016). Spheroid culture-based models keep being published with various objectives. They are often focusing one defined setting and a target readout that alters upon a certain stimulus. Although the readout complexity is continuously improved through e.g. orthogonal analyses, the illustration of drug compound effects became the most important aspect within an experimental set-up. Therefore, structural integrity of analyzed spheroid cultures is not always ensured (Huang et al., 2020). With respect to the high tissue stiffness in physiological bone (Mulder et al., 2008), firm spheroids were defined as crucial for reliable *in vitro* screening approaches in the context of BSP secretion. Since also distinct cells may secrete influencing factors, this subpopulation had to be diminished.

First, the harmonization of appropriate media compositions was addressed. Comparable studies were associated with an increased MDA-MB-231 proliferation and invasion potential in enriched media and further revealed interdependencies with mesenchymal stem cells conditioning the cell supplementation (Brown et al., 2019). Furthermore, an MDA-MB-231 expression screening study based on media composition revealed that IL-8 is decreased, while the overall S1004A level increased when MEM-media was supplemented with 10 % horse serum compared with 10 % FBS. Reducing the FBS concentration from 10 % to 0.1 % enhanced these effects and similar results were observed when reducing the confluency of 2D-cultures from 90 % to 50 % before analysis. Finally, also changing the basal media from MEM to DMEM or RPMI-1640 altered corresponding expression profiles (Kim et al., 2015). The S100 protein family consists of proteins that are associated with increased cellular migration, invasion, and cell growth in breast cancer. No enzymatic activity is known for S1004A, but interactions with calcium-dependent partners may lead to ECM modulation based on MMP upregulation, while protease inhibitors are rather downregulated. Therefore, a modulation of ECM-contained transcription factors can be estimated (Helfman et al., 2005). On the other hand, the decreased IL-8 level could be associated with a lower invasiveness of the MDA-MB-231 cells *in vitro*, while in nude mice tumor growth was promoted (Yao et al., 2007). This is at first counter-intuitive but may refer to different developmental stages in the metastatic evolution of cancer and intercellular signaling. In fact, xenograft cells exhibited elevated IL-8 levels compared to their cell culture counterparts and may therefore activate mitogen-activated protein kinase (MAPK) and phosphatidylinositol-3-kinase (PI3K) signaling that both induce cell proliferation, survival, and invasion (Todorović-Raković and Milovanović, 2013). Comparable discrepancies have been reported for CD44 as surface glycoprotein that commonly serves as therapeutic target (Yang et al., 2015) and vimentin as mesenchymal marker upregulated in migrating cells (Kokkinos et al., 2007). Together with a loss of E-cadherin expression (Kowalski et al., 2003), the resulting EMT can be regarded as dependent on media composition and overall cellular environment.

Second, spheroid integrity was ensured with appropriate methodological screenings, but the microarray-based set-up was desired as beneficial method for co-culture investigations. It is seen as improvement compared to the basic spheroid model in terms of cellular polarity and associated intercellular signaling. The tuneability in terms of mechanical support, cell-surface adhesion, and intercellular composition with independently established cultures in neighboring cavities that have further local gradients may facilitate a more physiological polarity of introduced cells. Type-I Collagen has been used as Dynarray coating, since collagen is the most redundant protein in the ECM and present in breast (Morris et al., 2016) and colon (Bode et al., 2000) tissue as entities of interest. With cancer cell homing in bone as special focus, this selection was further validated, since aberrant modifications like overhydroxylation of lysyl residues can be associated with pathological effects such as matrix fragility (Tzaphlidou, 2008). Since proper bone mineralization depends on matured collagenous structures in the osteoid, interactions with collagen producing osteoblasts might be crucial for metastatic niche formation and the observed metabolic coupling with fibroblasts may be extrapolated. Furthermore, the abundant collagen deposition in other tissues served as an initial crosslinker to on-site tumor biology, since cancer cells might already start with stromal cell interference before metastasis and continue their signaling after being attracted by increased collagen densities and released growth factors at the bone remodeling site (Canalis et al., 1988). Especially on this aspect, collagen might be superior to BME for investigations on slight metabolic changes mediated by alternated ECM secretion. Although both provided matrices are complex and therefore might include alternating concentrations of various undefined factors, especially for extracts like Matrigel, bioactive quantities are known for decades (Vukicevic et al., 1992). Additionally, Type-IV collagen is dominant in BME. It is physiologically addressed to basement membranes rather than bone tissue (Khoshnoodi et al., 2008). Increased amounts of Type-IV collagen usually serve as indication for tumorigenesis, since its increased structural flexibility supports cellular migration and angiogenesis (Öhlund et al., 2009). In summary, Type-I collagen appears to be the ECM supplement of choice for early on cancer development modelling.

While the upstream process of cell culture development and sample generation is setting the basis of successful investigations, processing of the sample and terminal detection of the target read-out also are crucial for proper analysis. Due to refractive index mismatches resulting in light scattering based on contained proteins, water and lipids, confocal imaging of biological samples is often restricted to a penetration depth of 50-70 μm (Schmitt and Kumar, 1998). Even with sectioning as time consuming sample preparation method, results may still not be representative due to heterogeneous distributions in complex samples (Renner et al., 2017). Therefore, a whole mount approach was desired with optical clearing as supportive intermediate step that allows comprehensive culture inspection. To improve the imaging depth and quality in complex cell culture samples, various clearing protocols were tested. With this, the characterization of cultures for ECM-dependent signal analysis as discussed in this work has been improved.

7.4 Broader considerations of relevant literature as future perspective

The patho-physiological effects of stromal cell and ECM-related stimuli on cancer cell metabolism and metastatic potential are multifaceted and extremely complex fields of science. Since many of these aspects could not be addressed during this thesis

project, some further interdependencies that are presently known are discussed in the following to outline possible future investigations.

EMT can be defined as a process in which epithelial cells lose their stable properties and polarity to instead start to obtain more fibroblastic and mesenchymal characteristics during a trans-differentiation. For example, a disordered ECM can lead to increased MAPK signaling based on insufficient growth inhibiting matrix receptors, thus supporting cancer progression and EMT (Bissel et al., 2005). Usually, this process is associated with epidermal growth factor receptor (EGFR) signaling (Vincent-Salomon and Thiery, 2003). EGFR signaling controls cell proliferation, apoptosis, and cancer progression. As a proto-oncogene, EGFR is commonly upregulated in various entities such as metastatic colorectal cancer or breast cancer. Numerous mutations alternating extracellular binding or activated signal transduction can over-activate versatile downstream pathways, including RAS-RAF-MEK-ERK MAPK and PI3K-AKT-mTOR (Wee and Wang, 2017). Physiologically, EGFR is expressed in most cell types and receptor-deficient mice died from abnormalities in brain, colorectal, skin, kidney, and liver tissue (Threadgill et al., 1995). This is of high pathological relevance, since EGF can also induce the expression of its own receptor, possibly starting a positive feedback loop upon aberration and therefore influencing systemic functions (Clark et al., 1985). Mutations in the receptor sequence often affect the extracellular ligand binding or the intracellular C-terminal tail that is associated with kinase auto-regulation (Pines et al., 2010).

MAPK is considered the major pathway in EGFR signal transduction. The corresponding tyrosine kinase cascades include MAPK molecules ERK1/2, ERK5, and JNK1/2/3, depending on the growth factor stimulus and additional environmental properties. Thereby, induction processes can also be adapted by other stimuli such as TGF β or oxidative stress, resulting in hundreds of downstream substrates and corresponding targets in various research fields (Wei and Liu, 2002). A comprehensive description of all of these may not be available within a narrow time frame, but new facets are continuously published (Morrison, 2012).

The PI3K-AKT-mTOR signaling pathway is probably the most important regulator of signal transduction in mammalian cells, since its versatile effects are related with mechanisms that may both, prevent and induce a cellular dysfunction and correlating diseases. Through tyrosine-kinase-mediated signal transduction, cellular metabolism, fate as well as physiological activity are influenced and therefore a dysfunction can be related to cancer, diabetes, and mental illnesses like schizophrenia. Since pathway interactions with upstream and downstream molecules are complex, further research is still needed and only the most abundant signaling processes are well understood so far (Xu et al., 2020). With PI3K already being divided into three subgroups based on their structural properties, these classes can further be defined by their mode of activation. The resulting AKT activity upon PI3K-activation cannot be anticipated easily since the cascade might be regulated by the cellular condition. Phosphorylated residues might stabilize active AKT with ATP-dependent mechanisms supporting this process. Other activation models correlate dephosphorylated AKT to higher activity under comparable conditions (Yudushkin, 2019). Subsequent mTORC1 induction is commonly addressed to metabolic actions only, but downstream HK-2 expression and corresponding feedback regulations rather imply protective reasons for the observed

signaling. In fact, associated glycolysis and autophagy are dependent on the availability of nutrients and cardiomyocytes only enter autophagy in glucose-low conditions (Roberts and Miyamoto, 2015). In the current work, evidence has shown that these effects could alternatively be induced upon the addition of stromal fibroblasts that established a reverse Warburg signaling independent from glucose levels. This coupling links the metabolic state with alternating signal transduction of ECM-related growth factors.

Cancer associated fibroblasts originate from cancer-stroma interactions and can be characterized by increased smooth muscle actin expression coming along with a loss of Caveolin-1 (Cav1) (Nishishita et al., 2018). Cav1 is part of membrane-dependent cell signaling and associated to three different structures: planar non-caveolar rafts, caveolae, and Cav1-scaffolds. All these consist of the common membrane subunits: phospholipids and glycolipids, but are further enriched with cholesterol, caveolin, and structure dependent subunits. Planar non-caveolar rafts are associated with active EGFR and enriched glycosylphosphatidylinositol (GPI) anchoring protein that enhance corresponding signaling and cell-cell interaction. The caveolae are plasma membrane invaginations that are stabilized by cholesterol and commonly associated to the insulin receptor. Caveolin1 scaffolds also remain planar but establish increased integrin binding and contained EGFR are usually inactive. Therefore, while exceptions are still reported, Cav1 is recapitulatory associated with reduced ERK and Ras signaling, maintained Akt, and both, nitric oxide synthesis increase, and decrease based on environmental properties. Since Cav1 most frequently binds EGFR to prevent signaling cascades that induce cellular migration, it is appropriate that it is downregulated during EMT. Furthermore, E-Cadherin binding correlates with increased Cav1 scaffolds and number of caveolae (Boscher and Nabi, 2012). Due to a lack of resolution on Cav1 detection, this analysis branch has not been focused within the current work, but might be addressed in future investigations, since the mere amount of both, EGFR and Cav1 signals do not necessarily correlate with corresponding signal transductions.

Finally, some outcomes did not match the up-front expectations and should therefore be further investigated to validate if they originate from exceptional regulations or unsuitable quantification methodology. Considering that succinate dehydrogenase levels were estimated to be decreasing upon co-cultivation of cancer cells and stromal fibroblasts, maintained signal intensities were observed. SDH as mitochondrial membrane-bound enzyme links oxidative phosphorylation and electron transfer in the respiratory chain. Therefore, it is used as measure for citrate cycle activity (Tian, 2016) that was estimated to decrease with emerging impact of glycolysis during reverse Warburg signaling. EMT can be associated with altered histone methylation based on succinate accumulation within cancer cells and is also favored by overall reduced SDH activity (Wong et al., 2017). That again can be linked with the observed increase of TGF β and corresponding metastatic potential (Wang et al., 2016) and therefore might justify further experiments.

7.5 Summarizing outlook

In this work, the interdependency of stromal cells, extracellular matrix-mediated stimuli, and cancer cells was studied. Mechanistic effects that regulate marker expressions linked to metastatic niche formation in bone and metabolic coupling or EMT on primary

tumor sites were observed in targeted 2D- and 3D-cell cultures. Finally, subcellular resolutions as well as cell type specific analysis were enabled by technological advances in both, cell culture methodology and downstream sample analysis.

BSP secretion as readout marker for metastatic niche formation was modulated by different culture conditions and ECM supplementation. It is commonly acknowledged, that compared to the cultivation of cell lines on 2D-surfaces, 3D-spheroids are more similar to the physiological *in vivo* situation based on cellular morphology. The impact of culture structure, stromal cells, and ECM supplementation with soluble factors have been rarely assessed in previous reports and were therefore directly addressed here. This showed, that BSP secretion can directly be regulated by provided ECM, since *de novo* synthesis and secretion correlated with enriched media composition and ECM-modulating stimuli such as applied proteolytic activity. TGF β is likely to be a main modulator of these alterations, since activation of its latent form was consistent with MMP-9 application initiating EMT.

It is reasonable, that cancer cell metabolism and metastatic potential are tightly linked. In fact, several interacting processes have been shown and therefore the cancer cell should not be seen as autonomous unit. Rather, it is interacting with its surroundings to exchange available stimuli contained in the ECM for meeting its own metabolic needs. The corresponding alterations of stromal cell types such as cancer associated fibroblasts revealed a metabolic coupling that mimics major features of the reverse Warburg effect *in vitro*. Thus, increased membrane carrier expression was observed, correlating with aerobic glycolysis and autophagy. This crucial effect during cancer progression has been analyzed in a cell type specific manner on novel 3D-cell culture arrays.

From a technological point of view, the cultivation of MDA-MB-231 breast cancer cells in spheroids was optimized for long-term studies. Furthermore, Dynarray cultures were found to be a promising tool to diminish artifacts of cellular physiology and morphology which may arise from a lack of mechanical support in spheroids. With upcoming artificial proteins like animal-free collagen, the effects of remaining growth factors and enzymatic residues might further be reduced, and future readouts could exclusively rely on cellular secretion of signaling factors. Through the application of optimized tissue clearing procedures adapted for the microarray-based co-culture design, more profound data could be achieved from 3D-samples. The evolution towards 3D-culture techniques has been already started. Therefore, further co-cultivation improvements should consecutively be implemented to adequately cover stromal cell and derived ECM dependency and to terminally help improving the ultimate cancer treatability.

8 SUMMARY

Primary tumor progression and metastasis are highly dependent on the cancer cell population and its interaction with surrounding stimuli, i.e. extracellular matrix (ECM) and stroma. Therefore, a comprehensive knowledge about processes involved in the remodeling of the ECM during niche formation and the metabolic coupling of cancer cells and stromal cell populations is needed in order to improve cancer treatment. Due to their ease in use and reproducibility, cell culture-based models have been widely used in cancer research. However, common models often lack important aspects of tumor biology, in particular, regarding ECM and stroma. For that reason, this work aimed at novel two- (2D) and three-dimensional (3D) models in mono- and co-culture that enable deeper insights into the role of ECM and stroma in cancer cell biology.

First, the effects of ECM compounds on the growth of 2D-cultures and 3D-spheroids of MDA-MB-231 human breast cancer cells were addressed. This showed that 3D-cultures of this cell line establish stable spheroids only in the presence of ECM supplementation but not in their absence. In parallel, MCF10A human breast epithelial cells were tested to evaluate their transferability towards co-culture modeling with distinct media compositions. This revealed highly altered spheroid morphologies and sizes when adapting mutual mono-culture protocols. In particular, MDA-MB-231 showed increased spheroid growth in enriched media commonly used for MCF10A cells, while the non-cancerous epithelial cells established proliferating subspheroids upon supplementation with basal membrane extract (BME).

Next, the role of ECM on biosynthesis and secretion of the bone metastasis marker, bone sialoprotein (BSP), were studied. Therefore, cultures in cell-repellent wells containing basal membrane extract served as robust 3D-culture model. This showed that BSP expression levels were higher in the presence of BME, Type-I collagen, and proteolytic activity associated with ECM remodeling, implying mechanistic interactions between matrix metalloprotease (MMP) activity, BSP expression and matrix acidification. Experiments with cycloheximide on samples processed with and without permeabilization indicated an induced protein neogenesis with consecutive secretion consistent with latent transforming growth factor beta or matrix MMPs being activated during ECM modulation.

After altered cellular activity of MDA-MB-231 cancer cells based on ECM stimuli was ensured, findings were transferred to HT-29 human colon cancer cells to enhance the significance of the readouts. Changing the cell culture model to an array-based 3D-culture system improved cell-cell interactions and mechano-transduction processes that were rather limited in spheroid cultures based to their compact structures and a lack of stronger physical support. Chip cultures revealed metabolic alterations in both, ECM producing fibroblasts and cancer cells, indicating mechanisms complying with the reverse Warburg effect. During this metabolic coupling process, the aerobic glycolysis is increased in stromal fibroblasts and membrane shuttling of metabolites can favor cancer progression and metastasis.

All 3D-studies were facilitated by progress in optical tissue clearing of intact fixed 3D-cancer cell cultures. Thus, the present work contributed to these novel protocols for cancer cell spheroids and 3D-cell-array cultures.

Altogether, links between ECM-mediated cancer progression and metabolic coupling as well as metastatic niche formation were described in this work using novel cell culture models. Technological advances in both, cell culture methodology and downstream sample analysis were achieved, which yielded new insights on intercellular signaling induced by ECM components or stromal cells. Therefore, considering co-culture compositions and ECM compounds, a promising tool for preclinical trials was established to help improving cancer research.

9 ZUSAMMENFASSUNG

Der Fortschritt primärer Tumore und dessen Metastasierung hängen stark von der Krebszellpopulation und ihren Wechselwirkungen mit umgebenden Reizen wie der extrazellulären Matrix (EZM) und dem Stroma ab. Um die Behandlung von Krebserkrankungen zu verbessern, ist es daher wichtig, umfassendes Wissen über die Nischenbildung und die Kopplung von Stoffwechselwegen zu erlangen, da es in diesen Prozessen zu einer Modellierung der EZM kommen kann. Die Krebsforschung setzt vermehrt auf zellkultur-basierte Modelle, da diese besonders einfach in der Handhabung sind und reproduzierbare Ergebnisse liefern. Verbreitete Methoden decken aber wichtige Aspekte der Tumorbiologie häufig nicht ab, vor allem in Bezug auf die extrazelluläre Matrix und umgebender Zelltypen werden einige Aspekte nicht immer beleuchtet. Aus diesem Grund wurde in dieser Arbeit ein besonderes Augenmerk auf neue zwei- (2D) und drei-dimensionale (3D) Modelle gelegt, um mit Hilfe von Mono- und Ko-Kulturen zu neuen Erkenntnissen bezüglich der Wechselspiele von Krebszellen und ihrer Umgebung zu gelangen.

Zunächst wurden Effekte von Komponenten der extrazellulären Matrix auf das Wachstum humaner MDA-MB-231 Brustkrebszellen in 2D-Kulturen und 3D-Sphäroiden betrachtet. Dabei zeigte sich eine direkte Abhängigkeit von der EZM, da diese Kulturen nur stabile Sphäroide ausbildeten, wenn eine entsprechende Supplementierung gewährleistet wurde. Gleichzeitig sollte mit Hilfe von humanen MCF10A Brustepithelzellen geprüft werden, ob Ergebnisse, die mit den jeweiligen Mono-Kulturmedien erzielt wurden, auf ein Ko-Kulturmodell übertragen werden können. Es stellte sich heraus, dass die Größe und die Form der einzelnen Sphäroide stark von der verabreichten Supplementierung abhängig waren. Während Kulturen der MCF10A Zellen durch die Zugabe von Extrakten der Basalmembran (BME) zusätzliche Substrukturen ausbildeten, bildeten MDA-MB-231 Zellen einen einzelnen Sphäroiden aus, dessen Wachstum durch ein angereichertes Medium stimuliert wurde.

Danach wurde getestet, wie sich die EZM auf die Biosynthese und die Sekretion von Knochen-Sialoprotein (BSP) auswirkt. Um diesen Marker für Knochenmetastasierung genauer zu untersuchen, wurde ein robustes 3D-Modell verwendet, bei dem die Zellen zusammen mit BME in Wannen mit zellabweisender Oberfläche kultiviert wurden. Hierbei konnte gezeigt werden, dass die Expression von BSP mit Hilfe von BME, Collagen Typ-I, oder durch die Applikation proteolytischer Aktivität stimuliert werden kann. Zusammenhänge mit der EZM-Modellierung deuteten dabei mechanistische Effekte an, bei denen die Aktivität von Matrix-Metalloproteasen (MMP), die Expression von BSP und die Ansäuerung der Matrix im direkten Zusammenhang stehen. Die Behandlung von verschiedenen Kulturen mit Cycloheximid und die anschließende Betrachtung von mit und ohne Permeabilisierung gefärbten Proben deuten eine Protein-Neusynthese mit nachfolgender Sekretion an. Dieser Einfluss könnte mit der Aktivierung latenter transformierender Wachstumsfaktoren und MMPs während der EZM Modellierung erklärt werden.

Nachdem sichergestellt werden konnte, dass sich das Verhalten von MDA-MB-231 Krebszellen durch Reize in der extrazellulären Matrix beeinflussen lässt, wurden diese Ergebnisse auf humane HT-29 Darmkrebszellen übertragen. Hierdurch sollte die Aussagekraft der erzielten Befunde gesteigert werden. Durch die Anpassung des 3D-Zellkulturmodells in ein Array-System wurden Zell-Zell-Interaktionen und Prozesse der

mechanischen Transduktion verbessert. Ihr kompakter Aufbau und das Fehlen weiterer physikalischer Stützen waren limitierende Faktoren für eine entsprechende Untersuchung im zuvor verwendeten Sphäroid-Modell. Die Array-basierten Kulturen zeigten induzierte Abweichungen in der Stoffwechsellistung von Krebszellen und EZM-produzierenden Fibroblasten. Diese Effekte stimmten mit dem Modell des reversen Warburg-Effekts überein, bei dessen Ausbildung Fibroblasten aus dem Tumor-Stroma vermehrt den Stoffwechselweg der aeroben Glykolyse nutzen. In diesem Zusammenhang treten erhöhte Membran-Transporter-Aktivitäten auf und freigesetzte Stoffwechselprodukte können den Krebsfortschritt und die Metastasierung begünstigen.

Alle dreidimensionalen Studien profitierten von Verbesserungen der optischen Gewebeklärung intakter 3D-Kulturen. Daher trug diese Arbeit zur Weiterentwicklung entsprechender Protokolle zur Analyse von Krebszell-Sphäroiden bei und entwickelte neue 3D-Array-Kulturen weiter.

Insgesamt werden verschiedene Einflüsse der EZM auf die biologischen Aktivitäten neuer Zellkulturmodelle in dieser Arbeit beschrieben. Es konnte eine Verbindung von Krebsfortschritt und damit verbundener Stoffwechsel-Kopplung mit Stromazellen auf der einen, und der Bildung von Tumornischen während der Metastasierung auf der anderen Seite aufgezeigt werden. Technologischer Fortschritt wurde erreicht und neue Einblicke in EZM-modulierten Signalen und Zell-Zell-Interaktionen wurden mit Verbesserungen der Zellkulturmethoden und der darauffolgenden Probenanalyse ermöglicht. Damit wurde ein vielversprechendes Instrument für präklinische Studien entwickelt, das dabei helfen kann, die Krebsforschung zu verbessern.

10 REFERENCES

Achilli, T.M., Meyer, J., and Morgan, J.R. (2012). Advances in the formation, use and understanding of multi-cellular spheroids. *Expert Opin. Biol. Ther.* *12*, 1347–1360.

Adwan, H., Bäuerle, T.J., and Berger, M.R. (2004). Downregulation of osteopontin and bone sialoprotein II is related to reduced colony formation and metastasis formation of MDA-MB-231 human breast cancer cells. *Cancer Gene Ther.* *11*, 109–120.

Al-Bari, A.A., and Al Mamun, A. (2020). Current advances in regulation of bone homeostasis. *FASEB BioAdvances* *2*, 668–679.

Alepee, N., Bahinski, A., Daneshian, M., De Wever, B., Fritsche, E., Goldberg, A., Hansmann, J., Hartung, T., Haycock, J., Hogberg, H., et al. (2014). State-of-the-art of 3D cultures (organs-on-a-chip) in safety testing and pathophysiology. *ALTEX* *31*, 441–477.

Allocca, G., Hughes, R., Wang, N., Brown, H.K., Ottewell, P.D., Brown, N.J., and Holen, I. (2019). The bone metastasis niche in breast cancer-potential overlap with the haematopoietic stem cell niche in vivo. *J. Bone Oncol.* *17*, 100244.

Andersen, T., Auk-Emblem, P., and Dornish, M. (2015). 3D Cell Culture in Alginate Hydrogels. *Microarrays* *4*, 133–161.

Ardi, V.C., Van den Steen, P.E., Opdenakker, G., Schweighofer, B., Deryugina, E.I., and Quigley, J.P. (2009). Neutrophil MMP-9 proenzyme, unencumbered by TIMP-1, undergoes efficient activation in vivo and catalytically induces angiogenesis via a basic fibroblast growth factor (FGF-2)/FGFR-2 pathway. *J. Biol. Chem.* *284*, 25854–25866.

Ariel, P. (2017). A beginner's guide to tissue clearing. *Int J Biochem Cell Biol* *84*, 35–39.

Arneson, T.J., Shuling Li, Y., Yi Peng, E.D., Weinhandl, E.D., Blaes, A., Cetin, K., Chia, V.M., Stryker, S., Pinzone, J.J., and Acquavella, J. (2012). Estimated number of prevalent cases of metastatic bone disease in the US adult population. *Clin. Epidemiol.* *4*, 87.

ATCC American Type Culture Collection (2012). Thawing, Propagating, and Cryopreserving Protocol; NCI-PBCF-HTB26 (MDA-MB231) Breast Adenocarcinoma.

Augsten, M. (2014). Cancer-Associated Fibroblasts as Another Polarized Cell Type of the Tumor Microenvironment. *Front. Oncol.* *4*, 820.

Bae, J.E., Huh, M. II, Ryu, B.K., Do, J.Y., Jin, S.U., Moon, M.J., Jung, J.C., Chang, Y., Kim, E., Chi, S.G., et al. (2011). The effect of static magnetic fields on the aggregation and cytotoxicity of magnetic nanoparticles. *Biomaterials* *32*, 9401–9414.

Baker, M. (2016). Reproducibility: Respect your cells! *Nature* *537*, 433–435.

Baker, B.M., and Chen, C.S. (2012). Deconstructing the third dimension-how 3D culture microenvironments alter cellular cues. *J. Cell Sci.* 125, 3015–3024.

Baptiste, T.A., James, A., Saria, M., and Ochieng, J. (2007). Mechano-transduction Mediated Secretion and Uptake of Galectin-3 in Breast Carcinoma cells: Implications in the Extracellular Functions of the Lectin. *Exp Cell Res.* 313, 652–664.

Barnes, D. (1986). Assay of cell attachment and spreading factors. *J. Tissue Cult. Methods* 69–74.

Barnes, G.L., Javed, A., Waller, S.M., Kamal, M.H., Hebert, K.E., Hassan, M.Q., Bellahcene, A., Van Wijnen, A.J., Young, M.F., Lian, J.B., et al. (2003). Osteoblast-related transcription factors Runx2 (Cbfa1/AML3) and MSX2 mediate the expression of bone sialoprotein in human metastatic breast cancer cells. *Cancer Res.* 63, 2631–2637.

Bassel, G.W. (2015). Accuracy in quantitative 3D image analysis. *Plant Cell* 27, 950–953.

Bauer, S., Wennberg Huld, C., Kanebratt, K.P., Durieux, I., Gunne, D., Andersson, S., Ewart, L., Haynes, W.G., Maschmeyer, I., Winter, A., et al. (2017). Functional coupling of human pancreatic islets and liver spheroids on-a-chip: Towards a novel human ex vivo type 2 diabetes model. *Sci. Rep.* 7, 14620.

Bäuerle, T., Peterschmitt, J., Hilbig, H., Kiessling, F., Armbruster, F.P., and Berger, M.R. (2006). Treatment of bone metastasis induced by MDA-MB-231 breast cancer cells with an antibody against bone sialoprotein. *Int. J. Oncol.* 28, 573–583.

Bellahcène, A., Antoine, N., Clause, N., Tagliabue, E., Fisher, L.W., Kerr, J.M., Jarès, P., and Castronovo, V. (1996). Detection of bone sialoprotein in human breast cancer tissue and cell lines at both protein and messenger ribonucleic acid levels. *Lab. Invest.* 75, 203–210.

Bellahcène, A., Castronovo, V., Ogbureke, K.U.E., Fisher, L.W., and Fedarko, N.S. (2008). Small Integrin-Binding Ligand N-linked Glycoproteins (SIBLINGs): Multifunctional proteins in cancer. *c Nat. Rev. Cancer* 8, 212–226.

Benton, G., Kleinman, H.K., George, J., and Arnaoutova, I. (2011). Multiple uses of basement membrane-like matrix (BME/Matrigel) in vitro and in vivo with cancer cells. *Int. J. Cancer* 128, 1751–1757.

Benton, J.A., Fairbanks, B.D., and Anseth, K.S. (2009). Characterization of valvular interstitial cell function in three dimensional matrix metalloproteinase degradable PEG hydrogels. *Biomaterials* 30, 6593–6603.

Benz, M.R., Czernin, J., Dry, S.M., Tap, W.D., Allen-Auerbach, M.S., Elashoff, D., Phelps, M.E., Weber, W.A., and Eilber, F.C. (2010). Quantitative F18-fluorodeoxyglucose positron emission tomography accurately characterizes peripheral nerve sheath tumors as malignant or benign. *Cancer* 116, 451–458.

- Bergers, G., Brekken, R., McMahon, G., Vu, T.H., Itoh, T., Tamaki, K., Tanzawa, K., Thorpe, P., Itohara, S., Werb, Z., et al. (2000). Matrix metalloproteinase-9 triggers the angiogenic switch during carcinogenesis. *Nat. Cell Biol.* **2**, 737–744.
- Berlanga, M.L., Phan, S., Bushong, E.A., Wu, S., Kwon, O., Phung, B.S., Lamont, S., Terada, M., Tasdizen, T., Martone, M.E., et al. (2011). Three-dimensional reconstruction of serial mouse brain sections: solution for flattening high-resolution large-scale mosaics. *Front. Neuroanat.* **5**, 17.
- Bhatia, S.N., and Ingber, D.E. (2014). Microfluidic organs-on-chips. *Nat. Biotechnol.* **32**, 760–772.
- Bianco, P., Fisher, L.W., Young, M.F., Termine, J.D., and Robey, P.G. (1991). Expression of bone sialoprotein (BSP) in developing human tissues. *Calcif. Tissue Int.* **49**, 421–426.
- Bierie, B., and Moses, H.L. (2006). Tumour microenvironment - TGFB: The molecular Jekyll and Hyde of cancer. *Nat. Rev. Cancer* **6**, 506–520.
- Bissel, M.J., Kenny, P.A., and Radisky, D.C. (2005). Microenvironmental Regulators of Tissue Structure and Function Also Regulate Tumor Induction and Progression: The Role of Extracellular Matrix and Its Degrading Enzymes. *Cold Spring Harb Symp Quant Biol* **70**, 343–356.
- Bissell, M.J., Rizki, A., and Mian, I.S. (2003). Tissue architecture: The ultimate regulator of breast epithelial function. *Curr. Opin. Cell Biol.* **15**, 753–762.
- Blank, A., Roberts, D.E., Dawson, H., Zlobec, I., and Lugli, A. (2018). Tumor Heterogeneity in Primary Colorectal Cancer and Corresponding Metastases. Does the Apple Fall Far From the Tree? *Front. Med.* **5**, 234.
- Blin, G., Sadurska, D., Migueles, R.P., Chen, N., Watson, J.A., and Lowell, S. (2019). Nessys: A new set of tools for the automated detection of nuclei within intact tissues and dense 3D cultures. *PLoS Biol.* **17**, 1–29.
- Bode, M.K., Karttunen, T.J., Makela, J., Risteli, L., and Risteli, J. (2000). Type I and III collagens in human colon cancer and diverticulosis. *Scand. J. Gastroenterol.* **35**, 747–752.
- Boire, A., Covic, L., Agarwal, A., Jacques, S., Sherifi, S., and Kuliopulos, A. (2005). PAR1 is a matrix metalloprotease-1 receptor that promotes invasion and tumorigenesis of breast cancer cells. *Cell* **120**, 303–313.
- Bonewald, L.F. (2011). The amazing osteocyte. *J. Bone Miner. Res.* **26**, 229–238.
- Boscher, C., and Nabi, I.R. (2012). Caveolin-1: Role in Cell Signaling. *Adv. Exp. Med. Biol.* **29–50**.

- Bossolani, G.D.P., Pintelon, I., Detrez, J.D., Buckinx, R., Thys, S., Zanoni, J.N., De Vos, W.H., and Timmermans, J.P. (2019). Comparative analysis reveals Ce3D as optimal clearing method for in toto imaging of the mouse intestine. *Neurogastroenterol. Motil.* *31*, 1–11.
- Boulefour, W., Boudiffa, M., Wade-Gueye, N.M., Bouët, G., Cardelli, M., Laroche, N., Vanden-Bossche, A., Thomas, M., Bonnelye, E., Aubin, J.E., et al. (2014). Skeletal development of mice lacking Bone Sialoprotein (BSP) - Impairment of long bone growth and progressive establishment of high trabecular bone mass. *PLoS One* *9*, 1–13.
- Boutin, M.E., Voss, T.C., Titus, S.A., Cruz-Gutierrez, K., Michael, S., and Ferrer, M. (2018). A high-throughput imaging and nuclear segmentation analysis protocol for cleared 3D culture models. *Sci. Rep.* *8*, 11135.
- Bovenzi, C.D., Hamilton, J., Tassone, P., Johnson, J., Cognetti, D.M., Luginbuhl, A., Keane, W.M., Zhan, T., Tuluc, M., Bar-Ad, V., et al. (2015). Prognostic Indications of Elevated MCT4 and CD147 across Cancer Types: A Meta-Analysis. *Biomed Res. Int.* *2015*, 242437.
- Brandão-Costa, R.M., Helal-Neto, E., Vieira, A.M., Barcellos-De-souza, P., Morgado-Diaz, J., and Barja-Fidalgo, C. (2020). Extracellular matrix derived from high metastatic human breast cancer triggers epithelial-mesenchymal transition in epithelial breast cancer cells through $\alpha\beta3$ integrin. *Int. J. Mol. Sci.* *21*, 1–20.
- Breslin, S., and O'Driscoll, L. (2013). Three-dimensional cell culture: The missing link in drug discovery. *Drug Discov. Today* *18*, 240–249.
- Brewer, G.J., and Cotman, C.W. (1989). Survival and growth of hippocampal neurons in defined medium at low density: advantages of a sandwich culture technique or low oxygen. *Brain Res.* *494*, 65–74.
- Brinkley, B.R., Beall, P.T., Wible, L.J., Mace, M.L., Turner, D.S., and Cailleau, R.M. (1980). Variations in cell form and cytoskeleton in human breast carcinoma cells in vitro. *Cancer Res.* *40*, 3118–3129.
- Brown, M.J., Bahsoun, S., Morris, M.A., and Akam, E.C. (2019). Determining conditions for successful culture of multi-cellular 3D tumour spheroids to investigate the effect of mesenchymal stem cells on breast cancer cell invasiveness. *Bioengineering* *6*.
- Burguera, E.F., Bitar, M., and Bruinink, A. (2010). Novel in vitro co-culture methodology to investigate heterotypic cell-cell interactions. *Eur. Cells Mater.* *19*, 166–179.
- Bussard, K.M., Gay, C. V., and Mastro, A.M. (2008). The bone microenvironment in metastasis; what is special about bone? *Cancer Metastasis Rev.* *27*, 41–55.
- Cailleau, R., Young, R., Olivé, M., and Reeves, W.J. (1974). Breast tumor cell lines from pleural effusions. *J. Natl. Cancer Inst.* *53*, 661–674.

- Calon, A., Lonardo, E., Berenguer-Llargo, A., Espinet, E., Hernando-Momblona, X., Iglesias, M., Sevillano, M., Palomo-Ponce, S., Tauriello, D.V.F., Byrom, D., et al. (2015). Stromal gene expression defines poor-prognosis subtypes in colorectal cancer. *Nat. Genet.* *47*, 320–329.
- Campuzano, S., and Pelling, A.E. (2019). Scaffolds for 3D Cell Culture and Cellular Agriculture Applications Derived From Non-animal Sources. *Front. Sustain. Food Syst.* *3*, 1–9.
- Canalis, E., McCarthy, T., and Centrella, M. (1988). Growth factors and the regulation of fetal growth. *J Clin Invest.* *81*, 277–281.
- Cannino, G., Ciscato, F., Masgras, I., Sánchez-Martín, C., and Rasola, A. (2018). Metabolic plasticity of tumor cell mitochondria. *Front. Oncol.* *8*.
- Capietto, A.H., Chan, S.R., Ricci, B., Allen, J.A., Su, X., Novack, D. V., Schreiber, R.D., and Faccio, R. (2016). Novel ER α positive breast cancer model with estrogen independent growth in the bone microenvironment. *Oncotarget* *7*, 49751–49764.
- Carey, S.P., Martin, K.E., and Reinhart-King, C.A. (2017). Three-dimensional collagen matrix induces a mechanosensitive invasive epithelial phenotype. *Sci. Rep.* *7*, 42088.
- Carvalho, M.R., Lima, D., Reis, R.L., Oliveira, J.M., and Correlo, V.M. (2017). Anti-Cancer Drug Validation: the Contribution of Tissue Engineered Models. *Stem Cell Rev Rep* *13*, 347–363.
- Cavo, M., Fato, M., Peñuela, L., Beltrame, F., Raiteri, R., and Scaglione, S. (2016). Microenvironment complexity and matrix stiffness regulate breast cancer cell activity in a 3D in vitro model. *Sci. Rep.* *6*, 35367.
- Cavo, M., Caria, M., Pulsoni, I., Beltrame, F., Fato, M., and Scaglione, S. (2018). A new cell-laden 3D Alginate-Matrigel hydrogel resembles human breast cancer cell malignant morphology, spread and invasion capability observed "in vivo". *Sci. Rep.* *8*, 5333.
- Cell Biolabs Inc. (2009). MDA-MB-231 / GFP Cell Line.
- Cevenini, A., Orrù, S., Mancini, A., Alfieri, A., Buono, P., and Imperlini, E. (2018). Molecular Signatures of the Insulin-like Growth Factor 1-mediated Epithelial-Mesenchymal Transition in Breast, Lung and Gastric Cancers. *Int. J. Mol. Sci.* *19*, 2411.
- Chaicharoenaudomrung, N., Kunhorm, P., and Noisa, P. (2019). Three-dimensional cell culture systems as an in vitro platform for cancer and stem cell modeling. *World J. Stem Cells* *11*, 1065–1083.
- Chan, H.F., Zhang, Y., Ho, Y.P., Chiu, Y.L., Jung, Y., and Leong, K.W. (2013). Rapid formation of multicellular spheroids in double-emulsion droplets with controllable microenvironment. *Sci. Rep.* *3*, 1–8.

- Chaubey, A., Ross, K.J., Leadbetter, R.M., and Burg, K.J.L. (2008). Surface patterning: Tool to modulate stem cell differentiation in an adipose system. *J. Biomed. Mater. Res. - Part B Appl. Biomater.* *84*, 70–78.
- Chen, C., Mehl, B.T., Sell, S.A., and Scott Martin, R. (2016a). Use of electrospinning and dynamic air focusing to create three-dimensional cell culture scaffolds in microfluidic devices. *Analyst* *141*, 5311–5320.
- Chen, F., Tillberg, P.W., and Boyden, E.S. (2015). Optical imaging. Expansion microscopy. *Science* *347*, 543–8.
- Chen, K., Wu, M., Guo, F., Li, P., Chan, C.Y., Mao, Z., Li, S., Ren, L., Zhang, R., and Huang, T.J. (2016b). Rapid formation of size-controllable multicellular spheroids: Via 3D acoustic tweezers. *Lab Chip* *16*, 2636–2643.
- Chen, L., Yan, C., and Zheng, Z. (2018). Functional polymer surfaces for controlling cell behaviors. *Mater. Today* *21*, 38–59.
- Chen, M.-T., Sun, H.-F., Zhao, Y., Fu, W.-Y., Yang, L.-P., Gao, S.-P., Li, L.-D., Jiang, H., and Jin, W. (2017). Comparison of patterns and prognosis among distant metastatic breast cancer patients by age groups: a SEER population-based analysis. *Sci. Rep.* *7*, 9254.
- Chen, W., Wong, C., Vosburgh, E., Levine, A.J., Foran, D.J., and Xu, E.Y. (2014). High-throughput image analysis of tumor spheroids: A user-friendly software application to measure the size of spheroids automatically and accurately. *J. Vis. Exp.*
- Chen, Y.C., Sosnoski, D.M., and Mastro, A.M. (2010). Breast cancer metastasis to the bone: mechanisms of bone loss. *Breast Cancer Res.* *12*, 215.
- Chen, Y., Tsai, Y.H., Liu, Y.A., Lee, S.H., Tseng, S.H., and Tang, S.C. (2013). Application of three-dimensional imaging to the intestinal crypt organoids and biopsied intestinal tissues. *ScientificWorldJournal* *2013*, 624342.
- Chen, Y., Shen, Q., White, S.L., Gokmen-Polar, Y., Badve, S., and Goodman, L.J. (2019). Three-dimensional imaging and quantitative analysis in CLARITY processed breast cancer tissues. *Sci Rep* *9*, 5624.
- Chen, Y.Y., Silva, P.N., Syed, A.M., Sindhvani, S., Rocheleau, J. V, and Chan, W.C. (2016c). Clarifying intact 3D tissues on a microfluidic chip for high-throughput structural analysis. *Proc Natl Acad Sci U S A* *113*, 14915–14920.
- Chiang, A.S., Lin, W.Y., Liu, H.P., Pszczolkowski, M.A., Fu, T.F., Chiu, S.L., and Holbrook, G.L. (2002). Insect NMDA receptors mediate juvenile hormone biosynthesis. *Proc Natl Acad Sci U S A* *99*, 37–42.
- Chiavarina, B., Whitaker-Menezes, D., Migneco, G., Martinez-Outschoorn, U.E., Pavlides, S., Howell, A., Tanowitz, H.B., Casimiro, M.C., Wang, C., Pestell, R.G., et al. (2010). HIF1- α functions as a tumor promoter in cancer associated fibroblasts, and as a tumor suppressor in breast cancer cells: Autophagy drives compartment-specific oncogenesis. *Cell Cycle* *9*, 3534–3551.

Chiricozzi, A., Romanelli, M., Panduri, S., Donetti, E., and Prignano, F. (2017). Relevance of in vitro 3-D skin models in dissecting cytokine contribution to psoriasis pathogenesis. *Histol Histopathol* 32, 893–898.

Christensen, J., Vonwil, D., and Shastri, V.P. (2015). Non-Invasive In Vivo Imaging and Quantification of Tumor Growth and Metastasis in Rats Using Cells Expressing Far-Red Fluorescence Protein. *PLoS One* 10, e0132725.

Chung, K., Wallace, J., Kim, S.Y., Kalyanasundaram, S., Andalman, A.S., Davidson, T.J., Mirzabekov, J.J., Zalocusky, K.A., Mattis, J., Denisin, A.K., et al. (2013). Structural and molecular interrogation of intact biological systems. *Nature* 497, 332–337.

Clark, A.J.L., Ishii, S., Richert, N., Merlino, G.T., and Pastan, I. (1985). Epidermal growth factor regulates the expression of its own receptor. *Proc. Natl. Acad. Sci. USA* 82, 8374–8378.

Cohen-Solal, K.A., Boregowda, R.K., and Lasfar, A. (2015). RUNX2 and the PI3K/AKT axis reciprocal activation as a driving force for tumor progression. *Mol. Cancer* 14, 137.

Coleman, R.E. (2001). Metastatic bone disease: clinical features, pathophysiology and treatment strategies. *Cancer Treat. Rev.* 27, 165–176.

Coleman, R.E. (2006). Clinical Features of Metastatic Bone Disease and Risk of Skeletal Morbidity. *Clin. Cancer Res.* 12, 6243s–6249s.

Coluccio, M.L., Perozziello, G., Malara, N., Parrotta, E., Zhang, P., Gentile, F., Limongi, T., Raj, P.M., Cuda, G., Candeloro, P., et al. (2019). Microfluidic platforms for cell cultures and investigations. *Microelectron. Eng.* 208, 14–28.

Contreras-Baeza, Y., Sandoval, P.Y., Alarcón, R., Galaz, A., Cortés-Molina, F., Alegría, K., Baeza-Lehnert, F., Arce-Molina, R., Guequén, A., Flores, C.A., et al. (2019). Monocarboxylate transporter 4 (MCT4) is a high affinity transporter capable of exporting lactate in high-lactate microenvironments. *J. Biol. Chem.* 294, 20135–20147.

Costa, A., Kieffer, Y., Scholer-Dahirel, A., Pelon, F., Bourachot, B., Cardon, M., Sirven, P., Magagna, I., Fuhrmann, L., Bernard, C., et al. (2018a). Fibroblast Heterogeneity and Immunosuppressive Environment in Human Breast Cancer. *Cancer Cell* 33, 463–479.e10.

Costa, E.C., Moreira, A.F., de Melo-Diogo, D., and Correia, I.J. (2018b). ClearT immersion optical clearing method for intact 3D spheroids imaging through confocal laser scanning microscopy. *Opt. Laser Technol.* 106, 94–99.

Costa, E.C., Moreira, A.F., Melo-Diogo, D. de, and Correia, I.J. (2018c). Polyethylene glycol molecular weight influences the Clear^{T2} optical clearing method for spheroids imaging by confocal laser scanning microscopy. *J. Biomed. Opt.* 23, 1-11,11.

Courtenay, J.C., Sharma, R.I., and Scott, J.L. (2018). Recent advances in modified cellulose for tissue culture applications. *Molecules* 23.

- Croisier, F., and Jérôme, C. (2013). Chitosan-based biomaterials for tissue engineering. *Eur. Polym. J.* *49*, 780–792.
- Cruz-Acuña, R., and García, A.J. (2019). Engineered materials to model human intestinal development and cancer using organoids. *Exp Cell Res* *337*, 109–114.
- Cui, X., Hartanto, Y., and Zhang, H. (2017). Advances in multicellular spheroids formation. *J. R. Soc. Interface* *14*.
- da Cunha, B.R., Domingos, C., Stefanini, A.C.B., Henrique, T., Polachini, G.M., Castelo-Branco, P., and Tajara, E.H. (2019). Cellular Interactions in the Tumor Microenvironment: The Role of Secretome. *J. Cancer* *10*, 4574–4587.
- Czyz, J., and Wobus, A.M. (2001). Embryonic stem cell differentiation: The role of extracellular factors. *Differentiation* *68*, 167–174.
- Das, V., Bruzzese, F., Konecny, P., Iannelli, F., Budillon, A., and Hajduch, M. (2015). Pathophysiologically relevant in vitro tumor models for drug screening. *Drug Discov Today* *20*, 848–855.
- Davidenko, N., Schuster, C.F., Bax, D. V., Farndale, R.W., Hamaia, S., Best, S.M., and Cameron, R.E. (2016). Evaluation of cell binding to collagen and gelatin: a study of the effect of 2D and 3D architecture and surface chemistry. *J. Mater. Sci. Mater. Med.* *27*.
- Davis, G.E. (1992). Affinity of integrins for damaged extracellular matrix: $\alpha\beta3$ binds to denatured collagen type I through RGD sites. *Biochem. Biophys. Res. Commun.* *182*, 1025–1031.
- DeBerardinis, R.J., Mancuso, A., Daikhin, E., Nissim, I., Yudkoff, M., Wehrli, S., and Thompson, C.B. (2007). Beyond aerobic glycolysis: Transformed cells can engage in glutamine metabolism that exceeds the requirement for protein and nucleotide synthesis. *Proc. Natl. Acad. Sci. U. S. A.* *104*, 19345–19350.
- Debnath, J., Muthuswamy, S.K., and Brugge, J.S. (2003). Morphogenesis and oncogenesis of MCF-10A mammary epithelial acini grown in three-dimensional basement membrane cultures. *Methods* *30*, 256–268.
- Demirkan, B. (2013). The Roles of Epithelial-to-Mesenchymal Transition (EMT) and Mesenchymal-to-Epithelial Transition (MET) in Breast Cancer Bone Metastasis: Potential Targets for Prevention and Treatment. *J. Clin. Med.* *2*, 264–282.
- Denton, A.E., Roberts, E.W., and Fearon, D.T. (2018). Stromal Cells in the Tumor Microenvironment. *Adv. Exp. Med. Biol.* *1060*, 99–114.
- Deryugina, E.I., and Quigley, J.P. (2010). Pleiotropic roles of matrix metalloproteinases in tumor angiogenesis: Contrasting, overlapping and compensatory functions. *Biochim. Biophys. Acta - Mol. Cell Res.* *1803*, 103–120.
- Desmaison, A., Guillaume, L., Triclin, S., Weiss, P., Ducommun, B., and Lobjois, V. (2018). Impact of physical confinement on nuclei geometry and cell division dynamics in 3D spheroids. *Sci Rep* *8*, 8785.

- Diel, I.J., Solomayer, E.F., Seibel, M.J., Pfeilschifter, J., Maisenbacher, H., Gollan, C., Pecherstorfer, M., Conradi, R., Kehr, G., Boehm, E., et al. (1999). Serum bone sialoprotein in patients with primary breast cancer is a prognostic marker for subsequent bone metastasis. *Clin. Cancer Res.* *5*, 3914–3919.
- Dingle, Y.-T.L., Boutin, M.E., Chirila, A.M., Livi, L.L., Labriola, N.R., Jakubek, L.M., Morgan, J.R., Darling, E.M., Kauer, J.A., and Hoffman-Kim, D. (2015). Three-Dimensional Neural Spheroid Culture: An In Vitro Model for Cortical Studies. *Tissue Eng. Part C. Methods* *21*, 1274–1283.
- Dotd, H.U., Leischner, U., Schierloh, A., Jahrling, N., Mauch, C.P., Deininger, K., Deussing, J.M., Eder, M., Zieglgansberger, W., and Becker, K. (2007). Ultramicroscopy: three-dimensional visualization of neuronal networks in the whole mouse brain. *Nat Methods* *4*, 331–336.
- Drost, J., and Clevers, H. (2018). Organoids in cancer research. *Nat Rev Cancer* *18*, 407–418.
- Ducy, P., Zhang, R., Geoffroy, V., Ridall, A.L., and Karsenty, G. (1997). *Osf2/Cbfa1*: a transcriptional activator of osteoblast differentiation. *Cell* *89*, 747–754.
- Duguay, S. (1999). Post-Translational Processing of Insulin-Like Growth Factors. *Horm. Metab. Res.* *31*, 43–49.
- Duivenvoorden, W.C.M., Hirte, H.W., and Singh, G. (1999). Transforming growth factor β 1 as an inducer of matrix metalloprotease expression and activity in human bone-metastasizing cancer cells. *Clin. Exp. Metastasis* *17*, 27–34.
- Dunn, J.C.Y., Tompkins, R.G., and Yarmush, M.L. (1992). Hepatocytes in collagen sandwich: Evidence for transcriptional and translational regulation. *J. Cell Biol.* *116*, 1043–1053.
- Dušková-Smrčková, M., Zavřel, J., Bartoš, M., Kaberova, Z., Filová, E., Zárubová, J., Šlouf, M., Michálek, J., Vampola, T., and Kubies, D. (2021). Communicating macropores in PHEMA-based hydrogels for cell seeding: Probabilistic open pore simulation and direct micro-CT proof. *Mater. Des.* *198*.
- Duval, K., Grover, H., Han, L.-H.H., Mou, Y., Pegoraro, A.F., Fredberg, J., and Chen, Z. (2017). Modeling Physiological Events in 2D vs. 3D Cell Culture. *Physiology (Bethesda)*. *32*, 266–277.
- Edinger, A.L. (2007). Controlling cell growth and survival through regulated nutrient transporter expression. *Biochem. J.* *406*, 1–12.
- Edmondson, R., Adcock, A.F., and Yang, L. (2016). Influence of Matrices on 3D-Cultured Prostate Cancer Cells' Drug Response and Expression of Drug-Action Associated Proteins. *PLoS One* *11*, e0158116.

- Ehret, F., Vogler, S., and Kempermann, G. (2015). A co-culture model of the hippocampal neurogenic niche reveals differential effects of astrocytes, endothelial cells and pericytes on proliferation and differentiation of adult murine precursor cells. *Stem Cell Res.* 15, 514–521.
- Engler, A.J., Sen, S., Sweeney, H.L., and Discher, D.E. (2006). Matrix Elasticity Directs Stem Cell Lineage Specification. *Cell* 126, 677–689.
- Erler, J.T., and Weaver, V.M. (2009). Three-dimensional context regulation of metastasis. *Clin. Exp. Metastasis* 26, 35–49.
- Erturk, A., Becker, K., Jahrling, N., Mauch, C.P., Hojer, C.D., Egen, J.G., Hellal, F., Bradke, F., Sheng, M., and Dodt, H.U. (2012). Three-dimensional imaging of solvent-cleared organs using 3DISCO. *Nat Protoc* 7, 1983–1995.
- Esquivel-Velázquez, M., Ostoa-Saloma, P., Palacios-Arreola, M.I., Nava-Castro, K.E., Castro, J.I., and Morales-Montor, J. (2015). The Role of Cytokines in Breast Cancer Development and Progression. *J. Interf. Cytokine Res.* 35, 1–16.
- Fang, Y., and Eglén, R.M. (2017). Three-Dimensional Cell Cultures in Drug Discovery and Development. *SLAS Discov.* 22, 456–472.
- Fedarko, N.S., Fohr, B., Robey, P.G., Young, M.F., and Fisher, L.W. (2000). Factor H Binding to Bone Sialoprotein and Osteopontin Enables Tumor Cell Evasion of Complement-mediated Attack. *J. Biol. Chem.* 275, 16666–16672.
- Fisher, L.W., and Fedarko, N.S. (2003). Six genes expressed in bones and teeth encode the current members of the SIBLING family of proteins. *Connect. Tissue Res.* 44 Suppl 1, 33–40.
- Fisher, L.W., Torchia, D.A., Fohr, B., Young, M.F., and Fedarko, N.S. (2001). Flexible structures of SIBLING proteins, bone sialoprotein, and osteopontin. *Biochem. Biophys. Res. Commun.* 280, 460–465.
- Fisusi, F.A., and Akala, E.O. (2019). Drug Combinations in Breast Cancer Therapy. *Pharm. Nanotechnol.* 7, 3–23.
- Fong, E.L., Wan, X., Yang, J., Morgado, M., Mikos, A.G., Harrington, D.A., Navone, N.M., and Farach-Carson, M.C. (2016). A 3D in vitro model of patient-derived prostate cancer xenograft for controlled interrogation of in vivo tumor-stromal interactions. *Biomaterials* 77, 164–172.
- Frantz, C., Stewart, K.M., and Weaver, V.M. (2010). The extracellular matrix at a glance. *J. Cell Sci.* 123, 4195–4200.
- Fridman, R., Kibbey, M.C., Royce, L.S., Zain, M., Sweeney, M., Jicha, D.L., Yannelli, J.R., Martin, G.R., and Kleinman, H.K. (1991). Enhanced tumor growth of both primary and established human and murine tumor cells in athymic mice after coinjection with Matrigel. *J. Natl. Cancer Inst.* 83, 769–774.

Friedrich, J., Seidel, C., Ebner, R., and Kunz-Schughart, L.A. (2009). Spheroid-based drug screen: considerations and practical approach. *Nat. Protoc.* 4, 309–324.

Fu, Y., Liu, S., Yin, S., Niu, W., Xiong, W., Tan, M., Li, G., and Zhou, M. (2017). The reverse Warburg effect is likely to be an Achilles' heel of cancer that can be exploited for cancer therapy. *Oncotarget* 8, 57813–57825.

Gallagher, J.C., and Sai, A.J. (2010). Molecular biology of bone remodeling: Implications for new therapeutic targets for osteoporosis. *Maturitas* 65, 301–307.

Gatenby, R.A., and Gillies, R.J. (2004). Why do cancers have high aerobic glycolysis? *Nat. Rev. Cancer* 4, 891–899.

Ge, L., Shenoy, S.K., Lefkowitz, R.J., and DeFea, K. (2004). Constitutive protease-activated receptor-2-mediated migration of MDA MB-231 breast cancer cells requires both β -arrestin-1 and -2. *J. Biol. Chem.* 279, 55419–55424.

Gentry, L.E., Lioubin, M.N., Purchio, A.F., and Marquardt, H. (1988). Molecular events in the processing of recombinant type 1 pre-pro-transforming growth factor beta to the mature polypeptide. *Mol. Cell. Biol.* 8, 4162–4168.

Georges, L.M.C., de Wever, O., Galván, J.A., Dawson, H., Lugli, A., Demetter, P., and Zlobec, I. (2019). Cell Line Derived Xenograft Mouse Models Are a Suitable *in vivo* Model for Studying Tumor Budding in Colorectal Cancer. *Front. Med.* 6, 139.

Gilbert, J., Henske, P., and Singh, A. (2003). Rebuilding Big Pharma's Business Model: The blockbuster business model that underpinned Big Pharma's success is now irreparably broken. The industry needs a new approach. *Vivo Bus. Med. Rep.* 2003.

Gillette, K.M., Forbes, K., and Sehgal, I. (2003). Detection of matrix metalloproteinases (MMP), tissue inhibitor of metalloproteinase-2, urokinase and plasminogen activator inhibitor-1 within matrigel and growth factor-reduced matrigel basement membrane. *Tumori* 89, 421–425.

Ginsburg, G.S., and Phillips, K.A. (2018). Precision medicine: From science to value. *Health Aff.* 37, 694–701.

Goldoni, S., and Iozzo, R. V. (2008). Tumor microenvironment: Modulation by decorin and related molecules harboring leucine-rich tandem motifs. *Int. J. Cancer* 123, 2473–2479.

Göppert, B., Sollich, T., Abaffy, P., Cecilia, A., Heckmann, J., Neeb, A., Bäcker, A., Baumbach, T., Gruhl, F.J., and Cato, A.C.B. (2016). Superporous Poly(ethylene glycol) Diacrylate Cryogel with a Defined Elastic Modulus for Prostate Cancer Cell Research. *Small* 12, 3985–3994.

Gordon, G.M., Ledee, D.R., Feuer, W.J., and Fini, M.E. (2009). Cytokines and signaling pathways regulating matrix metalloproteinase-9 (MMP-9) expression in corneal epithelial cells. *J. Cell. Physiol.* 221, 402–411.

Graf, B.W., and Boppart, S.A. (2010). Imaging and analysis of three-dimensional cell culture models. *Methods Mol. Biol.* *591*, 211–227.

Griffith, L.G., and Swartz, M.A. (2006). Capturing complex 3D tissue physiology in vitro. *Nat. Rev. Mol. Cell Biol.* *7*, 211–224.

Grist, S.M., Nasser, S.S., Poon, T., Roskelley, C., and Cheung, K.C. (2016). On-chip clearing of arrays of 3-D cell cultures and micro-tissues. *Biomicrofluidics* *10*, 44107.

Grootjans, J., Hundscheid, I.H., Lenaerts, K., Boonen, B., Renes, I.B., Verheyen, F.K., Dejong, C.H., von Meyenfeldt, M.F., Beets, G.L., and Buurman, W.A. (2013). Ischaemia-induced mucus barrier loss and bacterial penetration are rapidly counteracted by increased goblet cell secretory activity in human and rat colon. *Gut* *62*, 250–258.

Gu, L., and Mooney, D.J. (2016). Biomaterials and emerging anticancer therapeutics: Engineering the microenvironment. *Nat. Rev. Cancer* *16*, 56–66.

Hadjidakis, D.J., and Androulakis, I.I. (2006). Bone remodeling. *Ann. N. Y. Acad. Sci.* *1092*, 385–396.

Hafner, M., Heiser, L.M., Williams, E.H., Niepel, M., Wang, N.J., Korkola, J.E., Gray, J.W., and Sorger, P.K. (2017a). Quantification of sensitivity and resistance of breast cancer cell lines to anti-cancer drugs using GR metrics. *Sci. Data* *4*, 170166.

Hafner, M., Niepel, M., Subramanian, K., and Sorger, P.K. (2017b). Designing Drug-Response Experiments and Quantifying their Results. *Curr Protoc Chem Biol* *9*, 96–116.

Hagemann, J., Jacobi, C., Hahn, M., Schmid, V., Welz, C., Schwenk-Zieger, S., Stauber, R., Baumeister, P., and Becker, S. (2017). Spheroid-based 3D Cell Cultures Enable Personalized Therapy Testing and Drug Discovery in Head and Neck Cancer. *Anticancer Res.* *37*, 2201–2210.

Hajdu, Z., Mironov, V., Mehesz, A.N., Norris, R.A., Roger, R., and Visconti, R.P. (2011). Analysis of Tissue Maturation. *4*, 659–664.

Halper, J., and Kjaer, M. (2014). Basic components of connective tissues and extracellular matrix: Elastin, fibrillin, fibulins, fibrinogen, fibronectin, laminin, tenascins and thrombospondins. *Adv. Exp. Med. Biol.* *802*, 31–47.

Hama, H., Kurokawa, H., Kawano, H., Ando, R., Shimogori, T., Noda, H., Fukami, K., Sakaue-Sawano, A., and Miyawaki, A. (2011). Scale: a chemical approach for fluorescence imaging and reconstruction of transparent mouse brain. *Nat Neurosci* *14*, 1481–1488.

Hama, H., Hioki, H., Namiki, K., Hoshida, T., Kurokawa, H., Ishidate, F., Kaneko, T., Akagi, T., Saito, T., Saido, T., et al. (2015). ScaleS: an optical clearing palette for biological imaging. *Nat Neurosci* *18*, 1518–1529.

- Hammerl, A., Diaz Cano, C.E., De-Juan-Pardo, E.M., van Griensven, M., and Poh, P.S.P. (2019). A Growth Factor-Free Co-Culture System of Osteoblasts and Peripheral Blood Mononuclear Cells for the Evaluation of the Osteogenesis Potential of Melt-Electrowritten Polycaprolactone Scaffolds. *Int. J. Mol. Sci.* *20*.
- Harbeck, N., and Gnant, M. (2017). Breast cancer. *Lancet* *389*, 1134–1150.
- Hardy, E., and Fernandez-Patron, C. (2020). Destroy to Rebuild: The Connection Between Bone Tissue Remodeling and Matrix Metalloproteinases. *Front. Physiol.* *11*, 1–24.
- Härmä, V., Schukov, H.-P., Happonen, A., Ahonen, I., Virtanen, J., Siitari, H., Akerfelt, M., Lötjönen, J., and Nees, M. (2014). Quantification of dynamic morphological drug responses in 3D organotypic cell cultures by automated image analysis. *PLoS One* *9*, e96426.
- Hattar, S., Asselin, A., Greenspan, D., Oboeuf, M., Berdal, A., and Sautier, J.-M.M. (2005). Potential of biomimetic surfaces to promote in vitro osteoblast-like cell differentiation. *Biomaterials* *26*, 839–848.
- Hatzivassiliou, G., Zhao, F., Bauer, D.E., Andreadis, C., Shaw, A.N., Dhanak, D., Hingorani, S.R., Tuveson, D.A., and Thompson, C.B. (2005). ATP citrate lyase inhibition can suppress tumor cell growth. *Cancer Cell* *8*, 311–321.
- Helfman, D.M., Kim, E.J., Lukanidin, E., and Grigorian, M. (2005). The metastasis associated protein S100A4: Role in tumour progression and metastasis. *Br. J. Cancer* *92*, 1955–1958.
- Hernández, J.C.R., Sánchez, M.S., Soria, J.M., Gómez Ribelles, J.L., and Pradas, M.M. (2007). Substrate chemistry-dependent conformations of single laminin molecules on polymer surfaces are revealed by the phase signal of atomic force microscopy. *Biophys. J.* *93*, 202–207.
- Herring, G.M. (1972). *The biochemistry and physiology of bone - The Organic Matrix of Bone*. New York & London: Academic Press. 127-189.
- Heuberger, D.M., and Schuepbach, R.A. (2019). Correction to: Protease-activated receptors (PARs): Mechanisms of action and potential therapeutic modulators in PAR-driven inflammatory diseases (*Thrombosis Journal* (2019) *17*: 4 DOI: 10.1186/s12959-019-0194-8). *Thromb. J.* *17*, 1–24.
- Hjortoe, G.M., Petersen, L.C., Albrektsen, T., Sorensen, B.B., Norby, P.L., Mandal, S.K., Pendurthi, U.R., and Rao, L.V.M. (2004). Tissue factor-factor VIIa-specific up-regulation of IL-8 expression in MDA-MB-231 cells is mediated by PAR-2 and results in increased cell migration. *Blood* *103*, 3029–3037.
- Hoarau-Véchet, J., Rafii, A., Touboul, C., and Pasquier, J. (2018). Halfway between 2D and animal models: Are 3D cultures the ideal tool to study cancer-microenvironment interactions? *Int. J. Mol. Sci.* *19*.

- Hochheimer, A., Krohn, M., Rudert, K., Riedel, K., Becker, S., Thirion, C., and Zinke, H. (2014). Endogenous gustatory responses and gene expression profile of stably proliferating human taste cells isolated from fungiform papillae. *Chem Senses* *39*, 359–377.
- Holliday, D.L., and Speirs, V. (2011). Choosing correct breast cancer cell line for breast cancer research. *Breast Cancer Res.* *13*, 1–7.
- Hongisto, V., Jernström, S., Fey, V., Mpindi, J.-P., Kleivi Sahlberg, K., Kallioniemi, O., and Perälä, M. (2013). High-throughput 3D screening reveals differences in drug sensitivities between culture models of JIMT1 breast cancer cells. *PLoS One* *8*, e77232.
- Hou, B., Zhang, D., Zhao, S., Wei, M., Yang, Z., Wang, S., Wang, J., Zhang, X., Liu, B., Fan, L., et al. (2015). Scalable and Dil-compatible optical clearance of the mammalian brain. *Front Neuroanat* *9*, 19.
- Howlader, N., Noone, A.M., Krapcho, M., Miller, D., Brest, A., Yu, M., Ruhl, J., Tatalovich, Z., Mariotto, A., Lewis, D.R., Chen, H.S., Feuer, E.J., Cronin, K., et al. (2020). SEER Cancer Statistics Review 1975-2017. *Natl. Cancer Inst.* 1975–2006.
- Hsiao, A.Y., Tung, Y.-C., Kuo, C.-H., Mosadegh, B., Bedenis, R., Pienta, K.J., and Takayama, S. (2012). Micro-ring structures stabilize microdroplets to enable long term spheroid culture in 384 hanging drop array plates. *Biomed. Microdevices* *14*, 313–323.
- Huang, H. (2018). Matrix metalloproteinase-9 (MMP-9) as a cancer biomarker and MMP-9 biosensors: Recent advances. *Sensors (Switzerland)* *18*, 5–7.
- Huang, W., Yang, S., Shao, J., and Li, Y.P. (2007). Signaling and transcriptional regulation in osteoblast commitment and differentiation. *Front. Biosci.* *12*, 3068–3092.
- Huang, Z., Yu, P., and Tang, J. (2020). Characterization of triple-negative breast cancer MDA-MB-231 cell spheroid model. *Onco. Targets. Ther.* *13*, 5395–5405.
- Huber, M.A., Kraut, N., and Beug, H. (2005). Molecular requirements for epithelial-mesenchymal transition during tumor progression. *Curr. Opin. Cell Biol.* *17*, 548–558.
- Hübner, J., Raschke, M., Rüttschle, I., Gräßle, S., Hasenberg, T., Schirrmann, K., Lorenz, A., Schnurre, S., Lauster, R., Maschmeyer, I., et al. (2018). Simultaneous evaluation of anti-EGFR-induced tumour and adverse skin effects in a microfluidic human 3D co-culture model. *Sci. Rep.* *8*, 15010.
- Huh, D., Hamilton, G.A., and Ingber, D.E. (2011). From 3D cell culture to organs-on-chips. *Trends Cell Biol.* *21*, 745–754.
- Imamura, Y., Mukohara, T., Shimono, Y., Funakoshi, Y., Chayahara, N., Toyoda, M., Kiyota, N., Takao, S., Kono, S., Nakatsura, T., et al. (2015). Comparison of 2D- and 3D-culture models as drug-testing platforms in breast cancer. *Oncol Rep* *33*, 1837–1843.

Ivanov, D.P., Parker, T.L., Walker, D.A., Alexander, C., Ashford, M.B., Gellert, P.R., and Garnett, M.C. (2014). Multiplexing spheroid volume, resazurin and acid phosphatase viability assays for high-throughput screening of tumour spheroids and stem cell neurospheres. *PLoS One* 9, e103817.

Ivascu, A., and Kubbies, M. (2006). Rapid Generation of Single-Tumor Spheroids for High-Throughput Cell Function and Toxicity Analysis. *J. Biomol. Screen.* 11, 922–932.
Jaipan, P., Nguyen, A., and Narayan, R.J. (2017). Gelatin-based hydrogels for biomedical applications. *MRS Commun.* 7, 416–426.

Jensen, C., and Teng, Y. (2020). Is It Time to Start Transitioning From 2D to 3D Cell Culture? *Front. Mol. Biosci.* 7, 1–15.

Jinka, R., Kapoor, R., Sistla, P.G., Raj, T.A., and Pande, G. (2012). Alterations in cell-extracellular matrix interactions during progression of cancers. *Int. J. Cell Biol.* 2012.

Jonkman, J., Brown, C.M., and Cole, R.W. (2014). Quantitative confocal microscopy. Beyond a pretty picture. *Methods in Cell Biology*, 123, 113-134.

Kabadi, P.K., Vantangoli, M.M., Rodd, A.L., Leary, E., Madnick, S.J., Morgan, J.R., Kane, A., and Boekelheide, K. (2015). Into the depths: Techniques for in vitro three-dimensional microtissue visualization. *Biotechniques* 59, 279–286.

Kabeya, Y., Mizushima, N., Ueno, T., Yamamoto, A., Kirisako, T., Noda, T., Kominami, E., Ohsumi, Y., and Yoshimori, T. (2000). LC3, a mammalian homologue of yeast Apg8p, is localized in autophagosome membranes after processing. *EMBO J.* 19, 5720–5728.

Kakonen, S.M., and Mundy, G.R. (2003). Mechanisms of osteolytic bone metastases in breast carcinoma. *Cancer* 97, 834–839.

Kalluri, R., and Weinberg, R.A. (2009). The basics of epithelial-mesenchymal transition. *J. Clin. Invest* 119, 1420–1428.

Kang, Y., Siegel, P.M., Shu, W., Drobnjak, M., Kakonen, S.M., Cordon-Cardo, C., Guise, T.A., and Massagué, J. (2003). A multigenic program mediating breast cancer metastasis to bone. *Cancer Cell* 3, 537–549.

Kapałczyńska, M., Kolenda, T., Przybyła, W., Zajkaczkowska, M., Teresiak, A., Filas, V., Ibbs, M., Bliźniak, R., Łuczewski, Ł., and Lamperska, K. (2018). 2D and 3D cell cultures - a comparison of different types of cancer cell cultures. *Arch. Med. Sci.* 14, 910–919.

Karadag, A., Ogbureke, K.U.E., Fedarko, N.S., and Fisher, L.W. (2004). Bone sialoprotein, matrix metalloproteinase 2, and alpha(v)beta3 integrin in osteotropic cancer cell invasion. *J. Natl. Cancer Inst.* 96, 956–965.

Kato, Y., Ozawa, S., Miyamoto, C., Maehata, Y., Suzuki, A., Maeda, T., and Baba, Y. (2013). Acidic extracellular microenvironment and cancer. *Cancer Cell Int.* 13, 1.

- Katt, M.E., Placone, A.L., Wong, A.D., Xu, Z.S., and Searson, P.C. (2016). In Vitro Tumor Models: Advantages, Disadvantages, Variables, and Selecting the Right Platform. *Front. Bioeng. Biotechnol.* *4*, 12.
- Ke, M.T., Fujimoto, S., and Imai, T. (2013). SeeDB: a simple and morphology-preserving optical clearing agent for neuronal circuit reconstruction. *Nat Neurosci* *16*, 1154–1161.
- Ke, M.T., Nakai, Y., Fujimoto, S., Takayama, R., Yoshida, S., Kitajima, T.S., Sato, M., and Imai, T. (2016). Super-Resolution Mapping of Neuronal Circuitry With an Index-Optimized Clearing Agent. *Cell Rep* *14*, 2718–2732.
- Keller, F., Rudolf, R., and Hafner, M. (2019). Towards optimized breast cancer 3D spheroid mono- and co-culture models for pharmacological research and screening. *J. Cell. Biotechnol.* *5*, 89–101.
- Keller, F., Bruch, R., Schneider, R., Meier-Hubberten, J., Hafner, M., and Rudolf, R. (2020). A Scaffold-Free 3-D Co-Culture Mimics the Major Features of the Reverse Warburg Effect In Vitro. *Cells* *9*, 1900.
- Keller, F., Bruch, R., Clauder, F., Hafner, M., and Rudolf, R. (2021). Extracellular Matrix Components Regulate Bone Sialoprotein Expression in MDA-MB-231 Breast Cancer Cells. *Cells* *10*.
- Kelm, J.M., Timmins, N.E., Brown, C.J., Fussenegger, M., and Nielsen, L.K. (2003). Method for generation of homogeneous multicellular tumor spheroids applicable to a wide variety of cell types. *Biotechnol. Bioeng.* *83*, 173–180.
- Kendall, R.T., and Feghali-Bostwick, C.A. (2014). Fibroblasts in fibrosis: Novel roles and mediators. *Front. Pharmacol.* *5*, 123.
- Kenny, P.A., Lee, G.Y., Myers, C.A., Neve, R.M., Semeiks, J.R., Spellman, P.T., Lorenz, K., Lee, E.H., Barcellos-Hoff, M.H., Petersen, O.W., et al. (2007). The morphologies of breast cancer cell lines in three-dimensional assays correlate with their profiles of gene expression. *Mol. Oncol.* *1*, 84–96.
- Kessenbrock, K., Plaks, V., and Werb, Z. (2010). Matrix Metalloproteinases: Regulators of the tumor. *Cell* *141*, 52–67.
- Khodabukus, A., Prabhu, N., Wang, J., and Bursac, N. (2018). In Vitro Tissue-Engineered Skeletal Muscle Models for Studying Muscle Physiology and Disease. *Adv Heal. Mater* *7*, e1701498.
- Khoshnoodi, J., Pedchenko, V., and Hudson, B. (2008). Mammalian Collagen IV. *Microsc Res Tech.* *71*, 357–370.
- Kibbey, M.C. (1994b). Maintenance of the EHS sarcoma and Matrigel preparation. *J Tiss Cult Methods* *16*, 227–230.
- Kim, B.J. (2005). Three-dimensional tissue culture models in cancer biology. *Semin. Cancer Biol.* *15*, 365–377.

- Kim, J.B., Stein, R., and O'Hare, M.J. (2004). Three-dimensional in vitro tissue culture models of breast cancer-- a review. *Breast Cancer Res. Treat.* *85*, 281–291.
- Kim, S.W., Kim, S.J., Langley, R.R., and Fidler, I.J. (2015). Modulation of the cancer cell transcriptome by culture media formulations and cell density. *Int. J. Oncol.* *46*, 2067–2075.
- Kingsley, L.A., Fournier, P.G.J., Chirgwin, J.M., and Guise, T.A. (2007). Molecular biology of bone metastasis. *Mol. Cancer Ther.* *6*, 2609–2617.
- Kirkham, G.R., and Cartmell, S.H. (2007). Genes and Proteins Involved in the Regulation of Osteogenesis. *Top. Tissue Eng.* *3*, 67–84.
- Kleinman, H.K., McGarvey, M.L., Liotta, L.A., Robey, P.G., Tryggvason, K., and Martin, G.R. (1982). Isolation and characterization of type IV procollagen, laminin, and heparan sulfate proteoglycan from the EHS sarcoma. *Biochemistry* *21*, 6188–6193.
- Kleinman, H.K., Philp, D., and Hoffman, M.P. (2003). Role of the extracellular matrix in morphogenesis. *Curr. Opin. Biotechnol.* *14*, 526–532.
- Klicks, J., Masslo, C., Kluth, A., Rudolf, R., and Hafner, M. (2019). A novel spheroid-based co-culture model mimics loss of keratinocyte differentiation, melanoma cell invasion, and drug-induced selection of ABCB5-expressing cells. *BMC Cancer* *19*, 402.
- Klionsky, D.J., Abdelmohsen, K., Abe, A., Abedin, M.J., Abeliovich, H., Zorzano, A., and Zughaier, S.M. (2016). Guidelines for the use and interpretation of assays for monitoring autophagy (3rd edition). *Autophagy* *12*, 1–222.
- Koch, T.M., Münster, S., Bonakdar, N., Butler, J.P., and Fabry, B. (2012). 3D Traction Forces in Cancer Cell Invasion. *PLoS One* *7*, e33476.
- Köhrmann, A., Kammerer, U., Kapp, M., Dietl, J., and Anacker, J. (2009). Expression of matrix metalloproteinases (MMPs) in primary human breast cancer and breast cancer cell lines: New findings and review of the literature. *BMC Cancer* *9*, 188.
- Kokkinos, M.I., Wafai, R., Wong, M.K., Newgreen, D.F., Thompson, E.W., and Waltham, M. (2007). Vimentin and epithelial-mesenchymal transition in human breast cancer - Observations in vitro and in vivo. *Cells Tissues Organs* *185*, 191–203.
- Kovacheva, M., Zepp, M., Berger, S.M., and Berger, M.R. (2014). Sustained conditional knockdown reveals intracellular bone sialoprotein as essential for breast cancer skeletal metastasis. *Oncotarget* *5*, 5510–5522.
- Kowalski, P.J., Rubin, M.A., and Kleer, C.G. (2003). E-cadherin expression in primary carcinomas of the breast and its distant metastases. *Breast Cancer Res.* *5*, 217–222.
- Kuwajima, T., Sitko, A.A., Bhansali, P., Jurgens, C., Guido, W., and Mason, C. (2013). ClearT: a detergent- and solvent-free clearing method for neuronal and non-neuronal tissue. *Development* *140*, 1364–1368.

LaBonia, G.J., Lockwood, S.Y., Heller, A.A., Spence, D.M., and Hummon, A.B. (2016). Drug penetration and metabolism in 3D cell cultures treated in a 3D printed fluidic device: Assessment of irinotecan via MALDI imaging mass spectrometry. *Proteomics* 16, 1814–1821.

Laemmli, U.K. (1970). Cleavage of structural proteins during the assembly of the head of bacteriophage T4. *Nature* 227, 680–685.

Lancaster, M.A., Renner, M., Martin, C.A., Wenzel, D., Bicknell, L.S., Hurler, M.E., Homfray, T., Penninger, J.M., Jackson, A.P., and Knoblich, J.A. (2013). Cerebral organoids model human brain development and microcephaly. *Nature* 501, 373–379.

Langhans, S.A. (2018). Three-Dimensional in Vitro Cell Culture Models in Drug Discovery and Drug Repositioning. *Front Pharmacol* 9, 6.

Langley, R.R., and Fidler, I.J. (2011). The seed and soil hypothesis revisited-The role of tumor-stroma interactions in metastasis to different organs. *Int. J. Cancer* 128, 2527–2535.

Laugisch, O., Cosgarea, R., Nikou, G., Nikolidakis, D., Donos, N., Salvi, G.E., Stavropoulos, A., Jepsen, S., and Sculean, A. (2019). Histologic evidence of periodontal regeneration in furcation defects: a systematic review. *Clin Oral Investig* 23, 2861–2906.

Lee, C.T., Bendriem, R.M., Wu, W.W., and Shen, R.F. (2017). 3D brain Organoids derived from pluripotent stem cells: promising experimental models for brain development and neurodegenerative disorders. *J Biomed Sci* 24, 59.

Lee, J.M., Dedhar, S., Kalluri, R., and Thompson, E.W. (2006). The epithelial-mesenchymal transition: New insights in signaling, development, and disease. *J. Cell Biol.* 172, 973–981.

Lee, K.S., Hong, S.H., and Bae, S.C. (2002). Both the Smad and p38 MAPK pathways play a crucial role in Runx2 expression following induction by transforming growth factor-beta and bone morphogenetic protein. *Oncogene* 21, 7156–7163.

Lee, K.S., Kim, H.J., Li, Q.L., Chi, X.Z., Ueta, C., Komori, T., Wozney, J.M., Kim, E.G., Choi, J.Y., Ryoo, H.M., et al. (2000). Runx2 is a common target of transforming growth factor beta1 and bone morphogenetic protein 2, and cooperation between Runx2 and Smad5 induces osteoblast-specific gene expression in the pluripotent mesenchymal precursor cell line C2C12. *Mol. Cell. Biol.* 20, 8783–8792.

Leeb, S.N., Vogl, D., Falk, W., Schölmerich, J., Rogler, G., and Gelbmann, C.M. (2002). Regulation of migration of human colonic myofibroblasts. *Growth Factors* 20, 81–91.

Leitinger, B., and Hohenester, E. (2007). Mammalian collagen receptors. *Matrix Biol.* 26, 146–155.

- Leong, A.S. (2004). Pitfalls in diagnostic immunohistology. *Adv Anat Pathol* 11, 86–93.
- Li, Y., and Kumacheva, E. (2018). Hydrogel microenvironments for cancer spheroid growth and drug screening. *Sci. Adv.* 4, 1–11.
- Li, J., Bao, Q., Chen, S., Liu, H., Feng, J., Qin, H., Li, A., Liu, D., Shen, Y., Zhao, Y., et al. (2017a). Different bone remodeling levels of trabecular and cortical bone in response to changes in Wnt/ β -catenin signaling in mice. *J. Orthop. Res.* 35, 812–819.
- Li, J., Wu, C., Chu, P.K., and Gelinsky, M. (2020). 3D printing of hydrogels: Rational design strategies and emerging biomedical applications. *Mater. Sci. Eng. R Reports* 140, 100543.
- Li, Q., Chen, C., Kapadia, A., Zhou, Q., Harper, M.K., Schaack, J., and LaBarbera, V.D. (2011). 3D models of epithelial-mesenchymal transition in breast cancer metastasis: high-throughput screening assay development, validation, and pilot screen. *J. Biomol. Screen.* 16, 141–154.
- Li, W., Germain, R.N., and Gerner, M.Y. (2017b). Multiplex, quantitative cellular analysis in large tissue volumes with clearing-enhanced 3D microscopy (Ce3D). *Proc Natl Acad Sci U S A* 114, E7321–e7330.
- Liberti, M. V., and Locasale, J.W. (2016). The Warburg Effect: How Does it Benefit Cancer Cells? *Trends Biochem. Sci.* 41, 211–218.
- Lih, E., Oh, S.H., Joung, Y.K., Lee, J.H., and Han, D.K. (2015). Polymers for cell/tissue anti-adhesion. *Prog. Polym. Sci.* 44, 28–61.
- Lin, R.Z., and Chang, H.-Y. (2008). Recent advances in three-dimensional multicellular spheroid culture for biomedical research. *Biotechnol. J.* 3, 1172–1184.
- Lin, X., Patil, S., Gao, Y.G., and Qian, A. (2020). The Bone Extracellular Matrix in Bone Formation and Regeneration. *Front. Pharmacol.* 11, 1–15.
- Liu, F., Bloch, N., Bhushan, K.R., De Grand, A.M., Tanaka, E., Solazzo, S., Mertyna, P.M., Goldberg, N., Frangioni, V.J., and Lenkinski, R.E. Humoral bone morphogenetic protein 2 is sufficient for inducing breast cancer microcalcification. *Mol. Imaging* 7, 175–186.
- Liu, X., Weaver, E.M., and Hummon, A.B. (2013). Evaluation of therapeutics in three-dimensional cell culture systems by MALDI imaging mass spectrometry. *Anal. Chem.* 85, 6295–6302.
- Liu, Y.L., Chou, C.K., Kim, M., Vasisht, R., Kuo, Y.A., Ang, P., Liu, C., Perillo, E.P., Chen, Y.A., Blocher, K., et al. (2019). Assessing metastatic potential of breast cancer cells based on EGFR dynamics. *Sci. Rep.* 9, 3395.
- Løberg, M., Kalager, M., Holme, Ø., Hoff, G., Adami, H.-O., and Bretthauer, M. (2014). Long-term colorectal-cancer mortality after adenoma removal. *N. Engl. J. Med.* 371, 799–807.

Loibl, S., Königs, A., Kaufmann, M., Costa, S.D., and Bischoff, J. (2006). PTHrP and Bone Sialoprotein as Prognostic Markers for Developing Bone Metastases in Breast Cancer Patients. *Zentralbl. Gynakol.* 128, 330–335.

Longati, P., Jia, X., Eimer, J., Wagman, A., Witt, M.-R., Rehnmark, S., Verbeke, C., Toftgård, R., Löhr, M., and Heuchel, R.L. (2013). 3D pancreatic carcinoma spheroids induce a matrix-rich, chemoresistant phenotype offering a better model for drug testing. *BMC Cancer* 13, 95.

Lu, P., Takai, K., Weaver, V.M., and Werb, Z. (2011). Extracellular Matrix degradation and remodeling in development and disease. *Cold Spring Harb. Perspect. Biol.* 3, 1–24.

Lu, P., Weaver, V.M., and Werb, Z. (2012). The extracellular matrix: A dynamic niche in cancer progression. *J. Cell Biol.* 196, 395–406.

Luca, A.C., Mersch, S., Deenen, R., Schmidt, S., Messner, I., Schafer, K.L., Baldus, S.E., Huckenbeck, W., Piekorz, R.P., Knoefel, W.T., et al. (2013). Impact of the 3D microenvironment on phenotype, gene expression, and EGFR inhibition of colorectal cancer cell lines. *PLoS One* 8, e59689.

Lunt, S.Y., and Vander Heiden, M.G. (2011). Aerobic glycolysis: Meeting the metabolic requirements of cell proliferation. *Annu. Rev. Cell Dev. Biol.* 27, 441–464.

Mabry, K.M., Payne, S.Z., and Anseth, K.S. (2016). Microarray analyses to quantify advantages of 2D and 3D hydrogel culture systems in maintaining the native valvular interstitial cell phenotype. *Biomaterials* 74, 31–41.

Macedo, F., Ladeira, K., Pinho, F., Saraiva, N., Bonito, N., Pinto, L., and Gonçalves, F. (2017). Bone metastases: an overview. *Oncol. Rev.* 11, 321.

Maehama, T., and Dixon, J.E. (1998). The tumor suppressor, PTEN/MMAC1, dephosphorylates the lipid second messenger, phosphatidylinositol 3,4,5-trisphosphate. *J. Biol. Chem.* 273, 13375–13378.

Maier, H.J., Wirth, T., and Beug, H. (2010). Epithelial-Mesenchymal transition in Pancreatic Carcinoma. *Cancers (Basel)*. 2, 2058–2083.

Manicone, A.M., and McGuire, J.K. (2008). Matrix Metalloproteinases as Modulators of Inflammation. *Semin Cell Dev Biol.* 19, 34–41.

Marchevsky, A.M., and Wick, M.R. (2015). Diagnostic difficulties with the diagnosis of small cell carcinoma of the lung. *Semin Diagn Pathol* 32, 480–488.

Martinez-Outschoorn, U.E., Pavlides, S., Whitaker-Menezes, D., Daumer, K.M., Milliman, J.N., Chiavarina, B., Migneco, G., Witkiewicz, A.K., Martinez-Cantarín, M.P., Flomenberg, N., et al. (2010). Tumor cells induce the cancer associated fibroblast phenotype via caveolin-1 degradation: Implications for breast cancer and DCIS therapy with autophagy inhibitors. *Cell Cycle* 9, 2423–2433.

- Martinez-Outschoorn, U.E., Pavlides, S., Howell, A., Pestell, R.G., Tanowitz, H.B., Sotgia, F., and Lisanti, M.P. (2011). Stromal-epithelial metabolic coupling in cancer: Integrating autophagy and metabolism in the tumor microenvironment. *Int. J. Biochem. Cell Biol.* *43*, 1045–1051.
- Martinez-Outschoorn, U.E., Lisanti, M.P., and Sotgia, F. (2014). Catabolic cancer-associated fibroblasts transfer energy and biomass to anabolic cancer cells, fueling tumor growth. *Semin. Cancer Biol.* *25*, 47–60.
- Mason, B.N., Starchenko, A., Williams, R.M., Bonassar, L.J., and Reinhart-King, C.A. (2013). Tuning three-dimensional collagen matrix stiffness independently of collagen concentration modulates endothelial cell behavior. *Acta Biomater.* *9*, 4635–4644.
- Masson, A., Escande, P., Frongia, C., Clouvel, G., Ducommun, B., and Lorenzo, C. (2015). High-resolution in-depth imaging of optically cleared thick samples using an adaptive SPIM. *Sci Rep* *5*, 16898.
- Maycotte, P., and Thorburn, A. (2011). Autophagy and cancer therapy. *Cancer Biol. Ther.* *11*, 127–137.
- McBeath, R., Pirone, D.M., Nelson, C.M., Bhadriraju, K., and Chen, C.S. (2004). Cell Shape, Cytoskeletal Tension, and RhoA Regulate Stem Cell Lineage Commitment. *Dev. Cell* *6*, 483–495.
- McCrea, P.D., and Gu, D. (2010). The catenin family at a glance. *J. Cell Sci.* *123*, 637–642.
- Meng, X.M., Chung, A.C.K., and Lan, H.Y. (2013). Role of the TGF- β /BMP-7/Smad pathways in renal diseases. *Clin. Sci.* *124*, 243–254.
- Merdad, A., Karim, S., Schulten, H.-J., Dallol, A., Buhmeida, A., Al-Thubaity, F., Gari, M.A., Chaudhary, A.G., Abuzenadah, A.M., and Al-Qahtani, M.H. (2014). Expression of matrix metalloproteinases (MMPs) in primary human breast cancer: MMP-9 as a potential biomarker for cancer invasion and metastasis. *Anticancer Res.* *34*, 1355–1366.
- Mertz, J. (2011). Optical sectioning microscopy with planar or structured illumination. *Nat Methods* *8*, 811–819.
- Midha, S., Murab, S., and Ghosh, S. (2016). Osteogenic signaling on silk-based matrices. *Biomaterials* *97*, 133–153.
- Mishra, A., Shiozawa, Y., Pienta, K.J., and Taichman, R.S. (2011). Homing of cancer cells to the bone. *Cancer Microenviron.* *4*, 221–235.
- Mizuno, M., Imai, T., Fujisawa, R., Tani, H., and Kuboki, Y. (2000). Bone sialoprotein (BSP) is a crucial factor for the expression of osteoblastic phenotypes of bone marrow cells cultured on type I collagen matrix. *Calcif. Tissue Int.* *66*, 388–396.

- Morris, B.A., Burkel, B., Ponik, S.M., Fan, J., Condeelis, J.S., Aguire-Ghiso, J.A., Castracane, J., Denu, J.M., and Keely, P.J. (2016). Collagen Matrix Density Drives the Metabolic Shift in Breast Cancer Cells. *EBioMedicine* 13, 146–156.
- Morrison, D.K. (2012). MAP kinase pathways. *Cold Spring Harb. Perspect. Biol.* 4, 1–6.
- Mueller, M.M., and Fusenig, N.E. (2004). Friends or foes - bipolar effects of the tumour stroma in cancer. *Nat. Rev. Cancer* 4, 839–849.
- Mulder, L., Koolstra, J.H., Den Toonder, J.M.J., and Van Eijden, T.M.G.J. (2008). Relationship between tissue stiffness and degree of mineralization of developing trabecular bone. *J. Biomed. Mater. Res. - Part A* 84, 508–515.
- Mundy, G.R. (2002). Metastasis to bone: causes, consequences and therapeutic opportunities. *Nat. Rev. Cancer* 2, 584–593.
- Murray, E., Cho, J.H., Goodwin, D., Ku, T., Swaney, J., Kim, S.Y., Choi, H., Park, Y.G., Park, J.Y., Hubbert, A., et al. (2015). Simple, Scalable Proteomic Imaging for High-Dimensional Profiling of Intact Systems. *Cell* 163, 1500–1514.
- Myllyharju, J., and Kivirikko, K.I. (2004). Collagens, modifying enzymes and their mutations in humans, flies and worms. *Trends Genet.* 20, 33–43.
- Nagase, H., Visse, R., and Murphy, G. (2006). Structure and function of matrix metalloproteinases and TIMPs. *Cardiovasc. Res.* 69, 562–573.
- Nakayama, Y., Nakajima, Y., Kato, N., Takai, H., Kim, D.-S., Arai, M., Mezawa, M., Araki, S., Sodek, J., and Ogata, Y. (2006). Insulin-like growth factor-I increases bone sialoprotein (BSP) expression through fibroblast growth factor-2 response element and homeodomain protein-binding site in the proximal promoter of the BSP gene. *J. Cell. Physiol.* 208, 326–335.
- Nam, J.S., Suchar, A.M., Kang, M.J., Stuelten, C.H., Tang, B., Michalowska, A.M., Fisher, L.W., Fedarko, N.S., Jain, A., Pinkas, J., et al. (2006). Bone Sialoprotein Mediates the Tumor Cell-Targeted Prometastatic Activity of Transforming Growth Factor β in a Mouse Model of Breast Cancer. *Cancer Res.* 66, 6327–6335.
- Nath, S., and Devi, G.R. (2016). Three-dimensional culture systems in cancer research: Focus on tumor spheroid model. *Pharmacol Ther* 163, 94–108.
- Nies, C., Rubner, T., Lorig, H., Colditz, V., Seelmann, H., Müller, A., and Gottwald, E. (2019). A Microcavity Array-Based 4D Cell Culture Platform. *Bioengineering* 6, 50.
- Nishishita, R., Morohashi, S., Seino, H., Wu, Y., Yoshizawa, T., Haga, T., Saito, K., Hakamada, K., Fukuda, S., and Kijima, H. (2018). Expression of cancer-associated fibroblast markers in advanced colorectal cancer. *Oncol. Lett.* 15, 6195–6202.
- Noreen, A., Rehman, A., Aftab, S., and Shakoori, A. (2019). Antiproliferative effect of oxidative stress induced by tellurite in breast carcinoma cells. *J Cancer Res Pr.* 68–75.

- Nunes, A.S., Barros, A.S., Costa, E.C., Moreira, A.F., and Correia, I.J. (2019). 3D tumor spheroids as in vitro models to mimic in vivo human solid tumors resistance to therapeutic drugs. *Biotechnol. Bioeng.* *116*, 206–226.
- Nürnberg, E., Vitacolonna, M., Klicks, J., von Molitor, E., Cesetti, T., Keller, F., Bruch, R., Ertongur-Fauth, T., Riedel, K., Scholz, P., et al. (2020). Routine Optical Clearing of 3D-Cell Cultures: Simplicity Forward. *Front Mol Biosci* *7*, 20.
- Obenauf, A.C., and Massagué, J. (2015). Surviving at a Distance: Organ-Specific Metastasis. *Trends in Cancer* *1*, 76–91.
- Ochiai, H., Okada, S., Saito, A., Hoshi, K., Yamashita, H., Takato, T., and Azuma, T. (2012). Inhibition of insulin-like growth factor-1 (IGF-1) expression by prolonged transforming growth factor- β 1 (TGF- β 1) administration suppresses osteoblast differentiation. *J. Biol. Chem.* *287*, 22654–22661.
- Ogata, Y. (2008). Bone sialoprotein and its transcriptional regulatory mechanism. *J. Periodontal Res.* *43*, 127–135.
- Ogata, Y., Niisato, N., Furuyama, S., Cheifetz, S., Kim, R.H., Sugiyama, H., and Sodek, J. (1997). Transforming growth factor-beta 1 regulation of bone sialoprotein gene transcription: identification of a TGF-beta activation element in the rat BSP gene promoter. *J. Cell. Biochem.* *65*, 501–512.
- Ogbureke, K.U.E., and Fisher, L.W. (2004). Expression of SIBLINGs and Their Partner MMPs in Salivary Glands. *J. Dent. Res.* *83*, 664–670.
- Ogbureke, K.U.E., and Fisher, L.W. (2005). Renal expression of SIBLING proteins and their partner matrix metalloproteinases (MMPs). *Kidney Int.* *68*, 155–166.
- Ogbureke, K.U.E., Nikitakis, N.G., Warburton, G., Ord, R.A., Sauk, J.J., Waller, J.L., and Fisher, L.W. (2007). Up-regulation of SIBLING proteins and correlation with cognate MMP expression in oral cancer. *Oral Oncol.* *43*, 920–932.
- Oguma, T., Asano, K., Tomomatsu, K., Kodama, M., Fukunaga, K., Shiomi, T., Ohmori, N., Ueda, S., Takihara, T., Shiraishi, Y., et al. (2011). Induction of Mucin and MUC5AC Expression by the Protease Activity of *Aspergillus fumigatus* in Airway Epithelial Cells. *J. Immunol.* *187*, 999–1005.
- Öhlund, D., Lundin, C., Ardnor, B., Öman, M., Naredi, P., and Sund, M. (2009). Type IV collagen is a tumour stroma-derived biomarker for pancreas cancer. *Br. J. Cancer* *101*, 91–97.
- Oldberg, A., Franzén, A., Heinegård, D., Franzen, A., and Heinegard, D. (1988). The primary structure of a cell-binding bone sialoprotein. *J. Biol. Chem.* *263*, 19430–19432.
- Ortega, N., and Werb, Z. (2002). New functional roles for non-collagenous domains of basement membrane collagens. *J. Cell Sci.* *115*, 4201–4214.
- Otto, A.M. (2016). Warburg effect(s)-a biographical sketch of Otto Warburg and his impacts on tumor metabolism. *Cancer Metab.* *4*, 5.

- Ouahoud, S., Voorneveld, P.W., van der Burg, L.R.A., de Jonge-Muller, E.S.M., Schoonderwoerd, M.J.A., Paauwe, M., de Vos, T., de Wit, S., van Pelt, G.W., Mesker, W.E., et al. (2020). Bidirectional tumor/stroma crosstalk promotes metastasis in mesenchymal colorectal cancer. *Oncogene* *39*, 2453–2466.
- Owen, R., and Reilly, G.C. (2018). In vitro models of bone remodelling and associated disorders. *Front. Bioeng. Biotechnol.* *6*, 1–22.
- Oxley, H.R., Corkhill, P.H., Fitton, J.H., and Tighe, B.J. (1993). Macroporous hydrogels for biomedical applications: methodology and morphology. *Biomaterials* *14*, 1064–1072.
- Ozhogina, O.A., Trexler, M., Bányai, L., Llinás, M., and Patthy, L. (2001). Origin of fibronectin type II (FN2) modules: Structural analyses of distantly-related members of the kringle family identify the kringle domain of neurotrypsin as a potential link between FN2 domains and kringles. *Protein Sci.* *10*, 2114–2122.
- Paguirigan, A., and Beebe, D.J. (2006). Gelatin based microfluidic devices for cell culture. *Lab Chip* *6*, 407–413.
- Pampaloni, F., Reynaud, E.G., and Stelzer, E.H.K. (2007). The third dimension bridges the gap between cell culture and live tissue. *Nat. Rev. Mol. Cell Biol.* *8*, 839–845.
- Pan, C., Kumar, C., Bohl, S., Klingmueller, U., and Mann, M. (2009). Comparative proteomic phenotyping of cell lines and primary cells to assess preservation of cell type-specific functions. *Mol. Cell. Proteomics* *8*, 443–450.
- Pan, C., Cai, R., Quacquarelli, F.P., Ghasemigharagoz, A., Loubopoulos, A., Matryba, P., Plesnila, N., Dichgans, M., Hellal, F., and Erturk, A. (2016). Shrinkage-mediated imaging of entire organs and organisms using uDISCO. *Nat Methods* *13*, 859–867.
- Pankov, R., and Yamada, K.M. (2002). Fibronectin at a glance. *J. Cell Sci.* *115*, 3861–3863.
- Park, M.K., Yao, Y., Xia, W., Setijono, S.R., Kim, J.H., Vila, I.K., Chiu, H.-H., Wu, Y., Billalabeitia, E.G., Lee, M.G., et al. (2019). PTEN self-regulates through USP11 via the PI3K-FOXO pathway to stabilize tumor suppression. *Nat. Commun.* *10*, 636.
- Park, S.J., Smith, C.P., Wilbur, R.R., Cain, C.P., Kallu, S.R., Valasapalli, S., Sahoo, A., Guda, M.R., Tsung, A.J., and Velpula, K.K. (2018). An overview of MCT1 and MCT4 in GBM: Small molecule transporters with large implications. *Am. J. Cancer Res.* *8*, 1967–1976.
- Parra-torres, A.Y., Valdés-flores, M., Orozco, L., and Velázquez-cruz, R. (2013). Molecular Aspects of Bone Remodeling. *Top. Osteoporos.* 1–28.
- Pastor-Pareja, J.C. (2020). Atypical basement membranes and basement membrane diversity - What is normal anyway? *J. Cell Sci.* *133*.

- Pavlidis, S., Vera, I., Gandara, R., Sneddon, S., Pestell, R.G., Mercier, I., Martinez-Outschoorn, U.E., Whitaker-Menezes, D., Howell, A., Sotgia, F., et al. (2012). Warburg meets autophagy: Cancer-associated fibroblasts accelerate tumor growth and metastasis via oxidative stress, mitophagy, and aerobic glycolysis. *Antioxid. Redox Signal.* *16*, 1264–1284.
- Pereira, J.F., Awatade, N.T., Loureiro, C.A., Matos, P., Amaral, M.D., and Jordan, P. (2016). The third dimension: new developments in cell culture models for colorectal research. *Cell Mol Life Sci* *73*, 3971–3989.
- Pérez-Escuredo, J., Dadhich, R.K., Dhup, S., Cacace, A., Van Hée, V.F., De Saedeleer, C.J., Sboarina, M., Rodriguez, F., Fontenille, M.J., Brisson, L., et al. (2016). Lactate promotes glutamine uptake and metabolism in oxidative cancer cells. *Cell Cycle* *15*, 72–83.
- Pfeiffer, T., Schuster, S., and Bonhoeffer, S. (2001). Cooperation and competition in the evolution of ATP-producing pathways. *Science* *292*, 504–507.
- Philipson, B. (1965). Composition of Cement Lines in Bone. *J. Histochem. Cytochem.* *13*, 270–281.
- Piccard, H., Van den Steen, P.E., and Opdenakker, G. (2007). Hemopexin domains as multifunctional liganding modules in matrix metalloproteinases and other proteins. *J. Leukoc. Biol.* *81*, 870–892.
- Piccinini, F. (2015). AnaSP: a software suite for automatic image analysis of multicellular spheroids. *Comput. Methods Programs Biomed.* *119*, 43–52.
- Piccinini, F., Tesei, A., Arienti, C., and Bevilacqua, A. (2015). Cancer multicellular spheroids: Volume assessment from a single 2D projection. *Comput. Methods Programs Biomed.* *118*, 95–106.
- Picon-Ruiz, M., Pan, C., Drews-Elger, K., Jang, K., Besser, A.H., Zhao, D., Morata-Tarifa, C., Kim, M., Ince, T.A., Azzam, D.J., et al. (2016). Interactions between Adipocytes and Breast Cancer Cells Stimulate Cytokine Production and Drive Src/Sox2/miR-302b-Mediated Malignant Progression. *Cancer Res.* *76*, 491–504.
- Pillé, J.Y., Denoyelle, C., Varet, J., Bertrand, J.R., Soria, J., Opolon, P., Lu, H., Pritchard, L.L., Vannier, J.P., Malvy, C., et al. (2005). Anti-RhoA and anti-RhoC siRNAs inhibit the proliferation and invasiveness of MDA-MB-231 breast cancer cells in vitro and in vivo. *Mol. Ther.* *11*, 267–274.
- Pines, G., Köstler, W.J., and Yarden, Y. (2010). Oncogenic mutant forms of EGFR: Lessons in signal transduction and targets for cancer therapy. *FEBS Lett.* *584*, 2699–2706.
- Polyak, K., Haviv, I., and Campbell, I.G. (2009). Co-evolution of tumor cells and their microenvironment. *Trends Genet.* *25*, 30–38.
- Porporato, P.E., Filigheddu, N., Pedro, J.M.B.-S., Kroemer, G., and Galluzzi, L. (2018). Mitochondrial metabolism and cancer. *Cell Res.* *28*, 265–280.

- Pozo-Guisado, E., Alvarez-Barrientos, A., Mulero-Navarro, S., Santiago-Josefat, B., and Fernandez-Salguero, P.M. (2002). The antiproliferative activity of resveratrol results in apoptosis in MCF-7 but not in MDA-MB-231 human breast cancer cells: Cell-specific alteration of the cell cycle. *Biochem. Pharmacol.* *64*, 1375–1386.
- Prasad, V., and Mailankody, S. (2017). Research and Development Spending to Bring a Single Cancer Drug to Market and Revenues After Approval. *JAMA Intern. Med.* *177*, 1569–1575.
- Prestwich, G.D. (2007). Simplifying the extracellular matrix for 3-D cell culture and tissue engineering: A pragmatic approach. *J. Cell. Biochem.* *101*, 1370–1383.
- Qian, Y., and Huang, H.Z. (2010). The role of RANKL and MMP-9 in the bone resorption caused by ameloblastoma. *J. Oral Pathol. Med.* *39*, 592–598.
- Qiao, M., Shapiro, P., Kumar, R., and Passaniti, A. (2004). Insulin-like growth factor-1 regulates endogenous RUNX2 activity in endothelial cells through a phosphatidylinositol 3-kinase/ERK-dependent and Akt-independent signaling pathway. *J. Biol. Chem.* *279*, 42709–42718.
- Qu, Y., Han, B., Yu, Y., Yao, W., Bose, S., Karlan, B.Y., Giuliano, A.E., and Cui, X. (2015). Evaluation of MCF10A as a reliable model for normal human mammary epithelial cells. *PLoS One* *10*, 1–16.
- Radisky, D.C. (2005). Epithelial-mesenchymal transition. *J. Cell Sci.* *118*, 4325–4326.
- Raggatt, L.J., and Partridge, N.C. (2010). Cellular and Molecular Mechanisms of Bone Remodeling. *J. Biol. Chem.* *285*, 25103–25108.
- Raghavan, S., Mehta, P., Horst, E.N., Ward, M.R., Rowley, K.R., and Mehta, G. (2016). Comparative analysis of tumor spheroid generation techniques for differential in vitro drug toxicity. *Oncotarget* *7*, 16948–16961.
- Rastegar, F., Shenaq, D., Huang, J., Zhang, W., Zhang, B., He, B., Chen, L., Zuo, G., Luo, Q., Shi, Q., et al. (2010). Mesenchymal stem cells: Characteristics and clinical applications. *World J Stem Cells* *2*, 67–80.
- Raymaekers, K., Stegen, S., van Gestel, N., and Carmeliet, G. (2015). The vasculature: a vessel for bone metastasis. *Bonekey Rep.* *4*, 742.
- Raynal, C., Delmas, P.D., and Chenu, C. (1996). Bone sialoprotein stimulates in vitro bone resorption. *Endocrinology* *137*, 2347–2354.
- Renier, N., Wu, Z., Simon, D.J., Yang, J., Ariel, P., and Tessier-Lavigne, M. (2014). iDISCO: a simple, rapid method to immunolabel large tissue samples for volume imaging. *Cell* *159*, 896–910.
- Renner, M., Lancaster, M.A., Bian, S., Choi, H., Ku, T., Peer, A., Chung, K., and Knoblich, J.A. (2017). Self-organized developmental patterning and differentiation in cerebral organoids. *EMBO J.* *36*, 1316–1329.

Reznikov, N., Chase, H., Brumfeld, V., Shahar, R., and Weiner, S. (2015). The 3D structure of the collagen fibril network in human trabecular bone: Relation to trabecular organization. *Bone* 71, 189–195.

Ricard-Blum, S. (2011). The Collagen Family. *Cold Spring Harb. Perspect. Biol.* 3, 1–19.

Richardson, D.S., and Lichtman, J.W. (2015). Clarifying Tissue Clearing. *Cell* 162, 246–257.

Riedl, A., Schleder, M., Pudielko, K., Stadler, M., Walter, S., Unterleuthner, D., Unger, C., Kramer, N., Hengstschläger, M., Kenner, L., et al. (2017). Comparison of cancer cells in 2D vs 3D culture reveals differences in AKT-mTOR-S6K signaling and drug responses. *J. Cell Sci.* 130, 203–218.

Roberts, D.J., and Miyamoto, S. (2015). Hexokinase II integrates energy metabolism and cellular protection: Akt on mitochondria and TORCing to autophagy. *Cell Death Differ.* 22, 248–257.

Roeb, E., Schleinkofer, K., Kernebeck, T., Pötsch, S., Jansen, B., Behrmann, I., Matern, S., and Grötzinger, J. (2002). The matrix metalloproteinase 9 (MMP-9) hemopexin domain is a novel gelatin binding domain and acts as an antagonist. *J. Biol. Chem.* 277, 50326–50332.

Roeder, A.H.K., Cunha, A., Burl, M.C., and Meyerowitz, E.M. (2012). A computational image analysis glossary for biologists. *Dev.* 139, 3071–3080.

Roelofs, A.J., and De Bari, C. (2019). Immunostaining of Skeletal Tissues. *Methods Mol Biol* 1914, 437–450.

Rohe, I., Huttner, F.J., Plendl, J., Drewes, B., and Zentek, J. (2018). Comparison of different histological protocols for the preservation and quantification of the intestinal mucus layer in pigs. *Eur J Histochem* 62, 2874.

Rosenbluth, J.M., Schackmann, R.C.J., Gray, G.K., Selfors, L.M., Li, C.M.C., Boedicker, M., Kuiken, H.J., Richardson, A., Brock, J., Garber, J., et al. (2020). Organoid cultures from normal and cancer-prone human breast tissues preserve complex epithelial lineages. *Nat. Commun.* 11.

Rozengurt, E. (1992). Growth factors and cell proliferation. *Curr. Opin. Cell Biol.* 4, 161–165.

Rustamov, V., Rudolf, R., Yagublu, V., Kuhn, H.-M., Vitacolonna, M., and Hafner, M. (2017). Long-term 3D culture of the SCC4 cell line using three different culture methods and initial seeding densities. *J. Cell. Biotechnol.* 3, 41–50.

Rustamov, V., Keller, F., Klicks, J., Hafner, M., and Rudolf, R. (2019). Bone Sialoprotein Shows Enhanced Expression in Early, High-Proliferation Stages of Three-Dimensional Spheroid Cell Cultures of Breast Cancer Cell Line MDA-MB-231. *Front. Oncol.* 9, 36.

Ryu, N.E., Lee, S.H., and Park, H. (2019). Spheroid Culture System Methods and Applications for Mesenchymal Stem Cells. *Cells* 8, 1–13.

Sasaki, N., and Clevers, H. (2018). Studying cellular heterogeneity and drug sensitivity in colorectal cancer using organoid technology. *Curr. Opin. Genet. Dev.* 52, 117–122.

Savci-Heijink, C.D., Halfwerk, H., Hooijer, G.K.J., Horlings, H.M., Wesseling, J., and van de Vijver, M.J. (2015). Retrospective analysis of metastatic behaviour of breast cancer subtypes. *Breast Cancer Res. Treat.* 150, 547–557.

Scadden, D.T. (2006). The stem-cell niche as an entity of actio. *Nature* 441, 1075–1079.

Schaefer, L., and Iozzo, R. V. (2008). Biological functions of the small leucine-rich proteoglycans: From genetics to signal transduction. *J. Biol. Chem.* 283, 21305–21309.

Schaefer, L., and Schaefer, R.M. (2010). Proteoglycans: From structural compounds to signaling molecules. *Cell Tissue Res.* 339, 237–246.

Scholnik-Cabrera, A., Chávez-Blanco, A., Domínguez-Gómez, G., and Dueñas-González, A. (2017). Understanding tumor anabolism and patient catabolism in cancer-associated cachexia. *Am. J. Cancer Res.* 7, 1107–1135.

Schindelin, J., Arganda-Carreras, I., Frise, E., Kaynig, V., Longair, M., Pietzsch, T., Preibisch, S., Rueden, C., Saalfeld, S., Schmid, B., et al. (2012). Fiji: an open-source platform for biological-image analysis. *Nat Methods* 9, 676–682.

Schittek, B., and Sinnberg, T. (2014). Biological functions of casein kinase 1 isoforms and putative roles in tumorigenesis. *Mol. Cancer* 13, 1–14.

Schmitt, J.M., and Kumar, G. (1998). Optical scattering properties of soft tissue: a discrete particle model. *Appl Opt* 37, 2788–2797.

Schmitz, A., Fischer, S.C., Mattheyer, C., Pampaloni, F., and Stelzer, E.H. (2017). Multiscale image analysis reveals structural heterogeneity of the cell microenvironment in homotypic spheroids. *Sci Rep* 7, 43693.

Schneider-Poetsch, T., Ju, J., Eyler, D.E., Dang, Y., Bhat, S., Merrick, W.C., Green, R., Shen, B., and Liu, J. (2010). Inhibition of Eukaryotic Translation Elongation by Cycloheximide and Lactimidomycin. *Nat Chem Biol.* 6, 209–217.

Schuldiner, M., Yanuka, O., Itskovitz-Eldor, J., Melton, D.A., and Benvenisty, N. (2000). Effects of eight growth factors on the differentiation of cells derived from human embryonic stem cells. *Proc. Natl. Acad. Sci. U. S. A.* 97, 11307–11312.

Sebastian, A., Buckle, A.M., and Markx, G.H. (2006). Formation of multilayer aggregates of mammalian cells by dielectrophoresis. *J. Micromechanics Microengineering* 16, 1769–1777.

Selvaggi, G., and Scagliotti, G. V. (2005). Management of bone metastases in cancer: A review. *Crit. Rev. Oncol. Hematol.* *56*, 365–378.

Selvamurugan, N., Kwok, S., and Partridge, N.C. (2004). Smad3 Interacts with JunB and Cbfa1/Runx2 for Transforming Growth Factor- β 1-stimulated Collagenase-3 Expression in Human Breast Cancer Cells. *J. Biol. Chem.* *279*, 27764–27773.

Sensi, F., D'Angelo, E., D'Aronco, S., Molinaro, R., and Agostini, M. (2018). Preclinical three-dimensional colorectal cancer model: The next generation of in vitro drug efficacy evaluation. *J. Cell. Physiol.* *234*, 181–191.

Senthebane, D.A., Jonker, T., Rowe, A., Thomford, N.E., Munro, D., Dandara, C., Wonkam, A., Govender, D., Calder, B., Soares, N.C., et al. (2018). The role of tumor microenvironment in chemoresistance: 3D extracellular matrices as accomplices. *Int. J. Mol. Sci.* *19*, 2861

Shafiee, G., Saidijam, M., Tavilani, H., Ghasemkhani, N., and Khodadadi, I. (2016). Genistein induces apoptosis and inhibits proliferation of HT29 colon cancer cells. *Int. J. Mol. Cell. Med.* *5*, 178–191.

Shakibaei, M., Kraehe, P., Popper, B., Shayan, P., Goel, A., and Buhrmann, C. (2015). Curcumin potentiates antitumor activity of 5-fluorouracil in a 3D alginate tumor microenvironment of colorectal cancer. *BMC Cancer* *15*, 1–15.

Shao, L., Wang, Y., Chang, J., Luo, Y., Meng, A., and Zhou, D. (2013). Hematopoietic stem cell senescence and cancer therapy-induced long-term bone marrow injury. *Transl. Cancer Res.* *2*, 397–411.

Sharick, J.T., Jeffery, J.J., Karim, M.R., Walsh, C.M., Esbona, K., Cook, R.S., and Skala, M.C. (2019). Cellular Metabolic Heterogeneity In Vivo Is Recapitulated in Tumor Organoids. *Neoplasia* *21*, 615–626.

Shen, Y., Zhu, D., Lu, W., Liu, B., Li, Y., and Cao, S. (2018). The characteristics of intrinsic fluorescence of type I collagen influenced by collagenase I. *Appl. Sci.* *8*.

Shi, M., Zhu, J., Wang, R., Chen, X., Mi, L., Walz, T., and Springer, T.A. (2016). Latent TGF- β structure and activation. *Nature* *474*, 343–349.

Shiga, K., Hara, M., Nagasaki, T., Sato, T., Takahashi, H., and Takeyama, H. (2015). Cancer-Associated Fibroblasts: Their Characteristics and Their Roles in Tumor Growth. *Cancers (Basel)*. *7*, 2443–2458.

Shiozawa, Y., Eber, M.R., Berry, J.E., and Taichman, R.S. (2015). Bone marrow as a metastatic niche for disseminated tumor cells from solid tumors. *Bonekey Rep.* *4*, 689.

Shoseyov, O., Posen, Y., and Grynspan, F. (2013). Human collagen produced in plants more than just another molecule. *Bioengineered* *5*, 37–41.

Shroyer, N.F. (2016). Tumor Organoids Fill the Niche. *Cell Stem Cell* *18*, 686–687.

- Shupp, A.B., Kolb, A.D., Mukhopadhyay, D., and Bussard, K.M. (2018). Cancer metastases to bone: Concepts, mechanisms, and interactions with bone osteoblasts. *Cancers (Basel)*. *10*, 1–37.
- Siegel, R.L., Miller, K.D., Fedewa, S.A., Ahnen, D.J., Meester, R.G.S., Barzi, A., and Jemal, A. (2017). Colorectal cancer statistics, 2017. *CA. Cancer J. Clin.* *67*, 177–193.
- Siegel, R.L., Miller, K.D., and Jemal, A. (2018). Cancer statistics, 2018. *CA. Cancer J. Clin.* *68*, 7–30.
- Silvestri, L., Costantini, I., Sacconi, L., and Pavone, F.S. (2016). Clearing of fixed tissue: a review from a microscopist's perspective. *J. Biomed. Opt.* *21*, 81205.
- Slaughter, B.V., Khurshid, S.S., Fisher, O.Z., Khademhosseini, A., and Peppas, N.A. (2009). Hydrogels in regenerative medicine. *Adv. Mater.* *21*, 3307–3329.
- Slavkin, H.C., Beierle, J., and Bavetta, L.A. (1968). Odontogenesis: Cell-Cell Interactions in vitro. *Nature* *217*, 269–270.
- Slifko, T.R., Huffman, D.E., Dussert, B., Owens, J.H., Jakubowski, W., Haas, C.N., and Rose, J.B. (2002). Comparison of tissue culture and animal models for assessment of *Cryptosporidium parvum* infection. *Exp. Parasitol.* *101*, 97–106.
- Smith, P., Reid, D.B., Environment, C., Palo, L., Alto, P., and Smith, P.L. (1979). A Threshold Selection Method from Gray-Level Histograms. *IEEE Trans. Syst. Man. Cybern.* *9*, 62–66.
- Smyrek, I., and Stelzer, E.H. (2017). Quantitative three-dimensional evaluation of immunofluorescence staining for large whole mount spheroids with light sheet microscopy. *Biomed Opt Express* *8*, 484–499.
- Solanki, A., King, D., Thibault, G., Wang, L., and Gibbs, S.L. (2020). Quantification of fluorophore distribution and therapeutic response in matched in vivo and ex vivo pancreatic cancer model systems. *PLoS One* *15*, 1–18.
- Soule, H.D., Maloney, T.M., Wolman, S.R., Peterson, W.D., Brenz, R., McGrath, C.M., Russo, J., Pauley, R.J., Jones, R.F., and Brooks, S.C. (1990). Isolation and characterization of a spontaneously immortalized human breast epithelial cell line, MCF-10. *Cancer Res.* *50*, 6075–6086.
- de Souza, N. (2017). Organoid culture. *Nat. Methods* *14*, 35–35.
- Stein, K.C., and Frydman, J. (2019). The stop-and-go traffic regulating protein biogenesis: How translation kinetics controls proteostasis. *J. Biol. Chem.* *294*, 2076–2084.
- Stines, J.-R., Dumas, D., Blondel, W., Didelon, J., and Guillemin, F. (2004). Discrimination between normal and cancerous cells by gap-FRAP: feasibility in endoscopy. *Opt. Sens.* *5459*, 383.

- Sun, Z., Liu, L., Wang, P.P., Roebathan, B., Zhao, J., Dicks, E., Cotterchio, M., Buehler, S., Campbell, P.T., McLaughlin, J.R., et al. (2012). Association of total energy intake and macronutrient consumption with colorectal cancer risk: Results from a large population-based case-control study in Newfoundland and Labrador and Ontario, Canada. *Nutr. J.* *11*, 18.
- Sundaram, K., Nishimura, R., Senn, J., Youssef, R.F., London, S.D., and Reddy, S. V. (2007). RANK ligand signaling modulates the matrix metalloproteinase-9 gene expression during osteoclast differentiation. *Exp. Cell Res.* *313*, 168–178.
- Sung, V., Stubbs, J.T., Fisher, L., Aaron, A.D., and Thompson, E.W. (1998). Bone sialoprotein supports breast cancer cell adhesion proliferation and migration through differential usage of the alpha(v)beta3 and alpha(v)beta5 integrins. *J. Cell. Physiol.* *176*, 482–494.
- Susaki, E.A., Tainaka, K., Perrin, D., Kishino, F., Tawara, T., Watanabe, T.M., Yokoyama, C., Onoe, H., Eguchi, M., Yamaguchi, S., et al. (2014). Whole-brain imaging with single-cell resolution using chemical cocktails and computational analysis. *Cell* *157*, 726–739.
- Swarm, R.L. (1963). Transplantation of a murine chondrosarcoma in mice of different inbred strains. *J. Natl. Cancer Inst.* *31*, 953–975.
- Tainaka, K., Kuno, A., Kubota, S.I., Murakami, T., and Ueda, H.R. (2016). Chemical Principles in Tissue Clearing and Staining Protocols for Whole-Body Cell Profiling. *Annu Rev Cell Dev Biol* *32*, 713–741.
- Tan, K., and Lawler, J. (2009). The interaction of Thrombospondins with extracellular matrix proteins. *J. Cell Commun. Signal.* *3*, 177–187.
- Tang, Y., Wu, X., Lei, W., Pang, L., Wan, C., Shi, Z., Zhao, L., Nagy, T.R., Peng, X., Hu, J., et al. (2009). TGF-B1-induced migration of bone mesenchymal stem cells couples bone resorption with formation. *Nat. Med.* *15*, 757–765.
- Taube, T., Elomaa, I., Blomqvist, C., Beneton, M.N.C., and Kanis, J.A. (1994). Histomorphometric evidence for osteoclast-mediated bone resorption in metastatic breast cancer. *Bone* *15*, 161–166.
- Thiery, J.P., Acloque, H., Huang, R.Y.J., and Nieto, M.A. (2009). Epithelial-Mesenchymal Transitions in Development and Disease. *Cell* *139*, 871–890.
- Thomas, D.A., and Massagué, J. (2005). TGF- β directly targets cytotoxic T cell functions during tumor evasion of immune surveillance. *Cancer Cell* *8*, 369–380.
- Threadgill, D.W., Dlugosz, A.A., Hansen, L.A., Tennenbaum, T., Lichti, U., Yee, D., LaMantia, C., Mourton, T., Herrup, K., Harris, R.C., et al. (1995). Targeted disruption of mouse EGF receptor: Effect of genetic background on mutant phenotype. *Science*. *269*, 230–234.
- Tian, P. (2016). Bio Technology : An Indian Journal Research Advances in Succinate Dehydrogenase. *Bio Technol. An Indian J. Rev. Biotechnol. An Indian J.* *12*, 1–7.

- Tiernan, J.P., Perry, S.L., Verghese, E.T., West, N.P., Yeluri, S., Jayne, D.G., and Hughes, T.A. (2013). Carcinoembryonic antigen is the preferred biomarker for in vivo colorectal cancer targeting. *Br. J. Cancer* *108*, 662–667.
- Todorović-Raković, N., and Milovanović, J. (2013). Interleukin-8 in breast cancer progression. *J. Interf. Cytokine Res.* *33*, 563–570.
- Toth, M., Chvyrkova, I., Bernardo, M.M., Hernandez-Barrantes, S., and Fridman, R. (2003). Pro-MMP-9 activation by the MT1-MMP/MMP-2 axis and MMP-3: Role of TIMP-2 and plasma membranes. *Biochem. Biophys. Res. Commun.* *308*, 386–395.
- Toyoshima, Y., Tokunaga, T., Hirose, O., Kanamori, M., Teramoto, T., Jang, M.S., Kuge, S., Ishihara, T., Yoshida, R., and Iino, Y. (2016). Accurate Automatic Detection of Densely Distributed Cell Nuclei in 3D Space. *PLoS Comput. Biol.* *12*, 1–20.
- Tsai, P.S., Kaufhold, J.P., Blinder, P., Friedman, B., Drew, P.J., Karten, H.J., Lyden, P.D., and Kleinfeld, D. (2009). Correlations of neuronal and microvascular densities in murine cortex revealed by direct counting and colocalization of nuclei and vessels. *J Neurosci* *29*, 14553–14570.
- Tzaphlidou, M. (2008). Bone architecture: Collagen structure and calcium/phosphorus maps. *J. Biol. Phys.* *34*, 39–49.
- Uriel, S., Labay, E., Francis-Sedlak, M., Moya, M.L., Weichselbaum, R.R., Ervin, N., Cankova, Z., and Brey, E.M. (2009). Extraction and assembly of tissue-derived gels for cell culture and tissue engineering. *Tissue Eng. - Part C Methods* *15*, 309–321.
- Valkenburg, K.C., de Groot, A.E., and Pienta, K.J. (2018). Targeting the tumour stroma to improve cancer therapy. *Nat. Rev. Clin. Oncol.* *15*, 366–381.
- Varma, D.M., Gold, G.T., Taub, P.J., and Nicoll, S.B. (2014). Injectable carboxymethylcellulose hydrogels for soft tissue filler applications. *Acta Biomater.* *10*, 4996–5004.
- Veit, G., Kobbe, B., Keene, D.R., Paulsson, M., Koch, M., and Wagener, R. (2006). Collagen XXVIII, a novel von Willebrand factor A domain-containing protein with many imperfections in the collagenous domain. *J. Biol. Chem.* *281*, 3494–3504.
- Velez, A.M.A., and Howard, M.S. (2012). Collagen IV in normal and in disease process. *N. Am. J. Med. Sci.* *4*, 1–8.
- Vincent-Salomon, A., and Thierry, J.P. (2003). Epithelia-mesenchymal transition in breast cancer development. *Breast Cancer Res.* *5*, 101–106.
- Vincent, K., and Durrant, M.C. (2013). A structural and functional model for human bone sialoprotein. *J. Mol. Graph. Model.* *39*, 108–117.
- Viola, M., Brüggemann, K., Karousou, E., Caon, I., Caravà, E., Vigetti, D., Greve, B., Stock, C., de Luca, G., Passi, A., et al. (2017). MDA-MB-231 breast cancer cell viability, motility and matrix adhesion are regulated by a complex interplay of heparan sulfate, chondroitin-/dermatan sulfate and hyaluronan biosynthesis. *Glycoconj. J.* *34*, 411–420.

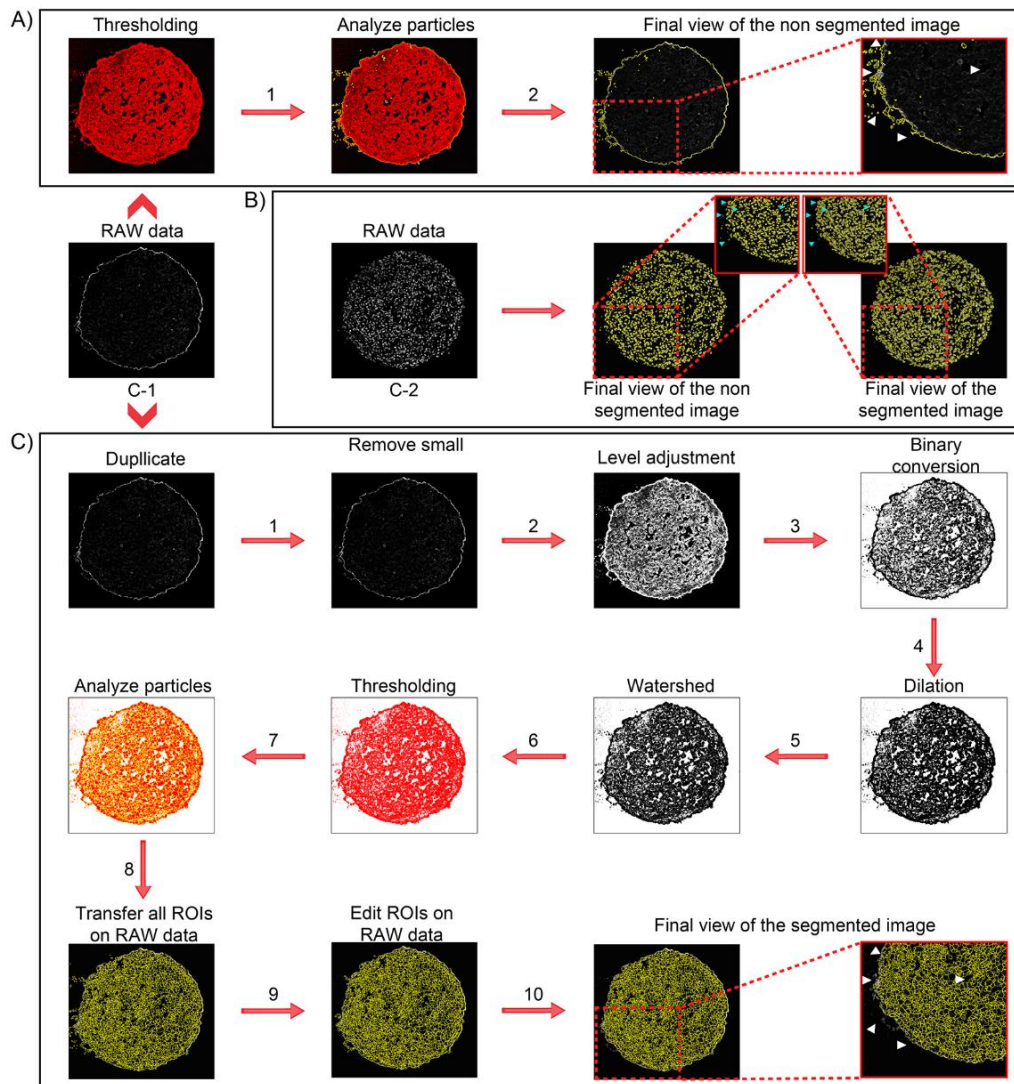
- Vukicevic, S., Kleinman, H.K., Luyten, F.P., Roberts, A.B., Roche, N.S., and Reddi, A.H. (1992). Identification of multiple active growth factors in basement membrane Matrigel suggests caution in interpretation of cellular activity related to extracellular matrix components. *Exp. Cell Res.* *202*, 1–8.
- Vyas, S., Zaganjor, E., and Haigis, M.C. (2016). Mitochondria and Cancer. *Cell* *166*, 555–566.
- Wallace, D.C. (2012). Mitochondria and cancer. *Nat. Rev. Cancer* *12*, 685–698.
- Wang, C., Tang, Z., Zhao, Y., Yao, R., Li, L., and Sun, W. (2014). Three-dimensional in vitro cancer models: a short review. *Biofabrication* *6*, 22001.
- Wang, H., Chen, Y., and Wu, G. (2016). SDHB deficiency promotes TGF β -mediated invasion and metastasis of colorectal cancer through transcriptional repression complex SNAIL1-SMAD3/4. *Transl. Oncol.* *9*, 512–520.
- Wee, P., and Wang, Z. (2017). Epidermal growth factor receptor cell proliferation signaling pathways. *Cancers (Basel)*. *9*, 1–45.
- Wei, Z., and Liu, H.T. (2002). MAPK signal pathways in the regulation of cell proliferation in mammalian cells. *Cell Res.* *12*, 9–18.
- Wei, Y., Zhang, J., Li, H., Zhang, L., and Bi, H. (2015). Multifunctional copolymer coating of polyethylene glycol, glycidyl methacrylate, and REDV to enhance the selectivity of endothelial cells. *J. Biomater. Sci. Polym. Ed.* *26*, 1357–1371.
- Wellen, K.E., Lu, C., Mancuso, A., Lemons, J.M.S., Ryczko, M., Dennis, J.W., Rabinowitz, J.D., Collier, H.A., and Thompson, C.B. (2010). The hexosamine biosynthetic pathway couples growth factor-induced glutamine uptake to glucose metabolism. *Genes Dev.* *24*, 2784–2799.
- Wenzel, C., Riefke, B., Grundemann, S., Krebs, A., Christian, S., Prinz, F., Osterland, M., Golfier, S., Rase, S., Ansari, N., et al. (2014). 3D high-content screening for the identification of compounds that target cells in dormant tumor spheroid regions. *Exp Cell Res* *323*, 131–143.
- Whitaker-Menezes, D., Martinez-Outschoorn, U.E., Lin, Z., Ertel, A., Flomenberg, N., Witkiewicz, A.K., Birbe, R.C., Howell, A., Pavlides, S., Gandara, R., et al. (2011). Evidence for a stromal-epithelial lactate shuttle in human tumors: MCT4 is a marker of oxidative stress in cancer-associated fibroblasts. *Cell Cycle* *10*, 1772–1783.
- Wilde, L., Roche, M., Domingo-Vidal, M., Tanson, K., Philp, N., Curry, J., and Martinez-Outschoorn, U. (2017). Metabolic coupling and the Reverse Warburg Effect in cancer: Implications for novel biomarker and anticancer agent development. *Semin. Oncol.* *44*, 198–203.
- Willard, J.J., Drexler, J.W., Das, A., Roy, S., Shilo, S., Shoseyov, O., and Powell, H.M. (2013). Plant-derived human collagen scaffolds for skin tissue engineering. *Tissue Eng. - Part A* *19*, 1507–1518.

- Williams, M.P.I., Rigon, M., Straka, T., Hörner, S.J., Thiel, M., Gretz, N., Hafner, M., Reischl, M., and Rudolf, R. (2019). A novel optical tissue clearing protocol for mouse skeletal muscle to visualize endplates in their tissue context. *Front. Cell. Neurosci.* *13*, 1–12.
- Wong, C.C., Qian, Y., and Yu, J. (2017). Interplay between epigenetics and metabolism in oncogenesis: Mechanisms and therapeutic approaches. *Oncogene* *36*, 3359–3374.
- Wong, C.H., Siah, K.W., and Lo, A.W. (2019). Estimation of clinical trial success rates and related parameters. *Biostatistics* *20*, 273–286.
- Wu, M., and Swartz, M.A. (2014). Modeling tumor microenvironments in vitro. *J Biomech Eng* *136*, 21011.
- Wu, X., Baig, A., Kasymjanova, G., Kafi, K., Holcroft, C., Mekouar, H., Carbonneau, A., Bahoric, B., Sultanem, K., and Muanza, T. (2016). Pattern of Local Recurrence and Distant Metastasis in Breast Cancer By Molecular Subtype. *Cureus* *8*, e924.
- Wu, Y., Yao, J., Xie, J., Liu, Z., Zhou, Y., Pan, H., and Han, W. (2018). The role of autophagy in colitis-associated colorectal cancer. *Signal Transduct. Target. Ther.* *3*, 31.
- Wuttke, M., Müller, S., Nitsche, D.P., Paulsson, M., Hanisch, F.G., and Maurer, P. (2001). Structural characterization of human recombinant and bone-derived bone sialoprotein. Functional implications for cell attachment and hydroxyapatite binding. *J. Biol. Chem.* *276*, 36839–36848.
- Xiao, Y., Kim, D., Dura, B., Zhang, K., Yan, R., Li, H., Han, E., Ip, J., Zou, P., Liu, J., et al. (2019). Ex vivo Dynamics of Human Glioblastoma Cells in a Microvasculature-on-a-Chip System Correlates with Tumor Heterogeneity and Subtypes. *Adv. Sci. (Weinheim, Baden-Wurttemberg, Ger.)* *6*, 1801531.
- Xu, F., Na, L., Li, Y., and Chen, L. (2020). Roles of the PI3K/AKT/mTOR signalling pathways in neurodegenerative diseases and tumours. *Cell Biosci.* *10*, 1–12.
- Xu, J., Ma, Y., Yu, T., and Zhu, D. (2019). Quantitative assessment of optical clearing methods in various intact mouse organs. *J. Biophotonics* *12*, e201800134.
- Xu, L., Zhang, Z., Sun, X., Wang, J., Xu, W., Shi, L., Lu, J., Tang, J., Liu, J., and Su, X. (2017). Glycosylation status of bone sialoprotein and its role in mineralization. *Exp. Cell Res.* *360*, 413–420.
- Yamada, K.M., and Cukierman, E. (2007). Modeling Tissue Morphogenesis and Cancer in 3D. *Cell* *130*, 601–610.
- Yamaguchi, Y., Kudoh, J., Yoshida, T., and Shimizu, N. (2014). In vitro co-culture systems for studying molecular basis of cellular interaction between Aire-expressing medullary thymic epithelial cells and fresh thymocytes. *Biol. Open* *3*, 1071–1082.

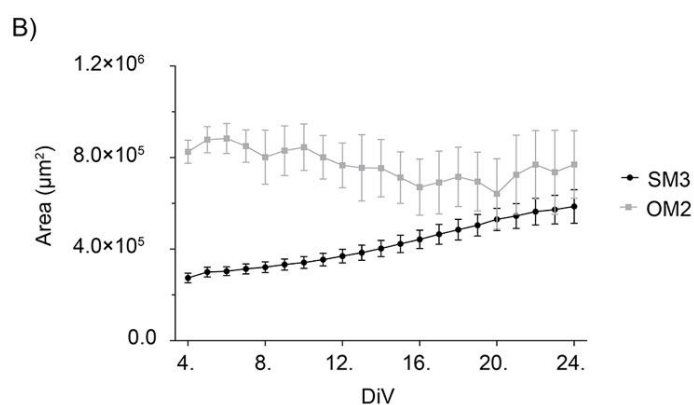
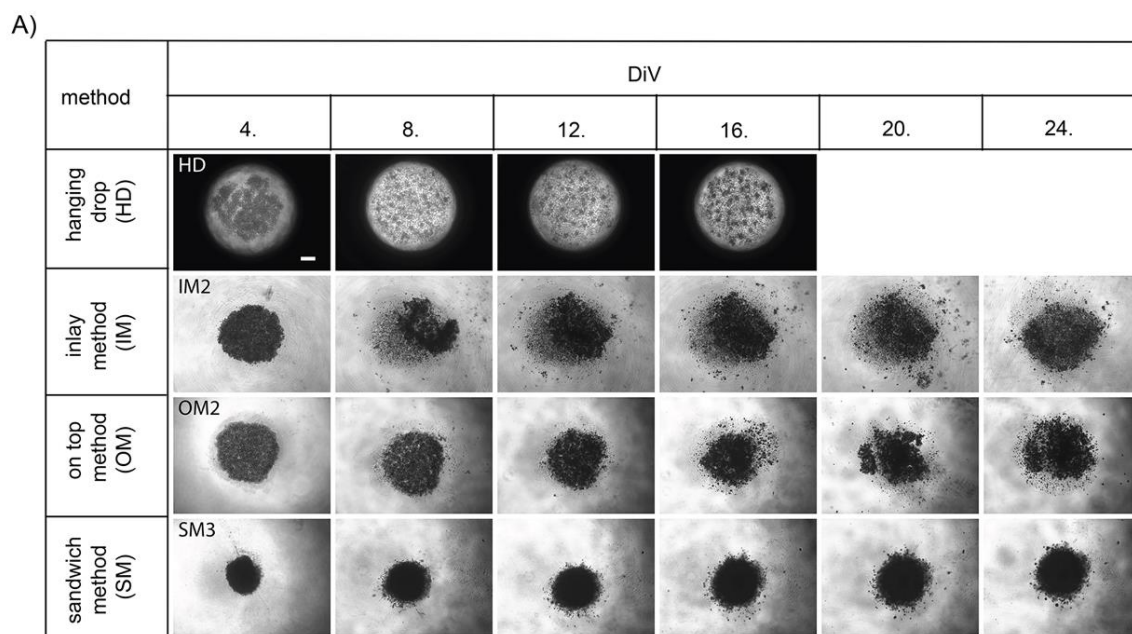
- Yang, B., Treweek, J.B., Kulkarni, R.P., Deverman, B.E., Chen, C.-K., Lubeck, E., Shah, S., Cai, L., and Gradinaru, V. (2014). Single-cell phenotyping within transparent intact tissue through whole-body clearing. *Cell* *158*, 945–958.
- Yang, C., He, Y., Zhang, H., Liu, Y., Wang, W., Du, Y., and Gao, F. (2015). Selective killing of breast cancer cells expressing activated CD44 using CD44 ligand-coated nanoparticles in vitro and in vivo. *Oncotarget* *6*, 15283–15296.
- Yao, C., Lin, Y., Chua, M.S., Ye, C.S., Bi, J., Li, W., Zhu, Y.F., and Wang, S.M. (2007). Interleukin-8 modulates growth and invasiveness of estrogen receptor-negative breast cancer cells. *Int. J. Cancer* *121*, 1949–1957.
- Yao, J., Xiong, S., Klos, K., Nguyen, N., Grijalva, R., Li, P., and Yu, D. (2001). Multiple signaling pathways involved in activation of matrix metalloproteinase-9 (MMP-9) by heregulin- β 1 in human breast cancer cells. *Oncogene* *20*, 8066–8074.
- Yeaman, C., Grindstaff, K.K., Hansen, M.D.H., and Nelson, W.J. (1999). Cell polarity: Versatile scaffolds keep things in place. *Curr. Biol.* *9*, 515–517.
- Yoshimaru, T., Ono, M., Bando, Y., Chen, Y.A., Mizuguchi, K., Shima, H., Komatsu, M., Imoto, I., Izumi, K., Honda, J., et al. (2017). A-kinase anchoring protein BIG3 coordinates oestrogen signalling in breast cancer cells. *Nat. Commun.* *8*, 1–12.
- Yu, Q., and Stamenkovic, I. (2000). Cell surface-localized matrix metalloproteinase-9 proteolytically activates TGF- β and promotes tumor invasion and angiogenesis. *Genes Dev.* *14*, 163–176.
- Yu, T., Qi, Y., Wang, J., Feng, W., Xu, J., Zhu, J., Yao, Y., Gong, H., Luo, Q., and Zhu, D. (2016). Rapid and pridium iodide-compatible optical clearing method for brain tissue based on sugar/sugar-alcohol. *J. Biomed. Opt.* *21*, 1-7,7.
- Yuan, F.L., Xu, M.H., Li, X., Xinlong, H., Fang, W., and Dong, J. (2016). The roles of acidosis in osteoclast biology. *Front. Physiol.* *7*, 1–8.
- Yudushkin, I. (2019). Getting the akt together: Guiding intracellular akt activity by pi3k. *Biomolecules* *9*.
- Zanoni, M., Piccinini, F., Arienti, C., Zamagni, A., Santi, S., Polico, R., Bevilacqua, A., and Tesei, A. (2016). 3D tumor spheroid models for in vitro therapeutic screening: A systematic approach to enhance the biological relevance of data obtained. *Sci. Rep.* *6*, 19103.
- Zarzynska, J.M. (2014). Two Faces of TGF-Beta1 in Breast Cancer. *Mediators Inflamm.* *2014*, 1–16.
- Zeleniak, A.E., Huang, W., Fishel, M.L., and Hill, R. (2018). PTEN-Dependent Stabilization of MTSS1 Inhibits Metastatic Phenotype in Pancreatic Ductal Adenocarcinoma. *Neoplasia* *20*, 12–24.

- Zepp, M., Armbruster, F.P., and Berger, M.R. (2010). Rat monoclonal antibodies against bone sialoprotein II inhibit tumor growth and osteolytic lesions in nude rats induced by MDA-MB-231 breast cancer cells. *Int. J. Clin. Pharmacol. Ther.* **48**, 462–464.
- Zepp, M., Kovacheva, M., Altankhuyag, M., Westphal, G., Berger, I., Gather, K.S., Hilbig, H., Neuhaus, J., Hänsch, G.M., Armbruster, F.P., et al. (2018). IDK1 is a rat monoclonal antibody against hypoglycosylated bone sialoprotein with application as biomarker and therapeutic agent in breast cancer skeletal metastasis. *J. Pathol. Clin. Res.* **4**, 55–68.
- Zeugolis, D.I., Li, B., Lareu, R.R., Chan, C.K., and Raghunath, M. (2008). Collagen solubility testing, a quality assurance step for reproducible electro-spun nano-fibre fabrication. A technical note. *J. Biomater. Sci. Polym. Ed.* **19**, 1307–1317.
- Zhang, L., Su, P., Xu, C., Yang, J., Yu, W., and Huang, D. (2010). Chondrogenic differentiation of human mesenchymal stem cells: A comparison between micromass and pellet culture systems. *Biotechnol. Lett.* **32**, 1339–1346.
- Zhao, H., Chen, Q., Alam, A., Cui, J., Suen, K.C., Soo, A.P., Eguchi, S., Gu, J., and Ma, D. (2018). The role of osteopontin in the progression of solid organ tumour. *Cell Death Dis.* **9**, 356.
- Zhu, L., Tang, Y., Li, X., Keller, E.T., Yang, J., Cho, J., Feinberg, T.Y., and Weiss, S.J. (2020). Osteoclast-mediated bone resorption is controlled by a compensatory network of secreted and membrane-tethered metalloproteinases. *Sci Transl Med.* **12**.
- Zschenker, O., Streichert, T., Hehlhans, S., and Cordes, N. (2012). Genome-wide gene expression analysis in cancer cells reveals 3D growth to affect ECM and processes associated with cell adhesion but not DNA repair. *PLoS One* **7**, e34279.
- Zu, X.L., and Guppy, M. (2004). Cancer metabolism: Facts, fantasy, and fiction. *Biochem. Biophys. Res. Commun.* **313**, 459–465.

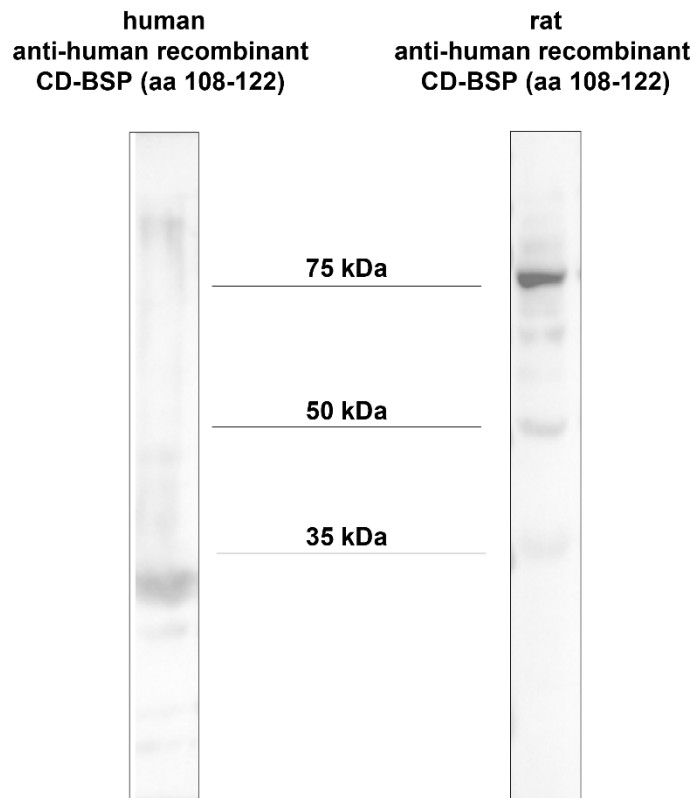
11 SUPPLEMENTARY MATERIAL



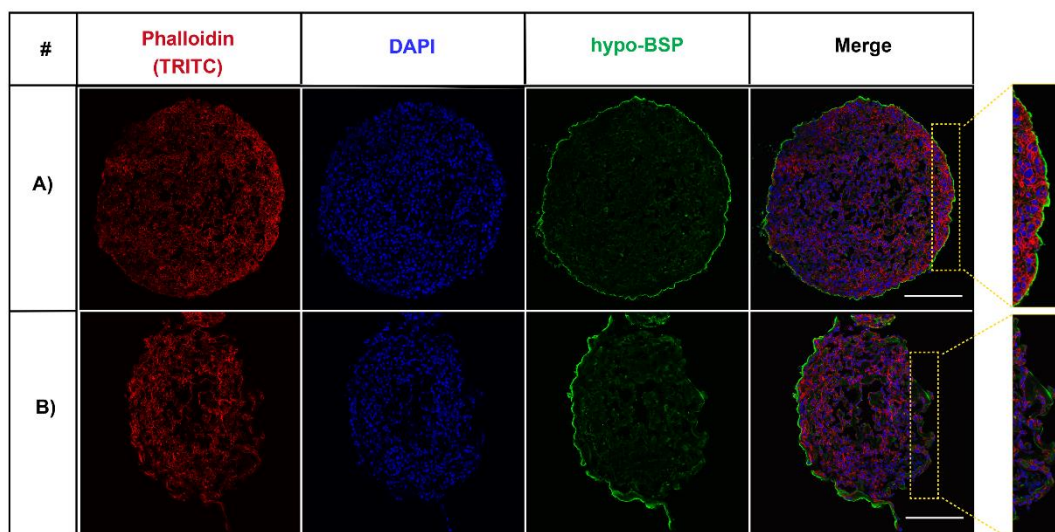
Supplementary Figure 1. Comparison of methods used to measure the region of interest (ROIs) of spheroids employing ImageJ software. Two-channel confocal slices of MDA-MB-231 spheroid 10- μ m thick cryosections comprising anti-BSP immunofluorescence (A and C, C-1) and nuclear staining (B, C-2) were analyzed by either simple threshold-based segmentation (“non-segmented”; A, B middle panels) or a more elaborate segmentation routine (“segmented”; B right panels, C). A) Confocal image of BSP expression area was threshold segmented (1) and then the selected area was analyzed using a size window from 50 pixels to infinity using the “Analyze particles” function of the ImageJ software (2). C) The same RAW data were duplicated, and noise pixels were removed with “Median” filter (1). The resulting image was binarized (2-3), dilated (4), watershed filtered (5), thresholded (6), and then the selected area was analyzed using a size window from 50 pixels to infinity using the “Analyze particles” function of the ImageJ software (7). Application of found ROIs on RAW data (8) and editing of few unwanted excess ROIs (9) yielded the final view (10) and numbers of BSP fluorescence intensity as used in Fig. 14. White arrowheads indicate differences in non-segmented (A) and segmented images (C). B) Comparison of the segmentation protocols for nuclear staining data (C-2). Blue arrowheads show differences for the detection of nuclear signals between routines explained in A and C. (Rustamov et al., 2019)(CC BY)



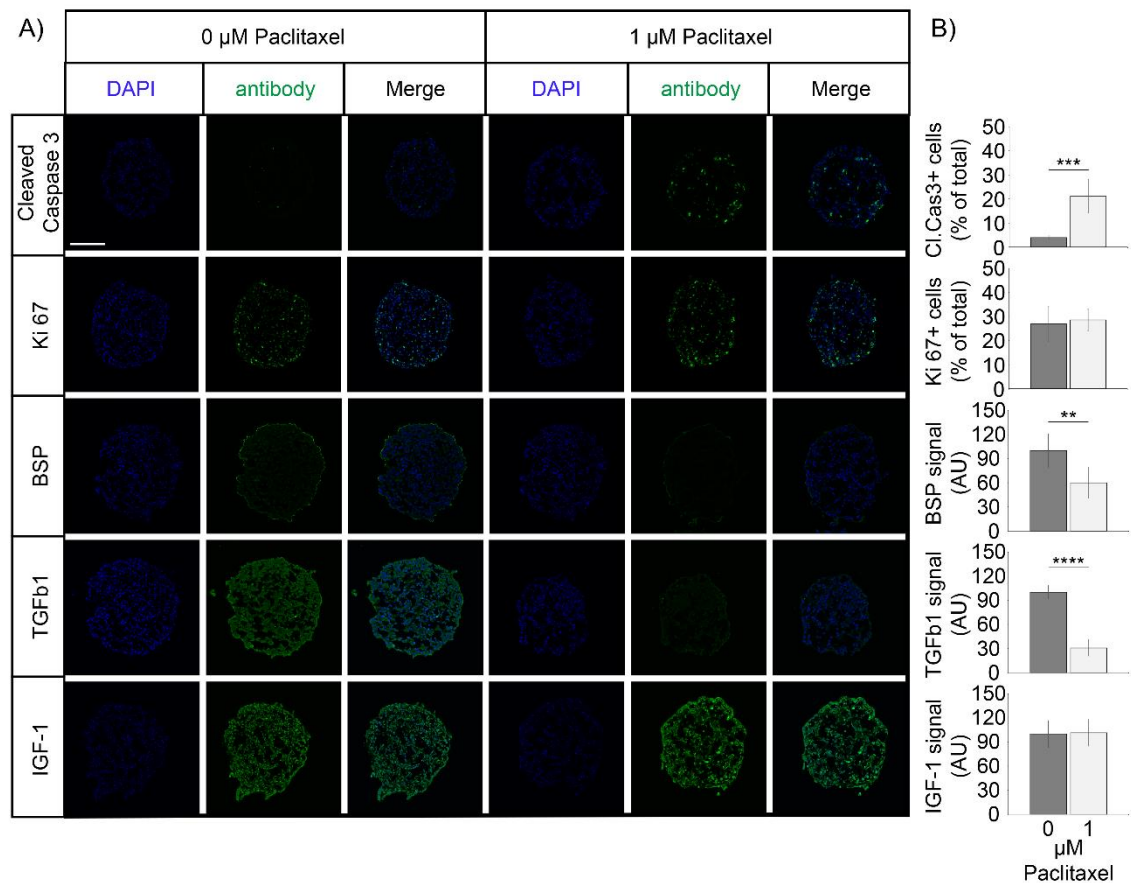
Supplementary Figure 2. Sandwich method yields most consistent growth of PC-3 spheroids. A) Representative phase-contrast microscopy images of PC-3 3D-cultures. These were generated using four different methods: hanging drop (HD), inlay method (IM), on top method (OM), and sandwich method (SM). From HD to SD, equal initial seeding densities were used (10,000 cells / well). Spheroids were cultured until day 24 in vitro (DiV). Representative images from DiV 4, 8, 12, 16, 20 and 24 are shown. Scale bar, 200 μm . B) Quantitative analysis of 3D-culture growth. Graph depicts areas of 3D-cultures as a function of DiV (mean values \pm SD, $n = 4$ independent experiments with 5 replicates). (Rustamov et al., 2019)(CC BY)



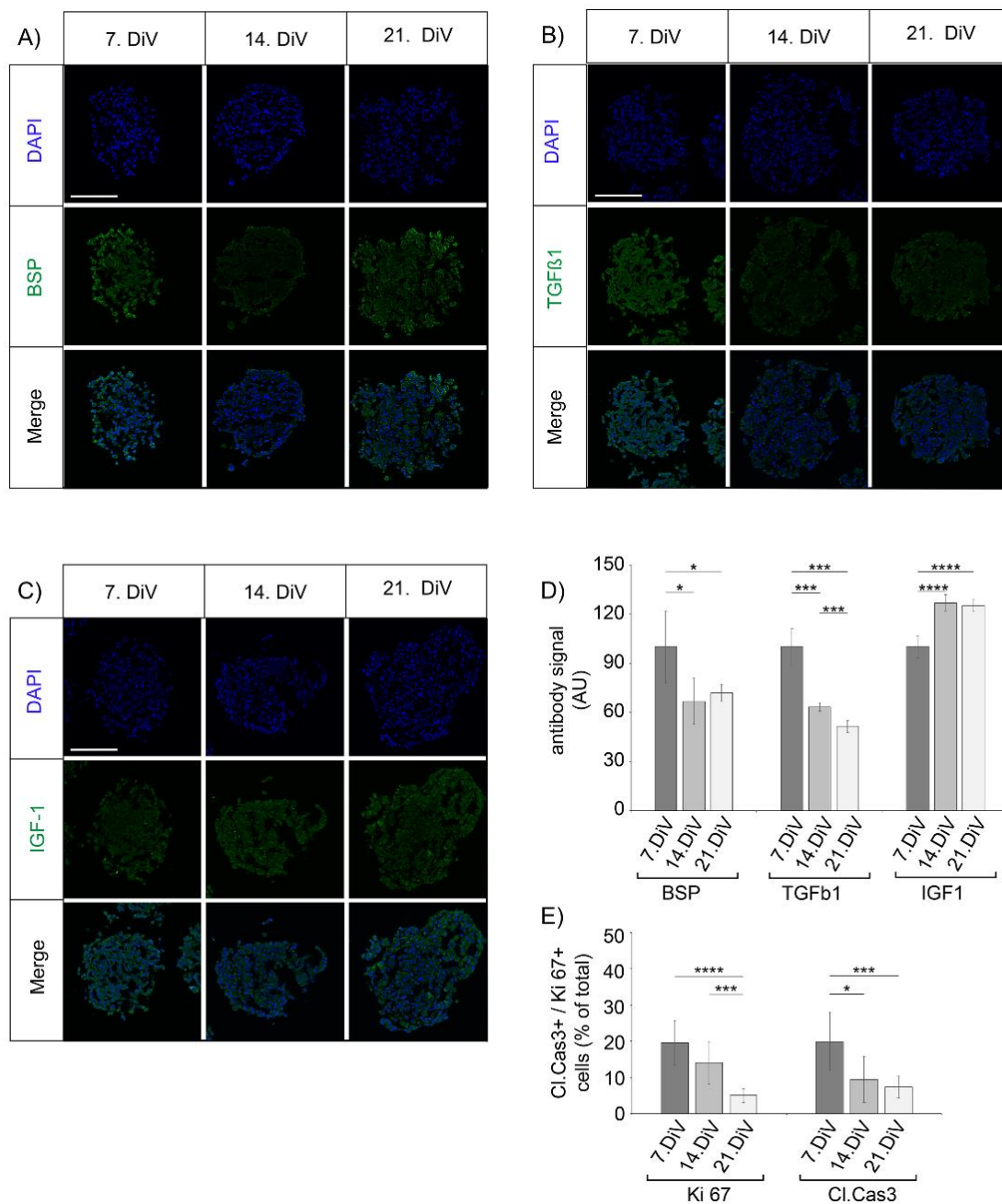
Supplementary Figure 3. Determination of glycosylation grade of BSP with different antibodies. Novel human anti-recombinant human CD-BSP mAb (aa 108-122 / AF165) detects bands at approximately 25 and 33 kDa. In contrast, commercially available rat anti-recombinant human CD-BSP mAb (aa 108-122 / IDK1) primarily detects a band at 75 kDa and additionally some weak bands at 45-50 kDa and 35 kDa. (Rustamov et al., 2019)(CC BY)



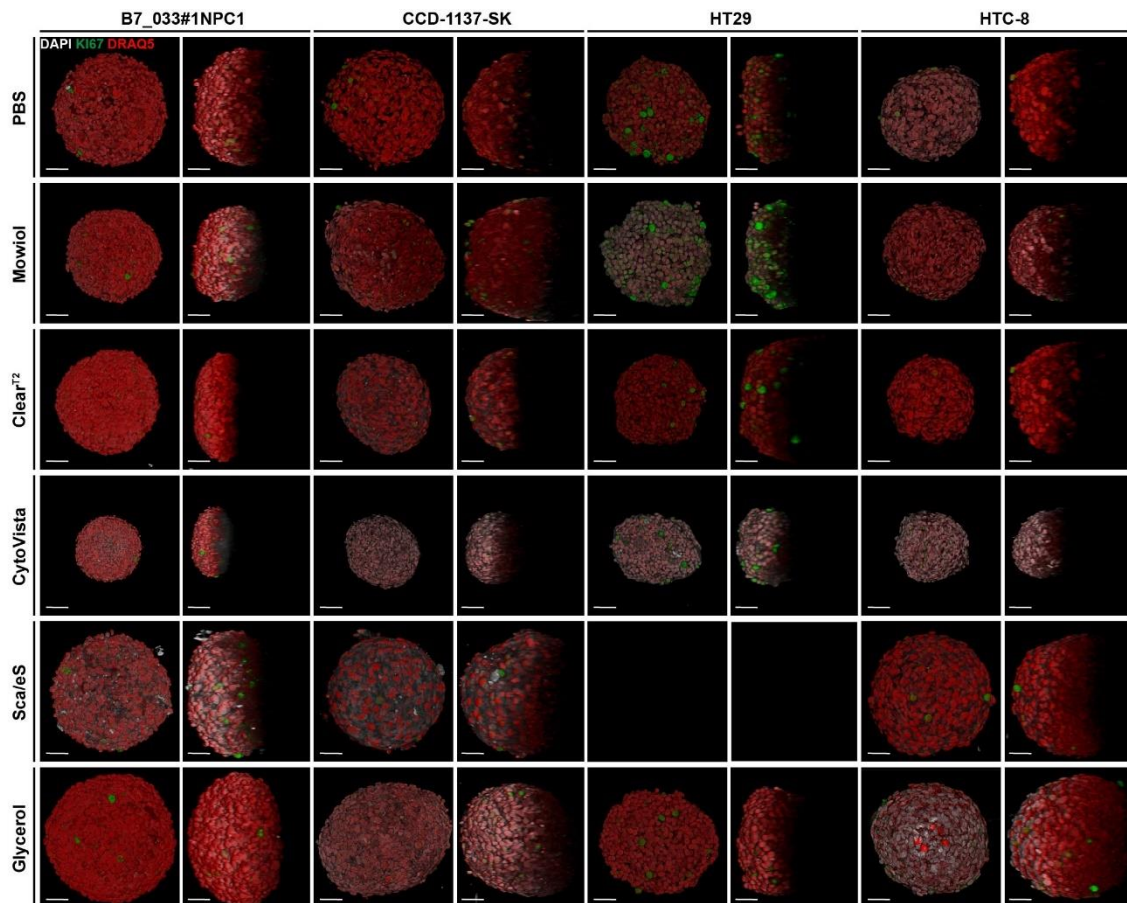
Supplementary Figure 4. Enrichment of hypo-BSP mAb signals in the spheroid surface appears to be specific. Intact (A) and partially clipped (B) MDA-MB-231 spheroids (14 DiV) were cryo sectioned (thickness 10 μ m), fixed and then stained with DAPI (nuclei), phalloidin TRIC (actin filaments) and CD-BSP (aa 108-122) anti-human mAb (hypo-BSP). Scale bars, 200 μ m. (Rustamov et al., 2019)(CC BY)



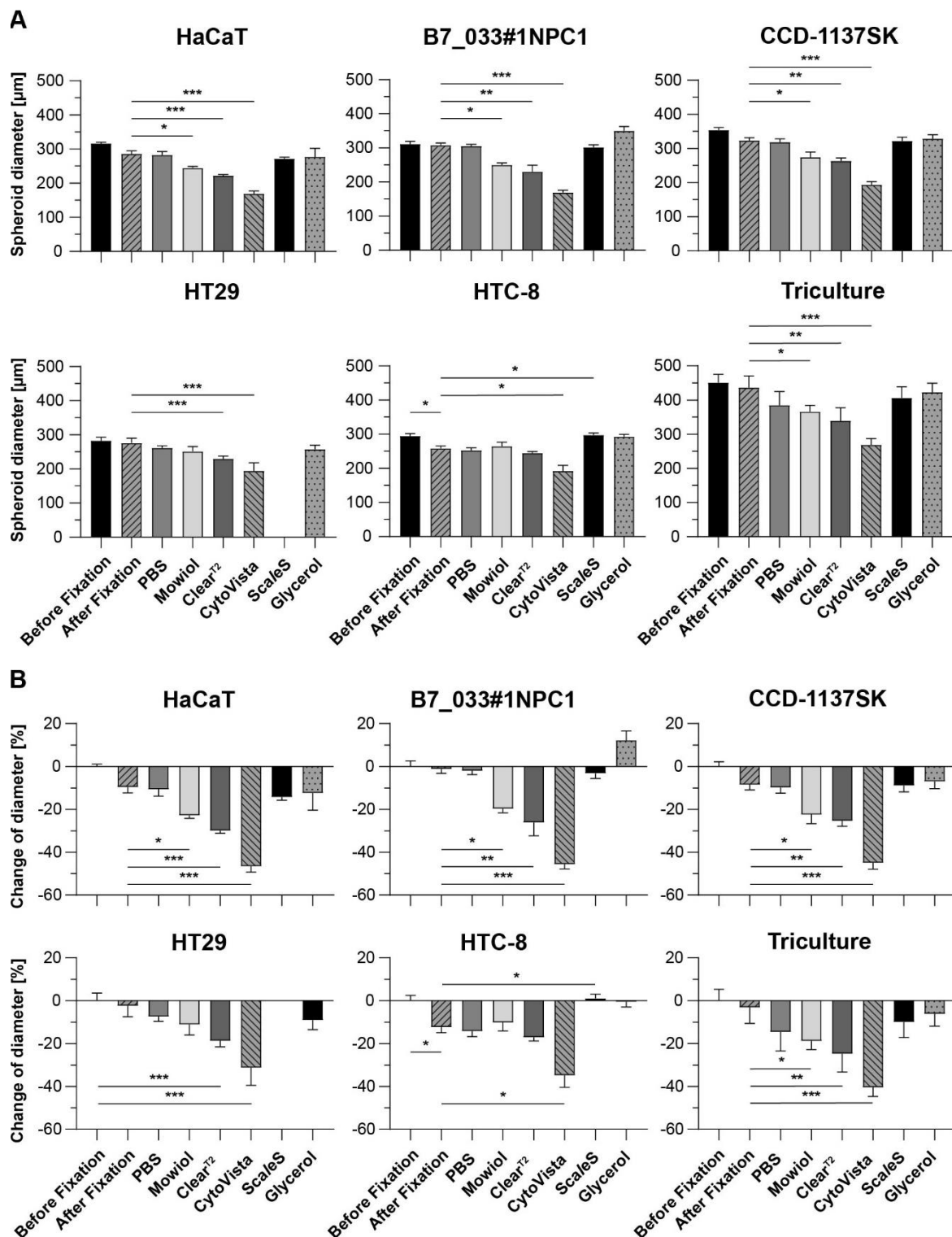
Supplementary Figure 5. Expression of both, BSP and TGF β 1, are reduced upon cytostatic treatment. 6. DiV SM3 spheroids were incubated for 48 h with 0 or 1 μ M of Paclitaxel, then harvested, fixed, sliced and stained against nuclei and either Cleaved Caspase 3, KI67, BSP, TGF β 1, or IGF1. A) Representative confocal images. Scale bar, 200 μ m. B) Quantitative analysis of either fractions of Cleaved Caspase 3/KI67 positive cells, or average intensity of BSP, TGF β 1, or IGF1. Graphs show mean \pm SD (6 spheroids for each condition. Statistical analysis was performed using a one-way ANOVA. **** P < 0.0001, *** P < 0.001, ** P < 0.01). (Rustamov et al., 2019)(CC BY)



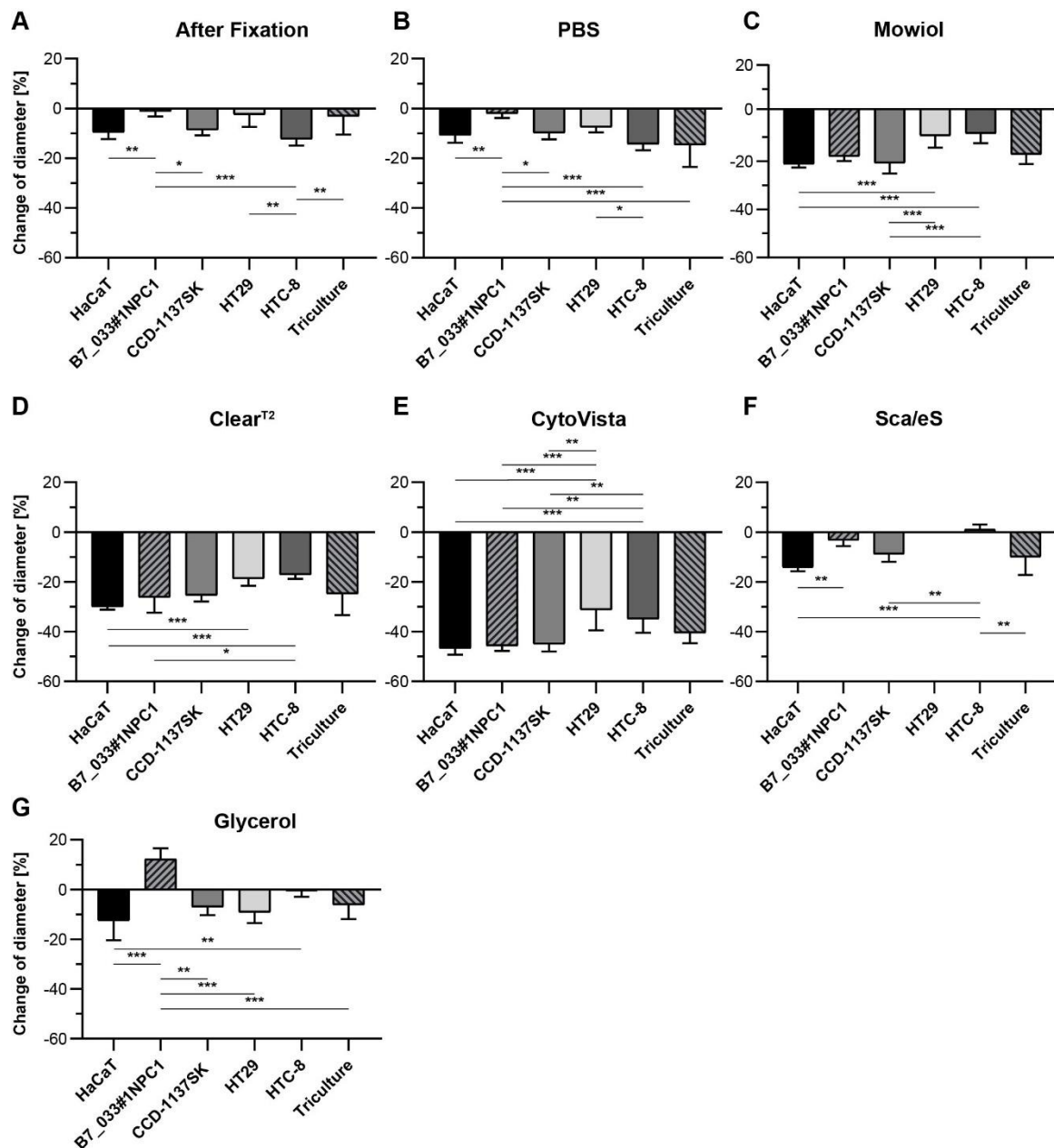
Supplementary Figure 6. Expression of BSP and TGFβ1 correlates in maturing co-cultures of MDA-MB-231 and CCD-1137Sk cells. 10,000 cells each of MDA-MB-231 and CCD-1137Sk cells were co-seeded in ultralow attachment plates. After 7., 14., and 21. DiV they were harvested, fixed, sliced and stained against nuclei and either Cleaved Caspase 3, Ki67, BSP, TGFβ1, or IGF1. A-C). Representative confocal images. Scale bars, 200 μm. D-E) Quantitative analysis of either average intensity of BSP, TGFβ1, or IGF1 (D) or fraction of Cleaved Caspase 3/Ki67 positive cells (E). Graphs show mean ± SD (6 spheroids of each condition). Statistical analysis was performed using one-way ANOVA. **** P < 0.0001, *** P < 0.001, * P < 0.05). (Rustamov et al., 2019)(CC BY)



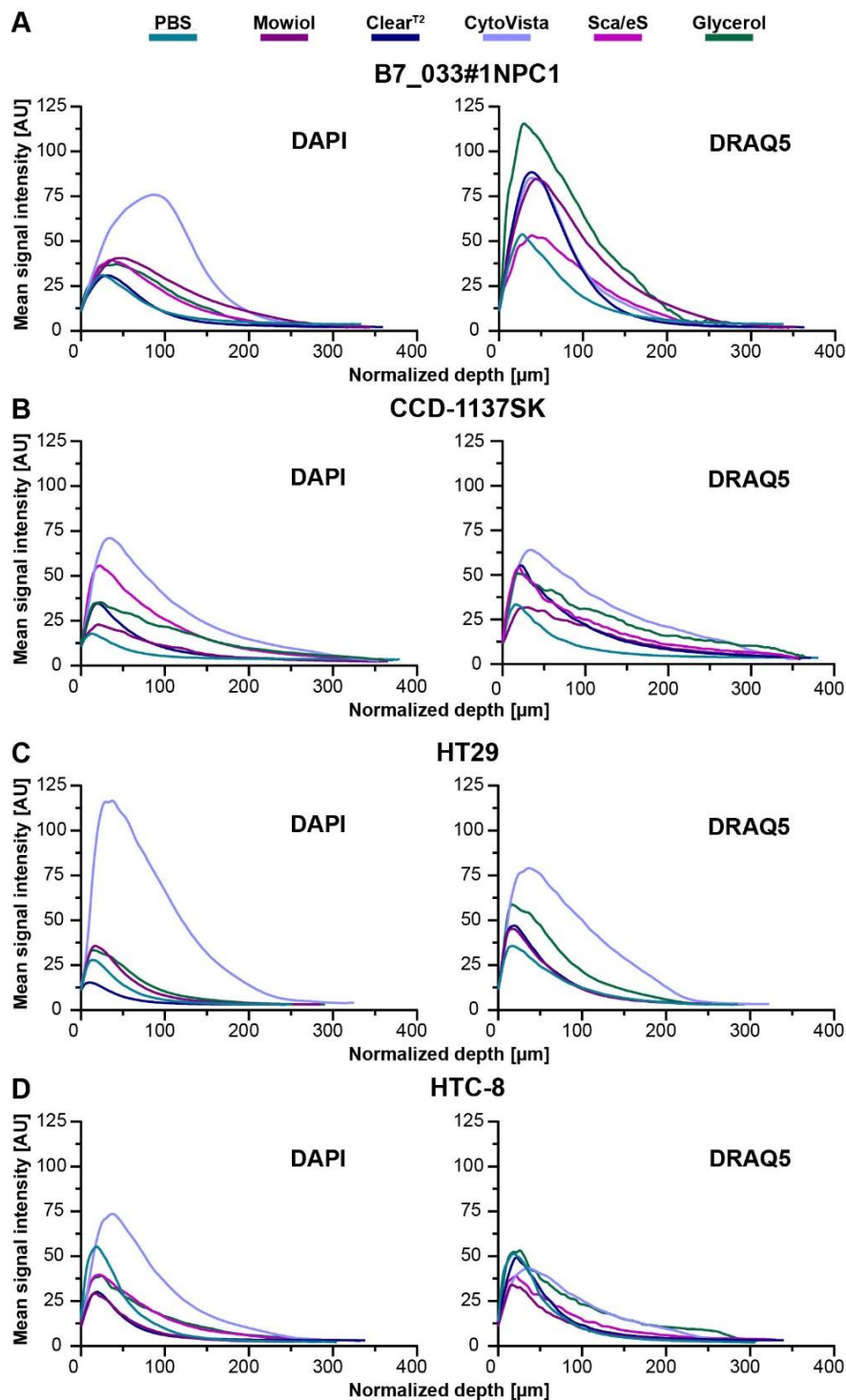
Supplementary Figure 7. Preservation of signal intensity, sample volume, and transparency upon clearing vary between different cell types. Glycerol provides the highest degree of consistency among different spheroid models. Upon growth to a diameter of approximately 300 μm , spheroids made of cell lines as indicated were fixed, stained with anti-KI67 (green) and nuclear dyes DAPI (Grey) and DRAQ5 (red), followed by optical tissue clearing or embedding as indicated and subsequent confocal whole mount microscopy. Images show representative top (left panels each cell type) and orthogonal 3D-volume projections (right panels for each cell type) of merged images after corresponding clearing method. Scale bars, 50 μm . (Nürnberg et al., 2020)(CC BY)



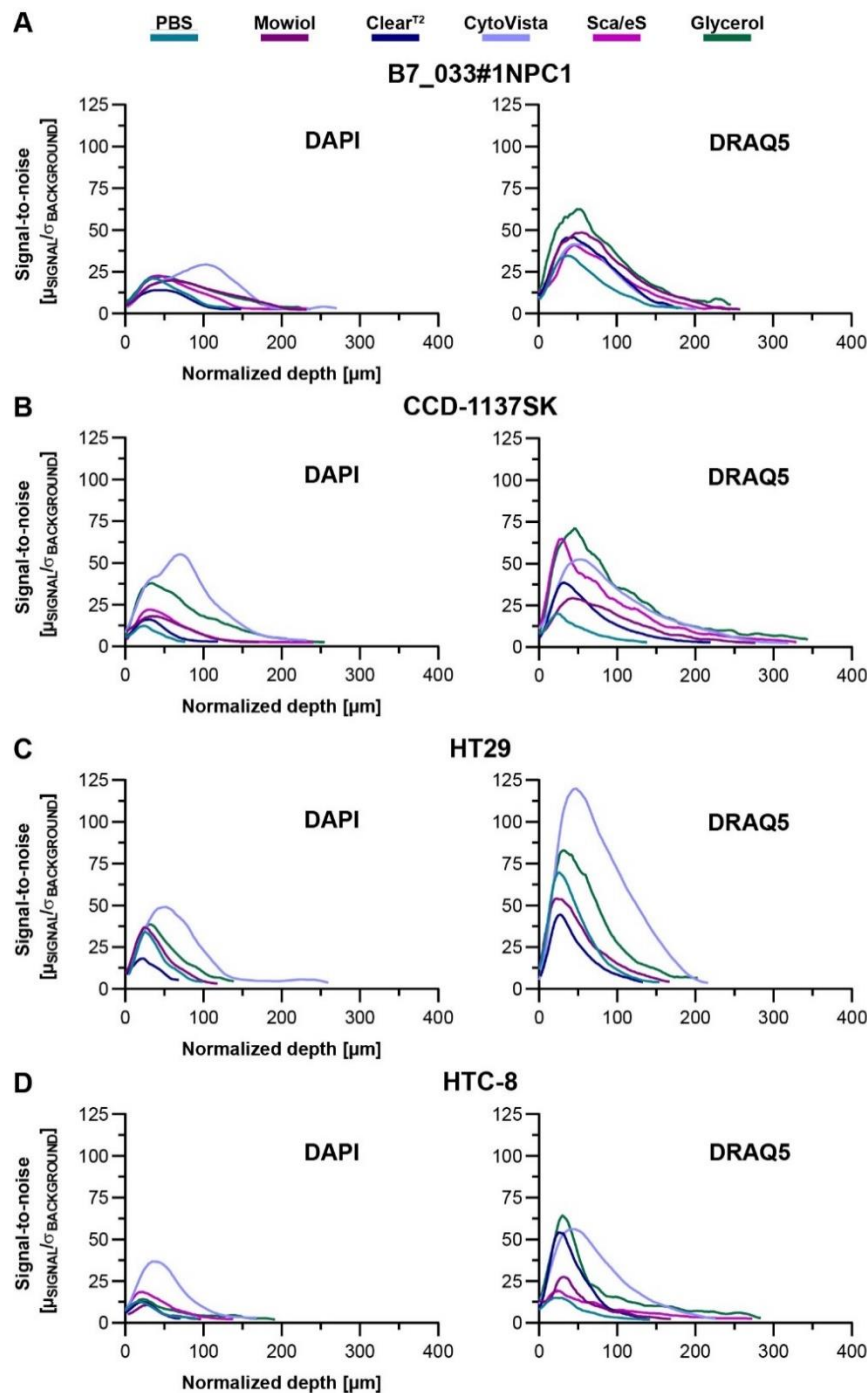
Supplementary Figure 8. Post-fixation changes of sample volume are best prevented by Glycerol and ScaleS. Whole spheroids of cell lines as indicated were fixed, stained with anti-Ki67, DAPI, and DRAQ5, followed by embedding/clearing in PBS, Mowiol, Clear^{T2}, CytoVista, ScaleS, or Glycerol. Spheroid diameters were determined from brightfield images before and after fixation and from confocal microscopy stacks after staining. Spheroids of all cell types had a pre-fixation diameter of approximately 300 μm , except for melanoma tri-cultures (here approximately 450 μm). A-B) Quantitative analysis of average spheroid diameter (A) and change of average spheroid diameter relative to pre-fixation state (B). Graphs depict mean \pm SD; $n \geq 7$; * $P \leq 0.05$, ** $P \leq 0.01$, *** $P < 0.001$. (Nürnberg et al., 2020)(CC BY)



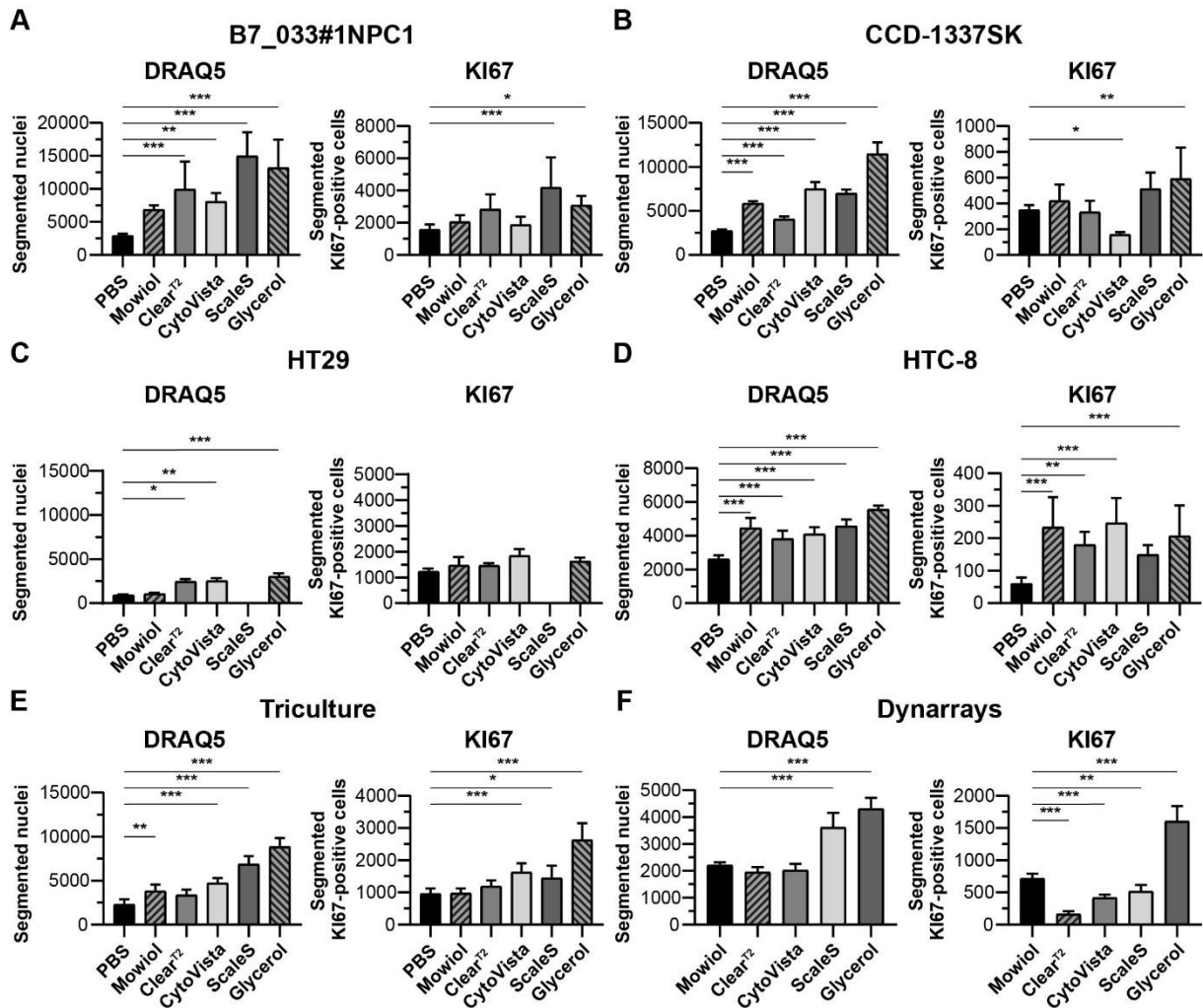
Supplementary Figure 9. Degree of clearing-induced volume change is cell line-dependent. Whole spheroids of cell lines as indicated were fixed, stained with anti-KI67, DAPI, and DRAQ5, followed by embedding/clearing in PBS, Mowiol, Clear^{T2}, CytoVista, ScaleS, or Glycerol. Spheroid diameters were determined from brightfield images before and after fixation and from confocal microscopy stacks after staining. Spheroids of all cell types had a pre-fixation diameter of approximately 300 μm , except for melanoma tri-cultures (here approximately 450 μm). A-G) Quantitative analysis of change of average spheroid diameter relative to pre-fixation state as a function cell line. Graphs depict mean + SD; $n \geq 7$; * $P \leq 0.05$, ** $P \leq 0.01$, *** $P < 0.001$. (Nürnberg et al., 2020)(CC BY)



Supplementary Figure 10. Maximum DAPI fluorescence observed with CytoVista for different cell types. Whole spheroids of cell lines as indicated were fixed, stained with anti-Ki67, DAPI, and DRAQ5, followed by embedding/clearing in PBS, Mowiol, Clear^{T2}, CytoVista, Sca/eS, or Glycerol. Upon confocal microscopy, depth-dependent signal intensities of DAPI and DRAQ5 were determined by selecting one circular region of interest (ROI) per sample through the central region of the spheroid followed by mean intensity measurement throughout the entire stack depth. To account for volume-changing effects of individual clearing methods, depth values were normalized by the method-dependent degree of swelling or shrinkage. A-D) Graphs, mean intensities of DAPI and DRAQ5 as a function of normalized z-depth ($n \geq 7$). (Nürnberg et al., 2020)(CC BY)



Supplementary figure 11. Increased depth-dependent SNR for DAPI is observed with CytoVista clearing. Whole spheroids of cell lines as indicated were fixed, stained with anti-Ki67, DAPI, and DRAQ5, followed by embedding/clearing in PBS, Mowiol, Clear^{T2}, CytoVista, Sca/eS, or Glycerol. Upon confocal microscopy, SNR values for DAPI and DRAQ5 were determined by selecting one circular ROI per sample through the central region of the spheroid followed by measurement of mean intensity and standard deviation of background and nuclear signal via semi-automated thresholding. Then, SNR was calculated as the ratio of mean signal intensity in identified nuclear regions to the average standard deviation of background intensity (μ SIGNAL/ σ BACKGROUND). To account for volume-changing effects of individual clearing methods, depth values were normalized by the method-dependent degree of swelling or shrinkage. A-D) Graphs, SNR values of DAPI and DRAQ5 as a function of normalized z-depth ($n \geq 7$). (Nürnberg et al., 2020)(CC BY)



Supplementary Figure 12. Optical clearing with Glycerol improves nuclear segmentation, whereas CytoVista clearing can lead to under-segmentation. 3D-cell cultures as indicated were fixed, stained with anti-KI67, DAPI, and DRAQ5, followed by embedding/clearing in PBS, Mowiol, Clear^{T2}, CytoVista, ScaleS, or Glycerol. Upon confocal *in toto* imaging without z-compensation, semi-automated image segmentation was performed to detect and count KI67⁺ and DRAQ5⁺ nuclei. A-F) Quantitative analysis of KI67⁺ and DRAQ5⁺ nuclei as a function of clearing/embedding protocol. Data show mean + SD; n ≥ 7; * P ≤ 0.05, ** P ≤ 0.01; *** P ≤ 0.001. (Nürnberg et al., 2020)(CC BY)

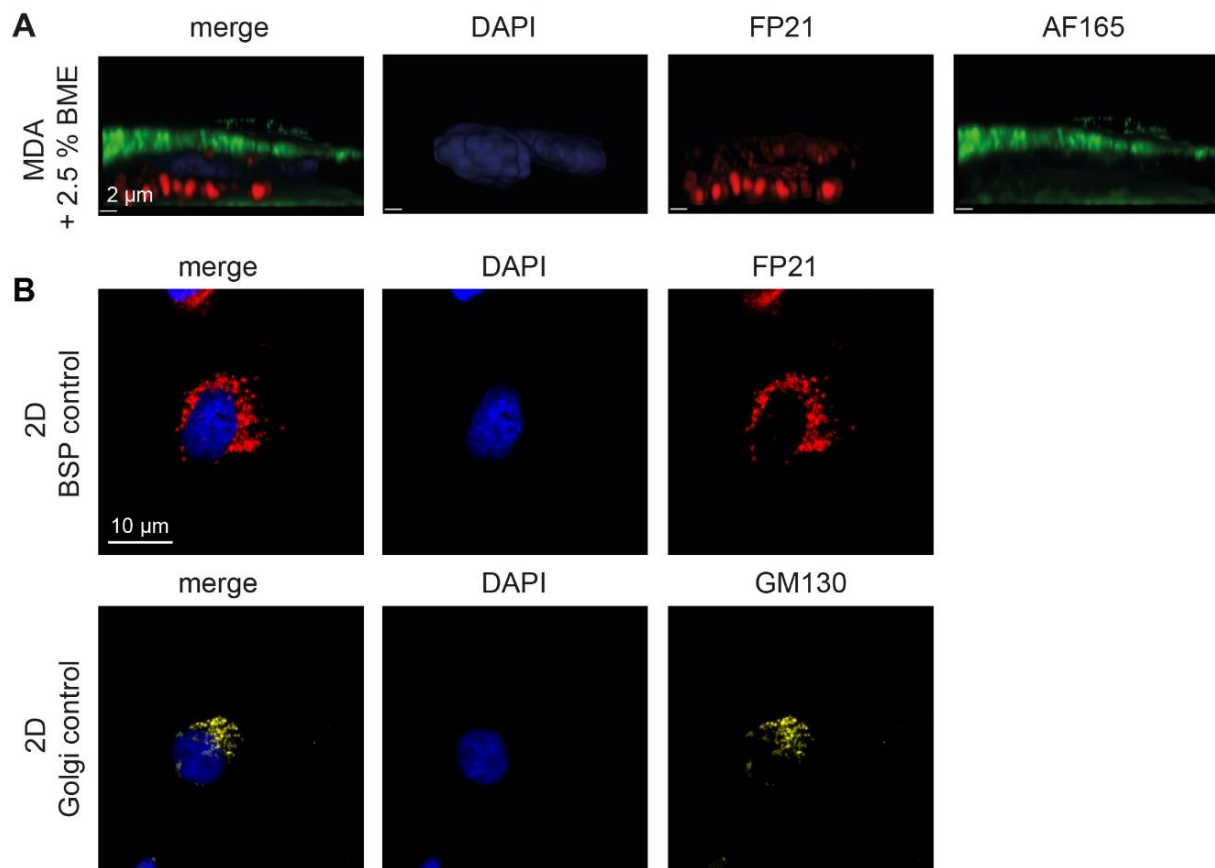


Figure S13. Localization of anti-BSP antibodies AF165 and FP21 in 2D-culture. 1,200,000 MDA-MB-231 cells were seeded in petri dishes containing glass cover slips. After 2 days, one culture was supplemented with 2.5 % BME within the media. Alternatively, no BME was added and after 4 days, cultures were PFA fixed and stained for DAPI, human BSP (AF165 and FP21), and GM130 as Golgi marker. A) Exemplary high-resolution side-view of confocal scans for BSP staining in volume projection. B) Representative confocal images in sum projections for direct comparison of FP21 and GM130 signal distribution. (Keller et al., 2021)(CC BY)

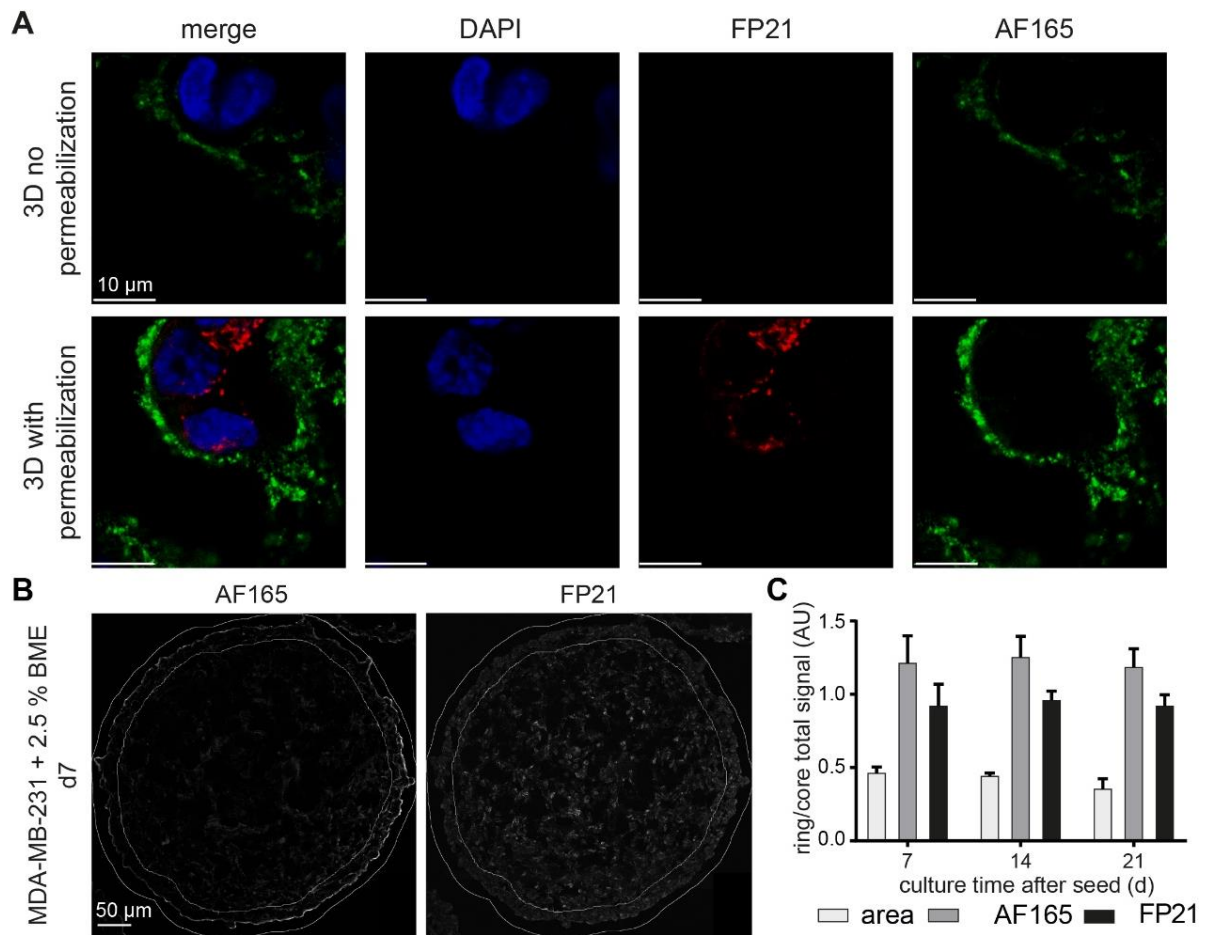


Figure S14. Localization of anti-BSP antibodies AF165 and FP21 in 3D-spheroids. 4,000 MDA-MB-231 cells were seeded in mono-culture spheroids and supplemented with 2.5 % BME upon seeding. After 4, 7, 14 and 21 days, spheroids were PFA fixed and stained for DAPI and human BSP (AF165 and FP21) with and without permeabilization as indicated. For spheroid slice quantification, a region of interest on the spheroid rim was set to match around half the total area and to contain roughly the same amount of background regions not containing cells. This ring was then quantified and compared with the corresponding core signal analysis and showed increased AF165 signal in the spheroid rim, while FP21 signal was evenly distributed throughout the investigated time-period. A) Exemplary optical slices of whole mount confocal scanned spheroids. B) Representative confocal scans of 10 μ m cryo-sectioned spheroids after 7 days in culture with indication of the ring quantification. C) Graphs showing quantitative analysis of summed up fluorescence intensities within the outer ring region, normalized with the corresponding core region quantification. (Keller et al., 2021)(CC BY)

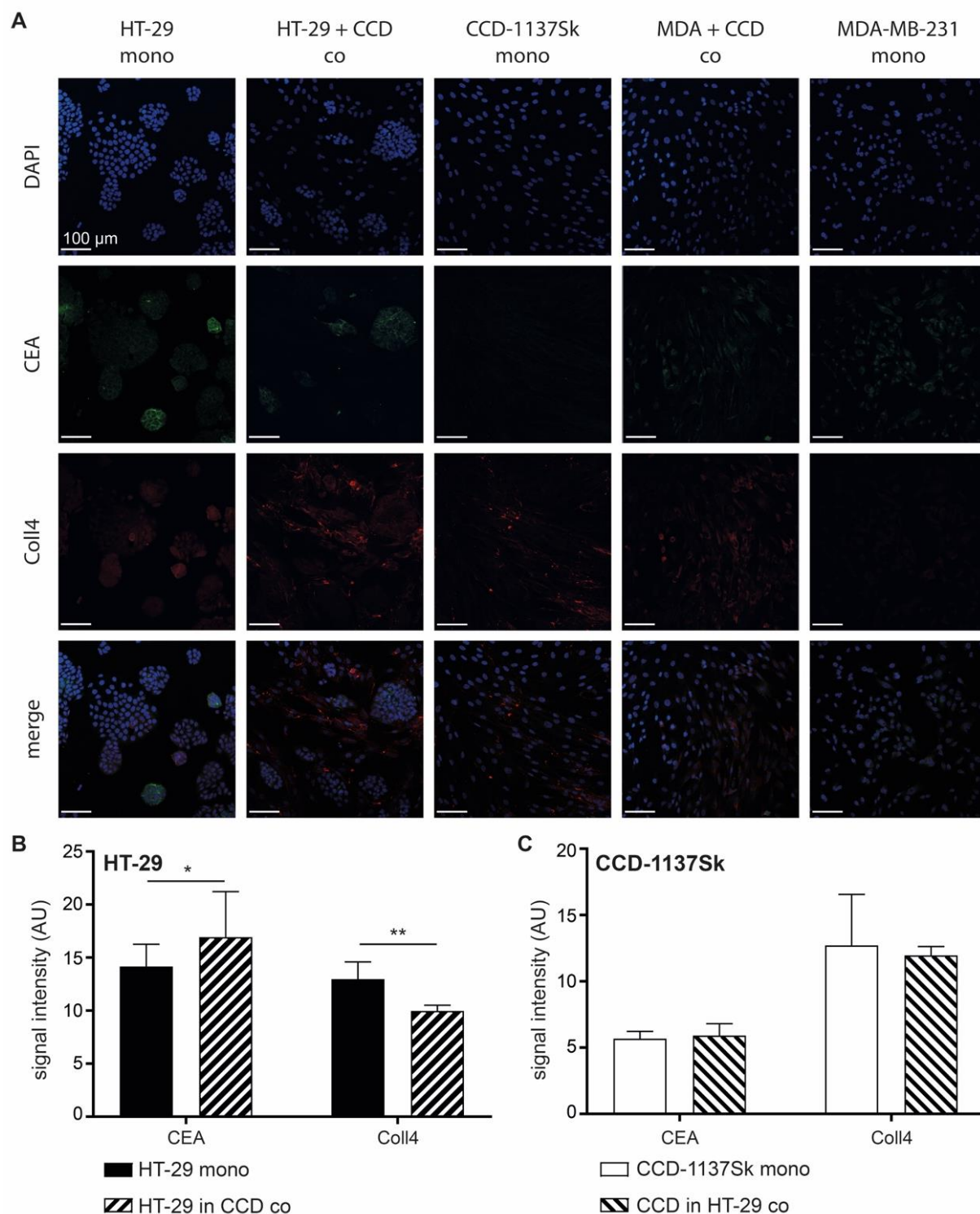


Figure S15. CEA can serve as a cancer-cell marker in 2D-mono- and co-cultures of HT-29, MDA-MB-231, and CCD-1137Sk cells. HT-29, MDA-MB-231, and CCD-1137Sk cells were either seeded alone or in co-culture as indicated and grown to a subconfluent state for 4 days. Then, cells were fixed and stained with DAPI (blue) as well as antibodies against CEA (green) and Coll4 (red). Scale bars, 100 μ m. A) Representative confocal images of fluorescence staining for markers and cultures as indicated. B–C) Quantitative analysis of CEA and Coll4 expression of HT-29 (B) and CCD-1137Sk cells (C). Mean + SEM (n = 3 experiments; * P < 0.05, ** P < 0.01). (Keller et al., 2020)(CC BY)

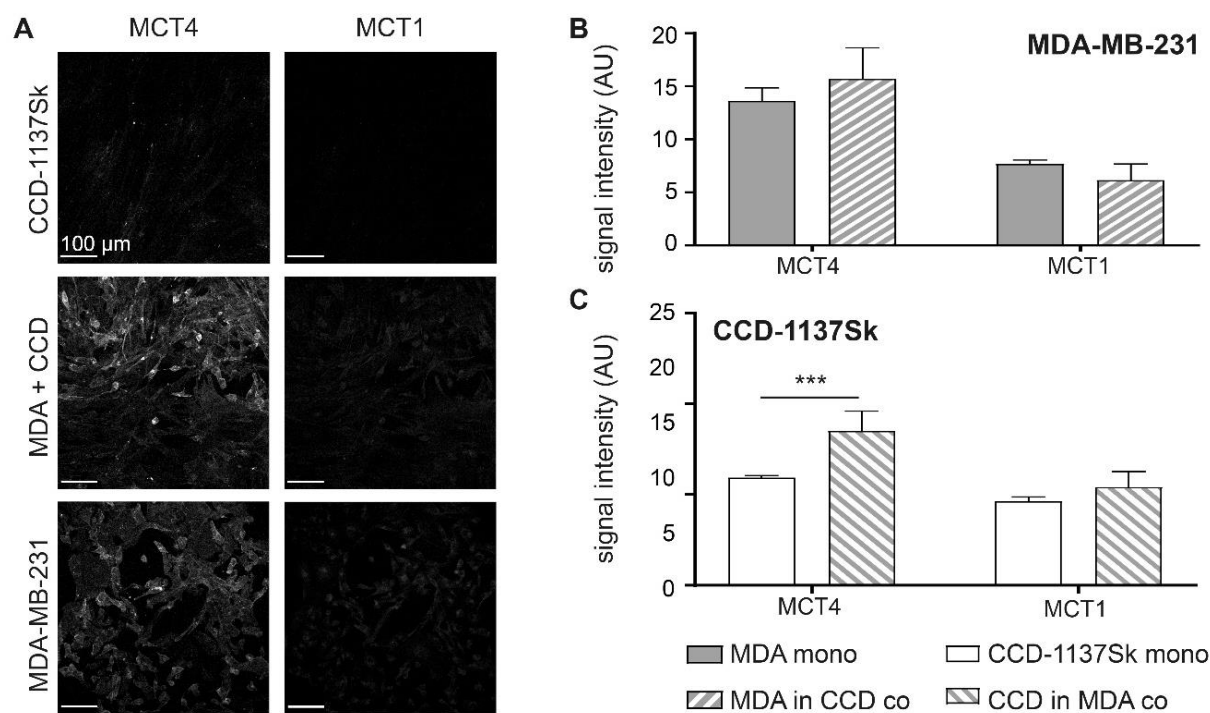


Figure S16. Mono-layer co-cultures of MDA-MB-231 and CCD-1137Sk show enhanced expression of MCT4 in fibroblasts. MDA-MB-231 and CCD-1137Sk cells were either seeded alone or in co-culture and grown to a subconfluent state for 4 days. Then, cells were fixed and stained with DAPI as well as antibodies against MCT4 and MCT1 as markers for nuclei, lactate export, and lactate import, respectively (A – C). Scale bars, 100 μ m. A) Representative confocal images of fluorescence staining for markers and cultures as indicated. B-C) Graphs showing quantitative analysis of fluorescence intensity values for markers and cell type as indicated. Mean + SEM (n = 3 experiments; *** P < 0.001). (Keller et al., 2020)(CC BY)

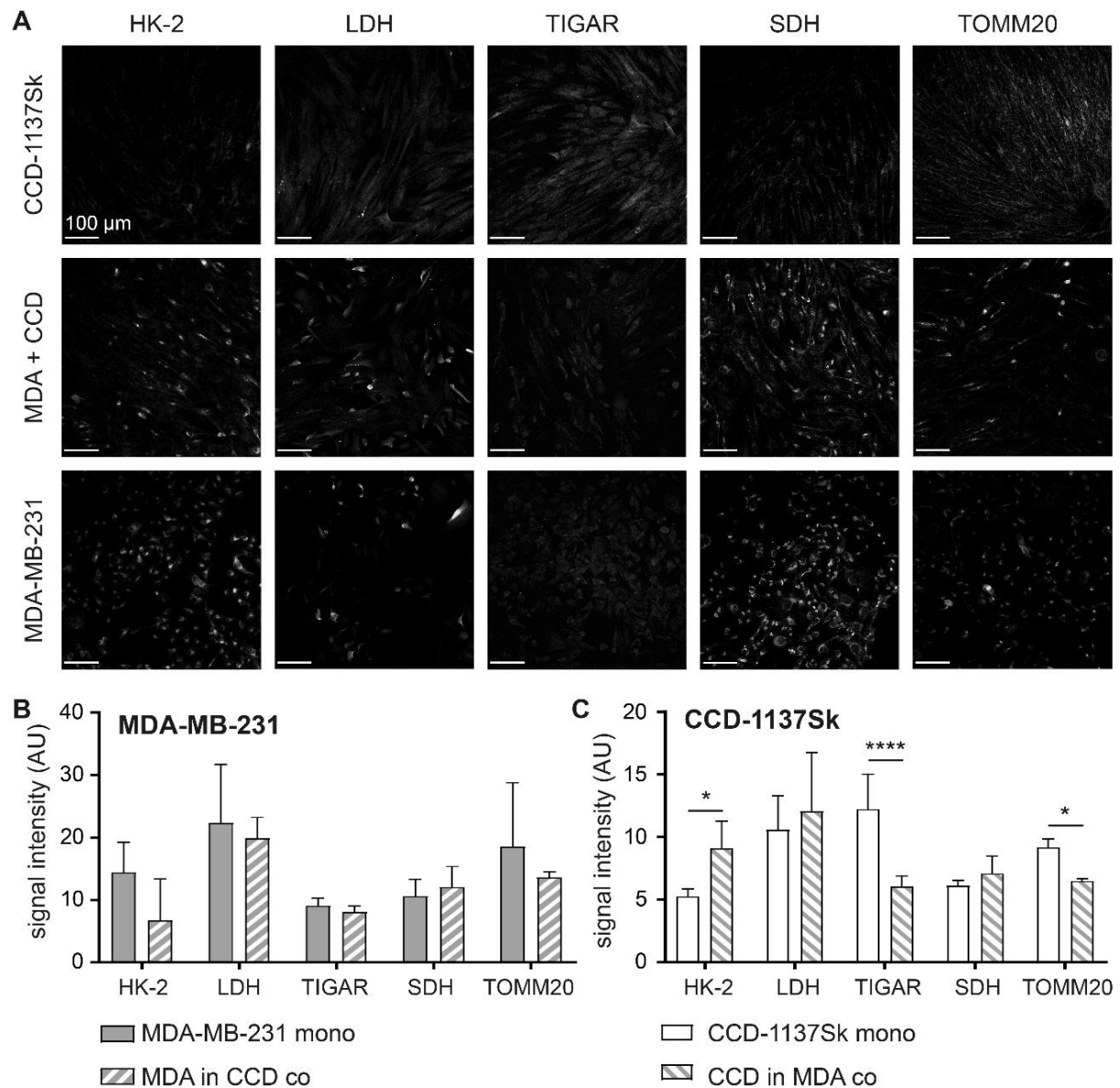


Figure S17. Fibroblasts in mono-layer co-cultures of MDA-MB-231 and CCD-1137Sk show enhanced glycolytic and reduced oxidative phosphorylation markers. MDA-MB-231 and CCD-1137Sk cells were either seeded alone or in co-culture and grown to a subconfluent state for 4 days. Then, cells were fixed and stained with DAPI as well as antibodies against HK-2, LDH, TIGAR, SDH, and TOMM20 as markers for nuclei, glucose breakdown, pyruvate-lactate metabolism, negative glycolysis regulation, oxidative phosphorylation, and mitochondrial content, respectively (A–C). Scale bars, 100 μ m. A) Representative confocal images of fluorescence staining for markers and cultures as indicated. B–C) Graphs showing quantitative analysis of fluorescence intensity values for markers and cell type as indicated. Mean + SEM (n = 3 experiments; * P < 0.05, **** P < 0.0001). (Keller et al., 2020)(CC BY)

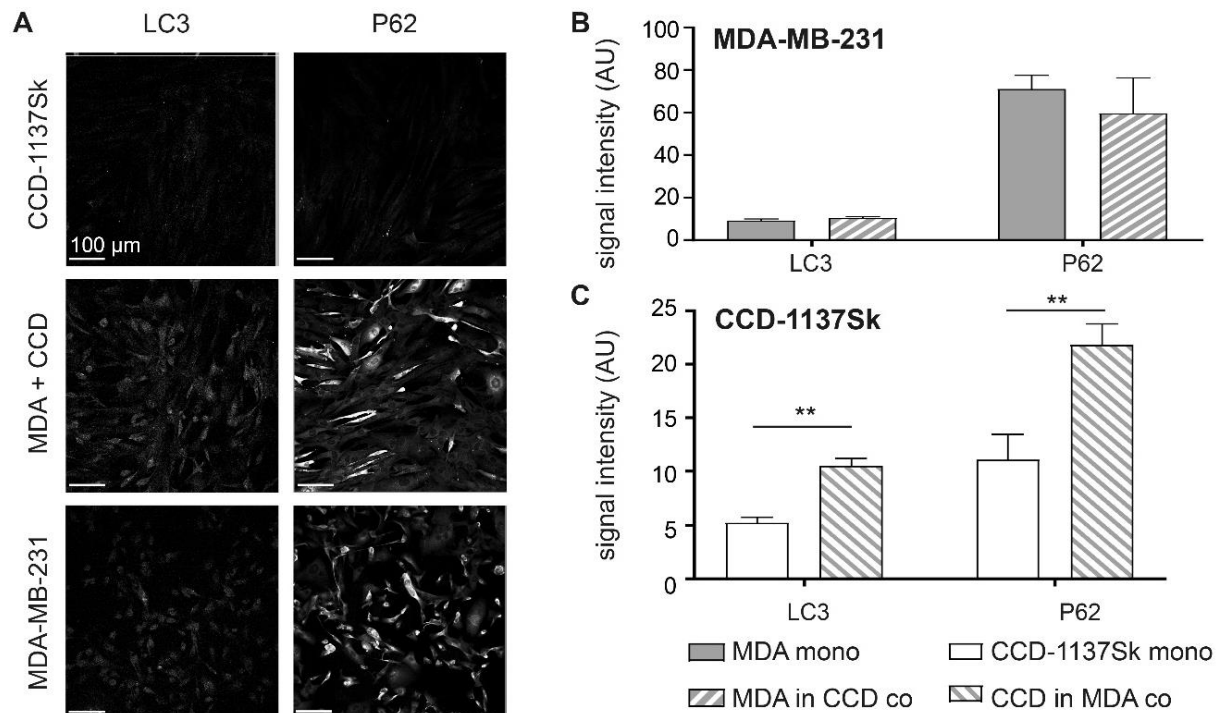


Figure S18. Fibroblasts in mono-layer co-cultures of MDA-MB-231 and CCD-1137Sk display enhanced levels of autophagy markers. MDA-MB-231 and CCD-1137Sk cells were either seeded alone or in co-culture and grown to a subconfluent state for 4 days. Then, cells were fixed and stained with DAPI as well as antibodies against LC3 and P62 as markers for nuclei and autophagy (A–C). Scale bars, 100 μ m. A) Representative confocal images of fluorescence staining for markers and cultures as indicated. B–C) Graphs showing quantitative analysis of fluorescence intensity values for markers and cell type as indicated. Mean + SEM (n = 3 experiments; ** P < 0.01). (Keller et al., 2020)(CC BY)

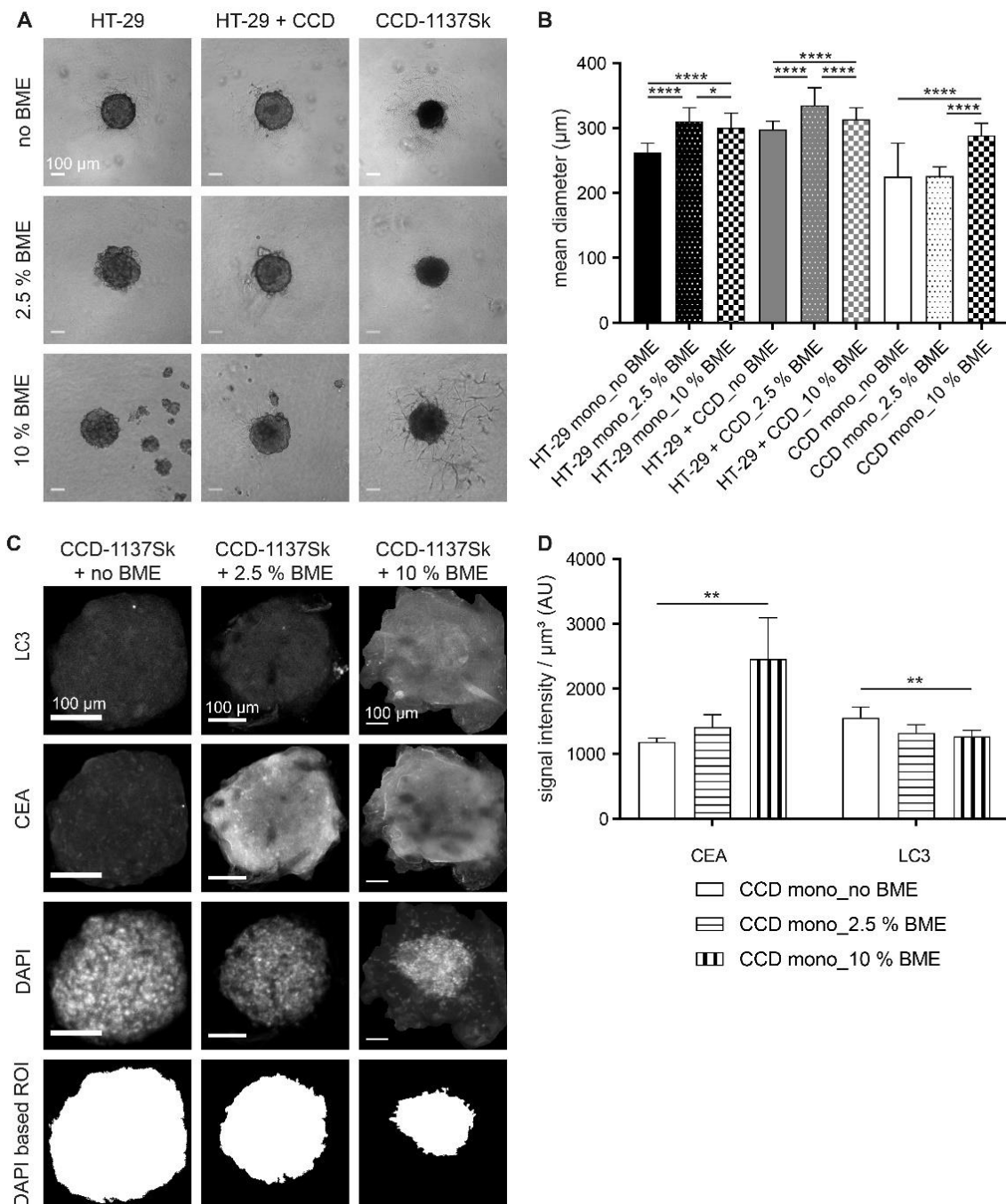


Figure S19. Culture-embedding in BME affects growth and fluorescence properties of spheroids. HT-29 and CCD-1137Sk cells were either seeded alone or in co-culture in the absence or presence of 2.5 % or 10 % BME to form spheroids. After 4 days, cultures were examined with bright-field microscopy (A) to determine spheroid diameters. Note extensive cellular anastomoses in CCD-1137Sk cultures with 10 % BME. B) Graph showing average spheroid diameters. Mean + SEM (n = 90; * P < 0.5, **** P < 0.0001). C-D) Upon wide-field microscopy, 3D-cultures were fixed, stained with DAPI, anti-CEA, and anti-LC3 and then imaged with confocal microscopy. C) representative sum-z projections of confocal image stacks for conditions and markers as indicated. Bottom panels show regions of interest (ROI) selected for quantitative image analysis. These contain the core spheroids with most of the nuclei. However, particularly the condition with 10 % BME shows a wide halo with scattered cells that were hard to distinguish and were therefore excluded from analysis. D) Quantitative analysis of the sum-projections. Mean + SEM (n = 5 experiments; ** P < 0.01). (Keller et al., 2020)(CC BY)

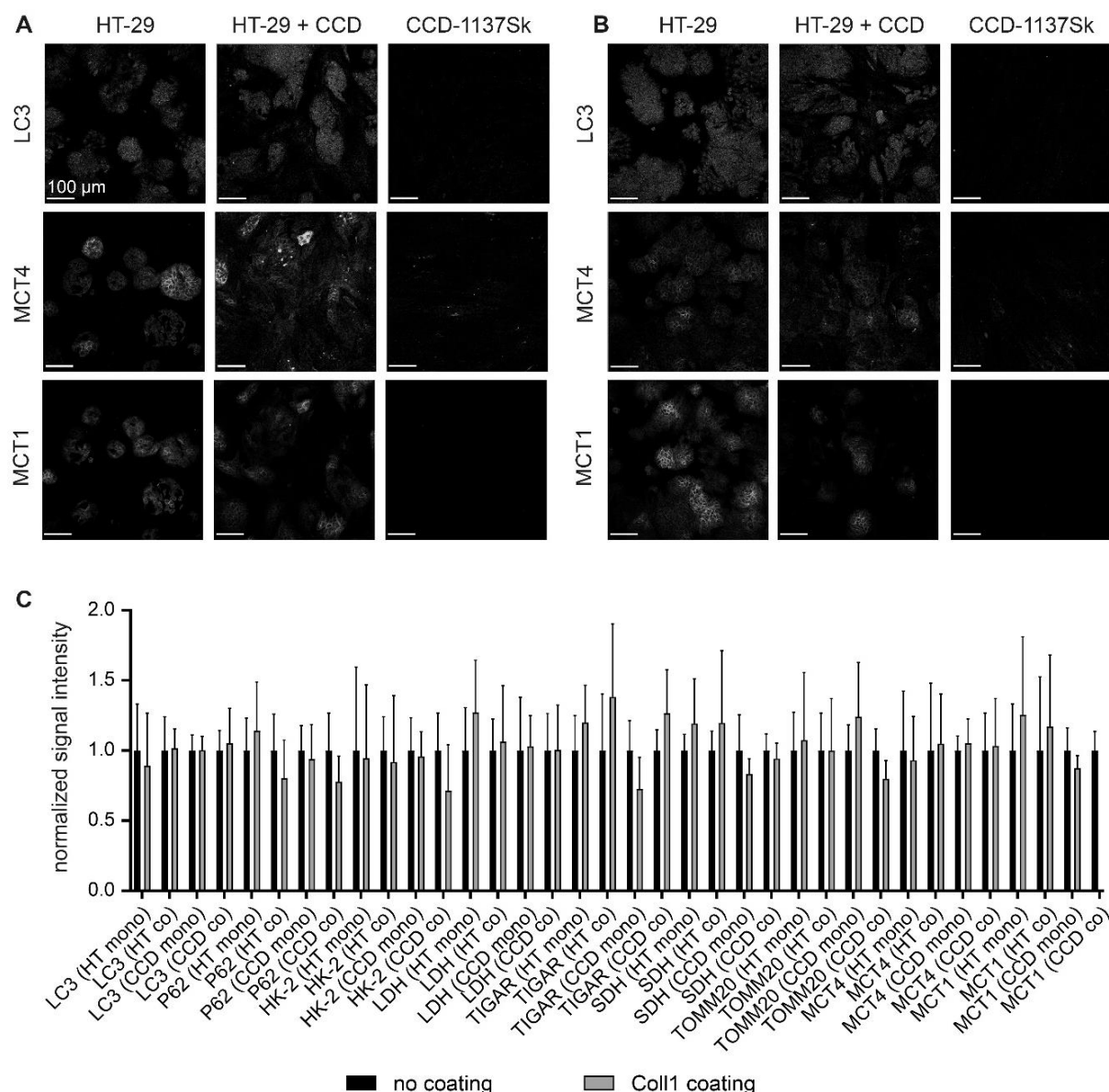


Figure S20. Surface coating with Type-I collagen does not alter the expression patterns of several metabolic markers. HT-29 and CCD-1137Sk cells were either seeded alone or in co-culture and grown to a subconfluent state for 4 days. Then, cells were fixed and stained with DAPI as well as antibodies against several markers as indicated. A-B) Representative confocal images of fluorescence staining for markers LC3, MCT1, and MCT4 of cultures as indicated in the absence (A) and presence (B) of Type-I collagen coating. Scale bars, 100 μ m. C) Graph showing quantitative analysis of fluorescence intensity values for markers and cell type as indicated. All values are normalized to the corresponding average value measured in the absence of coating with Type-I collagen. Mean + SEM (n = 3 experiments). None of the differences was significant. (Keller et al., 2020)(CC BY)

Supplementary Table 1. List of antibodies and dyes used for western blot (WB) and immunofluorescence studies (IF) (Article 1).

Targeted antigen / cells		Manufacturer / Catalog No.	Host / Isotype / Clone	Working Dilution	
				WB	IF
Primary antibodies:					
Apoptotic cells	Cleaved Caspase 3	Cell signaling / 9661	Rabbit / pAb	—	1:500
Carbohydrate deficient bone sialoprotein	Recombinant CD-BSP (aa 108-122)	Immunodiagnostik AG, Germany	Human / IgG / mAb	1:250	1:250
	Recombinant CD-BSP (aa 108-122) IDK1	Immunodiagnostik AG, Germany / 4217.VP	Rat / IgG1 / mAb	1:250	—
Type-I collagen	Anti-Collagen Type 1	Rockland Immunochemicals Inc. / 600-401-103-0.5	Rabbit / IgG / pAb	—	1:150
GAPDH	Recombinant GAPDH	Thermo Fisher Scientific / MA5-15738	Mouse / IgG1 / mAb	1:10000	—
IGF1	Anti IGF1	Thermo Fisher Scientific / PA5-27207	Rabbit / IgG / pAb	1:1000	1:100
Proliferating cells	KI67	Merck / AB9260	Rabbit / pAb	—	1:500
RUNX2	Anti RUNX2	Cell signaling / D1L7F	Rabbit / mAb	1:200	—
TGF- β 1	Anti TGF- β 1	Abcam / ab92486	Rabbit / IgG / pAb	1:1000	1:500
Secondary antibodies:					
Goat anti human (H+L), Alexa Fluor 488		Thermo Fisher Scientific / A11013	Goat / IgG / pAb	—	1:1000
Goat anti human HRP		Dianova / 109-035-098	Goat / IgG / pAb	1:50000	—
Goat anti mouse HRP		Sigma-Aldrich / A2304	Goat / IgG / pAb	1:10000	—
Goat anti rabbit (H+L), Alexa Fluor 488		Invitrogen / A21206	Goat / IgG / pAb	—	1:1000
Goat anti rabbit (H+L), Alexa Fluor 647		Invitrogen / A21246	Goat / IgG / pAb	—	1:1000
Rabbit anti rat HRP		Sigma-Aldrich / A5795	Rabbit / IgG / pAb	1:10000	—
Dyes:					
Actin, Cytoskeleton	Rhodamine Phalloidin (TRITC)	Thermo Fisher Scientific	—	—	1:1000
Nucleus	DAPI	Thermo Fisher Scientific	—	—	1:1000

(Rustamov et al., 2019)(CC BY)

Supplementary Table 2. Chemicals and reagents that were used for this study (Article 3).

Reagent	Supplier	Ordering No.	Lot No.
Cell culture media and reagents			
10x Trypsin-EDTA solution	Sigma-Aldrich	59418C	SLCC3240
B27 Supplement (50x), serum free	Invitrogen	17504044	1987565
Basal Iscove Medium	Biochrome	F0465	1173E
Collagen 1 from rat tail tendon	Sigma-Aldrich	1117917900 1	38429220
DMEM	Capricorn	DMEM-HPA	CP18-2096
DMEM/Ham's F-12, with GlutaMAX supplement	Invitrogen	10565018	2124955
Fetal calf serum (FCS)	Capricorn	FBS-12A	CP16-1422
Gentamicine	Biochrome	A2712	950302
GlutaMAX	Invitrogen	35050061	2063464
IMDM	Sigma-Aldrich	I3390	RNBG9989
Insulin	Sigma-Aldrich	I-6634	74H00845
L-Glutamine (200 mM)	Capricorn	GLN-B	CP17-1801
McCoy's 5A	Capricorn	MCC-A	CP19-2689
MCDB	Biochrome	F8105	0674G
Minimum Essential Medium Nonessential Amino Acids (MEM-NEAA)	Invitrogen	10370070	2026977
N-2 Supplement (100x)	Invitrogen	17502048	1911689
Pen/Strep (10.000 U penicillin, 10 mg / mL streptomycin)	Sigma-Aldrich	P4333	049M4857V
Recombinant human FGF-2 Type 147	Cell Guidance Systems	GFH28-100	0313
TrypLE Express Enzyme (1X), no phenol red	Invitrogen	12604021	2085298
Transfection Reagents			
5 % Asel enzyme	New England Biolabs	R0526S	131701
Alkaline phosphatase	Invitrogen	100012546	1752270
Asel buffer 3.1	New England Biolabs	B7203S	421612
Other chemicals and reagents			
Albumin Fraktion V (BSA)	Carl Roth	8076.3	69279339
CytoVista 3D Cell Culture Clearing Reagent	Invitrogen	V11315	9QZ53
Dimethylsulfoxid (DMSO)	Carl Roth	A994.1	199282083
D-sorbitol	Sigma-Aldrich	1077581000	M529358845

Formamide	Sigma-Aldrich	47671	372879/144997
Glycerol	Carl Roth	3783.2	237259780
Glycine	Carl Roth	3908.2	177257836
Heparin sodium salt from porcine intestinal mucosa	Sigma-Aldrich	H3149-250KU	SLBN6012V
Mowiol 4-88	Sigma-Aldrich	713.2	269278961
Paraformaldehyd	Carl Roth	335.3	259284291
Polyethylenglykol 8000 (PEG)	Sigma-Aldrich	P5413	BCCC6496
Triton X-100	Carl Roth	T9284	19K01512
Tween-20	Sigma-Aldrich	P9416-50ML	125K01031
Urea	Sigma-Aldrich	1084871000	K40676887002
Dyes & Antibodies			
Anti-KI67 Antibody (rabbit polyclonal)	Sigma-Aldrich	AB9260	3195946
CellTracker Green CMFDA Dye	ThermoFisher Scientific	C2925	1781143
CellTracker Red CMPTX Dye	ThermoFisher Scientific	C34552	1890538
DAPI dihydrochloride	Sigma-Aldrich	D9542-5MG	28114320
Donkey anti-Rabbit IgG (H+L) Alexa Fluor Plus 488	ThermoFisher Scientific	A32790	TI271741
Donkey anti-Rabbit IgG (H+L) Alexa Fluor Plus 647	ThermoFisher Scientific	A32795	TJ271043
DRAQ5 Fluorescent Probe Solution (5 mM)	ThermoFisher Scientific	62252	511DR50200

(Nürnberg et al., 2020)(CC BY)

Supplementary Table 3. Percentage loss of depth-dependent signal intensity in cleared HaCaT spheroids. Upon growth to a diameter of approximately 300 μm , HaCaT spheroids were fixed, stained with DAPI and DRAQ5, followed by optical clearing or embedding as indicated, and subsequent confocal whole mount microscopy without z-compensation. The Table reports the mean percentage loss of signal intensity with corresponding standard deviation (SD), calculated from the individual maximum signal intensity of each condition, at absolute imaging depths of 25-200 μm . $N \geq 7$.

		DAPI							
	Depth [μm]	25	50	75	100	125	150	175	200
PBS	% of darkening	21.55	62.33	76.67	80.56	82.05	82.66	83.51	100
	SD [%]	15.05	8.25	2.31	0.73	0.42	0.83	0.29	0
Mowiol	% of darkening	18.08	59.85	81.99	89.52	92.06	93.10	93.67	94.06
	SD [%]	7.44	5.99	2.88	1.47	0.86	1.03	0.98	0.71

Clear^{T2}	% of darkening	13.87	60.90	80.54	86.54	88.74	89.88	100	100
	SD [%]	4.77	1.78	0.51	0.27	0.16	0.11	0	0
CytoVista	% of darkening	5.89	48.01	69.51	80.65	91.05	100	100	100
	SD [%]	14.12	9.17	5.88	3.40	3.27	0	0	0
ScaleS	% of darkening	3.44	8.54	37.04	59.91	73.80	83.02	88.14	90.38
	SD [%]	14.77	10.74	7.66	4.22	2.85	1.75	0.98	0.71
Glycerol	% of darkening	3.73	25.16	50.88	68.77	79.06	85.03	87.85	88.26
	SD [%]	10.81	8.54	7.21	6.15	5.48	5.55	6.34	7.77
DRAQ5									
	Depth [µm]	25	50	75	100	125	150	175	200
PBS	% of darkening	14.72	56.42	77.53	85.64	88.44	89.54	90.14	100
	SD [%]	27.40	15.45	6.32	2.32	0.89	0.46	0.36	0
Mowiol	% of darkening	15.42	49.38	73.52	85.54	91.34	94.08	95.73	96.41
	SD [%]	6.65	7.39	3.65	2.68	1.32	0.66	0.57	0.51
Clear^{T2}	% of darkening	7.96	52.97	78.93	89.30	92.95	94.96	100	100
	SD [%]	30.54	15.53	6.89	3.44	2.25	1.85	0	0
CytoVista	% of darkening	1.98	32.87	56.19	73.60	89.32	86.46	100	100
	SD [%]	20.65	11.87	6.48	2.85	5.47	0	0	0
ScaleS	% of darkening	0	15.83	42.47	59.44	70.33	77.91	83.09	86.18
	SD [%]	12.67	7.41	5.82	4.19	2.62	2.46	1.07	1.35
Glycerol	% of darkening	8.18	25.84	47.51	62.50	73.38	80.13	84.78	86.55
	SD [%]	13.39	13.20	8.06	5.95	3.61	3.60	5.84	9.16

(Nürnberg et al., 2020)(CC BY)

Supplementary Table 4. Overview of fluorescence penetration and SNR in depth of simple spheroids sorted by cell type. Upon growth to a diameter of approximately 300 µm, spheroids made of cell lines as indicated were fixed, stained with DAPI and DRAQ5, followed by optical tissue clearing or embedding as indicated and subsequent confocal whole mount microscopy without z-compensation. The table reports the average values for absolute and normalized depth of 50 % signal loss, 90 % signal loss, and SNR < 5 for DAPI and DRAQ5 in the absence of z-compensation. n ≥ 7. For clarity, maximal values are depicted with green shading.

B7_033#1NPC1												
	DAPI						DRAQ5					
	Absolute depth [µm]			Normalized depth [µm]			Absolute depth [µm]			Normalized depth [µm]		
	50 % signal loss	90 % signal loss	SNR < 5	50 % signal loss	90 % signal loss	SNR < 5	50 % signal loss	90 % signal loss	SNR < 5	50 % signal loss	90 % signal loss	SNR < 5
PBS	75,0	--	103,5	76,6	--	105,7	78,0	216,0	139,5	79,6	220,5	142,4
Mowiol	111,0	220,5	154,5	138,2	274,5	192,4	94,5	190,5	171,0	117,7	237,2	212,9
Clear ^{T2}	60,0	153,0	73,5	81,3	207,2	99,5	64,5	117,0	123,0	87,4	158,4	166,6

CytoVista	78,0	118,5	96,0	143,5	218,0	176,6	49,5	99,0	85,5	91,1	182,1	157,3
Sca/eS	102,0	214,5	133,5	105,4	221,6	137,9	114,0	211,5	187,5	117,8	218,5	193,7
Glycerol	133,5	237,0	201,0	118,9	211,1	179,0	123,0	226,5	265,5	109,6	201,8	236,5
HaCaT												
	DAPI						DRAQ5					
	Absolute depth [µm]			Normalized depth [µm]			Absolute depth [µm]			Normalized depth [µm]		
	50 % signal loss	90 % signal loss	SNR < 5	50 % signal loss	90 % signal loss	SNR < 5	50 % signal loss	90 % signal loss	SNR < 5	50 % signal loss	90 % signal loss	SNR < 5
PBS	40,5	--	64,5	45,4	--	72,2	45,0	156,0	87,0	50,4	174,7	97,4
Mowiol	43,5	103,5	69,0	56,3	134,1	89,4	49,5	117,0	105,0	64,1	151,6	136,0
Clear ^{IT2}	42,0	154,5	61,5	60,0	220,6	87,8	48,0	103,5	96,0	68,5	147,8	137,1
CytoVista	51,0	121,5	117,0	95,6	227,7	219,3	66,0	126,0	117,0	123,7	236,2	219,3
Sca/eS	88,5	189,0	153,0	103,2	220,4	178,4	84,0	232,5	205,5	98,0	271,2	239,7
Glycerol	73,5	--	142,5	84,0	--	162,8	78,0	--	195,0	89,1	--	222,8
CCD-1337SK												
	DAPI						DRAQ5					
	Absolute depth [µm]			Normalized depth [µm]			Absolute depth [µm]			Normalized depth [µm]		
	50 % signal loss	90 % signal loss	SNR < 5	50 % signal loss	90 % signal loss	SNR < 5	50 % signal loss	90 % signal loss	SNR < 5	50 % signal loss	90 % signal loss	SNR < 5
PBS	49,5	--	51,0	54,9	--	56,6	52,5	--	85,5	58,2	--	94,9
Mowiol	75,0	--	85,5	96,7	--	110,3	103,5	276,0	154,5	133,5	355,9	199,2
Clear ^{IT2}	48,0	222,0	54,0	64,4	297,7	72,4	58,5	199,5	120,0	78,4	267,5	160,9
CytoVista	60,0	156,0	105,0	109,0	283,5	190,8	73,5	171,0	142,5	133,6	310,7	258,9
Sca/eS	84,0	244,5	102,0	92,2	268,3	111,9	78,0	303,0	243,0	85,6	332,5	266,7
Glycerol	123,0	327,0	175,5	132,3	351,7	188,8	127,5	331,5	309,0	137,1	356,6	332,4
HT-29												
	DAPI						DRAQ5					
	Absolute depth [µm]			Normalized depth [µm]			Absolute depth [µm]			Normalized depth [µm]		
	50 % signal loss	90 % signal loss	SNR < 5	50 % signal loss	90 % signal loss	SNR < 5	50 % signal loss	90 % signal loss	SNR < 5	50 % signal loss	90 % signal loss	SNR < 5
PBS	31,5	--	53,5	50,3	--	85,9	39,5	115,5	81,5	63,2	186,5	131,4
Mowiol	34,5	122,5	58,5	57,4	205,8	97,9	43,5	133,5	89,5	72,5	224,4	150,2
Clear ^{IT2}	27,5	--	37,5	49,8	--	68,3	34,5	102,5	68,5	62,8	188,3	125,5
CytoVista	50,5	96,5	70,5	109,1	209,4	152,7	56,5	100,5	92,5	122,2	218,1	200,7
Sca/eS												
Glycerol	43,5	151,5	81,5	70,9	249,1	133,6	49,5	121,5	Full Range	80,8	199,6	Full Range
HTC-8												
	DAPI						DRAQ5					
	Absolute depth [µm]			Normalized depth [µm]			Absolute depth [µm]			Normalized depth [µm]		
	50 % signal loss	90 % signal loss	SNR < 5	50 % signal loss	90 % signal loss	SNR < 5	50 % signal loss	90 % signal loss	SNR < 5	50 % signal loss	90 % signal loss	SNR < 5
PBS	45,0	112,5	45,0	52,5	131,2	52,5	46,5	124,5	64,5	54,2	145,2	75,2
Mowiol	51,0	168,0	40,5	56,8	187,0	45,1	58,5	184,5	102,0	65,1	205,4	113,5
Clear ^{IT2}	43,5	--	42,0	52,5	--	50,6	52,5	150,0	96,0	63,3	180,9	115,8
CytoVista	63,0	145,5	79,5	96,7	223,3	122,0	75,0	162,0	129,0	115,1	248,6	198,0
Sca/eS	85,5	259,5	88,5	84,5	256,6	87,5	81,0	312,0	162,0	80,1	308,5	160,2
Glycerol	84,0	264,0	85,5	84,5	265,4	86,0	85,5	276,0	232,5	86,0	277,5	233,7

(Nürnberg et al., 2020)(CC BY)

Supplementary Table 5. Overview of fluorescence penetration and SNR in depth in complex 3D-cell cultures. Melanoma tri-culture spheroids and Dynarray chip-based co-cultures of MDA-MB-231-ECFP and CCD-1137Sk cells were fixed, stained with DAPI (Melanoma tri-culture) or DRAQ5 (Dynarray culture), followed by optical tissue clearing or embedding as indicated and subsequent confocal whole mount microscopy. In tri-cultures, melanoma cells were labeled prior to seeding with CellTracker Green, in Dynarray cultures, CCD-1137Sk cells were marked with CellTracker Red. The table reports the average values for absolute and normalized depth of 50 % signal loss, 90 % signal loss, and SNR < 5 for DAPI and Cell Tracker Green (tri-culture) or CellTracker Red and DRAQ5 (Dynarrays) in the absence of z-compensation. $n \geq 5$. For clarity, maximal values are depicted with green shading.

Tri-culture												
	DAPI						CellTracker Green					
	Absolute depth [μm]			Normalized depth [μm]			Absolute depth [μm]			Normalized depth [μm]		
	50 % signal loss	90 % signal loss	SNR < 5	50 % signal loss	90 % signal loss	SNR < 5	50 % signal loss	90 % signal loss	SNR < 5	50 % signal loss	90 % signal loss	SNR < 5
PBS	25,5	90,5	34,5	43,9	158,1	59,7	27,5	--	--	47,4	--	--
Mowiol	38,5	81,5	78,5	70,2	149,6	144,1	30,5	--	--	55,4	--	--
Clear ^{T2}	30,5	80,5	47,5	59,8	159,5	93,7	28,5	--	--	55,8	--	--
CytoVista	33,5	71,5	59,5	83,1	178,9	148,6	21,5	--	--	52,9	--	--
Sca/eS	48,5	168,5	67,5	80,0	279,9	111,6	33,5	--	--	55,0	--	--
Glycerol	49,5	128,5	88,5	78,3	204,5	140,6	34,5	--	--	54,3	--	--
Dynarrays												
	CellTracker Red						DRAQ5					
	Absolute depth [μm]			Normalized depth [μm]			Absolute depth [μm]			Normalized depth [μm]		
	50 % signal loss	90 % signal loss	SNR < 5	50 % signal loss	90 % signal loss	SNR < 5	50 % signal loss	90 % signal loss	SNR < 5	50 % signal loss	90 % signal loss	SNR < 5
PBS	--	--	--	--	--	--	--	--	--	--	--	--
Mowiol	58,5	--	--	--	--	--	56,5	--	74,5	--	--	--
Clear ^{T2}	47,5	--	--	--	--	--	44,5	--	64,5	--	--	--
CytoVista	42,5	--	--	--	--	--	43,5	--	45,5	--	--	--
Sca/eS	92,5	--	--	--	--	--	91,5	--	115,5	--	--	--
Glycerol	85,5	--	--	--	--	--	74,5	148,5	112,5	--	--	--

(Nürnberg et al., 2020)(CC BY)

12 PUBLICATIONS

Keller, F., Bruch, R., Clauder, F., Hafner, M., and Rudolf, R. (2021). Extracellular Matrix Components Regulate Bone Sialoprotein Expression in MDA-MB-231 Breast Cancer Cells. *Cells* 10.

Keller, F., Bruch, R., Schneider, R., Meier-Hubberten, J., Hafner, M., and Rudolf, R. (2020). A Scaffold-Free 3-D Co-Culture Mimics the Major Features of the Reverse Warburg Effect In Vitro. *Cells* 9, 1900.

Nürnberg, E., Vitacolonna, M., Klicks, J., von Molitor, E., Cesetti, T., **Keller, F.**, Bruch, R., Ertongur-Fauth, T., Riedel, K., Scholz, P., et al. (2020). Routine Optical Clearing of 3D-Cell Cultures: Simplicity Forward. *Front Mol Biosci* 7, 20.

Keller, F., Rudolf, R., and Hafner, M. (2019). Towards optimized breast cancer 3D spheroid mono- and co-culture models for pharmacological research and screening. *J. Cell. Biotechnol.* 5, 89–101.

Rustamov, V., **Keller, F.**, Klicks, J., Hafner, M., and Rudolf, R. (2019). Bone Sialoprotein Shows Enhanced Expression in Early, High-Proliferation Stages of Three-Dimensional Spheroid Cell Cultures of Breast Cancer Cell Line MDA-MB-231. *Front. Oncol.* 9, 36.

13 CURRICULUM VITAE

PERSONALIEN

Name und Vorname: Keller Florian
Geburtsdatum: 11.12.1991
Geburtsort: Karlsruhe, Deutschland
Vater: Arnold Josef Keller
Mutter: Karin Keller (geb. Schmitt)

SCHULISCHER WERDEGANG

(2002) – (2011) St. Paulusheim Bruchsal
(26.05.2011) Abitur

UNIVERSITÄRER WERDEGANG

WS2011 – SS2014 Studium (Biotechnologie)
an der Hochschule MCI Management Center Innsbruck
07.2013 – 09.2013 Bachelorarbeit 1 (Karlsruher Institut für Technologie)
Thema: Herstellung von 3D-Zellgerüstträgern basierend auf
einem synthetischen Polymer
04.2014 – 06.2014 Bachelorarbeit 2 (MCI Management Center Innsbruck)
Thema: Analyse von hitzeinduzierbaren Promotorelementen
in *Chlamydomonas reinhardtii*
21.07.2014 Bachelor of Science in Engineering (BSc)
WS2014 – SS2016 Hauptstudium (Biotechnologie)
an der Hochschule MCI Management Center Innsbruck
02.2016 – 10.2016 Masterarbeit (Roche Diagnostics)
Thema: Entwicklung einer neuen Erntestrategie für die
Produktion diagnostischer Einsatzstoffe
26.09.2016 Master of Science in Engineering (MSc), Note: 1,3

14 DANKSAGUNG

Zuerst danke ich Herrn Prof. Dr. Mathias Hafner dafür, mir als Doktorvater die Möglichkeit zur Promotion eröffnet zu haben. Ohne das Vertrauen, das Sie mir entgegengebracht haben und Ihre Ermutigung zur kumulativen Abfassung, hätte es diese Arbeit und die damit zusammenhängenden Publikationen in der vorliegenden Form nicht gegeben.

Besonderen Dank schulde ich meinem Betreuer an der Hochschule Mannheim, Prof. Dr. Rüdiger Rudolf. Es gab zu Beginn noch sehr viel zu lernen; und auch wenn das natürlich nach wie vor so ist, so konnte ich mich vor allem durch die hohen Standards weiterentwickeln, die mir Tag für Tag vorgelebt wurden. Dabei fand ich auch in anstrengenden Phasen immer ein offenes Ohr und bekam wertvollen Rat.

Dem ganzen MZB-Labor möchte ich für den Zusammenhalt und den guten Umgang miteinander danken. Besonders die Arbeit mit meinen Kollegen Maximilian Schäfer, Roman Bruch, Dr. Elena von Molitor, Elina Nürnberg, Valeh Rustamov, Tatjana Straka, Sarah Hörner und Dr. Anett Pomowski, aber auch den Leitern der Praktika, Ariane Tomsche und Jessica Martin hat dafür gesorgt, dass ich immer gerne an das Institut gekommen bin. Darüber hinaus halfen Dr. Matteo Rigon, Patrick Williams, Daniele Gueiber, Frederik Gertz, Valentin Kramer, Regina Martens und Cordula Stahl mit ihrer positiven Art, ein angenehmes Arbeitsklima zu erhalten.

Mit aufkommenden Fragen konnte ich mich immer an Dr. Mario Vitacolonna, Dr. Tiziana Cesetti, Dr. Andreas Holloschi, Dr. Hella-Monika Kuhn, Prof. Dr. Petra Kioschis-Schneider, Prof. Dr. Philipp Wiedemann und speziell zu Beginn meiner Arbeit auch an Dr. Julia Klicks, Dr. Franziska Ebeling oder Dr. Heiko Flamman wenden. Insgesamt hat mir der Austausch innerhalb des MZB dabei geholfen, die vielen großen und kleinen Herausforderungen im Laboralltag zu meistern. Ich bin auch froh, einen Teil der dabei gemachten Erfahrungen an Vanessa Blomeyer weitergeben zu können, die mit ihrer motivierten Arbeitsweise zu großartigen Ergebnissen kommen und die Projekte gut weiterführen wird.

Ohne Dr. Rüdiger Bauer hätte ich das Promotionsvorhaben im Anschluss an meine Masterarbeit vielleicht nicht angetreten. Er hat mich in meiner Arbeitsweise bestärkt und dabei geholfen, den Grundstein für die weitere akademische Laufbahn zu legen.

Nun möchte ich noch meinen größten Dank ausdrücken. Natürlich gebührt er meiner Familie. Meine Eltern Arno und Karin Keller haben immer an mich geglaubt und mir das Studium und die Promotion durch ihre grenzenlose Liebe und Aufopferung überhaupt erst ermöglicht. Ich bin nur dank euch derjenige, der sich heute bedanken darf. Mir fehlen dafür die richtigen Worte, und ihr wisst, was das bedeutet.

Es gab auch Menschen, bei denen ich mich nicht mehr bedanken kann. Aber ich werde euch immer in meinem Herzen behalten.

Apropos Herz: Mit Ramona Ullrich gibt es noch eine ganz besondere Person, bei der ich mich viel zu selten bedanke, ohne die ich aber nicht mehr sein möchte. Ich freue mich auf die kommenden, gemeinsamen, Herausforderungen in unserer eigenen kleinen Familie.